

ISSN 0911-5730

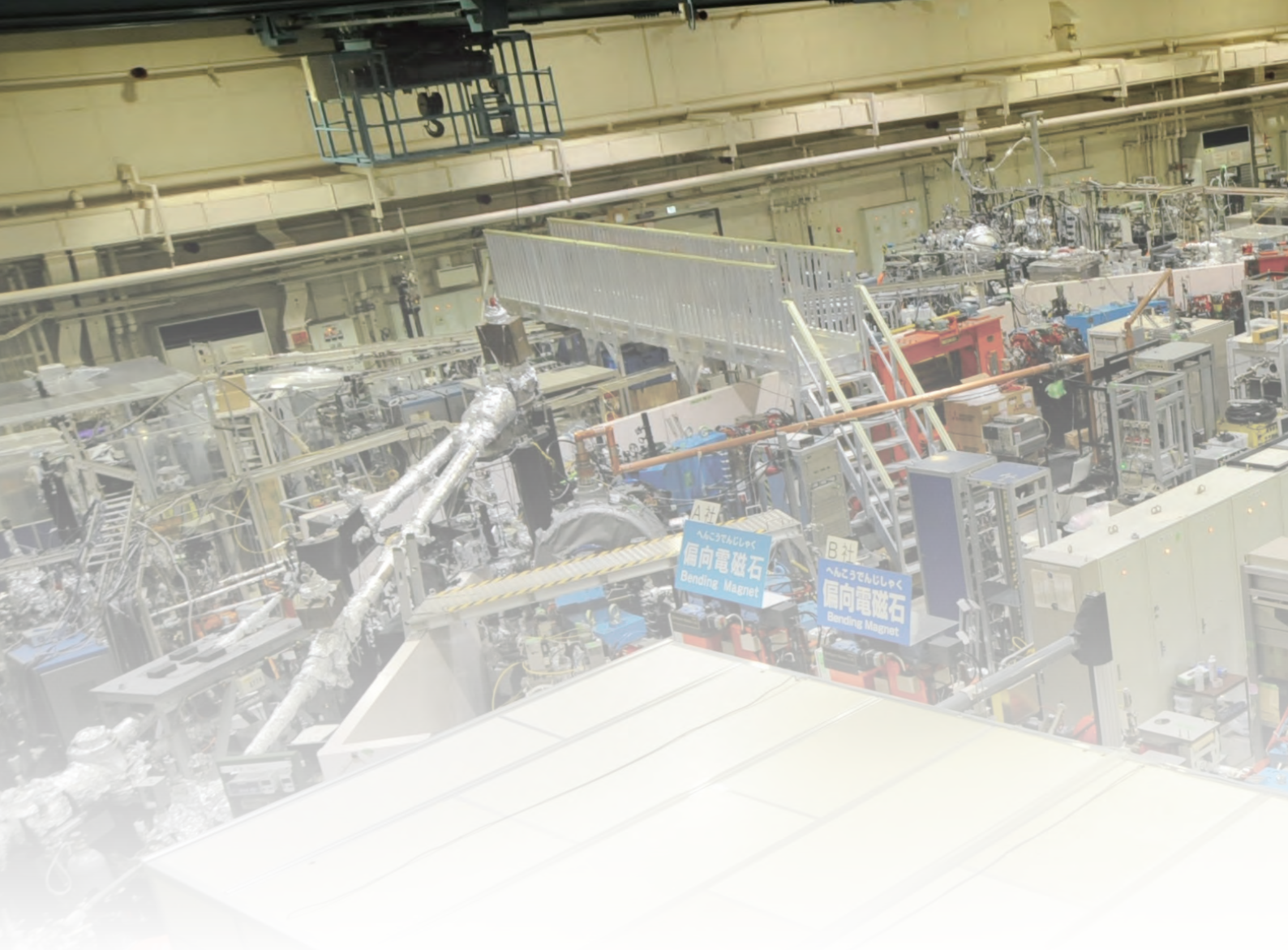
UVSOR-48

August 2021

UVSOR ACTIVITY REPORT 2020

UVSOR Synchrotron Facility
Institute for Molecular Science
National Institutes of Natural Sciences

UVSOR II
since 2012



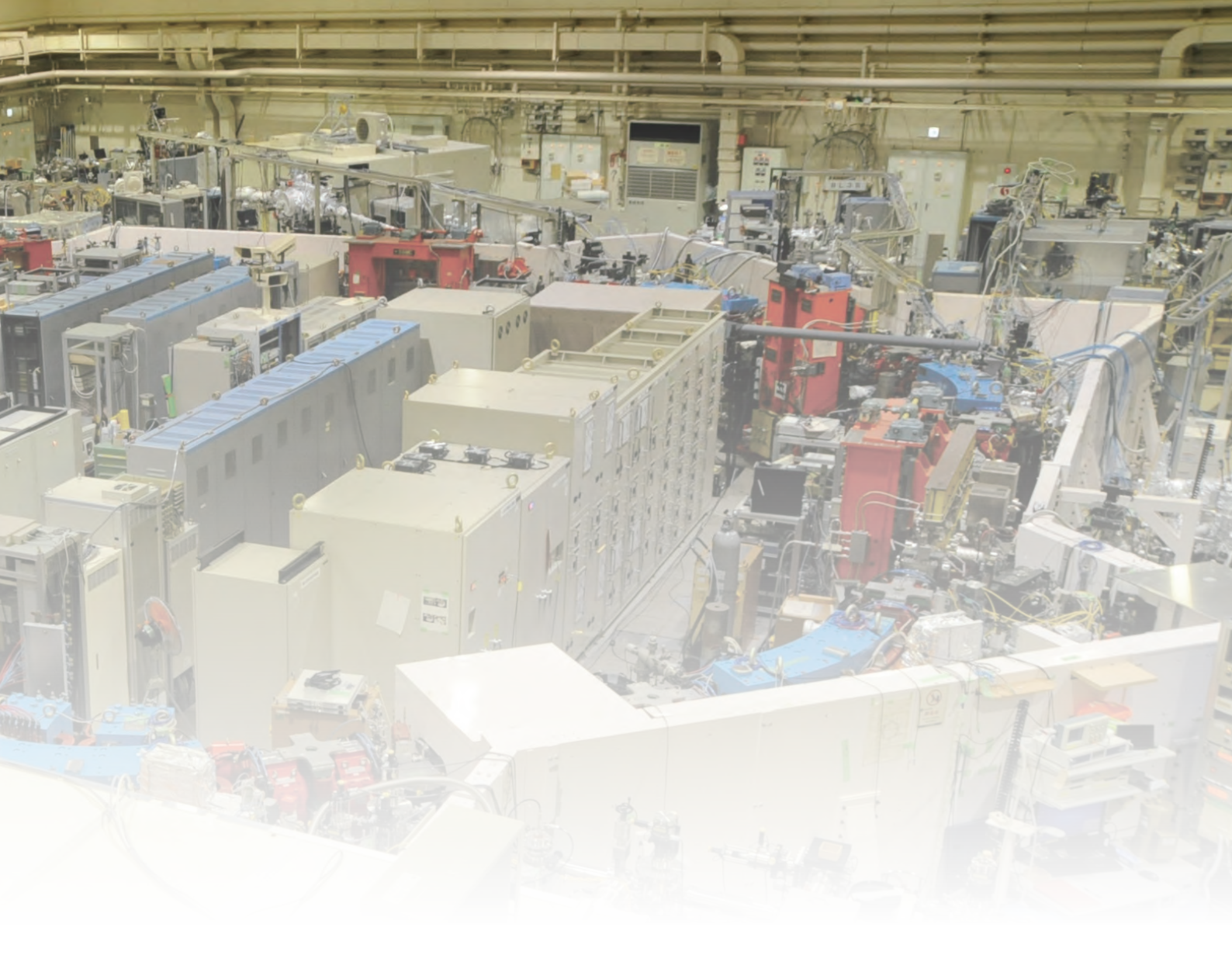
Preface

This Activity Report covers scientific and technological activities carried out using the UVSOR-III Synchrotron in FY2020 (April 2020 - March 2021). We present scientific examples of how the users study at the UVSOR Synchrotron Facility.

The present UVSOR-III Synchrotron is one of the most advanced low-energy SR facilities of the 3rd generation SR in the world and is now one of the critical resources in doing molecular science. The UVSOR-

III Synchrotron has a small electron storage ring but has powerful 6-undulator beamlines (3 VUV and 3 in-vacuum soft X-ray undulators) with 8-dipole beamlines. We never stop improving and upgrading our micro- and nano-scale photoabsorption and photoemission approaches and in situ/operando measurements in the VUV and soft X-ray regions, based on our strategic international collaboration program in molecular science. We are grateful to all the people who use our facility and support our efforts.

UVSOR operates for 40 weeks/year (ca. 2,200 h user time), accepts ~230 proposals, about ~1,000 individual researchers counting total ~ 4,000 people*day/year. Most users stay for one or two weeks for experimenting. To continue high-level achievements in science and technology at the UVSOR-III Synchrotron, our in-house staff is constantly committed to maintaining and improving high-performance accelerators and beamlines. The FY2020 was a challenging year for all researchers, and COVID-19 issues gave a major impact on synchrotron users around the world. Almost all the projects have been done after rearrangement of the beamtime,



fortunately, however, we might be realized in the future there was a problem in experimental quality in a sense of limited manpower in the experiments as well as a lack of experience for on-site experiments of the students. The details on the action are described in the Activity Report.

On the experimental side, technology development will not stop, hence we will make a progress on the imaging-related techniques to inspire advanced molecular science. We have started to construct the new endstation at the undulator-based soft X-ray beamline BL6U. The new apparatus of the photoelectron momentum microscope is developing day by day. Indeed, the project was affected a bit by COVID due to a delay of the construction term and installation steps, etc. In the beamline BL1U, we have conducted in developing the novel light sources, including pulsed- γ ray and their use for the measurements. To optimize the high-power laser light to UVSOR-III for versatile use, we arranged the endstation layout of BL1U. The advanced SR-related instrument will offer opportunities in characterizing the electronic structure of surface atomic sites, thin films, molecular adsorbates, bulk crystals, and so on.

We started to discuss the possibility to construct the post-UVSOR-III as a long-term plan for sustainable development. We look forward to receiving your feedback and suggestions on the continuing evolution of the UVSOR Synchrotron Facility. And we hope many users will perform excellent work by fully utilizing the UVSOR-III Synchrotron as a unique international hub for the SR research in advanced molecular science.

April 2021

Satoshi Kera

Director of the UVSOR Synchrotron Facility

The 39th CSJ Award for Technical Achievements Given to Mr. Eiken Nakamura

Mr. Eiken Nakamura, Facility Chief Engineer in UVSOR Synchrotron Facility, has been awarded the 39th Chemical Society of Japan (CSJ) Award for Technical Achievements for “Development of UVSOR Beamlines and Their Experimental Apparatuses for Promoting Molecular Science”. The award is given by CSJ to persons who have made significant contributions to the improvement/development of devices/instruments/plants for chemistry and the chemical industry with their special skills.

Arriving at UVSOR Synchrotron Facility in 1984 (soon after the first synchrotron-light creation (1983)), Mr. Nakamura started his career in the construction, maintenance, and modification of beamlines and end stations. He made great contributions to the development of various monochromators such as a grasshopper monochromator and a plane-grating monochromator, and also of experimental apparatuses. Among a large number of contributions, some highlights can be found in the development of new beamlines: a far-infrared beamline (BL6B, 1985), which is the first one in the world, a device/instrument calibration beamline (BL5B, 1988), which has been active for a long time, and an undulator beamline (BL6U, 2003), where a state-of-the-art momentum microscope system (UVSOR MM) is currently being developed (see the next page). Another remarkable contribution is to the modification of the soft-X-ray beamline BL4B to utilize the circularly polarized light component of bending radiation, which was successful with Mr. Nakamura’s invention of L-shaped water-cooling four-quadrant slit system.

As above, Mr. Nakamura played an important role in keeping the UVSOR facility on the cutting edge of science and technology. Many UVSOR users have benefited from this effort and have also been supported by him in various ways to carry out experiments.



Double award celebration!!
The CSJ award is one of the awards.



The 39th CSJ Award for Technical Achievements Given to Mr. Eiken Nakamura

Mr. Eiken Nakamura, Facility Chief Engineer in UVSOR Synchrotron Facility, has been awarded the 39th Chemical Society of Japan (CSJ) Award for Technical Achievements for “Development of UVSOR Beamlines and Their Experimental Apparatuses for Promoting Molecular Science”. The award is given by CSJ to persons who have made significant contributions to the improvement/development of devices/instruments/plants for chemistry and the chemical industry with their special skills.

Arriving at UVSOR Synchrotron Facility in 1984 (soon after the first synchrotron-light creation (1983)), Mr. Nakamura started his career in the construction, maintenance, and modification of beamlines and end stations. He made great contributions to the development of various monochromators such as a grasshopper monochromator and a plane-grating monochromator, and also of experimental apparatuses. Among a large number of contributions, some highlights can be found in the development of new beamlines: a far-infrared beamline (BL6B, 1985), which is the first one in the world, a device/instrument calibration beamline (BL5B, 1988), which has been active for a long time, and an undulator beamline (BL6U, 2003), where a state-of-the-art momentum microscope system (UVSOR MM) is currently being developed (see the next page). Another remarkable contribution is to the modification of the soft-X-ray beamline BL4B to utilize the circularly polarized light component of bending radiation, which was successful with Mr. Nakamura’s invention of L-shaped water-cooling four-quadrant slit system.

As above, Mr. Nakamura played an important role in keeping the UVSOR facility on the cutting edge of science and technology. Many UVSOR users have benefited from this effort and have also been supported by him in various ways to carry out experiments.



Double award celebration!!
The CSJ award is one of the awards.

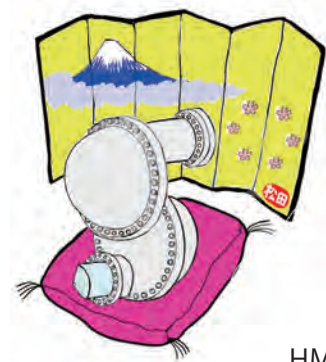
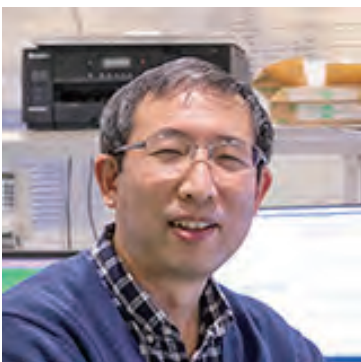


The NAGAI Foundation for Science & Technology Encouragement Award Given to Dr. Fumihiko Matsui

Dr. Fumihiko Matsui, Senior Researcher in UVSOR Synchrotron Facility, has been awarded the NAGAI Foundation for Science & Technology Encouragement Award for “Development of micro area analysis of surfaces of materials with unique electronic properties by the momentum microscope”. The award is given by the NAGAI Foundation for Science & Technology to researchers who made significant achievements in the materials processing industry and related research fields.

Since taking up his post in April, 2018, Dr. Matsui has been conducting the development of a unique state-of-the-art surface and materials analysis system at the soft-X-ray beamline BL6U of the UVSOR-III synchrotron, introducing and advancing a momentum microscope (MM) in collaboration with SPECS GmbH. The system aims at extracting accurate and sufficient information on atomic and electronic structure and spin distribution carried by photoelectrons, in order to promote detailed atomic-level investigation to solve, ultimately, global energy and environmental issues.

The award encourages the development of this promising system, which is somewhat slowly but steadily in progress in the coronavirus pandemic. The development is performed in three steps: Step 1, already completed, was to install and optimize a single HDA (Hemispherical Deflection Analyzer) system, in which satisfactory performance was achieved. Step 2, currently being progressed, is to upgrade the system with twin HDAs and to construct a branch beamline at BL7U, which allows normal light incidence on sample dually. Step 3 is to introduce a spin detector to the twin-HDA system, for which a novel technique for resolving 3D spin polarization was invented. With these steps, the UVSOR MM system would become the first and only experimental station that can determine the true nature of materials in view of electron’s energy, momentum, spin, and space.



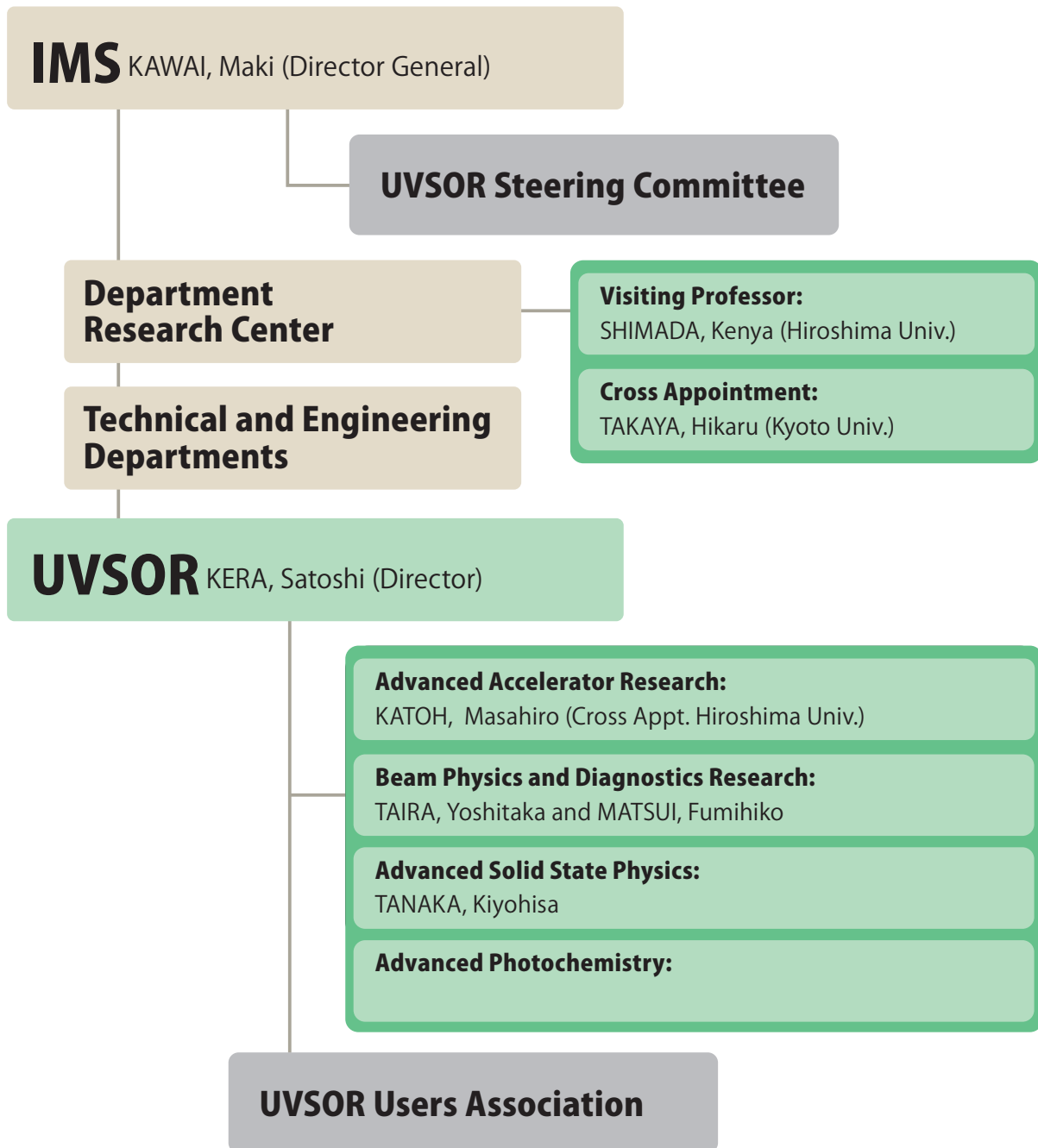
I

Organization and Staff List



UVSOR Synchrotron Facility Organization

May 2021



Staff List

UVSOR Staff

Director

KERA, Satoshi	Professor	kera@ims.ac.jp
---------------	-----------	----------------

Division of Advanced Accelerator Research

KATOH, Masahiro	Project Professor (Cross Appt. Hiroshima Univ.)	mkatoh@ims.ac.jp
-----------------	--	------------------

FUJIMOTO, Masaki	Assistant Professor	mfmoto@ims.ac.jp
------------------	---------------------	------------------

SALEHI, Elham	Project Research Staff	elham@ims.ac.jp
---------------	------------------------	-----------------

Division of Beam Physics and Diagnostics Research

TAIRA, Yoshitaka	Associate Professor	yostaira@ims.ac.jp
------------------	---------------------	--------------------

MATSUI, Fumihiko	Senior Researcher	matui@ims.ac.jp
------------------	-------------------	-----------------

OHIGASHI, Takuji	Assistant Professor	ohigashi@ims.ac.jp
------------------	---------------------	--------------------

SUGITA, Kento	Assistant Professor	ksugita@ims.ac.jp	(since Apr. 2021)
---------------	---------------------	-------------------	-------------------

MATSUDA, Hiroyuki	Project Research Staff	hmatsuda@ims.ac.jp
-------------------	------------------------	--------------------

Division of Advanced Solid State Physics

TANAKA, Kiyohisa	Associate Professor	k-tanaka@ims.ac.jp
------------------	---------------------	--------------------

IDETA, Shin-ichiro	Assistant Professor	idetas@ims.ac.jp	(until Mar. 2021)
--------------------	---------------------	------------------	-------------------

Division of Advanced Photochemistry

IWAYAMA, Hiroshi	Assistant Professor	iwayama@ims.ac.jp
------------------	---------------------	-------------------

Technical Staff

HAYASHI, Kenji	Engineer (Unit Leader)	h-kenji@ims.ac.jp
----------------	------------------------	-------------------

KONDO, Naonori	Technician	nkondo@ims.ac.jp
----------------	------------	------------------

NAKAMURA, Eiken	Chief Engineer	eiken@ims.ac.jp
-----------------	----------------	-----------------

OKANO, Yasuaki	Chief Technician	yokano@ims.ac.jp
----------------	------------------	------------------

SAKAI, Masahiro	Chief Technician	sakai@ims.ac.jp
-----------------	------------------	-----------------

TESHIMA, Fumitsuna	Technician	tetsu@ims.ac.jp
--------------------	------------	-----------------

MAKITA, Seiji	Engineer	makita@ims.ac.jp
---------------	----------	------------------

YAMAZAKI, Jun-ichiro	Chief Technician	yamazaki@ims.ac.jp
----------------------	------------------	--------------------

YANO, Takayuki	Chief Technician	yano@ims.ac.jp
----------------	------------------	----------------

YUZAWA, Hayato	Technician	hayato@ims.ac.jp
----------------	------------	------------------

OTA, Hiroshi	Technician	ota@ims.ac.jp
--------------	------------	---------------

HORIGOME, Toshio	Technical Fellow	horigome@ims.ac.jp
------------------	------------------	--------------------

MIZUKAWA, Tetsunori	Technical Fellow	mizukawa@ims.ac.jp	(since Apr. 2021)
MINAKUCHI, Aki	Technical Fellow	minakuchi@ims.ac.jp	

Secretary

INAGAKI, Itsuko		itsuko@ims.ac.jp	(until Apr. 2021)
ISHIHARA, Mayumi		mayu@ims.ac.jp	
KAMO, Kyoko		kyoko@ims.ac.jp	(since May. 2021)

Departments in IMS (* Group Leader)

Division of Photo-Molecular Science III

KERA, Satoshi *	Professor		
TAKAYA, Hikaru	Associate Professor (Cross Appt. Kyoto Univ.)		
NAGASAKA, Masanori	Assistant Professor		
FUKUTANI, Keisuke	Assistant Professor		(since Apr. 2021)
HASEGAWA, Yuri	Post-Doctoral Fellow		(until Mar. 2021)

Division of Photo-Molecular Science IV

SHIMADA, Kenya	Visiting Professor (Hiroshima Univ.)		(since Apr. 2020)
----------------	--------------------------------------	--	-------------------

Division of Electronic Structure

YOKOYAMA, Toshihiko *	Professor		
KIMURA, Shin-ichi	Professor (Cross Appt. Osaka Univ.)		
KOITAYA, Takanori	Assistant Professor		
YAMAMOTO, Kohei	Assistant Professor		

Graduate Students

KIMURA, Shinnosuke	Nagoya Univ.		(until Nov. 2020)
KOSUGI, Naoki	Nagoya Univ.		(until Dec. 2020)
SHIKANO, Yusuke	Nagoya Univ.		(until Sep. 2020)
NAKAO, Kaito	Nagoya Univ.		(until Dec. 2020)
FURUTA, Kanji	Nagoya Univ.		(until Dec. 2020)
HOSOYA, Tomoki	Nagoya Univ.		(until Dec. 2020)
HORI, Haruki	Nagoya Univ.		(until Dec. 2020)
KOUYAMA, Kazuki	Nagoya Univ.		(since Oct. 2020)
MATSUNAGA, Kazuya	Nagoya Univ.		(since Oct. 2020)
YAMAMOTO, Ryo	Nagoya Univ.		(since Oct. 2020)
YAMAMOTO, Ryohei	Nagoya Univ.		(since Oct. 2020)
MIYATA, Takeshi	Chubu Univ.		(since Feb. 2021)
KANAZAWA, Shingo	Chiba Univ.		(since May. 2021)

UVSOR Steering Committee (* Chair)

KERA, Satoshi *	UVSOR, IMS
KATOH, Masahiro	UVSOR, IMS
TANAKA, Kiyohisa	UVSOR, IMS
TAIRA, Yoshitaka	UVSOR, IMS
MATSUI, Fumihiko	UVSOR, IMS
SHIMADA, Kenya	UVSOR, IMS (Hiroshima Univ.)
OKUDA, Taichi	Hiroshima Univ.
KANEMITSU, Yoshihiko	Kyoto Univ,
KIMURA, Shin-ichi	Osaka Univ.
KUMIGASHIRA, Hiroshi	Tohoku Univ.
HATSUI, Takaki	RIKEN
HARADA, Yoshihisa	Univ. of Tokyo
FUKUSHIMA, Takanori	Tokyo Insititute of Technology
KAWAI, Maki	IMS, Director General
AKIYAMA, Shuji	IMS
KUSAMOTO, Tetsuro	IMS
YAMAMOTO, Hiroshi	IMS
YOKOYAMA, Toshihiko	IMS
SHIGEMASA, Eiji	IMS
HAYASHI, Kenji	IMS
NAKAMURA, Toshikazu	IMS

UVSOR Users Association (* Chair)

KIMURA, Shin-ichi *	Osaka Univ.
KITaura, Mamoru	Yamagata Univ.
OKABAYASHI, Jun	Univ. of Tokyo
YAMANE, Hiroyuki	Tohoku Univ.
HIKOSAKA, Yasumasa	Toyama Univ.

A large, white, stylized Roman numeral 'II' is centered in the upper half of the page. The background is a vibrant teal color with abstract, glowing light patterns and a grid of small dots at the bottom.

Current Status of
Light Sources and
Beamlines

Light Source in 2020

1. Status of UVSOR Accelerators

In the fiscal year 2020, we had scheduled to operate UVSOR-III from May to March, for 36 weeks for users. Because of the COVID-19 pandemic, some of the users experiments were canceled. However, we operated the accelerators as scheduled. We had a few minor machine troubles, such as a discharge of the electron gun, malfunction of the cooling water system for the RF cavity, unstable operation of the klystron pulse modulator of the injection linac and unstable operation of the timing system. Fortunately, all of them could be solved quickly and we extended the operation time and compensated the scheduled users beam time.

We had a scheduled shutdown period in April for 4 weeks. This was for the scheduled maintenance works as usual. In addition, this year, we replaced the coils of one third of the multipole magnets as described later. We had one week shut down period in August and October, two week one around the New Year's Day and one week one at the end of March. We had 2 weeks for machine and beamline conditioning in May after the spring shut down. We had 4 weeks for machine conditionings and studies. One of them in November was mainly for the machine conditioning after the annual planned power outage.

We operated the machine for 34 weeks in the multi-bunch top-up mode at 300 mA, and 2 weeks in the single-bunch top-up mode at approximately 40 mA. The monthly statistics of the operation time and the integrated beam current are shown in Fig. 1.



Fig. 1. Monthly statistics in FY2020.

The weekly operation schedule is as follows. On Monday, from 9 am to 9 pm, the machine is operated for machine conditionings and studies. On Tuesday and Wednesday, from 9 am to 9 pm, the machine is operated for users. From Thursday 9 am to Friday 9 pm, the machine is operated for 36 hours continuously for users. Therefore, the beam time for users in a week

is 60 hours. In the single bunch operation weeks, the machine is operated for 12 hours per day from Tuesday to Friday.



Fig. 2. Replacing sextupole coil for multipole magnets.

2. Improvements and Developments

The cooling water leakage from the sextupole coils wound on the pole faces of the multipole (quadrupole/sextupole) magnets had been getting more frequent. We confirmed that the hollow conductor walls have been eroded by the water flow during the fifteen-year operation. We decided replacing all the coils and, in March, 2020, we replaced the one-third of the coils. The remainder will be replaced in April, 2021.

We started a design study for the future plan of UVSOR, UVSOR-IV. As its first step, we have analyzed the present magnetic lattice, seeking a possibility to reduce the emittance more [1]. Although, we did not find a drastically low emittance solution, we have found a few interesting solutions which may be useful for some machine studies which requires lower emittance as possible.

We continue the efforts to develop novel light sources technologies and their applications such as free electron lasers, coherent harmonic generation, coherent synchrotron radiation, laser Compton scattering gamma-rays, intense polarized and vortex UV radiation at the source development station BL1U, which was constructed under the support of Quantum Beam Technology Program by MEXT/JST.

In these years, we are focusing on studying the temporal structure of undulator radiation and exploring its application. In collaboration with atomic physicists, we have successfully demonstrated ultrafast spectroscopy with undulator radiation [2] and polarization utilization of tandem undulator radiation [3].

Laser Compton gamma-ray source is another research subject which we are focusing in these years. The applications are spreading to a range of research fields, quantum electrodynamics, imaging technologies, material sciences and so on [4,5]. The research activity at the gamma-ray source is now shifting from source development studies to users experiments.

We have been collaborating with Nagoya University on the electron source development. In these years, we investigated utilizing graphene as a material for photocathode [6].

- [1] E. Salehi and M. Katoh, presented at iPAC2021 (2021).
- [2] T. Kaneyasu *et al.*, Physical Review Letters **126**(11) (2021) 1132202.
- [3] T. Kaneyasu *et al.*, New J. Phys. **22**(8) (2020) 083062.
- [4] K. Ali *et al.*, IEEE Trans. Nucl. Sci. **67**(8) (2020) 1976.
- [5] K Fujimori *et al.*, Appl. Phys. Express **13**(8) (2020) 085505.
- [6] L Guo *et al.*, Appl. Phys. Lett. **116**(25) (2020) 251903

Masahiro KATOH (UVSOR Synchrotron)

UVSOR Accelerator Complex

Injection Linear Accelerator

Energy	15 MeV
Length	2.5 m
Frequency	2856 MHz
Accelerating RF Field	$2\pi/3$ Traveling Wave
Klystron Power	1.8 MW
Energy Spread	~ 1.6 MeV
Repetition Rate	2.6 Hz

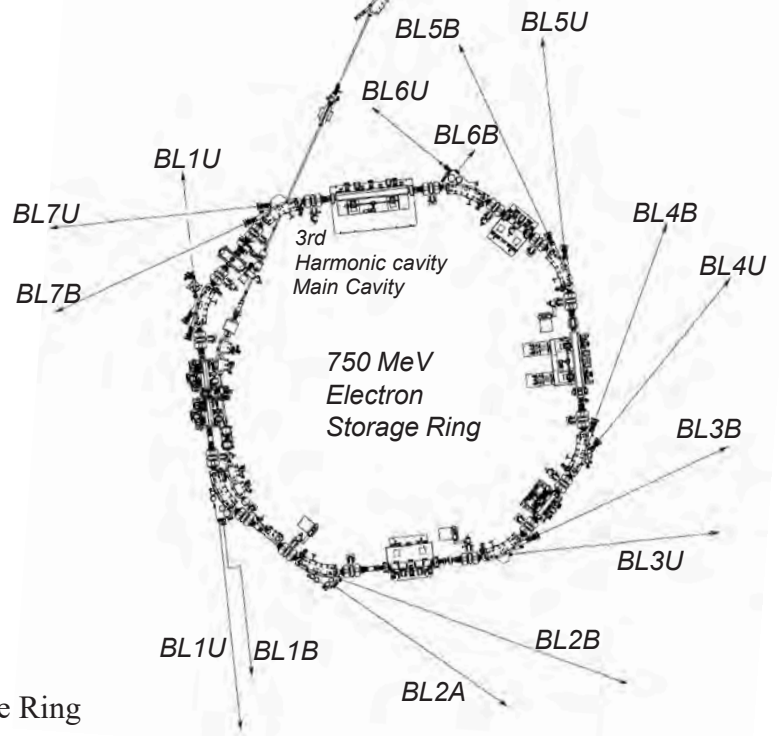
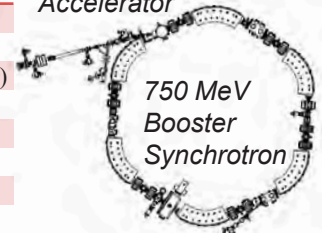
UVSOR-III Storage-Ring

Energy	750 MeV
Injection Energy	750 MeV
Maximum Storage Current	500 mA (multi bunch) 100 mA (single bunch)
Normal operation current (Top-up mode)	300 mA (multi bunch) 50 mA (single bunch)
Natural Emittance	17.5 nm-rad
Circumference	53.2 m
RF Frequency	90.1 MHz
Harmonic Number	16
Bending Radius	2.2 m
Lattice	Extended DB \times 4
Straight Section	(4 m \times 4)+(1.5 m \times 4)
RF Voltage	120 kV
Betatron Tune	
Horizontal	3.75
Vertical	3.20
Momentum Compaction	0.030
Natural Chromaticity	
Horizontal	-8.1
Vertical	-7.3
Energy Spread	5.26×10^{-4}
Coupling Ratio	1%
Natural Bunch Length	128 ps

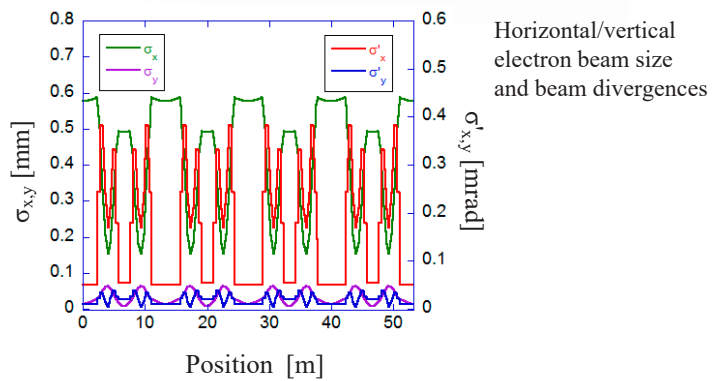
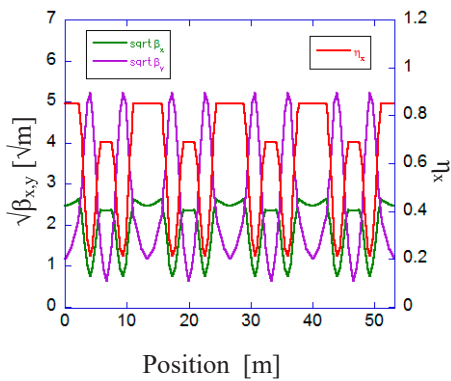
Booster Synchrotron

Energy	750 MeV
Injection Energy	15 MeV
Normal Operation Current	12 mA (uniform filling)
Circumference	26.6 m
RF Frequency	90.1 MHz
Harmonic Number	8
Bending Radius	1.8m
Lattice	FODO \times 6
Betatron Tune	
Horizontal	2.25
Vertical	1.25
Momentum Compaction	0.138
Repetition Rate	1 Hz (750 MeV)

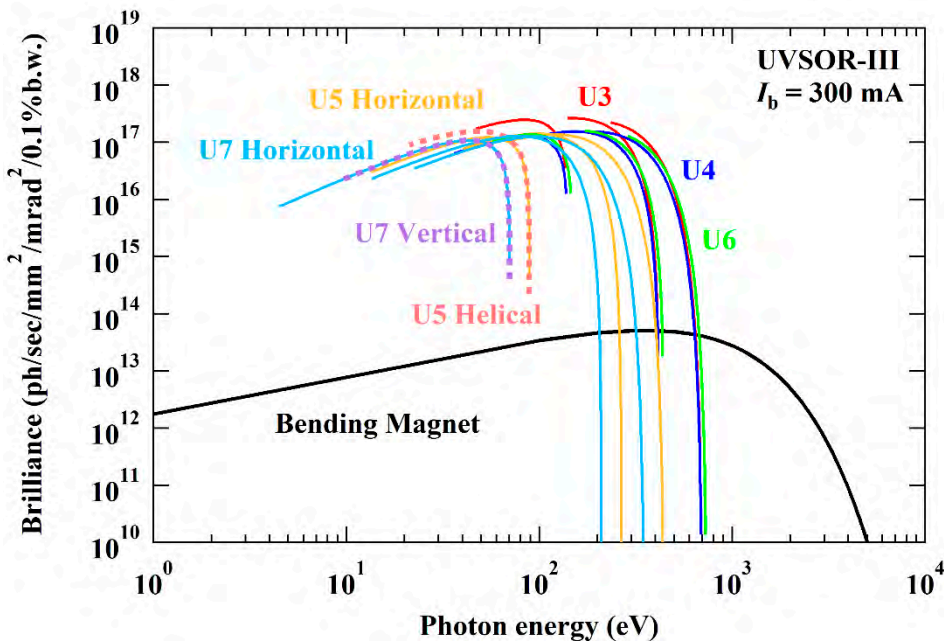
15 MeV
Linear
Accelerator



Electron Beam Optics of UVSOR-III Storage Ring



Insertion Device



Brilliance of radiation from the insertion devices (U3, U4, U5, U6 and U7) and a bending magnet of UVSOR-III

U1 Apple-II Undulator /

Optical Klystron

Number of Periods	10+10
Period length	88 mm
Pole Length	0.968 m + 0.968 m
Pole Gap	24-200 mm
Deflection Parameter	7.36 (Max. Horizontal) 4.93 (Max. Vertical) 4.06 (Max. Helical)

U3 In-vacuum Undulator

Number of Periods	50
Period length	38 mm
Pole Length	1.9 m
Pole Gap	16.5-40 mm
Deflection Parameter	1.8-0.24

U4 In-vacuum Undulator

Number of Periods	26
Period length	38 mm
Pole Length	0.99 m
Pole Gap	13-40 mm
Deflection Parameter	2.4-0.19

U5 Apple-II

Variable Polarization Undulator

Number of Periods	38
Period length	60 mm
Pole Length	2.28 m
Pole Gap	24-190 mm
Deflection Parameter	3.4 (Max. Horizontal) 2.1 (Max. Vertical) 1.8 (Max. Helical)

U6 In-vacuum Undulator

Number of Periods	26
Period length	36 mm
Pole Length	0.94 m
Pole Gap	13-40 mm
Deflection Parameter	1.78 - 0.19

U7 Apple-II

Variable Polarization Undulator

Number of Periods	40
Period length	76 mm
Pole Length	3.04 m
Pole Gap	24-200 mm
Deflection Parameter	5.4 (Max. Horizontal) 3.6 (Max. Vertical) 3.0 (Max. Helical)

Bending Magnets

Bending Radius	2.2 m
Critical Energy	425 eV

Beamlines in 2020

Yoshitaka TAIRA

UVSOR synchrotron Facility, Institute for Molecular Science

UVSOR is one of the highest-brilliance light sources in the extreme-ultraviolet region among the synchrotron radiation facilities with electron energies of less than 1 GeV. The natural emittance of the UVSOR-III storage ring is as low as 17.5 nm-rad after the successful completion of the storage ring upgrade project (the UVSOR-III project) in 2012.

Eight bending magnets and six insertion devices are available as synchrotron light sources at UVSOR. As of 2018 there are a total of fourteen operational beamlines, which are classified into two categories. Twelve of them are the so-called “Open beamlines”, which are open to scientists from universities and research institutes belonging to the government, public organizations, private enterprises and also those from foreign countries. The remaining two beamlines are the “In-house beamlines”, and are dedicated to the use of research groups within Institute for Molecular Science (IMS).

There is one soft X-ray station equipped with a double-crystal monochromator, seven extreme ultraviolet and soft X-ray stations with grazing incidence monochromators, three vacuum ultraviolet (VUV) stations with normal incidence monochromators, two infrared (IR) stations equipped with Fourier-Transform interferometers, and one direct radiation station located after two tandem undulators, as shown in the appended table (next page) for all available beamlines at UVSOR in 2020. The details of the updates for several beamlines are the followings.

A new associate professor, Yoshitaka Taira, was appointed in April 2020. He is in charge of BL1U. In BL1U, the development of a new light source and the utilization of gamma-rays is being carried out. Gamma-ray induced positron annihilation spectroscopy, which can analyze nanometer scale defects in bulk materials, is provided to users. Array detectors using eight BaF₂ scintillators were developed to increase the count rate of annihilation gamma-rays. The measurement can be completed in a few hours for metals.

BL4U, which is equipped with a scanning transmission soft X-ray microscope (STXM), is actively used not only by academic users but also by many industrial users. In FY2020, it became possible to image the

lithium K-edge with a spatial resolution of 72 nm. Final adjustments for the airtight sample transport system and the sample transport container are being carried out in preparation for the organic substance analysis of the Hayabusa2 returned samples scheduled for the summer of FY2021.

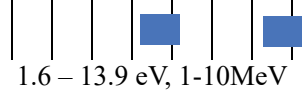
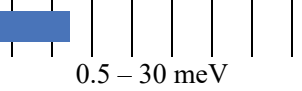
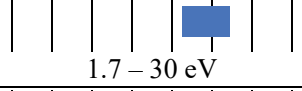
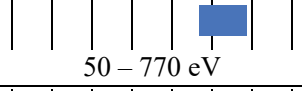
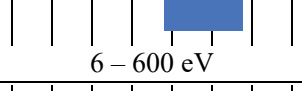
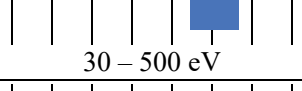
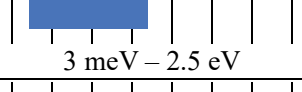
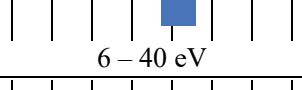
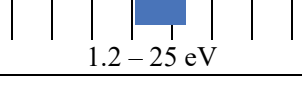
At BL6U, one of the in-house beamlines, photoelectron momentum microscope (PMM), which is a new high-efficiency electronic structure measurement system with high resolution in real space and momentum space, has been installed and is in operation. Experiments such as valence band photoelectron spectroscopy on the micrometer scale and resonance photoelectron diffraction by soft X-ray excitation can be performed. In FY2020, resonant photoelectron spectroscopy of graphenes, high-temperature superconductors, dichalcogenides, and organic molecular adsorbates were conducted in collaboration with several groups.

Next generation spectro-microscopy and micro-spectroscopy workshop, involving BL4U and 6U, was held on October 28-29, 2020 (<https://sites.google.com/ims.ac.jp/uvSOR-ws2020/home?authuser=0>).

In BL5U, high energy resolution angle-resolved photoemission spectroscopy (ARPES) is available. Users can now use so-called “deflector mapping” for all kinetic energies and lens modes by using the latest version of ARPES analyzer. A system that can deposit alkali metals such as potassium while the sample is still mounted on the manipulator at low temperatures has been installed. As part of the development of spin-resolved ARPES, a two-dimensional image of the spin-resolved spectrum of the Rashba splitting of gold (111) surface has been successfully obtained.

Those wishing to use the open and in-house beamlines are recommended to contact the appropriate beamline master (see next page). Applications can be submitted at NOUS ([https:// nous.nins.jp/user/signin](https://nous.nins.jp/user/signin)). All users are required to refer to the beamline manuals and the UVSOR guidebook, on the occasion of conducting the actual experimental procedures. For updated information on UVSOR, please see <http://www.uvsor.ims.ac.jp>.

Beamlines at UVSOR

Beamline	Monochromator / Spectrometer	Energy Range	Targets	Techniques	Contact
BL1U	Free electron laser, Tandem undulator, LSC Gamma-rays	 1.6 – 13.9 eV, 1-10MeV		(Irradiation)	Y. Taira yostaira@ims.ac.jp
BL1B	Martin-Puplett FT-FIR	 0.5 – 30 meV	Solid	Reflection Absorption	K. Tanaka k-tanaka@ims.ac.jp
BL2A	Double crystal	 585 – 4 keV	Solid	Reflection Absorption	K. Tanaka k-tanaka@ims.ac.jp
BL2B	18-m spherical grating (Dragon)	 24 – 205 eV	Solid	Photoemission	S. Kera kera@ims.ac.jp
BL3U	Varied-line-spacing plane grating (Monk-Gillieson)	 60 – 800 eV	Gas Liquid Solid	Absorption Photoemission Photon-emission	M. Nagasaka nagasaka@ims.ac.jp
BL3B	2.5-m off-plane Eagle	 1.7 – 30 eV	Solid	Reflection Absorption Photon-emission	K. Tanaka k-tanaka@ims.ac.jp
BL4U	Varied-line-spacing plane grating (Monk-Gillieson)	 50 – 770 eV	Gas Liquid Solid	Absorption (Microscopy)	T. Ohigashi ohigashi@ims.ac.jp
BL4B	Varied-line-spacing plane grating (Monk-Gillieson)	 25 eV – 1 keV	Gas Solid	Photoionization Photodissociation Photoemission	H. Iwayama iwayama@ims.ac.jp
BL5U	Spherical grating (SGM-TRAIN [†])	 5 – 250 eV	Solid	Photoemission	K. Tanaka k-tanaka@ims.ac.jp
BL5B	Plane grating	 6 – 600 eV	Solid	Calibration Absorption	K. Tanaka k-tanaka@ims.ac.jp
BL6U*	Variable-included-angle varied-line-spacing plane grating	 30 – 500 eV	Gas Solid	Photoionization Photodissociation Photoemission	F. Matsui matui@ims.ac.jp
BL6B	Michelson FT-IR	 3 meV – 2.5 eV	Solid	Reflection Absorption IR microscope	K. Tanaka k-tanaka@ims.ac.jp
BL7U	10-m normal incidence (modified Wadsworth)	 6 – 40 eV	Solid	Photoemission	S. Ideta idetas@ims.ac.jp
BL7B	3-m normal incidence	 1.2 – 25 eV	Solid	Reflection Absorption Photon-emission	K. Tanaka k-tanaka@ims.ac.jp

Yellow columns represent undulator beamlines.

* In-house beamline.

Countermeasures against COVID-19

Yoshitaka TAIRA

UVSOR synchrotron Facility, Institute for Molecular Science

II

In Japan, the first wave of covid-19 began at the end of March 2020, followed by the second wave in August and the third wave in January 2021. As a result, a state of emergency was declared twice, from April 7 to May 25, 2020, and from January 8 to March 21, 2021.

To avoid stagnation of research activities, UVSOR accepted users at all times after taking countermeasures to prevent the spread of infection. Users were asked to take and record their temperature two weeks before the start of the experiment. A non-contact thermometer was placed at the entrance of the user waiting room, as shown in the photo below, and users were asked to take and record their temperature and wear a mask every day. Chairs in the user waiting room were placed at intervals to ensure social distance (see photo below). By March 2021, no one has been infected from UVSOR.

In FY2020, all the first half-year proposals were copied and pasted into the second half-year proposals. The beam time allocated in the first half-year was still

valid, and if users were able to come to UVSOR according to the regulations of their institutions, users could carry out their experiments. New applications for beam time in the second half-year were suspended, and the remaining beam time was allocated to special calls for proposals as needed. UVSOR was able to accept users, but some proposals were canceled because the users could not travel due to the regulations of their institutions. The implementation rate of the proposals was 63 % in the first half-year and 86 % in the second half-year. There were five proposals that could not be implemented. Substitute measurements were conducted in 20 cases. The total number of visitors decreased by 23 % from the previous year to 2,806, due to a significant decrease in the number of domestic students and international visitors. We have started to examine technologies for automation, remoteness, AI analysis processing, and standardization.



BL1U

Light Source Development Station

II

▼ Description

BL1U is dedicated for developments and applications of novel light sources. This beamline is equipped with a dedicated tandem undulator for variable polarization with a buncher section, which can be used for free electron laser in the range from visible to deep UV, VUV coherent harmonic generation (CHG), and generation of spatiotemporal structured light such as an optical vortex beam, a vector beam and double-pulse wave packets. It is also equipped with a femto-second laser system synchronized with the accelerator, which is used for the generation of CHG, laser Compton scattered gamma-rays, and coherent THz radiation. Nowadays, material analysis by positron annihilation spectroscopy using laser Compton scattered gamma rays is actively used.

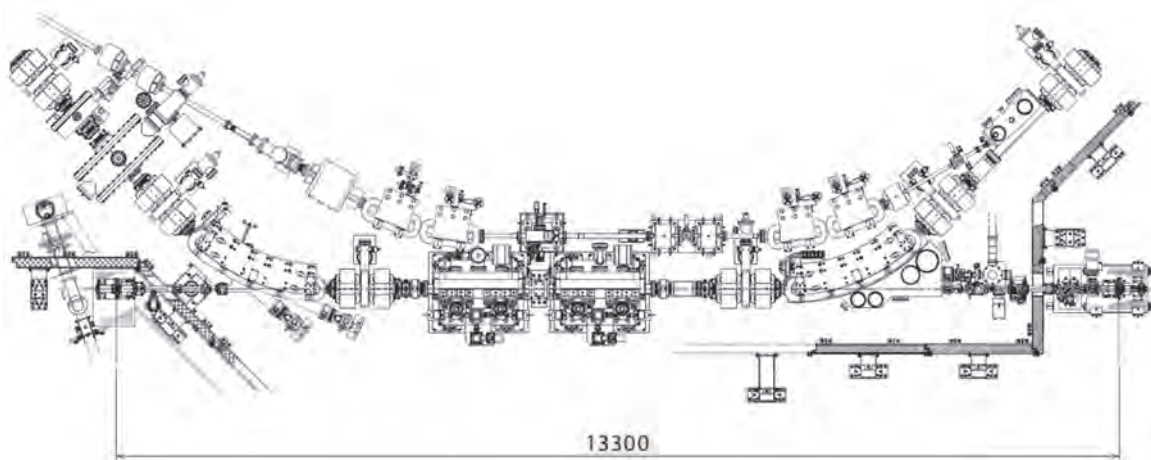


Fig. 1. Configuration of the free electron laser

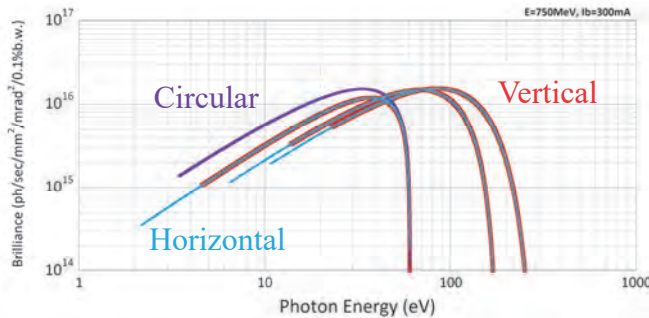


Fig. 2. Brilliance of BL1U Apple-II Undulator

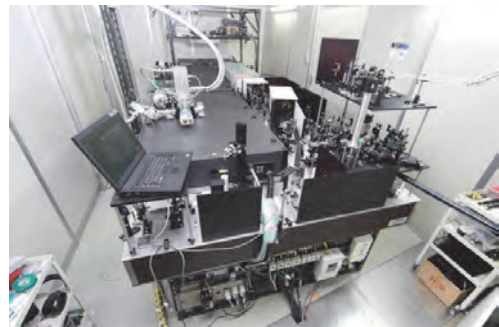


Fig. 3. Accelerator Synchronized Laser System

▼ Technical Data of FEL

Wave Length	199-800 nm
Spectral Band Width	$\sim 10^{-4}$
Polarization	Circular/Linear
Pulse Rate	11.26 MHz
Max. Ave. Power	~ 1 W

▼ Technical Data of Ti:Sa Laser

Wave Length	800 nm
Pulse Length	130 fsec
Oscillator	90.1 MHz
Pulse Energy	2.5 mJ 10 mJ 50 mJ
Repetition Rate	1 kHz 1 kHz 10 Hz

BL1B

Terahertz Spectroscopy Using Coherent Synchrotron Radiation

▼ Description

Coherent synchrotron radiation (CSR) is a powerful light source in the terahertz (THz) region. This beamline has been constructed for basic studies on the properties of THz-CSR. However, it can be also used for measurements of reflectivity and transmission spectra of solids using conventional synchrotron radiation.

The emitted THz light is collected by a three-dimensional magic mirror (3D-MM, M0) of the same type as those already successfully installed at BL43IR in SPring-8 and BL6B in UVSOR-II. The 3D-MM was installed in bending-magnet chamber #1 and is controlled by a 5-axis pulse motor stage (x , z translation; θ_x , θ_y , θ_z rotation). The acceptance angle was set at 17.5-34 degrees (total 288 mrad) in the horizontal direction. The vertical angle was set at ± 40 mrad to collect the widely expanded THz-CSR.

The beamline is equipped with a Martin-Puplett type interferometer (JASCO FARIS-1) to cover the THz spectral region from 4 to 240 cm^{-1} ($h\nu = 500 \mu\text{eV}$ -30 meV). There is a reflection/absorption spectroscopy (RAS) end-station for large samples (\sim several mm). At the RAS end-station, a liquid-helium-flow type cryostat with a minimum temperature of 4 K is installed.

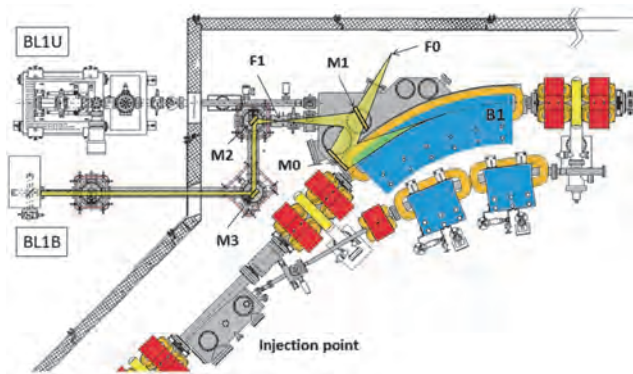


Fig. 1. Schematic top view of the beam extraction part of the THz-CSR beamline, BL1B. The three-dimensional magic mirror (3D-MM, M0) and a plane mirror (M1) are located in the bending-magnet chamber. A parabolic mirror (M2) is installed to form a parallel beam. The straight section (BL1U) is used for coherent harmonic generation (CHG) in the VUV region.

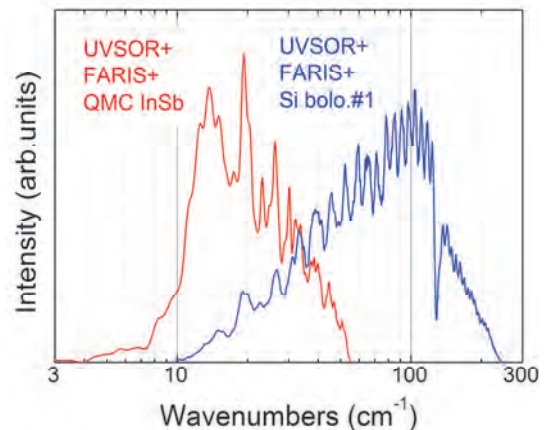


Fig. 2. Obtained intensity spectra with the combination of a light source (UVSOR), interferometer (FARIS-1), and detectors (Si bolometer and InSb hot-electron bolometer).

▼ Technical Data

Interferometer	Martin-Puplett (JASCO FARIS-1)
Wavenumber range (Energy range)	4-240 cm^{-1} (500 μeV -30 meV)
Resolution in cm^{-1}	0.25 cm^{-1}
Experiments	Reflection/transmission spectroscopy
Miscellaneous	Users can use their experimental system in this beamline.

BL2A

Soft X-Ray Beamline for Photoabsorption Spectroscopy

II

▼ Description

BL2A is a soft X-ray beamline for photoabsorption spectroscopy. The beamline is equipped with a pre-focusing mirror and a double-crystal monochromator [1]. The monochromator serves soft X-rays in the energy region from 585 to 4000 eV using several types of single crystals, such as beryl, KTP (KTiOPO₄), and InSb. The throughput spectra measured using a Si photodiode (AXUV-100, IRD Inc.) are shown in Fig. 1. The typical energy resolution ($E / \Delta E$) of the monochromator is approximately 1500 for beryl and InSb.

There is a small vacuum chamber equipped with an electron multiplier (EM) detector. Photoabsorption spectra for powdery samples are usually measured in total electron yield mode, with the use of the EM detector. In addition, a hemispherical electron analyzer for photoelectron spectroscopy is equipped.

Recently, a new omnidirectional photoelectron acceptance lens (OPAL) has been developed aiming to realize 2π -steradian photoelectron spectroscopy and photoelectron holography [2]. By combining OPAL and the existing hemispherical electron analyzer, a photoelectron spectrometer with high energy resolution can be realized, and a full range ($\pm 90^\circ$) 1D angular distribution can be measured at once. This upgrade is currently in the commissioning phase.

[1] Hiraya *et al.*, Rev. Sci. Instrum. **63** (1992) 1264.

[2] H. Matsuda and F. Matsui, Jpn. J. Appl. Phys. **59** (2020) 046503.

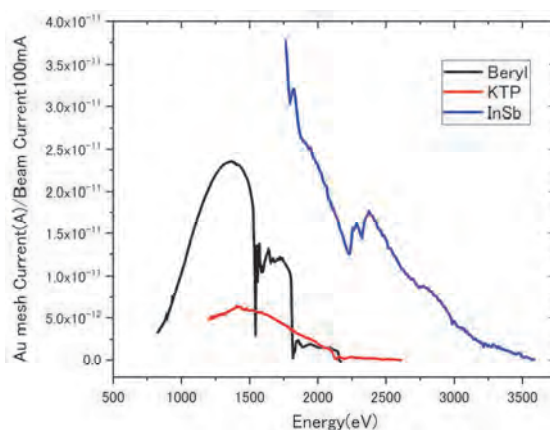


Fig. 1. Throughput spectra of the double-crystal monochromator at BL2A.

▼ Technical Data

Monochromator	Double crystal monochromator
Monochromator crystals: (2d value, energy range)	beryl (15.965 Å, 826–2271 eV), KTP (10.95 Å, 1205–3310 eV), InSb (7.481 Å, 1764–4000 eV), Ge (6.532 Å, 2094–4000 eV)
Resolution	$E/\Delta E = 1500$ for beryl and InSb
Experiments	Photoabsorption spectroscopy (total electron yield using EM and partial fluorescence yield using SDD)

BL2B

Photoelectron spectroscopy of molecular solids

▼ Description

This beamline previously dedicated for experiments in the field of gas phase photoionization and reaction dynamics. Then, the beamline has been reconstructed for photoelectron spectroscopy of molecular solids with a new end station, and experiments can be performed from May 2014. The monochromator is a spherical grating Dragon type with 18-m focal length. High throughput (1×10^{10} photons s^{-1}) and high resolution ($E/\Delta E = 2000 - 8000$) are achieved simultaneously under the condition of the ring current of 100 mA [1]. The optical system consists of two pre-focusing mirrors, an entrance slit, three spherical gratings (G1 - G3), two folding mirrors, a movable exit slit, and a refocusing mirror [2]. The monochromator is designed to cover the energy range of 23–205 eV with the three gratings: G1 (2400 lines mm^{-1} , $R = 18$ m) at 80–205 eV; G2 (1200 lines mm^{-1} , $R = 18$ m) at 40–100 eV; G3 (2400 lines mm^{-1} , $R = 9.25$ m) at 23–50 eV. The percentage of the second-order light contamination at $h\nu = 45.6$ eV is 23 % for G2 or 7 % for G3.

A UHV chamber is placed downstream of the refocusing mirror chamber and equipped silicon photodiode, sapphire plate Au mesh and filters for absolute photon flux measurement, monitor the photon-beam position, relative photon flux measurements and attenuate higher order light, respectively.

The new end station consists of a main chamber with a hemispherical analyzer (SCIENTA R3000) and a liquid-He-cooled cryostat (temperature range of 15-400 K) with 5-axis stage, a sample preparation chamber with a fast-entry load-lock chamber and a cleaning chamber with LEED, ion gun for sputtering and IR heating unit.

[1] M. Ono, H. Yoshida, H. Hattori and K. Mitsuke, Nucl. Instrum. Meth. Phys. Res. A **467-468** (2001) 577.

[2] H. Yoshida and K. Mitsuke, J. Synchrotron Radiation **5** (1998) 774.

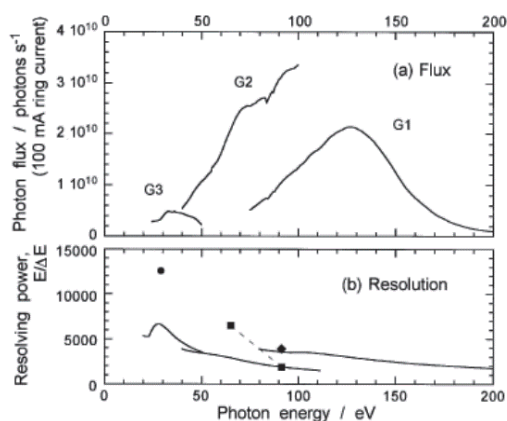


Fig. 1. Throughput from Dragon monochromator.

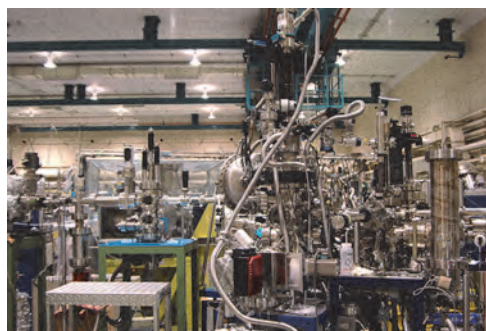


Fig. 2. End station of BL2B for photoelectron spectroscopy of molecular solids.

▼ Technical Data

Monochromator	18 m spherical grating Dragon-type
Wavelength Range	23-205 eV
Resolution	2000–8000 depending on the gratings
Experiments	Angle-resolved ultraviolet photoelectron spectroscopy

BL3U

Varied-Line-Spacing Plane Grating Monochromator for Molecular Soft X-Ray Spectroscopy

II

▼ Description

The beamline BL3U is equipped with an in-vacuum undulator composed of 50 periods of 3.8 cm period length. The emitted photons are monochromatized by the varied-line-spacing plane grating monochromator (VLS-PGM) designed for various spectroscopic investigations in the soft X-ray range. Three holographically ruled laminar profile plane gratings are designed to cover the photon energy range from 40 to 800 eV. The beamline has liquid cells for soft X-ray absorption spectroscopy (XAS) in transmission mode as shown in Fig. 1. The liquid cell is in the atmospheric helium condition, which is separated by a 100 nm thick Si_3N_4 membrane with the window size of $0.2 \times 0.2 \text{ mm}^2$ from the beamline in an ultrahigh vacuum condition. The thin liquid layer is assembled by using two 100 nm thick Si_3N_4 membranes. The thickness of the liquid layer is controllable from 20 to 2000 nm by adjusting the helium pressures around the liquid cell in order to transmit soft X-rays. Liquid samples are exchangeable *in situ* by using a tubing pump. The liquid cell has two types of windows: one is the liquid part to obtain the soft X-ray transmission of liquid (I), and the other is the blank part to obtain the transmission without liquid (I_0). We can obtain the reliable XAS spectra based on the Lambert-Beer law $\ln(I_0/I)$. Since the liquid cell is in the atmospheric condition, we can measure XAS of liquid samples in the real environment. *Operando* XAS observation of several chemical reactions such as catalytic, electrochemical reactions are also possible by using our liquid cells developed for these purposes.

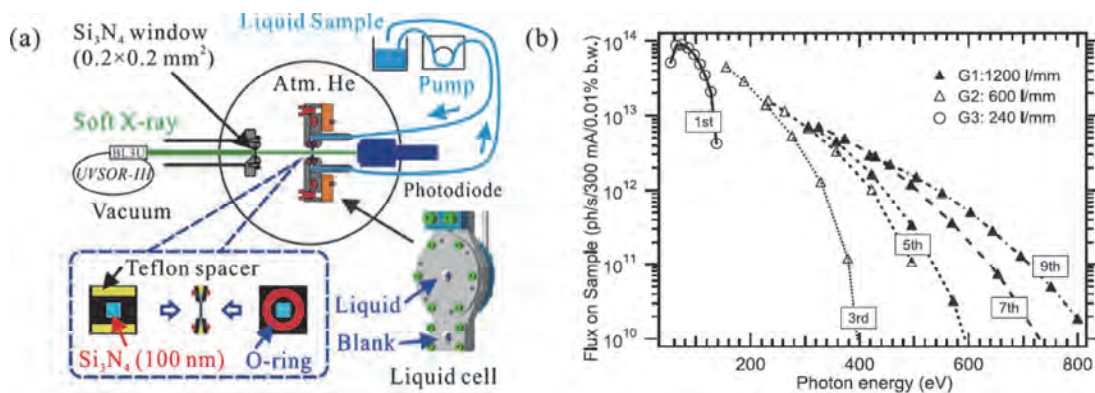


Fig. 1. (a) Schematics of a liquid cell for XAS in transmission mode settled in BL3U. The blowup shows a thin liquid layer assembled by two Si_3N_4 membranes with the thickness of 100 nm. (b) Flux at the sample position with the resolving power of $\lambda/\Delta\lambda=10^4$.

▼ Technical Data

Monochromator	Varied-line-spacing plane grating monochromator
Energy Range	40-800 eV
Resolution	$E / \Delta E > 10\,000$
Experiments	Soft X-ray absorption spectroscopy of liquid in transmission mode

BL3B (HOTRLU)

VIS-VUV Photoluminescence and Reflection/Absorption Spectroscopy

▼ Description

BL3B has been constructed to study photoluminescence (PL) in the visible (VIS) to vacuum ultraviolet (VUV) region. This beamline consists of a 2.5 m off-plane Eagle type normal-incidence monochromator, which covers the VUV, UV, and VIS regions, i.e., the energy (wavelength) region of 1.7-31 eV (40-730 nm), with three spherical gratings having constant grooving densities of 1200, 600, and 300 l/mm optimized at the photon energies of ~ 20 , ~ 16 , and ~ 6 eV, respectively. The schematic side view and top view layouts are shown in Figs. 1(a) and 1(b), respectively. The FWHM of the beam spot at the sample position is 0.25 mm (V) \times 0.75 mm (H). Low energy pass filters (LiF, quartz, WG32, OG53) can be inserted automatically to maintain the optical purity in the G3 (300 l/mm) grating region (1.7 \sim 11.8 eV). Figure 2 shows the throughput spectra (photon numbers at a beam current of 300 mA) for each grating with entrance and exit slit openings of 0.1 mm (resolving power $E / \Delta E$ of ~ 2000 (G3, ~ 6.8 eV)). Since both slits can be opened up to 0.5 mm, a monochromatized photon flux of 10^{10} photons/s or higher is available for PL measurements in the whole energy region.

The end station is equipped with a liquid-helium-flow type cryostat for sample cooling and two detectors; one of which is a photomultiplier with sodium salicylate and the other a Si photodiode for reflection/absorption measurement. For the PL measurements in the wide energy region from VIS to VUV, two PL monochromators, comprising not only a conventional VIS monochromator but also a VUV monochromator with a CCD detector, are installed at the end station.

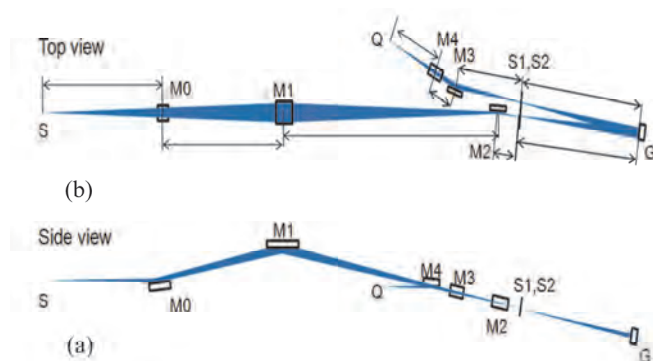


Fig. 1. Schematic layout of the BL3B (a) side view and (b) top view.

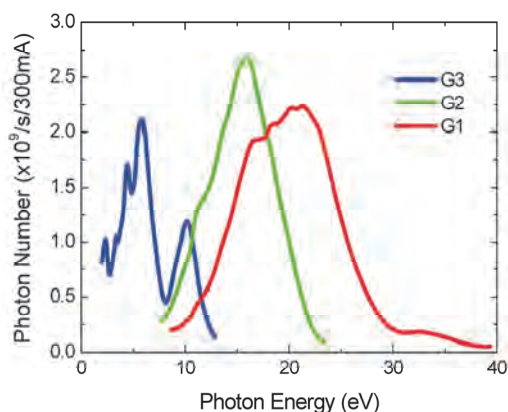


Fig. 2. Throughput spectra for each grating (G1:1200 l/mm, G2:600 l/mm and G3:300 l/mm) with $S_1 = S_2 = 0.1$ mm.

▼ Technical Data

Monochromator	-2.5 m normal-incidence monochromator
Energy range	1.7-31 eV (40~730 nm)
Resolution ($\Delta h\nu / h\nu$)	≥ 12000 (at ~ 6.9 eV, 0.02 mm slits, G1 (1200 l/mm))
Experiments	Photoluminescence, reflection, and absorption spectroscopy, mainly for solids

BL4U

Scanning Transmission X-ray Microscopy in the Soft X-ray Region

II

▼ Description

In the soft x-ray region, there are several absorption edges of light elements and transition metals. The near edge X-ray absorption fine structure (NEXAFS) brings detailed information about the chemical state of target elements. A scanning transmission X-ray microscope (STXM) in the soft X-ray region is a kind of extended technique of the NEXAFS with high spatial resolution. The STXM has a capability of several additional options, for example, in-situ observations, 3-dimensional observation by computed tomography and ptychography, by utilizing the characteristics of the X-rays. The STXM can be applied to several sciences, such as polymer science, material science, cell biology, environmental science, and so on.

This beamline equips an in-vacuum undulator, a varied-line-spacing plane grating monochromator and a fixed exit slit. The soft X-ray energy range from 50 to 770 eV with the resolving power ($E/\Delta E$) of 6,000 is available. The aperture size of the fixed exit slit determines not only the resolving power but also the size of a microprobe. A Fresnel zone plate is used as a focusing optical device through an order select aperture and its focal spot size of ~ 30 nm is available at minimum. An image is acquired by detecting intensities of the transmitted X-rays by a photomultiplier tube with scintillator with scanning a sample 2-dimensionally. By changing the energy of the incident beam, each 2-dimensional NEXAFS image is stacked. A main chamber of STXM is separated from the beamline optics by a silicon nitride membrane of 50-nm thickness; therefore, sample folders can be handled in vacuum or in helium.

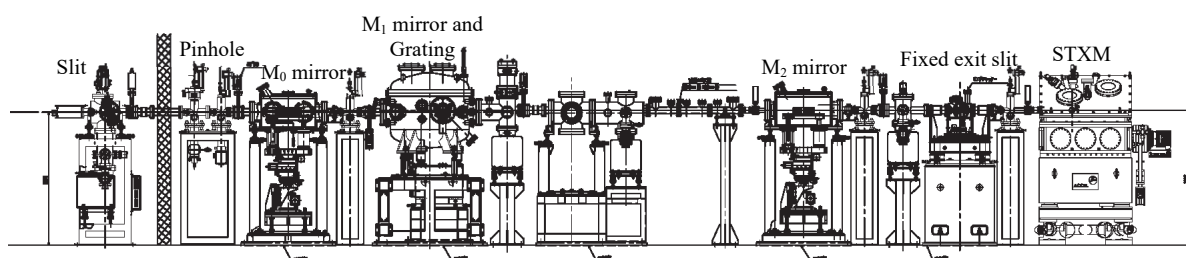


Fig. 1. Schematic image of BL4U

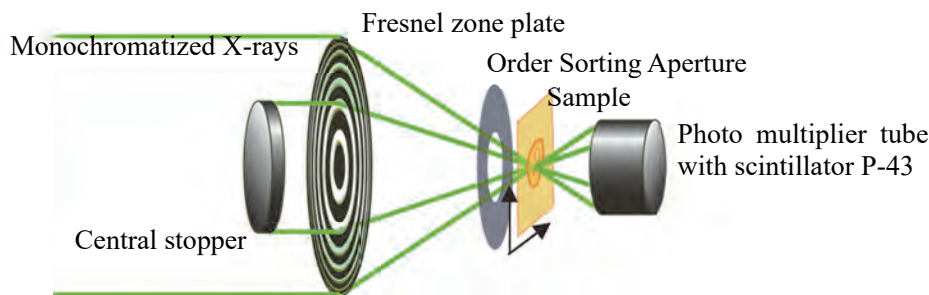


Fig. 2. Schematic image of STXM

▼ Technical Data

Energy range (E)	50 -770 eV
Resolving power ($E/\Delta E$)	$\sim 6,000$
Photon flux on a sample (photons/s)	$\sim 2 \times 10^7$ @400 eV
Focusing optical element	Fresnel zone plate
Spatial resolution	~ 30 nm
Experiments	2-dimensional absorption spectroscopy
Measurement environment	standard sample folder in vacuum or in helium, specially designed sample cell in ambient condition

BL4B

Varied-Line-Spacing Plane Grating Monochromator for Molecular Soft X-Ray Spectroscopy

II

▼ Description

The beamline BL4B equipped with a varied-line-spacing plane grating monochromator (VLS-PGM) was constructed for various spectroscopic investigations in a gas phase and/or on solids in the soft X-ray range. Three holographically ruled laminar profile plane gratings with SiO₂ substrates are designed to cover the photon energy range from 25 to 800 eV. The gratings with groove densities of 100, 267, and 800 l/mm cover the spectral ranges of 25–100, 60–300, and 200–1000 eV, respectively, and are interchangeable without breaking the vacuum. Figure 1 shows the absolute photon flux for each grating measured using a Si photodiode (IRD Inc.), with the entrance- and exit-slit openings set at 50 and 50 μm, respectively. The maximum resolving power ($E/\Delta E$) achieved for each grating exceeds 5000.

There is no fixed endstation on this beamline. A small vacuum chamber equipped with an electron multiplier (EM) detector is available. Soft X-ray absorption spectra of solid samples are usually measured by means of the total electron yield method using EM, and the partial fluorescence yield method using a silicon drift detector (SDD).

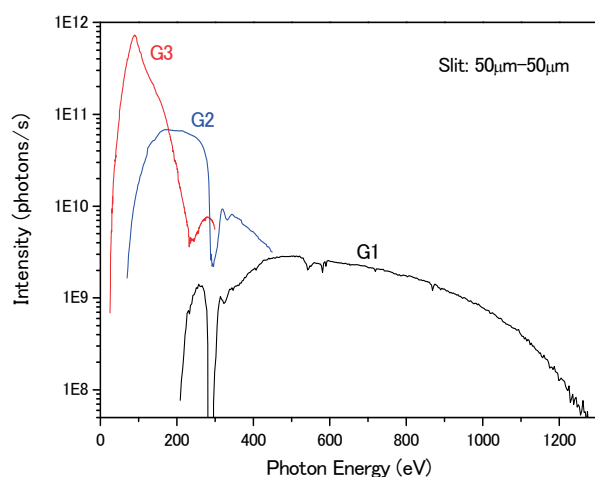


Fig. 1. Throughput from the VLS-PGM monochromator on BL4B.



Fig. 2. Photo of BL4B.

▼ Technical Data

Monochromator	Varied-line-spacing Plane Grating Monochromator
Energy range	25-1000 eV
Resolution	$E / \Delta E > 5000$ (at maximum)
Experiments	Soft X-ray spectroscopy (mainly, photoabsorption spectroscopy for solid targets by means of total electron yield method using EM and partial fluorescence yield method using SDD)

BL5U

Photoemission Spectroscopy of Solids and Surfaces

II

▼ Description

Since the monochromator of BL5U was an old-style spherical grating type SGMTRAIN constructed in 1990s and the throughput intensity and energy resolution were poor, the whole beamline has been replaced to state-of-the-art monochromator and end station. The new beamline has been opened to users from FY2016 as high-energy resolution ARPES beamline. Samples can be cooled down to 3.8 K with newly developed 5-axis manipulator to perform high energy resolution measurements. Users can also obtain spatial-dependence of the electronic structure of solids using micro-focused beam ($\sim 50 \mu\text{m}$). The new electron lens system makes it possible to obtain ARPES spectra without moving samples. This beamline will also have new capability to perform high-efficient spin-resolved ARPES in the future.

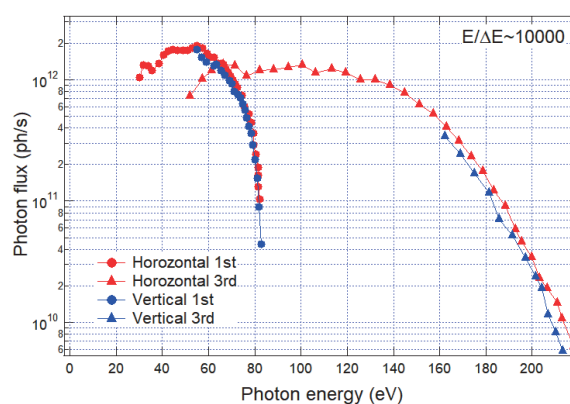


Fig. 1. Picture and photon flux of BL5U.

▼ Technical Data (Expected Performance)

Light source	APPLE-II type undulator ($\lambda_u = 60 \text{ mm}$, $N = 38$) vertical/horizontal, right/left circular (depending on $h\nu$)
Monochromator	Monk-Gillieson VLS-PGM
Energy Range	20-200 eV
Resolution	$h\nu / \Delta E > 10,000$ for $< 10 \mu\text{m}$ slits
Experiment	ARPES, Space-resolved ARPES, Spin-resolved ARPES
Flux	$< 10^{12}$ photons/s for $< 10 \mu\text{m}$ slits (at the sample position)
Beam spot size	23 (H) x 40 (V) μm
Main Instruments	Hemispherical photoelectron analyzer with deflector scan (MBS A-1 Lens#4), Liq-He flow cryostat with 5-axis manipulator (3.8 K-350 K)

BL5B

Calibration Apparatus for Optical Elements and Detectors

▼ Description

BL5B has been constructed to perform calibration measurements for optical elements and detectors. This beamline is composed of a plane grating monochromator (PGM) and three endstations in tandem. The most upstream station is used for the calibration measurements of optical elements, the middle one for optical measurements for solids, and the last for photo-stimulated desorption experiments. The experimental chamber at the most downstream station is sometimes changed to a chamber for photoemission spectroscopy. The calibration chamber shown in Fig. 2 is equipped with a goniometer for the characterization of optical elements, which has six degrees of freedom, X-Y translation of a sample, and interchanging of samples and filters. These are driven by pulse motors in vacuum. Because the polarization of synchrotron radiation is essential for such measurements, the rotation axis can be made in either the horizontal or vertical direction (s- or p-polarization).

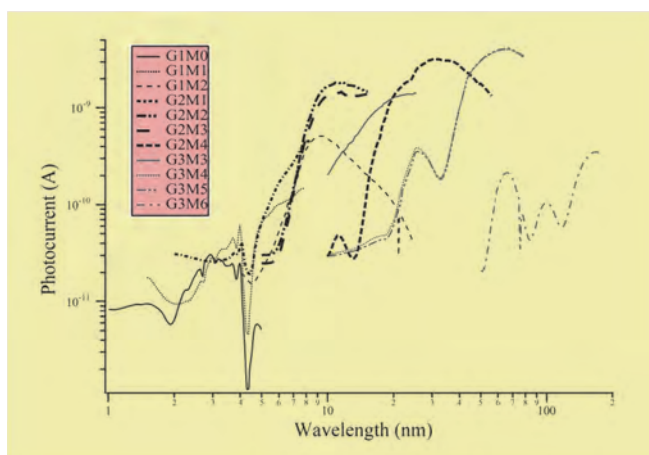


Fig. 1. Throughput spectra for possible combinations of gratings and mirrors at BL5B measured by a gold mesh.

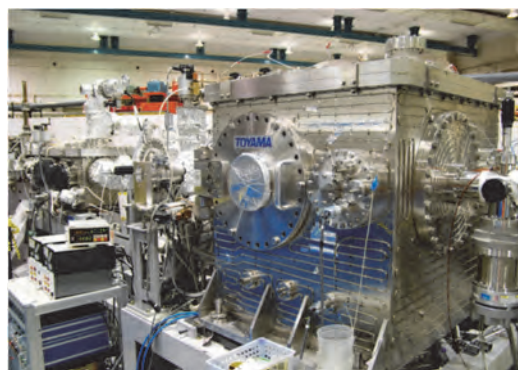


Fig. 2. A side view of the experimental chamber for calibration measurements.

▼ Technical Data

Monochromator	Plane Grating Monochromator
Energy range	6-600 eV (2-200 nm)
Resolution	$E / \Delta E \sim 500$
Experiments	Calibration of optical elements, reflection and absorption spectroscopy mainly for solids

BL6U

Variable-Included-Angle / Variable-Line-Spacing Plane Grating Monochromator for Soft X-Ray photoelectron Spectroscopy

▼ Description

The beamline BL6U equipped with a variable-included-angle Monk-Gillieson mounting monochromator with a varied-line-spacing plane grating was constructed for various spectroscopic investigations requiring high-brilliance soft X-rays on solid surfaces. Through a combination of undulator radiation and sophisticated monochromator design (entrance slit-less configuration and variable-included-angle mechanism), using a single grating, the monochromator can cover the photon energy ranging from 40 to 500 eV, with resolving power of greater than 10000 and photon flux of more than 10^{10} photons/s. Figure 1 shows an example of the monochromator throughput spectra measured using a Si photodiode, with the exit-slit opening set at 30 μm , which corresponds to the theoretical resolving power of 10000 at 80 eV.

A new Momentum Microscope experimental station for photoelectron spectroscopy resolved in 3D momentum space with a microscopic field of view has been built at BL6U (SPECS KREIOS 150 MM). A momentum resolution of 0.01 \AA^{-1} in k_x/k_y , as well as k_z is achieved. A spatial resolution of 50 nm, an energy resolution of 20 meV at 9 K, and a field of view of 2 μm for ARPES are successfully demonstrated. This experimental station specializes in characterizing the electronic structure of surface atomic sites, thin films, molecular adsorbates, and bulk crystals. This method opens the door to direct observation of the Fermi surface of μm -sized crystals, which was difficult with conventional ARPES-type hemispherical analyzers.

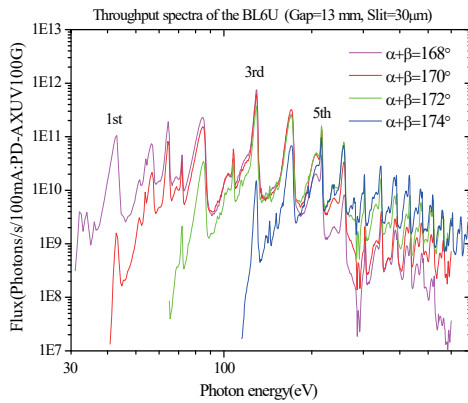


Fig. 1. Throughput spectra of the BL6U monochromator at various included angles.

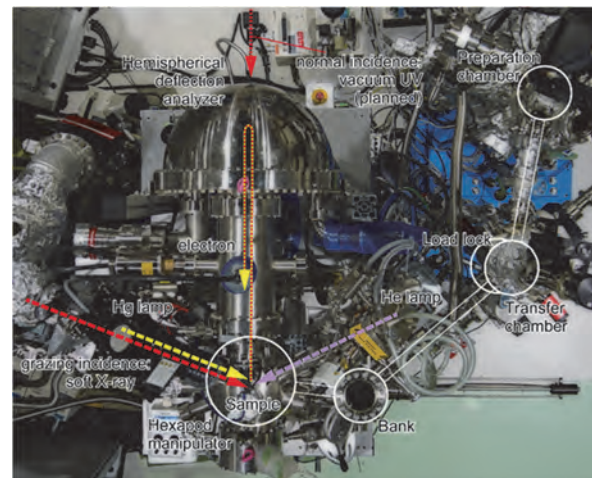


Fig. 2. Photograph of BL6U end station

▼ Technical Data

Monochromator	Variable-included-angle Varied-line-spacing Plane Grating Monochromator
Energy range	45-600 eV(practical)
Resolution	$E / \Delta E > 10000$ (at maximum)
Experiments	High-resolution soft X-ray spectroscopy (photoelectron spectroscopy for solid surfaces)

BL6B

Infrared and Terahertz Spectroscopy of Solids

▼ Description

Synchrotron radiation (SR) has good performance (high brilliance and high flux) not only in the VUV and soft X-ray (SX) regions but also in the infrared (IR) and THz regions. BL6B covers the IR and THz regions. The previous beamline, BL6A1, which was constructed in 1985, was the pioneer in IRSR research. The beamline was deactivated at the end of FY2003 and a new IR/THz beamline, BL6B (IR), was constructed in FY2004. The front-end part including bending duct #6 was replaced with a new part having a higher acceptance angle ($215 \text{ (H)} \times 80 \text{ (V)} \text{ mrad}^2$) using a magic mirror, as shown in Fig. 1.

There are two Michelson type interferometers in this endstation; with first one (Bruker Vertex70v), which covers a wide spectral region from 30 to 20,000 cm^{-1} ($h\nu = 4 \text{ meV} - 2.5 \text{ eV}$), reflection/absorption spectroscopy measurements of large samples (up to several mm) and IR/THz microscopy measurements of tiny samples (up to several tens of μm) can be performed. For reflection/absorption spectroscopy measurements, a liquid-helium-flow type cryostat with a minimum temperature of 4 K is installed. The other interferometer (Jasco FT/IR-6100), which covers 350 to 15,000 cm^{-1} ($h\nu = 45 \text{ meV} - 1.8 \text{ eV}$), has been available for IR microscopy imaging measurements from FY2014. One can also perform ATR measurements using diamond ATR prism.

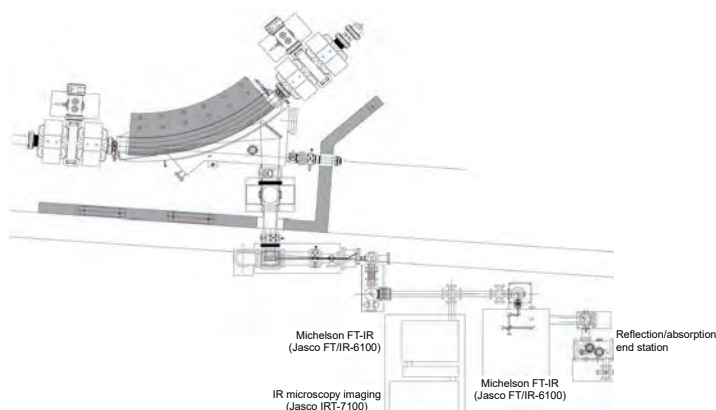


Fig. 1. Schematic top view of BL6B.

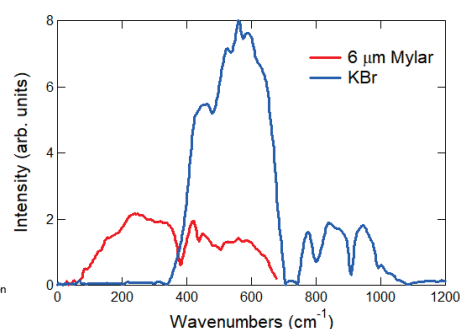


Fig. 2. Obtained intensity spectra with the combination of a light source (UVSOR), detector (Si bolometer), and interferometer (Bruker Vertex70v) with different beamsplitters ($6 \mu\text{m}$ Mylar and KBr). (Only low energy side is shown).

▼ Technical Data

Interferometer	Michelson (Bruker Vertex70v)	Michelson (Jasco FT/IR-6100)
Wavenumber Range (Energy range)	30-20,000 cm^{-1} (4 meV-2.5 eV)	350-15,000 cm^{-1} (45 meV-1.8 eV)
Resolution in cm^{-1}	0.1 cm^{-1}	0.5 cm^{-1}
Experiments	Reflectivity and transmission spectroscopy THz Microspectroscopy	IR microscopy imaging (JASCO IRT-7000) ATR spectroscopy

BL7U (SAMRAI)

Angle-Resolved Photoemission of Solids in the VUV Region

II

▼ Description

Beamline 7U, named the Symmetry- And Momentum-Resolved electronic structure Analysis Instrument (SAMRAI) for functional materials, was constructed to provide a photon flux with high energy resolution and high flux mainly for high-resolution angle-resolved photoemission spectroscopy, so-called “ARPES”, of solids [1]. An APPLE-II-type variable-polarization undulator is installed as the light source. The undulator can produce intense VUV light with horizontal/vertical linear and right/left circular polarization. The undulator light is monochromatized by a modified Wadsworth type monochromator with three gratings (10 m radius; 1200, 2400, and 3600 lines/mm optimized at $h\nu = 10, 20,$ and 33 eV). The energy resolution of the light ($h\nu/\Delta h\nu$) is more than 10^4 with a photon flux of 10^{11} - 10^{12} ph/s or higher on samples in the entire energy region. The beamline has a photoemission end-station equipped with a 200 mm-radius hemispherical photoelectron analyzer (MB Scientific AB, A-1 analyzer) with a wide-angle electron lens and a liquid-helium-cooled cryostat with 6-axis pulse motor control. The main function of the beamline is to determine the electronic structure of solids and its temperature dependence in order to reveal the origin of their physical properties.

[1] S. Kimura, T. Ito, M. Sakai, E. Nakamura, N. Kondo, K. Hayashi, T. Horigome, M. Hosaka, M. Katoh, T. Goto, T. Ejima and K. Soda, Rev. Sci. Instrum. **81** (2010) 053104.

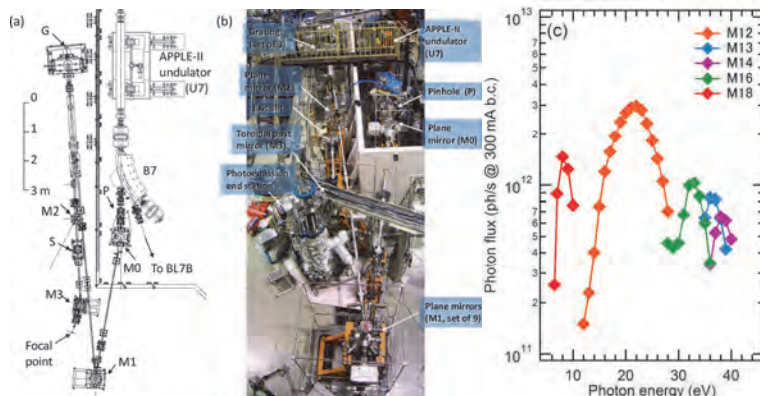


Fig. 1. SAMRAI beamline [(a), (b)] consisting of an APPLE-II type undulator (U7), a modified Wadsworth type monochromator (M0-S), and a high-resolution photoemission analyzer at the focal point. The monochromator has five major optical components: two plane mirrors (M0 and M1) with water cooling, one set of three spherical gratings (G), an exit slit (S), and one toroidal refocusing mirror (M3). (c) Example of flux intensity *versus* photon energy [1]

▼ Technical Data

Light source	APPLE-II type undulator ($\lambda_u = 76$ mm, $N = 36$) vertical/horizontal, right/left circular (depending on $h\nu$)
Monochromator	10 m normal-incidence monochromator (modified Wadsworth type)
Photon energy range	6 – 40 eV ($\lambda = 30 - 200$ nm)
Resolution ($h\nu/\Delta h\nu$)	$E / \Delta E > 10000$ - 50000
Photon flux on sample	$\geq 10^{11}$ - 10^{12} ph/s (depending on $h\nu$)
Beam size on sample	200 (H) \times 50 (V) μm^2
Experiments	Angle-resolved photoemission of solids (MV Scientific A-1 analyzer, acceptance angle: ± 18 deg)

BL7B

3 m Normal-Incidence Monochromator for Solid-State Spectroscopy

▼ Description

BL7B has been constructed to provide sufficiently high resolution for conventional solid-state spectroscopy, sufficient intensity for luminescence measurements, wide wavelength coverage for Kramers–Kronig analyses, and minimum deformation to the polarization characteristic of incident synchrotron radiation. This beamline consists of a 3-m normal incidence monochromator, which covers the vacuum ultraviolet, ultraviolet, visible, and infrared, i.e., the wavelength region of 50–1000 nm, with three gratings (1200, 600, and 300 l/mm). Two interchangeable refocusing mirrors provide two different focusing positions. For the mirror with the longer focal length, an LiF or a MgF₂ window valve can be installed between the end valve of the beamline and the focusing position. Figure 1 shows the absolute photon intensity for each grating with the entrance and exit slit openings of 0.5 mm. A silicon photodiode (AXUV-100, IRD Inc.) was utilized to measure the photon intensity and the absolute photon flux was estimated, taking the quantum efficiency of the photodiode into account.

The cooling system for the pre-focusing mirror has been removed, resulting in longer beam settling times. Currently, BL7B is opened during single bunch mode, but limited use is possible during multi bunch mode.

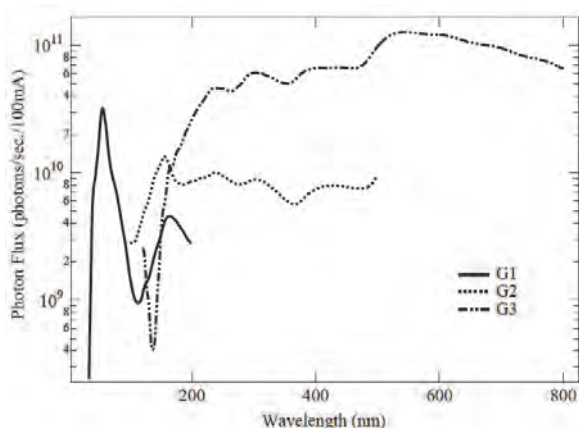


Fig. 1. Throughput spectra of BL7B measured using a silicon photodiode.



Fig. 2. Photo of BL7B.

▼ Technical Data

Monochromator	3 m Normal-Incidence Monochromator
Wavelength Range	50-1000 nm (1.2-25 eV)
Resolution	$E / \Delta E = 4000-8000$ for 0.01 mm slits
Experiments	Absorption, reflection, and fluorescence spectroscopy, mainly for solids

III-1

Accelerators and
Instruments

BL3U

Development of Resonant Soft X-ray Scattering for Soft Materials at UVSOR BL3U

H. Iwayama^{1,2} and T. Horigome¹¹UVSOR Synchrotron Facility, Institute for Molecular Science, Okazaki 444-8585, Japan²School of Physical Sciences, The Graduate University for Advanced Studies, SOKENDAI, Okazaki 444-8585, Japan

The liquid crystal is one of the most important materials for display devices. Their molecules have characteristic shapes such as rod and disc. This enables them to have both liquidity and symmetry of molecular alignments, which expresses interesting physical property such as a birefringence. In particular, chiral liquid crystal materials can have various kinds of phase, which are shown in Fig. 1. Depending on the phase, the sample is ferroelectric or anti-ferroelectric. In addition, they have intermediate phases between ferroelectric and anti-ferroelectric. To understand these physical properties, we need to know a periodic length of molecular layers, d . A typical value of d is from several nm to 100 nm. Since liquid crystal molecules mainly consist of light elements such as carbon, nitrogen and oxygen, resonant soft x-ray scattering is powerful tool.

We developed the equipment for resonant soft x-ray scattering (RSoXS) measurements. Figure 2 shows a schematic draw of an experimental setup. Our sample is S-MHPOBC and sandwiched between two 100 nm-Si₃N₄ membranes to avoid evaporations in a vacuum chamber. Sample can be heated up to 120 °C to observe various kinds of chiral smectic phases. Experiments were performed at UVSOR BL3U. Sample is irradiated with soft x-rays and scattering x-rays are detected by x-ray camera (Andor BN940P). We can measure scattering angles from 15° to 45°.

Figure 3 shows diffraction images at resonance and non-resonance photon energies and corresponding scattering angles. Here resonance is C 1s→ π^* core excitation, whose photon energy is $h\nu = 285$ eV ($\lambda = 4.3$ nm). For the resonance scattering, we found three ring structures at $y = -10, -4$ and 8 mm. At the resonance photon energy, intensities of ring structures at 8 mm strongly increase. By using Bragg's law, $d = \lambda/2\sin\theta$, we obtained d spectra for resonance and non-resonance. Here d is a periodic length, λ is a wavelength of photons, and 2θ is a scattering angle. We find peaks at $6.4, 9.7$ and 13.0 nm. Considering single molecular length of 3 nm, these peaks correspond to $2, 3$ and 4 molecular layer. Resonant enhancement of peak intensity for $d = 6.4$ nm suggests that the phase of the sample is anti-ferroelectric. Now we analyze the data in detail and investigate intermediate phases between ferroelectric and anti-ferroelectric one.

The RSoXS technique enables us to probe meso-scale (nm - μ m) structures with both elemental and chemical environment sensitivity and is ideal tool to study meso-scale materials such as polymer, block copolymer, composite morphology, particle assembly, organic

photovoltaic morphology, organic LEDs, membranes, porous materials, batteries and fuel cells, biomaterials, and so on [1].

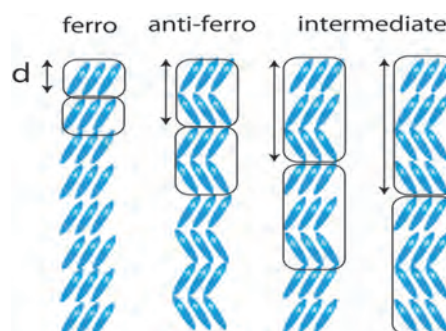


Fig. 1. Schematic view of molecular alignments for various kinds of chiral smectic phases.

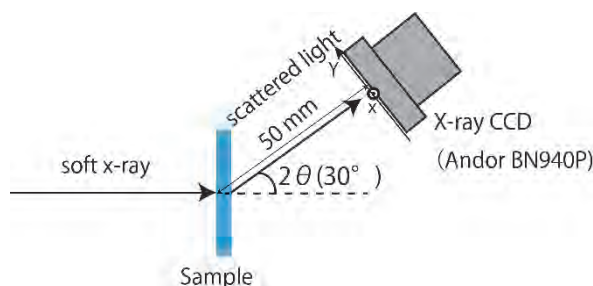


Fig. 2. Schematic draw of a new experimental setup for resonant soft x-ray scattering.

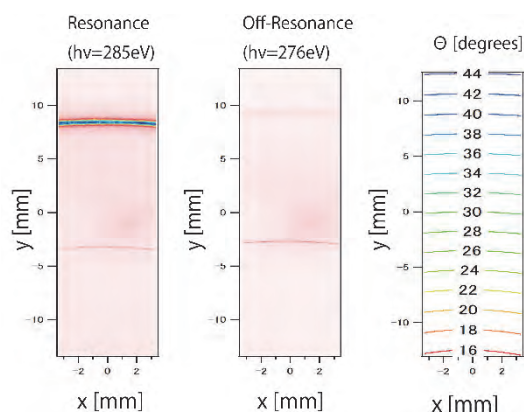


Fig. 3. Diffraction images for resonance and off-resonance and scattering angle map.

[1] F. Liu, M.A. Brady and C. Wang, *Eur. Polym. J.* **81** (2016) 555.

Others

Development of Nuclear Emulsion with Different Silver Halide Crystal Sizes for Cosmic-ray Imaging

A. Nishio, K. Morishima, K. Kuwabara, T. Yoshida and M. Nakamura
F-lab., Department of Physics, Nagoya University, Nagoya 464-8602, Japan

Cosmic ray imaging is the a new non-destructive inspection technique of large-scale constructions with cosmic ray muon. Cosmic ray muon has high penetrating power and it always comes from the whole sky. In the same way of taking a X-ray photograph, we can obtain integrated density of constructions which thickness are several tens cm to several km. We had ever applied this technique to the pyramid of khufu at Egypt, and discovered a large void [1].

In cosmic-ray imaging observations, we used nuclear emulsion as a detector. Nuclear emulsion is a kind of photographic film and has sensitivity for ionizing radiation. The film records tracks of charged particle with angular accuracy under several mrad. In Nagoya University, started a emulsion gel production machine in 2010. It was enabled us to develop new-type emulsion gel by ourselves.

We have succeeded to develop the Large crystal Nuclear Emulsion and the relationship between the size of silver halide crystals in nuclear emulsion and their sensitivity to the minimum ionized particles was investigated.

Gold-sulfur-sensitized silver iodobromide crystals with a diameter of approximately 180 - 540 nm were prepared (Fig.1), and their photo sensitivity and minimum ionized particle sensitivity were investigated.

First, we confirmed that the photo sensitivity was proportional to the crystal volume and that the quantum sensitivity to light was sufficiently high (Fig. 2).

After that, minimum ionized particle sensitivity was investigated (Fig. 3). The grain density was found to be 1.3 to 1.4 times higher with the same volume occupancy of crystals by increasing the crystal size to 400 nm in diameter than the conventional size of 220 nm. It was also found that the grain density could not be significantly increased due to the decrease in the number of crystals, even if the crystal size was larger than 400 nm.

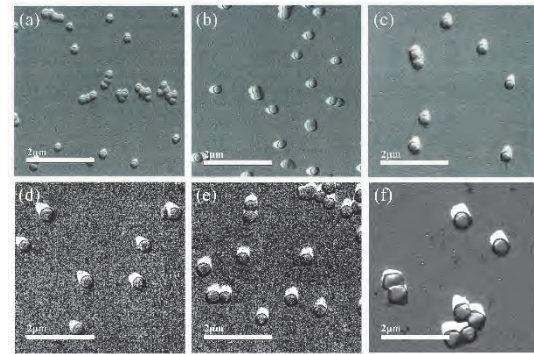


Fig. 1. EM images of silver halide crystals of different sizes.

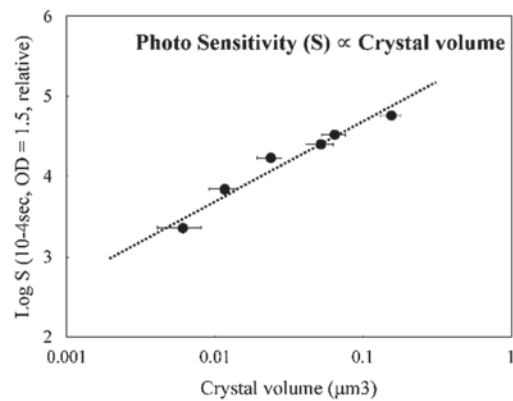


Fig. 2. Relationship between photo sensitivity S (relative value) and crystal volume.

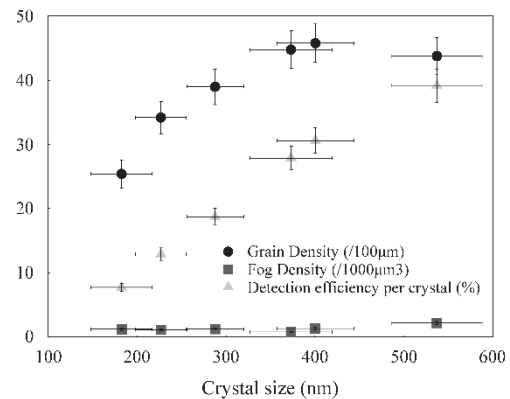


Fig. 3. Crystal size dependence of sensitivity to the minimum ionized particles; Grain density, Fog density, and detection efficiency per crystal.

[1] K. Morishima *et al.*, Nature **552** (2017) 386.

Survey of Low Emittance Optics for UVSOR-III

E. Salehi¹ and M. Katoh^{1,2}

¹UVSOR Synchrotron Facility, Institute for Molecular Science, Okazaki 444-8585, Japan

²Hiroshima Synchrotron Radiation Center, Hiroshima University, Higashi-Hiroshima 739-0046, Japan

This is a study on a future plan of UVSOR synchrotron to provide diffraction-limited light in the vacuum ultraviolet range. For this purpose, the small emittance less than at 1 nm is required. UVSOR is a low energy synchrotron light source. After some major upgrades [1-4], it is now called UVSOR-III, which has a moderately small emittance of about 17 nm and provide vacuum ultraviolet light of high brightness.

As the first step of the study, we have analyzed the present magnetic lattice of UVSOR III to seek a possible low emittance without major changes of the lattice. We draw a “tie diagram” of UVSOR III as shown in Fig.1, which indicates the quadrupole parameter region where a periodic solution exists, as well as the emittance of each parameter set is shown by the color. In reality, UVSOR-III has four quadrupole families. However, to draw the tie diagram, they are grouped into two families (QF and QD) located symmetrically around the bending magnets. The code, Elegant [5], was used and the two quadrupole strengths are surveyed. Figure 1 shows that there are a few areas which has significantly smaller emittance around 10 nm than the present value, 17 nm. However, there seems no solution which gives the emittance much smaller than 10 nm. The hardware limitations of the quadrupole field strengths are indicated in the figure. For the operation energy, 750 MeV, a part of the low emittance region is out of the limitation. However, if the machine is operated at 600 MeV, most of the low emittance area is within the limitation. It should be noted that the emittance is proportional to the square of the electron energy, the low energy operation would give even smaller emittance.

On the tie diagram, we can find some solutions which give a smaller emittance than the present value. Making these parameters as the initial values for four quadrupole families, we designed some optics which may be worth to investigate further. The optic presented in Fig. 2 has an emittance smaller than 10 nm at the electron energy, 750 MeV. In this optics, the vertical betatron function at the straight sections are not as small as the present optics. Therefore, this optics may not be compatible with the operation of the narrow gap undulators. In some special studies which requires a small emittance as possible, this optics may be useful. Another interesting optic is shown in Fig. 3, which gives a small emittance, 13 nm, with a fewer numbers of quadrupoles. In this optics, we can remove one quadrupole family at the short straight sections. This may be beneficial to install new devices for beam handlings, beam monitors or light source developments.

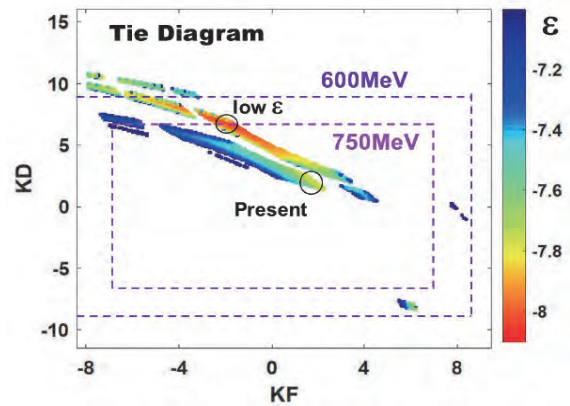


Fig. 1. Tie diagram of UVSOR-III magnetic lattice. KF and KD are quadrupole strengths.

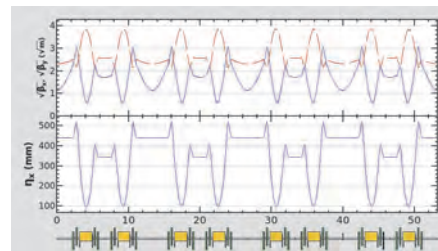


Fig. 2. An optic whit a small emittance of 9.4 nm at 750 MeV.

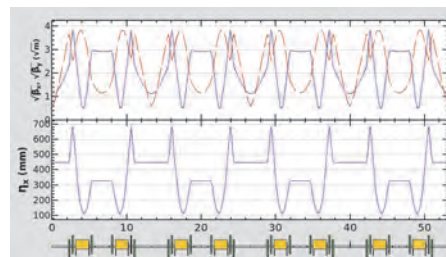


Fig. 3. An optic which gives a moderately small emittance of 13.3 nm with less numbers of quadrupoles.

- [1] M Katoh, K Hayashi, *et al.*, Nucl. Instr. Meth. A **467** (2001) 68.
- [2] M Katoh, M Hosaka, *et al.*, AIP Conf. Proc. **705** (2004) 49.
- [3] M Adachi, H Zen, *et al.*, J. Phys. Conf. Ser. **425** (2013) 04201.
- [4] M. Katoh, M. Adachi, *et al.*, AIP Conf. Proc. **1234** (2010) 531.
- [5] M. Borland, APS LS-287 (2000).
<https://www.aps.anl.gov/Accelerator-Operations-Physics/Software>

BL1U

Selective Isotope 3D-CT Imaging in UVSOR-BL1U

H. Ohgaki¹, K. Ali¹, H. Zen¹, T. Kii¹, T. Hayakawa², T. Shizuma², H. Toyokawa³,
M. Fujimoto⁴, Y. Taira⁴ and M. Katoh^{4,5}

¹Institute of Advanced Energy, Kyoto University, Uji 611-0011, Japan

²Tokai Quantum Beam Science Center, National Institutes for Quantum and Radiological Science and Technology, Tokai-mura 319-1106, Japan

³National Institute of Advanced Industrial Science and Technology (AIST), Tsukuba 3058568, Japan

⁴UVSOR Synchrotron Facility, Institute for Molecular Science, Okazaki 444-8585, Japan

⁵Hiroshima University, Higashi-Hiroshima 739-8511, Japan

A Nuclear Resonance Fluorescence (NRF) method is a powerful tool for investigating nuclear physics and isotope imaging inside the spent nuclear fuel canisters and nuclear wastes. We have been developing an isotope imaging technique using the NRF scattering method in AIST [1] and transmission method in UVSOR-III [2].

We successfully got 2D NRF-CT images by using an LCS gamma-ray beam with two enriched isotope targets, ²⁰⁶Pb (>93.3 %) and ²⁰⁸Pb (>97.8 %), inserted in an aluminum holder at the beamline BL1U in UVSOR-III in 2019 [3]. In 2020, we tried to obtain a 3D image of the same CT target. The geometry of the CT target is shown in Fig. 1.

The LCS gamma-ray beam with a maximum energy of 5.528 MeV was generated by using a fiber laser (wavelength of 1,896 μm, 50 W). The gamma-ray beam with a 10 photon · s⁻¹ · eV⁻¹ flux density was used to excite J^π=1⁻ state at 5.512 MeV of ²⁰⁸Pb with a 2-mm lead collimator. The gamma-ray absorption by the CT target was measured at 4-mm step in the horizontal direction (x= -12 to +12 mm) and 30° step in the rotation angle (θ=0° to 150°). Three vertical positions (z=3, 11, and 17 mm from the holder's bottom) were taken. Two HP-Ge detectors measured the NRF signals from the witness target (²⁰⁸Pb enriched) with 100 % and 130 % relative efficiencies. The transmission gamma-rays have been measured by a 3.5" × 4" LaBr₃(Ce) detector, which gives a density distribution by the atomic absorption process of the sample target at the same time. After suppressing the atomic absorption process measured by the LaBr₃(Ce) detector, the NRF-CT images, which selectively indicate the distributions of ²⁰⁸Pb, were obtained. Figure 2 shows a typical one-layer CT image (z=3 mm case). By stacking 3-layer NRF-CT images, a rough 3D NRF-CT image of ²⁰⁸Pb distribution in the CT target was successfully obtained, as shown in the Fig. 3.

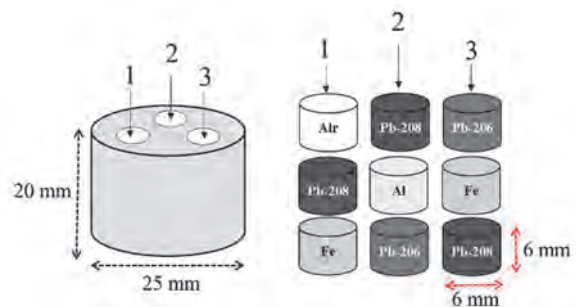


Fig. 1. Geometry of the CT target. Right figure shows the configuration of enriched rods inserted to the aluminium cylinder shown in the left figure.

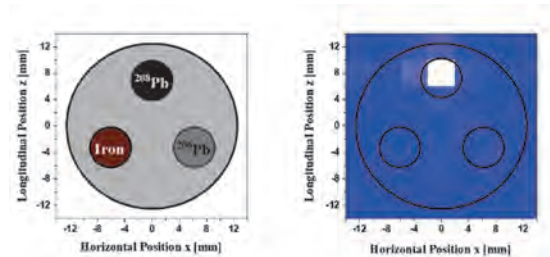


Fig. 2. NRF-CT image at z= 3 mm

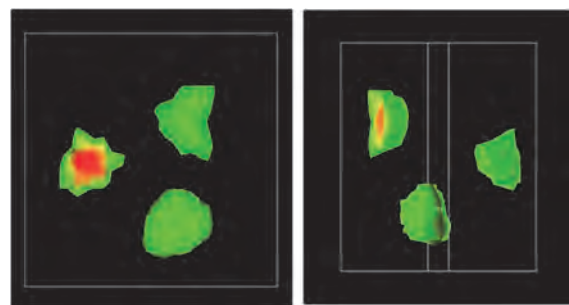


Fig. 3. 3D NRF-CT image

[1] N. Kikuzawa *et al.*, Appl. Phys. Express **2** (2009) 036502.

[2] H. Zen *et al.*, AIP Advances **9** (2019) 035101.

[3] K. Ali *et al.*, IEEE Trans. Nucl. Sci. **67** (2020) 1976.

BL1U

Elastic Scattering of Gamma-rays with Energies of 10 MeV

T. Hayakawa¹, K. Kawase¹, T. Shizuma¹, R. Hajima¹, J. K. Koga², H. Zen³, T. Kii³,
H. Ohgaki³, M. Fujimoto⁴, Y. Taira⁴ and M. Katoh^{4,5}

¹National Institutes for Quantum and Radiological Science and Technology, Tokai-mura 319-1106, Japan

²National Institutes for Quantum and Radiological Science and Technology, Kizugawa 619-0215, Japan

³Institute of Advanced Energy, Kyoto University, Kyoto 611-0011, Japan

⁴UVSOR Synchrotron Facility, Institute for Molecular Science, Okazaki 444-8585, Japan

⁵Hiroshima University, Higashi-Hiroshima 739-8511, Japan

QED theory predicted unresolved nonlinear effects such as photon-photon interactions [1,2]. Recently, virtual photon – virtual photon scattering with energies of 5 TeV has been measured using a high energy accelerator [1]. One of the photon-photon interactions is Delbrück scattering, which is an elastic scattering of gamma-rays. However, there was a critical problem that one cannot calculate the scattering using only the amplitude of Delbrück scattering due to the interference of other elastic scattering. Koga and Hayakawa [3] have presented that it is possible to measure selectively the amplitude of Delbrück scattering using linearly polarized gamma-rays.

To study Delbrück scattering we have installed a CO₂ laser [4]. Here, we have installed a fiber laser with a wavelength of 1064 nm and an average power of 10 W. The pulse width is 1 ns and the pulse energy is 25 μ J. The maximum repetition is 400 kHz and can be controlled by an external trigger. The laser Compton scattering (LCS) gamma-rays with a maximum energy of 10 MeV were generated by interactions with electron beams having an energy of 750 MeV stored in UVSOR-III. To generate linearly polarized gamma-rays we used a linear polarized laser. We newly developed a collimator system and detector frame. The tungsten target with a diameter of 5 mm and a length of 50 mm was used. The gamma-rays scattered from the target were measured with two 3.5'' \times 4'' LaBr₃(Ce) scintillation detectors, which were placed at $\phi = 0$ and 90 degrees from the linear polarization plane at $\theta = 90$ degrees away from the gamma-ray propagation axis (see Fig. 1). Figure 2 shows the measured energy spectra. A broad peak is observed in an energy region from 5–7 MeV in Fig. 2(b) but it is not observed in Fig. 2(a). This peak originates from Compton scattering on a mirror inside the beamline. The elastic scattering is not clearly observed.

[1] ATLAS Collaboration, *Nature Physics* **13** (2017) 852.

[2] T. Inada, *et al.*, *Phys. Lett. B* **732** (2014) 356.

[3] J. K. Koga and T. Hayakawa, *Phys. Rev. Lett.* **118** (2017) 204801.

[4] H. Zen *et al.*, *J. Phys.: Conf. Ser.* **1067** (2018) 092003.

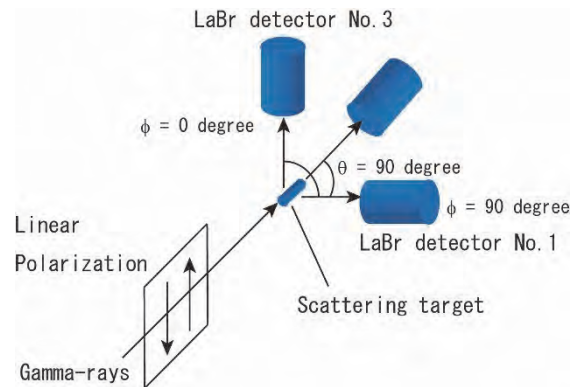


Fig. 1. A schematic view of the scattering experiment. The gamma-rays scattered from the target were measured with two LaBr₃(Ce) scintillation detectors.

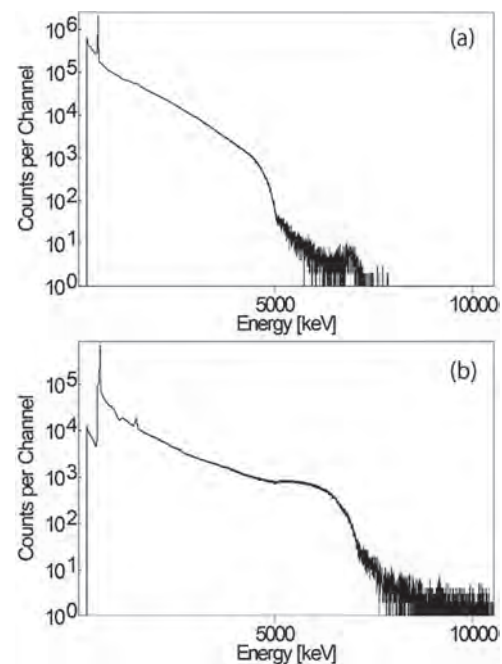


Fig. 2. Measured gamma-ray spectra using LaBr₃(Ce) scintillation detectors. The spectrum measured at $\phi = 0^\circ$ away from the linear polarization plane (a) and that at $\phi = 90^\circ$ (b).

BL1U

Improvement of Interferometer for Measuring The Coherence Length of Light from an Undulator

A. Mano¹, S. Kimura¹, M. Hosaka¹, T. Takashima¹ and M. Katoh^{2,3}

¹Nagoya University, Nagoya 464-8603, Japan

²Hiroshima University, Higashi-Hiroshima, 739-0046, Japan

³UVSOR Synchrotron Facility, Institute for Molecular Science, Okazaki 444-8585, Japan

We are experimentally studying the time domain structure of light from an undulator so-called coherence length, which is wave packet length emitted from a single electron passing through the undulator.

We attempted to measure the coherence length of light from an undulator using a Michelson-type interferometer [1]. The light from the undulator is split by the first beam splitter (non-polarizing type). After split lights are folded back by the retroreflector and overlapped again by the second beam splitter. By moving one of the retroreflectors, a difference in the optical path is created. The overlapping lights interfere with each other, causing fluctuation in intensity according to the optical path difference. The intensity fluctuation is called an interferogram. If the overlapping light is angled, the image forms interference fringes, but the interferogram corresponds to the intensity fluctuation of a single point in the image. The interferogram is the autocorrelation of the undulator light wave packet.

At first, we constructed an interferometer using $\phi 20$ mm pedestal posts. We use 10 mm square cube type beam splitters and right-angle prisms as retroreflectors. This interferometry is shown in Fig.1. This optical system generated a lot of stray light and was difficult to adjust. Further, this optical system had low rigidity and the optical elements were prone to vibration. The system was exposed, therefore it was easily affected by fluctuations in the atmosphere. The image of the interference fringes obtained by this optical system is shown in Fig. 2. In Fig. 2. (b), the fringes are blurred, probably due to vibration. In Fig. 2. (c), the phase of the fringes is shifted, probably due to atmospheric fluctuations. Thus, the interferogram measurement proved to be very difficult with this optical system.

We attempted to improve the interferometer. By changing the single-point support of the pedestal post to multi-point support by the optical cage system, the rigidity of the system has been improved and rough alignment is no longer necessary. To reduce stray light, the beam splitter cube was replaced with a beam splitter plate and the retroreflector was replaced with two mirrors. Further, the use of a kinematic holder for the folded mirror made it easier to adjust the overlay of the two split beams. Furthermore, by covering the area around the optical system, it was protected from atmospheric fluctuations. These improvements made it possible to obtain stable images of interference fringes.

More details on the results from the improved

interferometer will be presented in a future paper.



Fig. 1. Photo of the interferometer we first constructed.

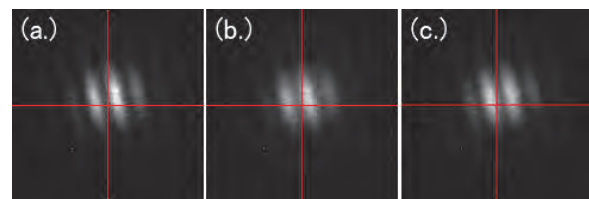


Fig. 2. Images of interference fringe in the same condition.



Fig. 3. Photo of the improved interferometer.

[1] S. Notsu *et al.*, UVSOR Activity Report 2019 47 (2020) 37.

BL2A

Evaluation of the Robustness of Back-illuminated CMOS Sensors Against Soft X-rays

N. Narukage

National Astronomical Observatory of Japan, Mitaka 181-8588, Japan

The solar corona is full of dynamic phenomena. They are accompanied by interesting physical processes, namely, magnetic reconnection, particle acceleration, shocks, waves, flows, evaporation, heating, cooling, and so on. The understandings of these phenomena and processes have been progressing step-by-step with the evolution of the observation technology in EUV and X-rays from the space. But there are fundamental questions remain unanswered, or haven't even addressed so far. Our scientific objective is to understand underlying physics of dynamic phenomena in the solar corona, covering some of the long-standing questions in solar physics such as particle acceleration in flares and coronal heating. In order to achieve these science objectives, we identify the imaging spectroscopy (the observations with spatial, temporal and energy resolutions) in the soft X-ray range (from ~ 0.5 keV to ~ 10 keV) is a powerful approach for the detection and analysis of energetic events [1]. This energy range contains many lines emitted from below 1 MK to beyond 10 MK plasmas plus continuum component that reflects the electron temperature.

The soft X-ray imaging spectroscopy is realized with the following method. We take images with a short enough exposure to detect only single X-ray photon in an isolated pixel area with a fine pixel Silicon sensor. So, we can measure the energy of the X-ray photons one by one with spatial and temporal resolutions. When we use a high-speed soft X-ray camera that can perform the continuous exposure with a rate of more than several hundred times per second, we can count the photon energy with a rate of several 10 photons / pixel / second. This high-speed exposure is enough to track the time evolution of spectra generated by dynamic phenomena in the solar corona, whose lifetimes are about from several ten seconds to several minutes.

For the first imaging spectroscopic observation of the solar corona in soft X-ray range, we launched a NASA's sounding rocket (FOXSI-3) on September 7th, 2018 and successfully obtained the unprecedented data [2] using a high-speed X-ray camera [3] with a back-illuminated CMOS sensor [4].

Though this back-illuminated CMOS sensor has an enough photon-counting capability for the X-ray imaging-spectroscopy as demonstrated by FOXSI-3 flight, we found that it is damaged by the incident X-rays (which themselves are the targets of detection) as shown in Fig. 1.

For the evaluation of the robustness of the sensor against the incident X-rays, we did the following

procedures:

1. Take dark image to monitor the dark level (bias level) and noise level (readout noise + dark noise).
2. Emit the monochromatic intense X-rays with BL2A for a certain period.
3. Repeat Procedures 1 and 2 until the dark level is saturated.

We did this evaluation with three monochromatic X-rays of 1 keV, 2 keV and 4 keV, for two types of back-illuminated CMOS sensors, whose difference is only the thickness of sensitive layers. The thicknesses are about $4\mu\text{m}$ and $10\mu\text{m}$. Based on these evaluations, we found that the sensor with the thicker sensitive layer can survive against the more incident X-ray photons. In the energy of each monochromatic X-rays, the detectable X-ray photon number without serious damage is roughly proportional to the absorption rate of the sensitive layer. Hence, we suspected that the presumable damaged part is the circuit layer, which is located behind the sensitive layer.

In our estimate based on these evaluations, more than $\sim 15\mu\text{m}$ sensitive layer is required for solar flare observations. We plan to confirm this result using the CMOS sensor with $25\mu\text{m}$ sensitive layer in FY2021.

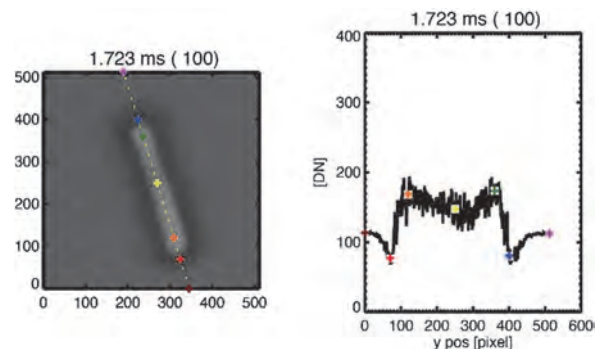


Fig. 1. Dark image of the CMOS damaged by X-rays.

[1] N. Narukage *et al.*, White paper of the “soft X-ray imaging spectroscopy”, arXiv:1706.04536 (2017).

[2] N. Narukage and S. Ishikawa, UVSOR Activity Report 2018 **46** (2019) 36.

[3] S. Ishikawa *et al.*, Nuclear Instruments and Methods in Physics Research Section A **912** (2018) 191.

[4] N. Narukage *et al.*, Nuclear Instruments and Methods in Physics Research Section A **950** (2020) 162974.

BL3U

Development of an Ultrathin Liquid Cell for Soft X-ray Absorption Spectroscopy in the Low-Energy Region

M. Nagasaka^{1,2}¹Institute for Molecular Science, Okazaki 444-8585, Japan²The Graduate University for Advanced Studies, SOKENDAI, Okazaki 444-8585, Japan

Soft X-ray absorption spectroscopy (XAS) is an element-specific method to investigate local structures of liquids and solutions. Recently, we have developed a transmission-type liquid cell for XAS of liquid samples, where a liquid layer is sandwiched between two Si_3N_4 membranes with the thickness of 100 nm and the liquid thickness is precisely controlled by adjusting the helium pressure around the liquid cell [1]. On the other hand, the low-energy region below 200 eV is important for chemical research since it includes K-edges of Li and B and L-edges of Si, P, S, and Cl. However, the soft X-ray transmission calculation [2] predicts that soft X-rays below 200 eV cannot transmit the present liquid cell, which consists of four Si_3N_4 membranes and 20 mm optical path of He gas. Recently, we have established the argon gas window, which is effective for the transmission of soft X-rays from 60 to 240 eV with the removal of high order X-rays [3]. We also found that soft X-rays in the low-energy region can transmit the ultrathin liquid cell with the optical length of 2.6 mm. In this study, we realize XAS in the low-energy region by developing the ultrathin liquid cell.

Figure 1(a) shows a schematic of the XAS measurement system including the ultrathin liquid cell. The experiment was performed at BL3U. In the ultrathin liquid cell, a liquid layer is sandwiched between two Si_3N_4 membranes and is in an atmospheric Ar condition. The soft X-ray beamline and a photodiode detector are under ultrahigh vacuum conditions and are separated from the atmospheric Ar chamber with Si_3N_4 membranes with a small window size ($0.2 \times 0.2 \text{ mm}^2$). Figure 1(b) shows photographs of the ultrathin liquid cell. In the left part, soft X-rays pass through the Si_3N_4 membranes settled in the center part of the liquid cell. In the right part, the thickness of the ultrathin liquid cell becomes 2.4 mm. Considering the thickness of the holders of small Si_3N_4 windows, the optical pass length of Ar gas is estimated to be 2.6 mm.

Figure 2 shows Cl L-edge XAS spectrum of 2 M LiCl solution by using the ultrathin liquid cell. The spectrum shows two peaks with the positions of 203 eV and 208 eV. We have also obtained Li K-edge XAS spectrum of 2 M LiCl solution although the signal-to-noise ratio is not sufficient due to the low photon flux at the Li K-edge. In the present study, we have confirmed the effectiveness of the ultrathin liquid cell for XAS in the low-energy region. However, the photon flux is still low due to the strong absorption of Si_3N_4 membranes at the Si L-edge (100 eV). It is difficult to optimize the absorbance of solute LiCl peaks with the increase of the

liquid thickness. In the future, we will prepare polymer membranes that consist of no Si atoms to obtain high photon flux of transmitted soft X-rays and measure XAS spectra in the low-energy region with a good signal-to-noise ratio.

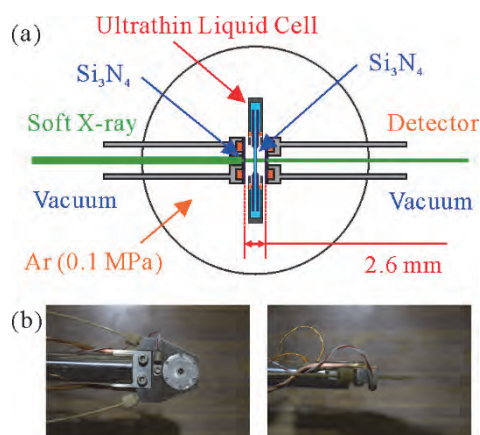


Fig. 1. (a) A schematic of the XAS measurement system in the low-energy region with the ultrathin liquid cell. (b) Photographs of the ultrathin liquid cell.

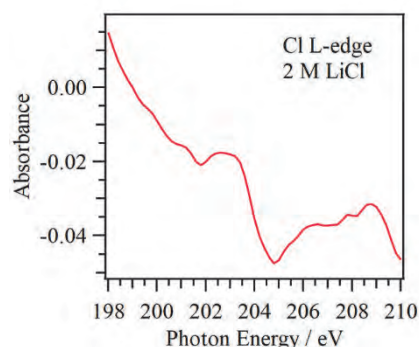


Fig. 2. Cl L-edge XAS of 2 M LiCl solution.

[1] M. Nagasaka, H. Yuzawa and N. Kosugi, *Anal. Sci.* **36** (2020) 95.

[2] C. T. Chantler, *J. Phys. Chem. Ref. Data* **29** (2000) 597.

[3] M. Nagasaka, *J. Synchrotron Rad.* **27** (2020) 959.

BL3B

Development of Ion Time-of-Mass Spectrometer at UVSOR BL3B

H. Iwayama^{1,2} and T. Horigome¹

¹UVSOR Synchrotron Facility, Institute for Molecular Science, Okazaki 444-8585, Japan

²School of Physical Sciences, The Graduate University for Advanced Studies, SOKENDAI, Okazaki 444-8585, Japan

Halogenated alkanes are used as flame retardants, fire extinguishants and refrigerant gases. While they are useful and widely used in commerce, they have also been shown to be serious pollutants and toxins. In particular, the chlorofluorocarbons have been shown to lead to ozone depletion. Photolysis and the reactions of these substances with hydroxyl radical, the main oxidizing agent of the troposphere, derived from the photolysis of ozone, determine their life-time in the atmosphere. In the stratosphere they interact with VUV light and produce halogen atoms which contribute to the ozone depletion process. Photodissociation and photoionization channels are very interesting since different fragmentation channels can lead to different radical and/or cations which can play a role in several fields, from atmospheric chemistry to etching and plasma assisted industrial process. In this work, we developed ion time-of-flight mass spectrometer at BL3B for photochemistry of halogenated alkanes in UV and VUV region.

The experiment was performed at UVSOR BL3B, where we use intense synchrotron light from visible to EUV regions. A schematic view of our experimental setup is shown in Fig. 1. The sample gas jet is generated from the capillary nozzle and irradiated by VUV light between ion and electron extract meshes. While a photoelectron is detected by the electron MCP detector, an ion is introduced to ion time-of-flight mass spectrometer. Detection signals of electron and ion are used as start and stop signal for time-of-flight spectrometer, respectively. The sample is R22 gases (CHF_2Cl).

Figure 2 shows ion time-of-flight mass spectra for CHF_2Cl molecules at photon energies of 15, 20 and 30 eV. At the photon energy of 15 eV, we find that dominant fragment ions are CHF_2^+ . This means that major photodissociation is $\text{CHF}_2\text{Cl} + h\nu (15\text{eV}) \rightarrow \text{CHF}_2^+ + \text{Cl}$ and generate a Cl radical. Here we note that relative abundance of parent molecular ions, CHF_2Cl^+ , is very low. Our results suggest that the C-Cl bond is easily broken by VUV photon absorptions. By increasing photon energies, we also find smaller fragment ions such as CF^+ , Cl^+ and CH^+ and H^+ ions. Since we also measured these ion yields as a function of photon energies, corresponding appearance energies of each fragment ions will be deduced. Now we analyzed these results in details.

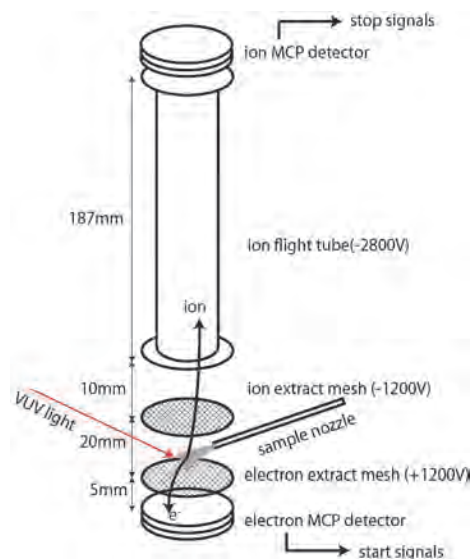


Fig. 1. Schematic view of our ion time-of-flight spectrometer.

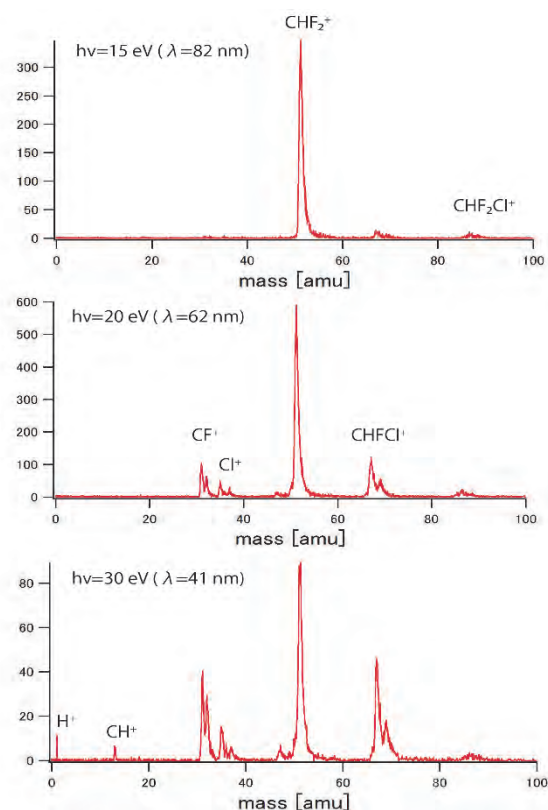


Fig. 2. Ion time-of-flight mass spectra for CHF_2Cl molecules at photon energies of 15, 20 and 30 eV.

BL4U

Study of STXM with IR Laser Optics Part I. – In-Situ Removal of Organic Contamination from Carbon Nanotube –

H. Yuzawa¹ and T. Ohigashi^{1,2}¹UVSOR Synchrotron Facility, Institute for Molecular Science, Okazaki 444-8585, Japan²School of Physical Sciences, The Graduate University for Advanced Studies, SOKENDAI, Okazaki 444-8585, Japan

Scanning Transmission X-ray Microscope (STXM) gives two-dimensional X-ray absorption spectroscopy (XAS) spectra of sample with ca. 50 nm spatial resolution, which is powerful to get the distribution of chemical state. However, the measurement immediately after heating sample in the STXM chamber is difficult because the focal length of a Fresnel zone plate (FZP) in soft X-ray region is short as shown in Fig. 1a. Main problems of this measurement are harmful influences for the optical elements, and large sample drift by thermal vibration. In the present study, we have carried out heating the sample by using an IR laser diode from outside of the chamber to reduce the remaining thermal source in there. As a test sample for heating, carbon nanotube (CNT) has been applied to in-situ removal of its organic contaminations, based on the user's request.

Figure 1b shows the picture of experimental set up for heating the sample. Diverging light of the multimode IR laser diode (3 W, 940 nm) is collimated with two cylindrical plane-convex lenses ($f = 5$ and 10 cm) and is focused to sample inside the STXM chamber with a spherical plane-convex lens ($f = 50$ cm).

CNT (NanoIntegrus Inc., IsoNanotube-S) was used as the sample, whose contaminations are iodixanol (Fig. 2) and some surfactant (its structure is not open) [1]. 0.5 mg of the CNT was dispersed into water (40 ml) by using an ultrasonic homogenizer, then the suspension (3 μ l) was dropped and dried on a Si₃N₄ membrane (window size, 0.5 \times 0.5 mm²). STXM measurements in C *K*-edge of the CNT were carried out after heating the sample at ca. 280 °C under vacuum for 15 min. During the heating of the sample, the sample and a detector stage were moved to 7 cm backward from its measuring position.

Figure 3a shows one of the STXM images of aggregated CNT in C *K*-edge XAS measurement. The drift of sample is at most 200 nm during the measurement. Since this value is enough small for basic measurements in BL4U, the harmful influence of the thermal source is successfully reduced by using the IR laser diode. Figure 3b shows the corresponding C *K*-edge XAS spectra. The spectral shape is gradually changed with increasing the integrated irradiation time of the IR laser. All the measuring region of CNT in Fig. 3a converges to the reported spectrum of it [2] for 75 min (Fig. 3b, blue line).

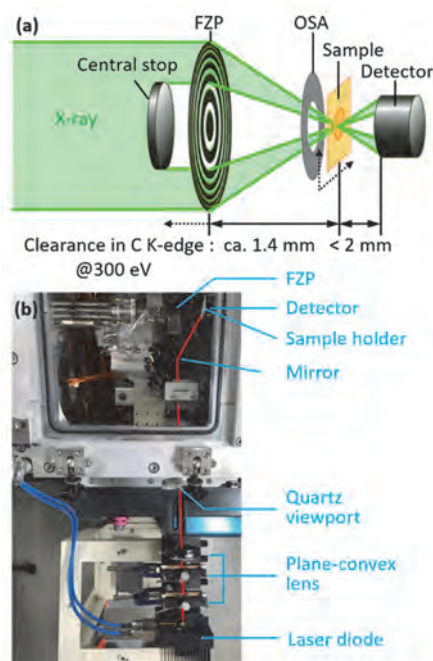


Fig. 1. (a) Side view of optical system around the sample in STXM chamber. Dotted-line arrows show the moving direction during measurements. (b) Top view of optical system for heating the sample by IR laser diode.

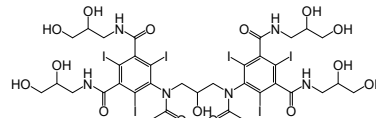


Fig. 2. Structural formula of iodixanol.

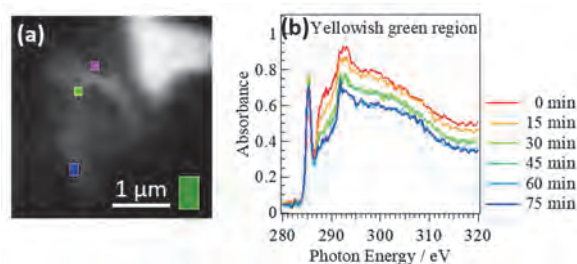


Fig. 3. (a) STXM image (based on absorbance [$= -\ln(I/I_0)$]) of aggregated CNT at 290 eV. I_0 was taken from green region. (b) C *K*-edge XAS spectra of yellowish green region in (a), measured every 15 min irradiation of the IR laser.

[1] Homepage of NanoIntegrus Inc.

[2] S. Banerjee *et al.*, *J. Phys. Chem. B* **109** (2005) 8489.

BL4U

Study of STXM with IR Laser Optics Part II. – In-Situ Observation of Mn₂O₃ Calcination –

H. Yuzawa¹ and T. Ohigashi^{1,2}¹UVSOR Synchrotron Facility, Institute for Molecular Science, Okazaki 444-8585, Japan²School of Physical Sciences, The Graduate University for Advanced Studies, SOKENDAI, Okazaki 444-8585, Japan

Defect formation in solid is an attractive research field in such as material chemistry and catalytic chemistry. For example, the defect in the photocatalyst influences photocatalytic activity and product selectivity [1]. Thus, the observation of defect formation is important under various conditions (e.g., temperature and pressure) of sample.

Scanning Transmission X-ray Microscopy (STXM) is powerful analytical method to get the two-dimensional distribution of chemical state. In the previous page of this activity report [2], we reported the thermal treatment of the CNT to remove the organic contaminations by using the IR laser diode. In the present study, we have applied this system to the observation of defect formation in Mn₂O₃ sample, which is one of the famous oxide catalysts.

Experiments were performed in the BL4U connected with the optical system of IR laser diode (see the Fig. 1(b) of [2]). 10 mg of Mn₂O₃ (Wako Pure Chemical Industries, Ltd.) was dispersed into 50 ml water with vigorous stirring, then the suspension (3 μ l) was dropped and dried on a Si₃N₄ membrane (window size, 1 \times 1 mm²). STXM measurements in O *K*-edge and Mn *L*-edge were carried out after heating the sample at ca. 300 °C under vacuum for 10 s. During the heating of the sample, the sample and a detector stage were moved to 7 cm backward from its measuring position.

Figure 1(a) shows the representative STXM image of aggregated Mn₂O₃ particles in Mn *L*-edge XAS measurement before the heating. Through the entire measurement (10 cycles of the IR laser radiation (100 s) and 11 cycles of STXM measurements for O *K*-edge (5.5 h) and Mn *L*-edge (6.5 h)), the sample shape was almost the same as that in Fig.1(a). On the other hand, in Figs. 1(b) and 1(c), both O *K*-edge and Mn *L*-edge XAS are varied with increasing the integrated heating time until 50 s, and then almost the constant spectra are obtained from 60 to 100 s. The finally obtained spectra of O *K*-edge and Mn *L*-edge are similar to those of Mn₃O₄ [3]. Thus, this spectral change indicates that the defect of oxygen is produced in Mn₂O₃ and the valence of Mn partially changed from III to II during the heating.

In another run of measurement, the influence of soft X-ray radiation on the state of Mn₂O₃ without heating was evaluated (Figure is not shown). As the result of 3 cycles of STXM measurement in O *K*-edge and Mn *L*-edge under vacuum at room temperature, the sample shape and the spectra did not change. This result indicates that any change of state in Figs. 1(b) and 1(c)

is not derived from soft X-ray radiation but the heating of sample.

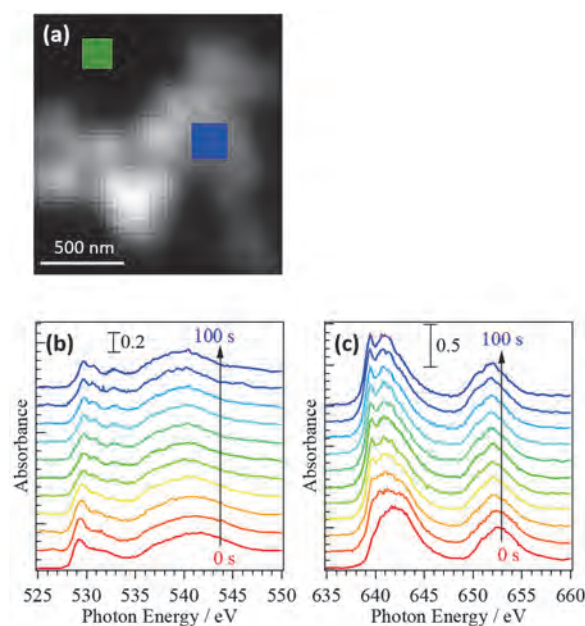


Fig. 1. (a) STXM image (based on absorbance [= -ln(I/I₀)] of aggregated Mn₂O₃ particles at 640 eV. I₀ was taken from green region. (b) O *K*-edge XAS spectra and (c) Mn *L*-edge XAS spectra of the blue region of (a), measured every 10 s IR laser radiation.

- [1] S. A. Rawool *et al.*, Chem. Sci. **12** (2021) 4267.
 [2] H. Yuzawa and T. Ohigashi, UVSOR Activity Report 2020 **48** (2021) 42.
 [3] B. Gilbert *et al.*, J. Phys. Chem. A **107** (2003) 2839.

BL4B

Development of High Efficiency Liquid Cell in Total Electron Yield Using Atomically-thin Graphene

I. Mitsuishi¹, K. Kashiwakura¹, Y. Niwa¹, T. Ogawa¹, Y. Tawara¹, R. Kitaura², P. Solís-Fernández³, K. Kawahara³, H. Ago³, T. Taniguchi⁴, K. Nomoto⁴, H. Kodaka⁴, T. Horigome⁵, E. Nakamura⁵, H. Iwayama⁵, M. Nagasaka⁵ and K. Tanaka⁵

¹Graduate School of Science, Division of Particle and Astrophysical Science, Nagoya University, Nagoya 464-8602, Japan

²Department of Chemistry, Nagoya University, Nagoya 464-8602, Japan

³Global Innovation Center, Kyushu University, Kasuga, 816-8580, Japan

⁴Optical Measurement Technology Development Department, R&D Division, USHIO INC., Yokohama 225-0004, Japan

⁵UVSOR Synchrotron Facility, Institute for Molecular Science, Okazaki 444-8585, Japan

X-rays are a powerful probe to investigate material properties through, e.g., X-ray absorption spectroscopy (XAS) which can reveal local atomic and electronic states of oxygen, carbon, etc.. Among the XAS methods for liquid, total electron yield is preferably utilized in some cases because short electron escape depth in this method makes it possible to examine atomic and electron states of liquid surface and solid-liquid interfaces. In order to realize high efficiency measurements through the total electron yield method, high efficiency films with high electron transmission are a key and therefore have been strongly desired.

To construct our original device for the total electron yield measurements, we propose to utilize graphene which is atomically thin and has high electron transmission [1]. As the first step, we tried to establish our original experimental setup to verify our idea as shown in Fig. 1. As a preliminary experiment, liquid water was sandwiched by two silicon nitride windows with apertures of 0.5 x 0.5 and 0.2 x 0.2 mm instead of graphene. We successfully detected transmitted lights and photoelectrons as shown in Figs. 2 and 3, respectively.

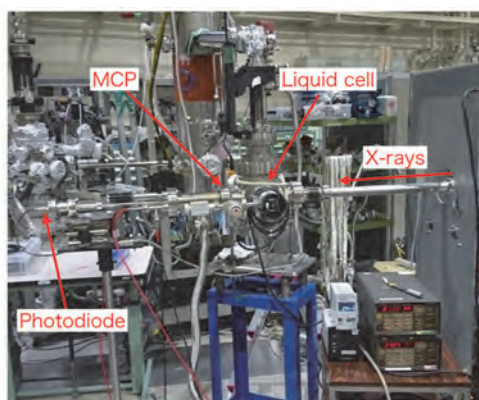


Fig. 1. Our original experimental setup for the high-efficient total electron yield method.

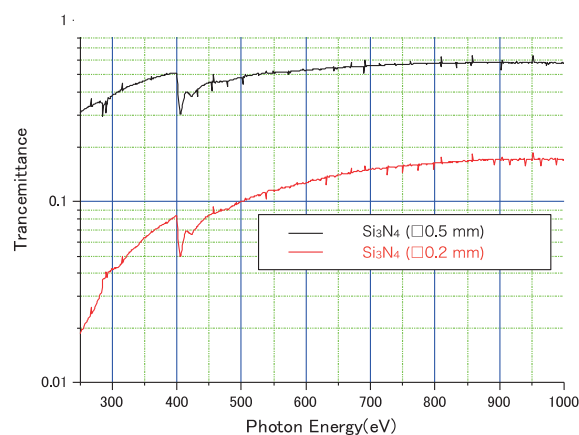


Fig. 2. Transmittance as a function of energy for the silicon nitride windows with aperture areas of 0.5 mm (black) and 0.2 mm (red).

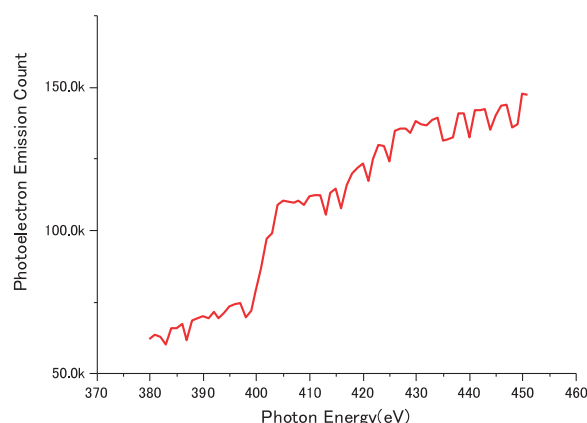


Fig. 3. Photoelectron count around the nitrogen edge structure.

[1] G. Hassink, R. Wanke, I. Rastegar, W. Braun, C. Stephanos, P. Herlinger, J. H. Smet and J. Mannhart, *APL Materials* **3** (2015).

BL5B

Development of Multilayer Coated Mirror for the Next Jupiter Mission

L. Huiyang¹, Y. Jie¹, S. Nishimura¹, K. Yoshioka^{1,2} and I. Yoshikawa^{1,2}

¹Department of Complexity Science and Engineering, Graduate School of Frontier Sciences, The University of Tokyo, Kashiwa 277-8561, Japan

²Department of Earth and Planetary Science, Graduate School of Science, The University of Tokyo, Tokyo 113-0033, Japan

Observation of solar planets in the extreme ultraviolet (EUV) spectral region is important to study dynamics of their magnetospheres. Recently, extension to shorter wavelength (XUV: x-ray and ultraviolet) is highly desired. However, there are still technical difficulties due to lack of techniques for collection of photons. Multilayer coated mirrors reflecting the XUV radiation at the normal incidence have potentials to overcome the difficulties [1].

Yoshikawa et al. (2005) showed the reflectivities of their newly developed multilayer coatings, consisting of 40 pairs of Mg and SiC [2]. The decrease in reflectivity was reported in high temperature (~ 55 °C) and high humidity (~ 65 %) environment. For science missions generally, science instruments have to survive high temperature and humidity environments. Therefore, we should develop robust instruments against environmental changes.

The measurement setup was illustrated in Figure 1. The B₄C/Mg-Si mirror was fixed on a L-shaped jig, and the L-shaped jig was mounted on the stage. Parallel movement by x,y motor and rotation by θ motor are possible.

The reflectivity is measured each 0.1 nm step from 25 nm to 35 nm. Figure 2 shows the reflectivity at different incident angles of the wavelength scan experiment before conducting the environmental test. Figure 3 shows the reflectivity of the wavelength scan experiment after conducting the environmental test. We conducted the environmental test in high temperature (50 °C) for 24 hours.

It can be seen from Fig. 2 that when the incident angle is 15 degrees and the wavelength is 31.6 nm, the reflectivity reaches its maximum, which is close to 30 %. On the other hand, Fig. 3 shows that after the environmental test, when the incident angle is 25 degrees and the wavelength is 29.2 nm, the reflectivity reaches its maximum value of 19 %, which is 2.4 nm shorter than the result before the environmental test.

[1] D.G. Stearns *et al.*, Multilayer mirror technology for soft-xray projection lithography, *Appl. Opt.* **32** (1993) 6952.

[2] Yoshikawa *et al.*, Characteristics of SiC/Mg multilayer mirrors, *Optics for EUV, X-Ray, and Gamma-Ray Astronomy II.* **59001A** (2005).

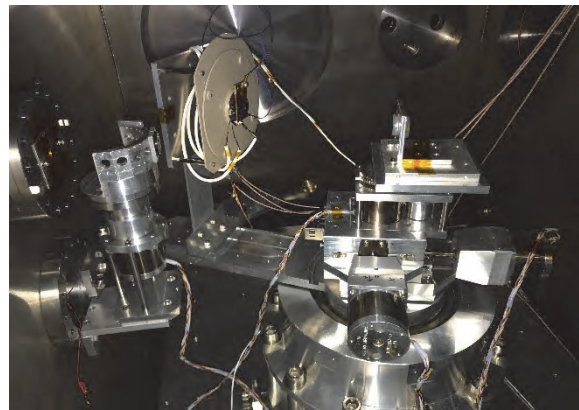


Fig. 1. Photo of the measurement setup.

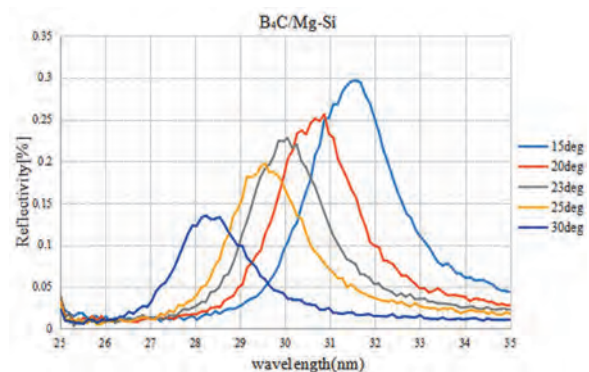


Fig. 2. Reflectivity of B₄C/Mg-Si multilayer mirror in a wavelength region 25-35 nm before conducting the environmental test.

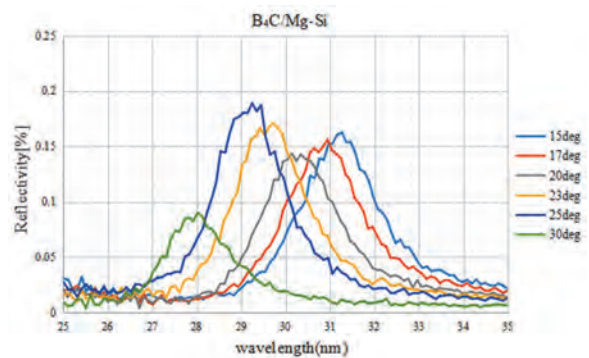


Fig. 3. Reflectivity of B₄C/Mg-Si multilayer mirror in a wavelength region 25-35 nm after conducting the environmental test.

BL5B

Performance Evaluation of Filaments used in the Hydrogen Absorption Cell

M. Kuwabara¹, K. Yoshioka², M. Taguchi³, Y. Suzuki⁴, S. Nishimura⁴ and T. Kosugi²

¹*Institute of Space and Astronautical Science, Japan Aerospace Exploration Agency, Sagamihara 252-5210, Japan*

²*Department of Complexity Science and Engineering, Graduate School of Frontier Sciences, The University of Tokyo, Kashiwa 277-8561, Japan*

³*College of Science, Rikkyo University, Tokyo 171-8501, Japan*

⁴*Department of Earth and Planetary Science, Graduate School of Science, The University of Tokyo, Tokyo 113-0033, Japan*

In the planetary exosphere, hydrogen atoms resonantly scatter the solar hydrogen Lyman-alpha radiation (121.567 nm) and form the hydrogen corona. Imaging observation of this emission provide us to obtain the spatial structure because of the dependency of its brightness on the number density of the hydrogen atoms.

An absorption cell technique is an efficient tool for the density and temperature measurements for the exospheric hydrogen atoms by remotely. Additionally, the absorption cell technique has some advantages over other instruments in terms of mass, size, and simplicity. Therefore, the absorption cell technique is suitable for future planetary exploration with small size spacecraft. See Kuwabara *et al.* [2018] for details on the principle of the absorption cell technique [1].

The absorptance of hydrogen Lyman-alpha radiation depends on the number of hydrogen atoms along the optical path in the absorption cell. The dissociation rate of hydrogen molecules depends on the surface area and temperature of the filament. In this experiment, therefore, we evaluated absorption performances of two filaments with different shapes by using the SOR beam with high intensity and stability. Table 1 shows the specifications of the filaments.

Figure 1 shows the configuration of the experiment. A hydrogen absorption cell imager consists of an absorption cell, MgF₂ band-pass filter, and photon detector. An assembly of microchannel plates (MCPs) and a resistive anode encoder (RAE) was used as the photon detector. The dependence of the absorptance of hydrogen Lyman-alpha radiation on the power consumption (i.e. filament temperature) was measured using each filament.

The result is shown in Fig. 2. The absorptance of hydrogen Lyman-alpha radiation when using the X10731 filament is higher than when using the X10478 filament. This is probably due to the large surface area of the X10731 filament. For the next step, further investigations such as long-term stability of absorption and durability of the filaments are required.

Table 1. Specifications of filaments.

	Cross-section	Coil length
X10478	Φ 48 μm	3 mm
X10731	11 x 61 μm	3 mm

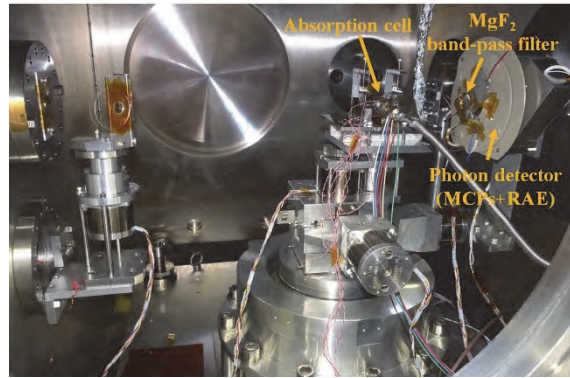


Fig. 1. Configuration of the experiment.

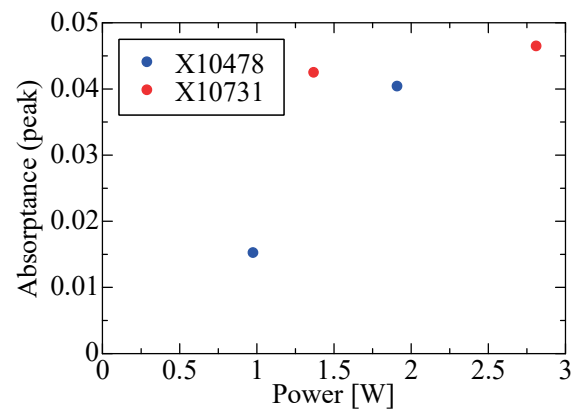


Fig. 2. Absorbance of the absorption cell.

[1] M. Kuwabara *et al.*, Review of Scientific Instruments **89** (2018) 023111.

BL5B

Trial to Mitigate Photon-Energy Drift of BL5B

H. Zen¹, E. Nakamura², K. Hayashi² and K. Tanaka^{2,3}

¹*Institute of Advanced Energy, Kyoto University, Uji 611-0011, Japan*

²*UVSOR Synchrotron Facility, Institute for Molecular Science, Okazaki 444-8585, Japan*

³*School of Physical Sciences, The Graduate University for Advanced Studies, SOKENDAI, Okazaki 444-8585, Japan*

The variation of the photon beam properties, such as beam position, photon energy, and so on, during user operation in the beamline is a big issue in synchrotron radiation (SR) facilities. A photon-energy drift at BL5B has been observed during user experiments [1]. We have started a detailed investigation of the source of the photon-energy drift. In 2019, we found that the M0 mirror, which is water cooled but directly illuminated with SR, in the beamline is not the major source of the energy drift but the M1 mirror could be the major source of that [2]. At that time, temperature of the M1 mirror holder was higher than the M1 mirror. This implied that the SR which was not reflected by the M0 mirror directly hit on the M1 mirror holder. At the same time, we found the correlation between the photon-energy drift and the temperature of the M1 mirror holder. We considered that the large temperature rise of the M1 mirror holder and heat induced deformation of it was the major source of the photon-energy drift.

In this fiscal year, a metallic mask was installed to avoid the SR directly hitting on the M1 mirror holder as shown in Fig. 1 left. In order to monitor the temperature of the mirror and mirror holder, four thermocouples (TCs) have been installed. For temperature stabilization of the mirror, a heater is installed at the center of the mirror. At first, effect of the mask was examined. The temperature variations of the M1 mirror and mirror holder with the mask are shown in Fig. 1 right. As the result, the temperature increased up to 35 deg. C in 36 hours with the mask. This was much smaller than the temperature rise without mask (up to 73 deg. C) [2]. The temperature rise of the mirror holder was greatly suppressed.

The photon-energy drift after the monochromator of BL5B was continuously monitored by using the absorption edge of an aluminum filter. Results are shown in Fig. 2 (a). The temperature of the mirror was stabilized by the feedback control of the heater power supply according to the temperature of the mirror center. Two temperature targets were examined in this test. One was the 60 deg. C, which was slightly higher than the saturated temperature of the mirror. The other was 80 deg. C, which was 20 deg. C higher than the saturated temperature of the mirror. Unfortunately, the photon-energy drift cannot be suppressed by installation of the mask and the temperature feedback of the M1 mirror. However, the photon-energy and the temperature of the mirror holder have same periodic variation and drift when the target temperature was set to 80 deg. C as one can see in Fig. 2 (b). This implies that the major source of the photon-energy drift is M1 mirror holder and not

M1 mirror itself.

To suppress the photon-energy drift of BL5B, temperature measurement points of M1 mirror holder should be increased and the most critical point must be found and temperature of the point must be stabilized.

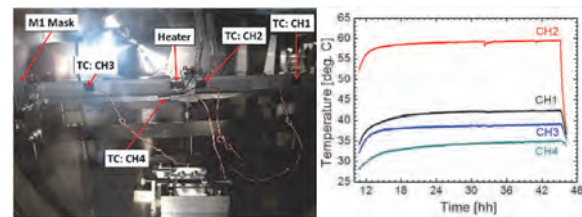


Fig. 1. (left) Photo of the M1 mirror and mirror holder with the mask, thermocouples (TCs) and a heater. (right) Temperature evolution during a SR irradiation for 36 hours with the M1 mask.

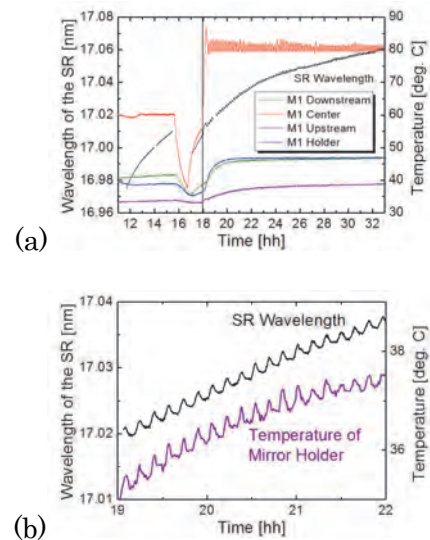
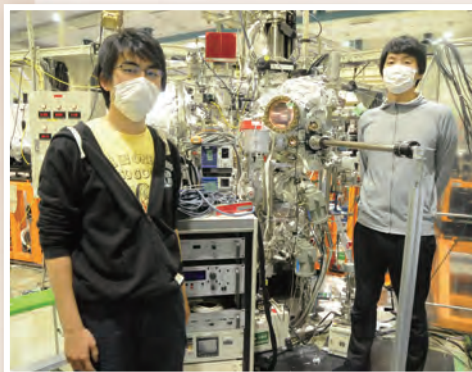
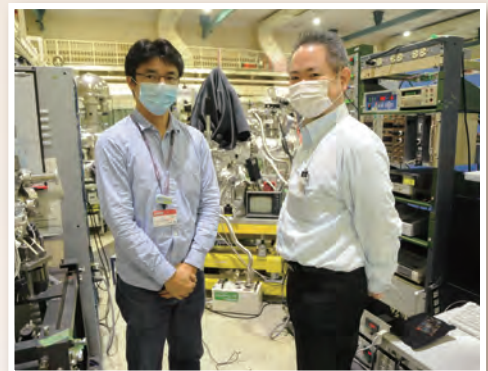
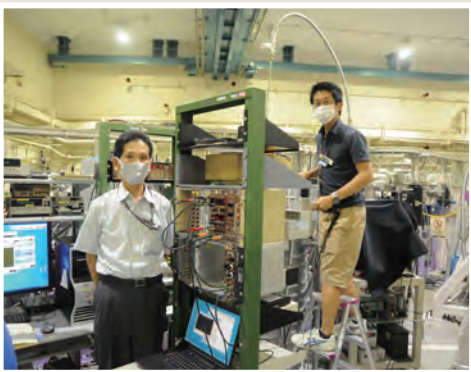
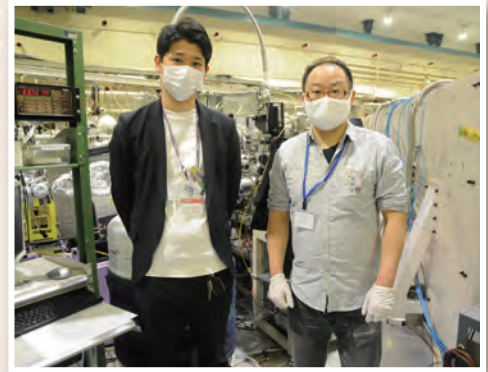
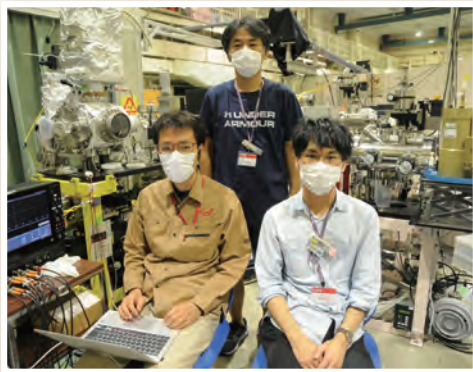
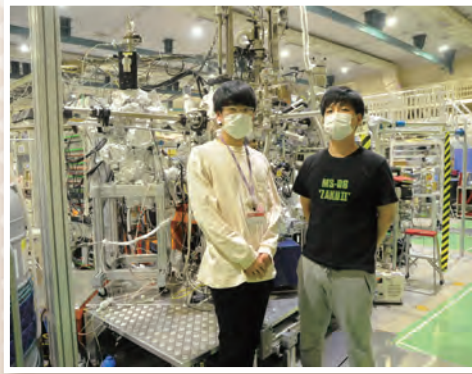
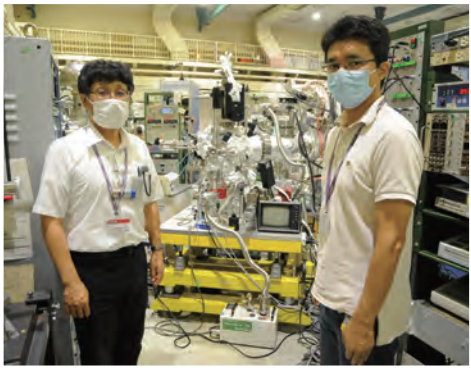


Fig. 2. (a) Measured photon-energy drift with temperature stabilization of M1 mirror. Up to 15:30, the target temperature of the feedback was 60 deg. C. From 18:00, the target temperature was 80 deg. C. (b) Closed up of 19-22 hour for SR wavelength and temperature of the mirror holder.

[1] K. Hayashi, UVSOR Activity Report 2011 **39** (2012) 121.

[2] H. Zen, UVSOR Activity Report 2019 **47** (2020) 42.

UVSOR User 4



III-2

Materials Sciences

BL6U

Angle-resolved Photoelectron Spectroscopic Study of TiSe_2 using a Newly Developed Software for the Momentum Microscope Apparatus

S. Tanaka¹, K. Ueno² and F. Matsui³¹The Institute of Scientific and Industrial Research, Osaka Univ., Ibaraki 567-0047, Japan²Graduate School of Science and Engineering Saitama University, Saitama 338-8570, Japan.³UVSOR Synchrotron Facility, Institute for Molecular Science, Okazaki 444-8585, Japan.

1T- TiSe_2 is one of the transition metal dichalcogenides (TMDC). Among TMDCs, TiSe_2 is quite interesting because it exhibits a unique charge-density-wave transition at T_c of $\sim 200\text{K}$ into the $(2 \times 2 \times 2)$ 3D superstructure despite the quasi-2D character of the TMDC. Currently, for the investigation of TiSe_2 , we are developing a new software for the analysis and presentation of the data obtained with a new momentum microscope apparatus. In this report, we demonstrate some of ARPES results of the TiSe_2 at the room temperature taken using the new software.

The software is written with the Python language with the help of some open-source libraries and additional software; e.g., “PyQtgraph”, “Mayavi”, “OpenCV”, “vtk”, “Paraview”. The software can be operated in multiple OS's; such as Windows-10, MacOS, and Linux. Fig.1 (a) shows the stereogram picture of the ARPES volume map of TiSe_2 taken at $h\nu=80\text{eV}$. In fact, the stereogram is created by using “Paraview”

which is well-known free software for a scientific visualization. We only prepare the input file for “Paraview” by transforming the ARPES data into the “vtk” format, which is standard as the 3D format. The usage of this sort of well-established software and format gives us advantages in many aspects including cutting the development time, and a convenience for an additional transformation, etc. Figures 1(b)-(d) are intensity maps in the 2D-cut indicated by the black lines in Fig. 1(a). These maps can be easily provided, thanks to our new program together with the “PyQtGraph” library, at any lines in the volume. The two momentum distribution curves and an energy distribution curve are also automatically created (not shown here).

We are progressing the investigation of the TiSe_2 by using the momentum microscope with the help of the new software.

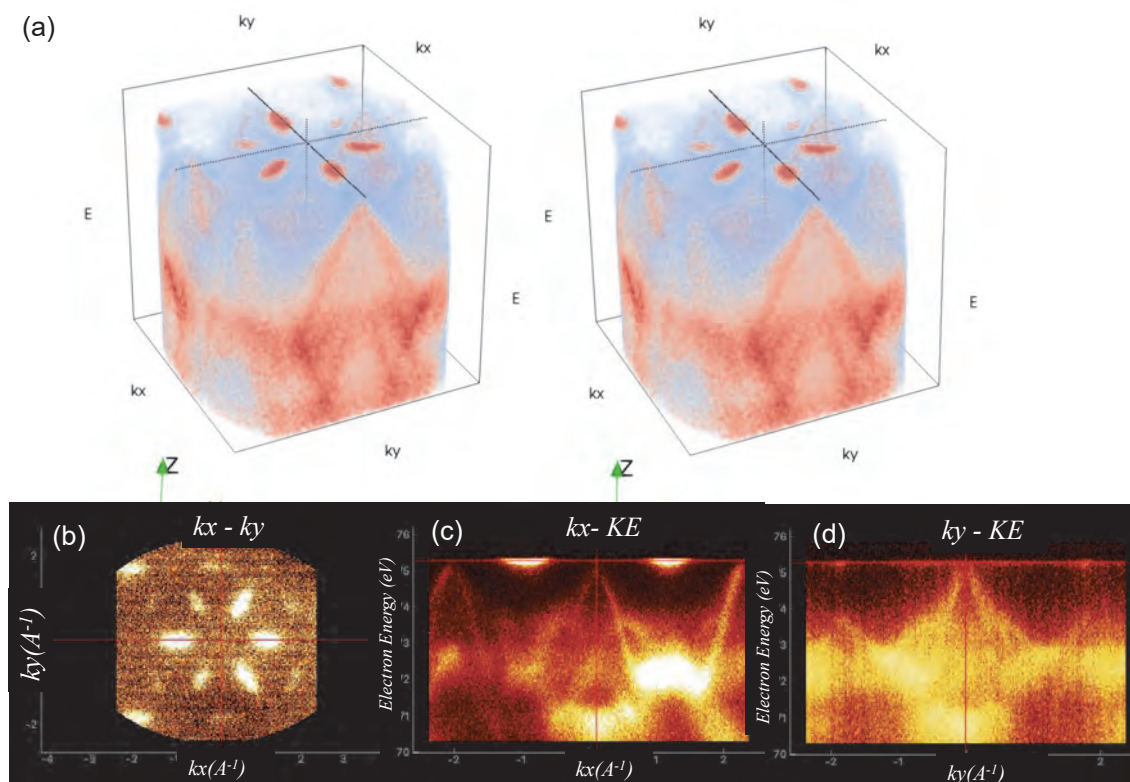


Fig. 1. ARPES volume maps of TiSe_2 at room temperature. The photon energy used is 80 eV. (a) : stereogram of the whole volume map, (b)-(d): intensity maps in 2D-cut along the black lines shown in (a).

BL1U, BL7B

Crystallinity Evaluation of Gd₃Al₂Ga₃O₁₂:Ce Crystals Grown by Cz and μ -PD Methods Using Gamma-ray-induced Positron Annihilation Lifetime Spectroscopy and High-Resolution UV Absorption Spectroscopy

M. Kitaura¹, Y. Taira^{2,3}, K. Kamada⁴, S. Watanabe⁵ and A. Ohnishi¹¹Faculty of Science, Yamagata University, Yamagata 990-4560, Japan²UVSOR Synchrotron Facility, Institute for Molecular Science, Okazaki 444-8585, Japan³The Graduate University for Advanced Studies, SOKENDAI, Okazaki 444-8585, Japan⁴New Industry Hatchery Center, Tohoku University, Sendai 980-8579, Japan⁵Institute of Innovative Research, Tokyo Institute of Technology, Tokyo 152-8550, Japan

The Czochralski (Cz) method is well-known to be a conventional technique to grow crystals from high-temperature melt [1]. The Cz method enables us to obtain large size crystals of high quality. Because the growth rate is not so high, it generally takes time to grow crystals. The micro-pulling down (μ -PD) method is a melt-growth technique similar to the Cz method [2]. There are a number of advantages for the μ -PD method: (i) The growth rate is relatively high, (ii) the effective doping of impurities is possible, and (iii) the crystal shape is controllable. The μ -PD method is suitable for the screening test in the development of functional crystalline materials. In comparison between the Cz and μ -PD methods, it has generally been believed that the crystallinity of Cz grown crystals are better than that of μ -PD grown crystals. However, to our knowledge, no comparison on crystallinity between the Cz and μ -PD methods has not yet been carried out. In the present study, we have investigated the existence of vacancy type defects and the local structures of Gd atoms in Cz and μ -PD grown Gd₃Al₂Ga₃O₁₂:Ce (GAGG:Ce) crystals by gamma-ray-induced positron annihilation lifetime spectroscopy (GiPALS), and UV and absorption spectroscopy, respectively. GiPALS experiment was performed at the BL1U. High resolution UV absorption spectroscopy were conducted at the BL7B, respectively.

The results of GiPALS analysis are shown in Table I. The data for the Cz crystal were reported [3]. The lifetimes for the μ -PD crystal are longer than those for the Cz crystal. The bulk lifetime was calculated to be 167 ps for GAGG [4]. This value was the same as the bulk lifetime for the Cz crystal, but did not agree with that (\approx 200 ps) for the μ -PD crystal. It is likely that the μ -PD crystal includes cation vacancies of high concentration, compared to the Cz crystal. The defect lifetime for the μ -PD crystal is longer than that for the Cz crystal, indicating that vacancy clusters are formed in the μ -PD crystal.

A number of peaks are observed in UV absorption spectra for GAGG:Ce crystals [5]. These peaks were assigned to the $^8S_{7/2} \rightarrow ^6P_{7/2}$, $^6P_{5/2}$ and $^6P_{3/2}$ transitions in the (4f)⁷ configuration of a Gd³⁺ ion. Because the peak position and full-width-half-maximum (FWHM) are sensitive for the local structure of Gd atoms, they can

be used as a simple probe to see the change in environment around the Gd atoms. The $^8S_{7/2} \rightarrow ^6P_{3/2}$ peak consisted of two subpeaks resulting from the Stark effect [6]. The peak positions and FWHM were evaluated by curve-fit analysis assuming the sum of two Lorentz functions. The results are listed in Table II. No differences are found between the Cz and μ -PD crystals. Detailed structural studies based on a single crystal X-ray diffraction (XRD) measurement will be performed to obtain more sophisticated information on the structure of the GAGG:Ce crystals.

Table I: Lifetimes and relative intensities determined by GiPALS analysis for the Cz and μ -PD crystals.

	Lifetime (ps)	Relative intensity (%)
Cz [3]	161 \pm 1.5	92.4 \pm 3.7
	304 \pm 19	7.6 \pm 3.7
μ -PD	198 \pm 1.1	98.45 \pm 0.21
	625 \pm 36	1.55 \pm 0.21

Table II: Peak positions and FWHM of the Gd³⁺ $^8S_{7/2} \rightarrow ^6P_{3/2}$ absorption peak for the Cz and μ -PD crystals.

	Peak position (nm)	FWHM (nm)
Cz	301.43	0.20
	301.65	0.21
μ -PD	301.42	0.19
	301.64	0.18

[1] J. Czochralski, *Zeitschrift für Physikalische Chemie* **92** (1918) 219.

[2] T. Fukuda, V. I. Chani, *Shaped crystals: micro-pulling-down technique and growth* (Springer, Berlin, New York, 2007).

[3] K. Fujimori *et al.* *Appl. Phys. Express* **13** (2020) 085505.

[4] M. Kitaura *et al.*, *J. JSSRR*. **34** (2021) 37 (in Japanese).

[5] M. Kitaura *et al.*, *J. Appl. Phys.* **115** (2014) 083517.

[6] M. Kitaura *et al.*, *J. Alloys Compd.* **867** (2021) 159055.

BL1U

Vacancy-Type Defect in Mg₂Sn Crystals Studied by Gamma-Ray-Induced Positron Annihilation Lifetime Spectroscopy

M. Kitaura¹, Y. Taira^{2,3}, S. Watanabe⁴, W. Saito⁵, K. Hayashi⁵ and A. Ohnishi¹

¹Faculty of Science, Yamagata University, Yamagata 990-4560, Japan

²UVSOR Synchrotron Facility, Institute for Molecular Science, Okazaki 444-8585, Japan

³The Graduate University for Advanced Studies, SOKENDAI, Okazaki 444-8585, Japan

⁴Institute of Innovative Research, Tokyo Institute of Technology, Tokyo 152-8550, Japan

⁵Graduate School of Engineering, Tohoku University, Sendai 980-8579, Japan

Thermoelectric (TE) materials attract much attention because they can directly convert waste heat into electricity. Exploration of TE materials is significant to secure energy resources in future. Intermetallic compounds are one of the promising candidates that can be applied to TE materials. Magnesium stannate (Mg₂Sn) has been studied for the TE application. The control of point defects such as vacancies and interstitials is crucial for this purpose, because they influence the carrier concentration and thermal conductivity included in the expression of the dimensionless figure of merit. Recently, an analysis of point defects was performed to reveal the relationship between point defects and TE properties [1]. Primary point defects in Mg₂Sn were Mg vacancies at the 8c site (V_{Mg}) and Mg interstitials at the 4b site (Mg_i), which generated valence holes and conduction electrons, respectively, by ionization of acceptors and donors. Saito *et al.* succeeded in observing the existence of V_{Mg} defects by a transmission electron microscope (TEM), and confirmed by an inductively coupled plasma mass spectroscopy. Furthermore, they demonstrated that the TE properties of Mg₂Sn are optimized by adjusting the fraction of V_{Mg}. It is therefore meaningful to evaluate the fraction of V_{Mg} quantitatively. In the present study, we have measured gamma-ray-induced positron annihilation lifetime spectroscopy (GiPALS) spectra of Mg₂Sn crystals grown under various conditions. Experiment was performed at the beamline 1U in UVSOR synchrotron facility. Details of GiPALS experiment were described in Ref. [2].

Figure 1 shows the GiPALS spectrum of the Mg₂Sn crystal grown from high-temperature melt under an Ar atmosphere of 0.6 atm. The data was obtained at room temperature. The GiPALS spectrum is of an exponential decay component with the lifetime of 255 ps. We performed a first-principles calculation using the ABINIT [3,4], to determine the positron annihilation lifetime at the bulk state (bulk lifetime) which means the crystal lattice without vacancy-type defects. The bulk lifetime was calculated 257 ps. This value is in good agreement with the lifetime determined from an curve fit analysis of the GiPALS spectrum. It is likely to assign this component to the positron annihilation at the bulk state.

In Ref. [1], the fraction of V_{Mg} was estimated 5.6 % by single crystal x-ray diffraction (SC-XRD). The

average size of V_{Mg} defects was also estimated 11 nm. Figure 1 revealed that only a bulk component appears in the GiPALS spectrum. This result does not mean that V_{Mg} defects are not included in the Mg₂Sn crystal investigated here, because GiPALS is silent for the existence of vacancies with the radii larger than a few nm [5]. The missing of defect components in the GiPALS spectrum is consistent with the result of SC-XRD analysis.

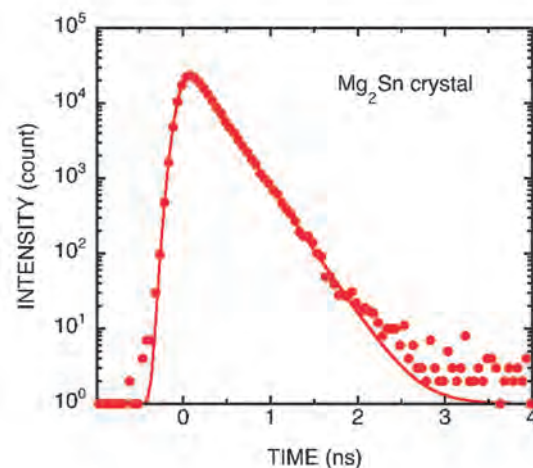


Fig. 1. GiPALS spectrum of a Mg₂Sn crystal, measured at room temperature.

- [1] W. Saito *et al.*, *Sci. Rep.* **10** (2020) 2020.
- [2] K. Fujimori *et al.*, *Appl. Phys. Express* **13** (2020) 085505.
- [3] X. Gonze *et al.*, *Computer Phys. Comm.* **248** (2020) 107042.
- [4] J. Wiktor *et al.*, *Phys. Rev. B* **92** (2015) 125113.
- [5] R. Krause-Rehberg and H. S. Leipner, *Positron Annihilation in Semiconductors: Defect Studies* Chap. 3 (Springer, Berlin, 2010),.

BL1U

In-situ Observation of Oxygen Vacancy in CeO₂ Using Gamma-ray Induced Positron Annihilation Spectroscopy

S. Dohshi¹, H. Toyokawa², K. Maeda¹, Y. Taira³ and T. Hirade⁴¹Osaka Research Institute of Industrial Science and Technology, Izumi 594-1157, Japan²National Institute of Advanced Industrial Science and Technology, Tsukuba 305-8568, Japan³UVSOR Synchrotron Facility, Institute for Molecular Science, Okazaki 444-8585, Japan⁴Japan Atomic Energy Agency, Tokai-mura 319-1195, Japan

CeO₂ has been extensively studied as a heterogeneous catalyst for automotive exhaust gas purification, CO oxidation, and VOC oxidation reactions. Such catalytic activity of CeO₂ is due to the redox property of Ce⁴⁺/Ce³⁺ and the associated formation of oxygen vacancies. Recently, it is reported that the existence of oxygen vacancies, especially oxygen vacancy clusters of CeO₂ surface is a key role for the oxidation reactions with molecular oxygen as an oxidant. The gaseous oxygen can be adsorbed and activated on the oxygen vacancy clusters of CeO₂ surface, resulting in the formation of active oxygen species and high catalytic activity [1].

On the other hand, positron annihilation spectroscopy (PAS) is a well-known method to detect lattice defects with high sensitivity. Among positron annihilation spectroscopy, gamma-ray induced positron annihilation spectroscopy (Gi-PAS) is an ultimate method to have the following features. 1) Since positrons could be generated inside a sample and observe their annihilation process, making it possible to perform measurements under harsh conditions such as high temperatures and/or high pressures. 2) In addition, the positron lifetime spectrum does not include the source component, which allows for detailed discussion of a positron lifetime [2].

In this study, we performed in-situ observation of oxygen vacancies in CeO₂ at a high temperature using Gi-PAS.

We have set up a gamma-ray spectroscopy system at the laser-Compton scattering (LCS) beamline of BL1U at UVSOR-III [3], and measured the lifetime of the annihilation gamma-rays at room temperature and 300 °C using BaF₂ scintillation detector. We used the software Lifetime9 (LT9) to analyze the spectra.

Figure 1 shows the positron annihilation lifetime spectra of CeO₂ measured at room temperature and 300 °C. The positron annihilation lifetime and relative intensity analyzed using LT9 are also listed in Table 1. The lifetime of the positron annihilation is able to give information about the size, type and relative concentration of defects/vacancies. The positron annihilation lifetime spectra of CeO₂ at room temperature and 300 °C yielded two distinct lifetime components, τ_1 and τ_2 with relative intensities I_1 ($I_1 = 100 - I_2$) and I_2 . At both temperatures, the lifetimes (τ_1 and τ_2) were almost the same, however the relative intensities (I_1 and I_2) were different: I_2 for 300 °C was larger than that for room temperature. Wang *et al.*

reported that molecular oxygen adsorbed on the oxygen vacancy clusters of CeO₂ surface desorbed at around 150 °C and lattice oxygen atoms of CeO₂ surfaces desorbed at around 450 °C [4]. Taking into this consideration, the result obtained in this study, i.e., the larger I_2 at 300 °C, is considered to be due to the desorption of oxygen molecules adsorbed on the oxygen vacancy clusters on the CeO₂ surface. In the next fiscal year, we will investigate the temperature and atmosphere dependence about the behavior of the oxygen vacancies of CeO₂ surface in detail.

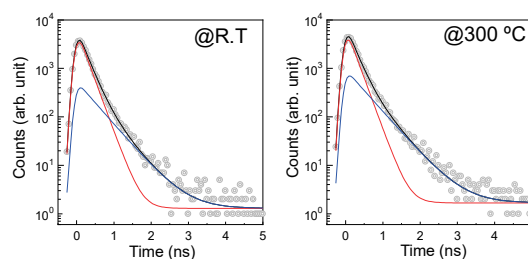


Fig. 1. Positron annihilation lifetime spectra of CeO₂ measured at room temperature and 300 °C

Table 1 Positron annihilation lifetime and relative intensity of CeO₂.

Temp.	τ_1 (ps)	τ_2 (ps)	I_2 (%)
R.T.	206.5 ± 1.7	489.0 ± 14	17.1 ± 3.0
300 °C	204.0 ± 3.3	490.0 ± 8.8	25.5 ± 1.0

- [1] X. Liu *et al.*, J. Am. Chem. Soc. **131** (2009) 3140.
 [2] H. Toyokawa *et al.*, Proc. AccApp'07 (2007) 331.
 [3] Y. Taira *et al.*, Rev. Sci. Instr. **84** (2013) 053305.
 [4] L. Wang *et al.*, Catal. Sci. Technol. **6** (2016) 4840.

BL1B

Existence of Shallow Donor in Mg₂Si Crystals Revealed by Terahertz Absorption Spectroscopy

M. Kitaura¹, M. Fujimoto^{2,3}, H. Uono⁴, S. Watanabe⁵ and A. Ohnishi¹

¹Faculty of Science, Yamagata University, Yamagata 990-4560, Japan

²UVSOR Synchrotron Facility, Institute for Molecular Science, Okazaki 444-8585, Japan

³The Graduate University for Advanced Studies, SOKENDAI, Okazaki 444-8585, Japan

⁴Department of Electrical and Electronics System Engineering, Ibaraki University, Mito 310-8512, Japan

⁵Institute of Innovative Research, Tokyo Institute of Technology, Tokyo 152-8550, Japan

Magnesium silicide (Mg₂Si) is known to be a semiconductor which has the fundamental absorption of an indirect transition type. The fundamental absorption edge locates at around 0.6 eV. Because Mg₂Si can responds to the infrared (IR) light with photon energies above 0.61 eV, this material is expected to be a plausible candidate for the application of an IR photodetector. Mg₂Si shows n-type conductivity without incorporating impurities. This is because an interstitial Mg atom at the 4b site works as an intrinsic donor [1]. Electrical properties of Mg₂Si crystals have been reported so far [2]. The existence of shallow donors with the activation energy of 8-9 meV was suggested in Mg₂Si crystals with the carrier density of 10¹⁵ cm⁻³ order. Although the Mg₂Si crystals were grown from high purity Mg and Si sources, they contained various impurities. Thus, it still remains unclear whether such shallow donors are associated with interstitial Mg atoms. Terahertz absorption spectroscopy is an experimental technique to explore the existence of shallow donors in solids. Practically, the existence of shallow donors in Si crystals has been found so far [3]. In the present study, we have carried out terahertz absorption spectroscopy for undoped Mg₂Si crystals to find the existence of shallow donors.

Mg₂Si crystals were grown from high-temperature melt in Ar atmosphere by a vertical Bridgeman furnace. Experiment was performed at the beamline BL1B. The carrier concentration of the sample used in this work was determined to be 4.3×10¹⁵ cm⁻³ by a Hall-effect measurement. The terahertz absorption spectra of an undoped Mg₂Si crystal is shown in Fig. 1. The data were obtained at 5 K. Two prominent peaks appear at 58 and 66 cm⁻¹. These peaks were weakened under irradiation with 800 nm photons from a Ti:Sa laser. Furthermore, the two peaks were weakened with increasing temperature, and disappeared around 20 K. The temperature dependence of the two peaks was analyzed by assuming a simple model that a donor creates a conduction electron. The activation energy for the donor originating in the two peaks was 7-8 meV, in good agreement with that determined from the temperature dependence of the carrier concentration [2]. It is therefore reasonable to assign the origin of the two peaks to shallow donors in Mg₂Si. The weakening of the two peaks by photoirradiation result is explained as photoionization of shallow donors. Now, we are

investigating experimentally and theoretically whether such shallow donors are formed by interstitial Mg atoms.

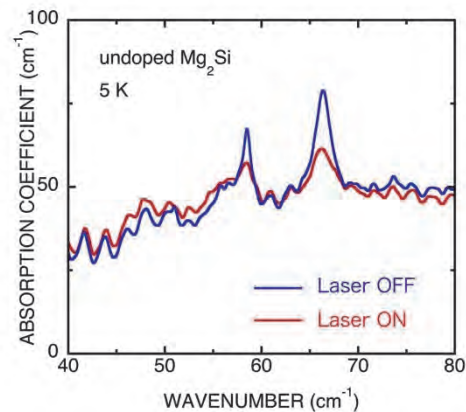


Fig. 1 Terahertz absorption spectra of an undoped Mg₂Si crystal, measured at 5 K under non-irradiation (blue) and irradiation (red) with 800 nm photons from a Ti:Sa laser.

[1] A. Kato *et al.*, *J. Phys.: Condens. Matter* **21** (2009) 205801.

[2] H. Uono *et al.*, *Jpn. J. Appl. Phys.* **54** (2015) 07JB06.

[3] A. Hara *et al.*, *Jpn. J. Appl. Phys.* **49** (2010) 050203.

BL1B

Electron-Irradiation Effects on Germanium

A. Hara and T. Awano

Faculty of Engineering, Tohoku Gakuin University, Tagajo 985-8537, Japan

Polycrystalline germanium (poly-Ge) is attractive as a material for three-dimensional integrated circuits owing to its high mobilities for both electrons and holes and its lower melting temperature than Si at approximately 450 °C. However, a large number of holes are generated in poly-Ge film because of crystal defects; hence, identification of the origin of the acceptors in poly-Ge is an important consideration.

As Ge has a high dielectric constant, the energy levels of the acceptors are expected to be shallow in Ge, similar to other group-III impurities; hence, the BL1B line of UVSOR is suitable for detecting defects attributable to the acceptors. In our previous research, we used electron irradiation (e-irradiation) to introduce vacancies and self-interstitials in bulk p-type [Indium (In)-doped] Ge samples of 2.0 mm thickness and 12 $\Omega\cdot\text{cm}$ resistivity; we observed that e-irradiation introduces donors that are eliminated at temperatures of 400 °C [1]. However, the main peaks (lines C and D [2, 3]) of the In acceptor were saturated owing to the high In concentration. Thus, we used the satellite peak referred to as line G to obtain the above results [1].

In the present work, we used low-In-content bulk Ge samples (33 $\Omega\cdot\text{cm}$) and high e-irradiation of 4.5 MeV and 6×10^{15} cm^{-2} . Following this, the samples were annealed at 100, 200, 300, and 400 °C for 30 min in a conventional furnace system to evaluate the changes to the spectra. The optical transmission spectra were measured at liquid He temperature using BL1B.

Figure 1 shows the spectra of as-grown and as-e-irradiated samples, along with samples annealed at 100, 200, 300, and 400 °C. The intensities of the lines corresponding to the In acceptor (lines C and D) decreased after e-irradiation, but began recovering to those of the as-grown sample when the annealing temperature increased to 400 °C. Figure 2 shows the variations in the peak intensities of lines C and G, which were normalized by those of as-grown Ge. Variation in the intensity of line G was obtained from the experimental results of Ref. [1], which indicates that e-irradiation introduces donor defects but eliminates at 400 °C.

In general, it is believed that e-irradiation introduces simple structural defects, such as vacancies, self-interstitials, and their aggregates. However, acceptors are generated in poly-Ge thin films crystallized at 500 °C. The difference in thermal stability between the e-irradiation-induced defects and acceptors in poly-Ge indicates that the acceptors in poly-Ge films are not simple defects, such as those introduced by e-irradiation.

In summary, the optical transmission spectra of e-irradiated Ge were measured at liquid He temperatures, and it was observed that e-irradiation generates donors

that are eliminated at temperatures of 400 °C. The difference in thermal stability between the e-irradiation defects and acceptors in poly-Ge thin films clearly indicates that the origins of these two types of defects are different.

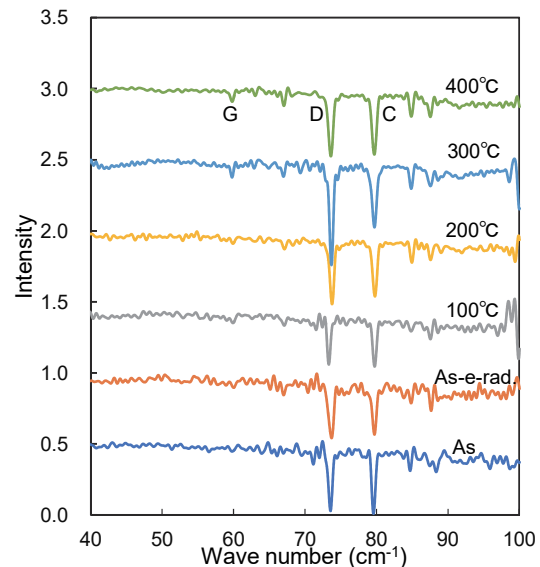


Fig. 1. Transmission spectra of e-irradiated p-type Ge

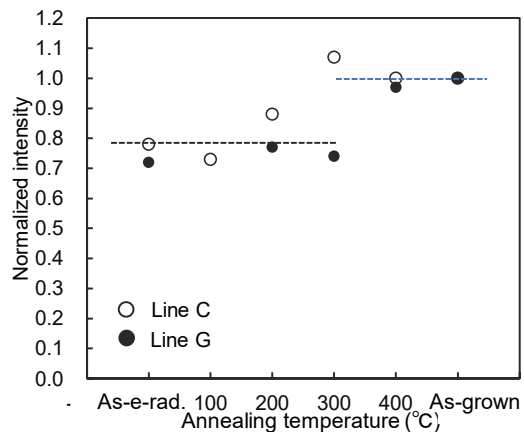


Fig. 2. Annealing dependencies of lines C and G. The plot of line G was obtained from Ref. [1].

[1] A. Hara and T. Awano, UVSOR activity report 2019 **47** (2020) 48.

[2] R. L. Jones and P. Fisher, *J. Phys. Chem. Solids* **26** (1965) 1125.

[3] W. Kohn, in *Solid State Physics*, ed. F. Seitz and D. Turnbull (Academic Press, New York, 1957) Vol. **5**, p. 257.

BL2A

Formation of Catalytically Active MoC_x Species during Methane Dehydroaromatization over Mo-V Co-Modified H-MFI Zeolites

K. Kuramochi¹, R. Yamazaki¹, Y. Nozawa², Y. Sonobe³ and H. Aritani^{2,3}

¹Advanced Science Research Laboratory, Saitama Institute of Technology, Fukaya 369-0293, Japan

²Graduate School of Engineering, Saitama Institute of Technology, Fukaya 369-0293, Japan

³Faculty of Engineering, Saitama Institute of Technology, Fukaya 369-0293, Japan

A Molybdenum-modified H-MFI zeolite (Mo/ H-MFI) catalyst is a typical GTL (Gas To Liquid) catalyst for methane dehydroaromatization. The reaction so-called MTB (Methane To Benzene) one is valuable for direct conversion from natural gases to useful petroleum compounds. Over the Mo/H-MFI catalysts, definite deactivation due to coke deposition has been a serious problem for enhancement of MTB reactivity, and thus, clarification of the deactivation process over the catalysts is one of the important points. A cause of the deactivation is based on coke deposition on strong acid sites over H-MFI and structural deactivation on carbonized Mo species. Thus, clarification of active Mo sites with high and durable activity for methane dehydrogenation is one of the most important subjects. In the present study, Mo L_{III}-edge XANES is applied to characterize the active Mo-carbide species on Mo/H-MFI and Mo-V co-modified H-MFI.

Mo(5wt%)/H-MFI and Mo-V/H-MFI (Mo/V=10) catalysts were prepared by impregnation of H-MFI, and followed by drying overnight and calcination at 773 K. The methane dehydroaromatization reactivity was evaluated at 1023 K as described in a previous report.[1, 2] Mo L_{III}-edge XANES spectra were obtained in BL2A of UVSOR-IMS in a total-electron yield mode using InSb double-crystal monochromator. REX-2000 (Rigaku) software were used for normalization of each XANES spectra.

For L-edge XANES spectra over Mo/H-MFI catalysts (on time course of the MTB reaction) as shown in Fig. 1, the active Mo species in both Mo/H-MFI and Mo-V/H-MFI are due to more deeply carbonized species than α -Mo₂C. It suggests the formation of MoC_x ($x > 0.5$) as an important species for high MTB reactivity. By Mo-V co-modification on H-MFI, the carbonization to form active MoC_x species became faster. It indicates the formation of easily reduced Mo sites to form deeply carbonized species. For 185 minutes on the MTB reaction (during the deactivation), excess carbonization was inhibited by V co-modification as exhibited in the edge energy shown in Table 1. The result is likely to relate to a suppression effect of deactivation.

[1] H. Aritani *et al.*, UVSOR Activity Report 2018 46 (2019) 49.

[2] H. Aritani *et al.*, UVSOR Activity Report 2017 45 (2018) 44.

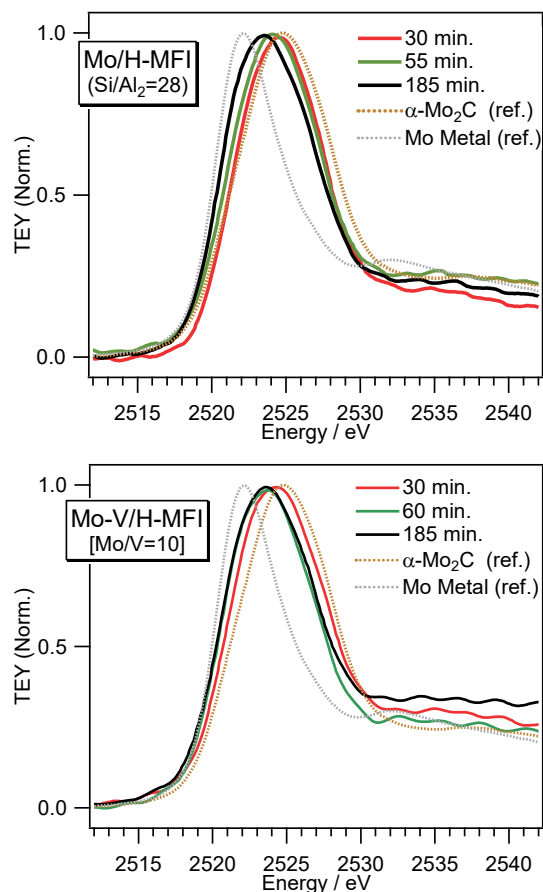


Fig. 1. Mo L_{III}-edge XANES spectra of Mo/H-MFI (Si/Al₂=28) and Mo-V/H-MFI (Mo/V=10) catalysts after methane dehydroaromatization at 1023 K for 30 – 185 min. The references, α -Mo₂C and Mo metal, are also shown in each figure.

Table 1. Edge energy values obtained by 1st derivatives of L_{III}-edge XANES shown in Fig. 1.

Mo/H-MFI(28)		Mo-V/H-MFI (Mo/V=10)	
Time on Stream / min.	Edge Energy / eV	Time on Stream / min.	Edge Energy / eV
30	2521.36	30	2520.96
55	2520.86	55	2520.86
185	2520.48	185	2520.60
α-Mo₂C	2520.96	α-Mo₂C	2520.96
Mo Metal	2520.22	Mo Metal	2520.22

BL2A

Local Environment of Heat Treated Ag-Doped PHI-Type Zeolite

H. Murata, Y. Minami and A. Nakahira

Department of Materials Science, Osaka Prefecture University, Sakai 599–8531, Japan.

Zeolites are crystalline aluminosilicates which have nano-sized cavities in their crystal structures. Zeolite frameworks were classified into over 250 types by the international zeolite associations. [1] They have cation-exchange abilities due to their unique crystal structures. Ag-doped zeolites have attracted many researchers as rare-earth free phosphors. [2] They were prepared by ion-exchange in Ag^+ aqueous solution and subsequent heat-treatments. In these processes, Ag nano-clusters were formed in zeolitic cavities and behave as luminescent center. In addition, some Ag-doped zeolites are not stable at high temperature and become amorphous phases. [3]

In the present study, we investigated local environments of heat-treated Ag-doped PHI-type zeolite (Ag-PHI) using X-ray absorption near edge structure (XANES).

Ag-PHI samples were synthesized by ion-exchange and subsequent heat treatments. PHI-type zeolite was prepared by a hydrothermal method. The starting material was soaked in 0.1 mol/L of $\text{Ag}(\text{NO}_3)_2$ aqueous solution for 1 h under dark condition. The samples were washed by ion-exchanged water and dried at 50 °C in air. Then, they were heated at 450 °C and 700 °C for 4 h.

XANES spectra were collected by the partial fluorescent yield method using a silicon drift detector at BL2A in UVSOR. Fluorescence X-ray spectra were deconvoluted using gauss functions, which was reported elsewhere. [4] X-ray beam was monochromated by KTP double crystals for Al-K and InSb ones for Si-K and Ag- L_3 .

X-ray diffraction (XRD) patterns of the Ag-PHI heated at 450 °C have same features to the starting material. On the other hand, the samples heated at 700 °C gave amorphous pattern. No Ag compound were observed. It is noted that Ag nano-particles were not observed by scanning electron microscope either.

Al-K and Si-K XANES were measured in order to investigate the structure of the amorphous samples. The samples heated at 700 °C have the similar features to those of PHI-type zeolite and Ag-PHI heated at 450 °C. The features were different from those of typical glasses. These results indicated that samples heated at 700 °C were not a mere glass, but partially collapsed zeolite.

Figure 1 shows Ag- L_3 XANES of the Ag-PHI samples. The samples heated at 450 °C and 700 °C have same features. Their spectra were different from those of typical Ag compounds while the absorption edge of the samples agrees that of Ag foil. These results indicated that Ag in the samples were metallic, but it has different local environment from bulk Ag metal. They

were still maintained in the partially collapsed zeolites. It has been reported that some Ag-doped zeolite phosphors are affected by humidity. [5] Our results lead to new phosphors stable in air since partially collapsed zeolite lost continuous pores.

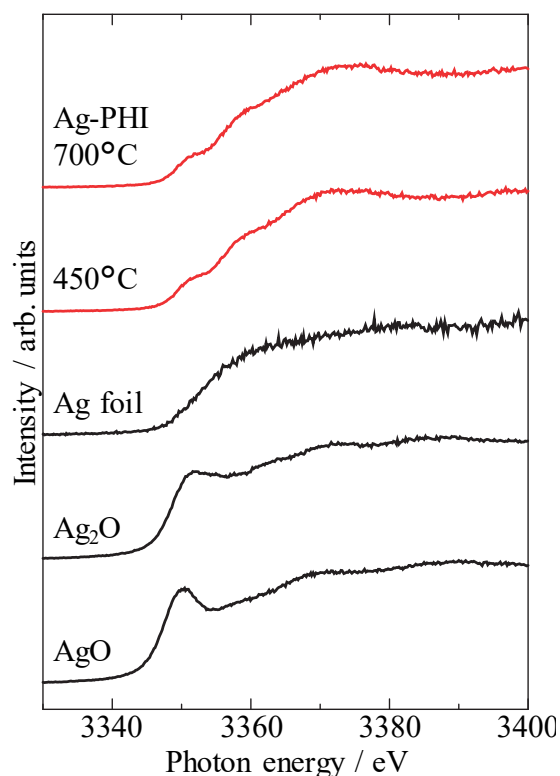


Fig. 1. Ag- L_3 XANES of Ag-doped PHI samples and references.

[1] C. Baerlocher and L.B. McCusker, *Database of Zeolite Structures*,

<http://www.iza-structure.org/databases/>

[2] D. Grandjean *et al.*, *Science* **361** (2018) 686.

[3] H. Aono *et al.*, *J. Ceram. Soc. Jpn.* **124** (2016) 82.

[4] H. Murata, *UVSOR Activity Report 2018* **46** (2019) 53.

[5] E. Coutino-Gonzalez *et al.*, *J. Vis. Exp.* **117** (2016) e54674.

BL2A

Local Structure Investigations of $\text{Mg}_{1-x}\text{Ni}_x\text{Al}_2\text{O}_4$ by NEXAFS

S. Yoshioka¹, K. Yasuda¹, S. Matsumura¹, E. Kobayashi² and K. Okudaira³

¹Department of Applied Quantum Physics and Nuclear Engineering, Kyushu University, Fukuoka 819-0395, Japan

²Kyushu Synchrotron Light Research Center, Tosu 841-0005, Japan

³Graduate school of Advanced Integration Science, Chiba University, Chiba 263-8522, Japan

Spinel oxides with the general formula AB_2O_4 can be formed with various kinds of divalent A and trivalent B cations. Owing to their unique mechanical, electronic, and magnetic properties, the spinel oxides have gained considerable attention not only from the fundamental research fields but also from the industrial application point of view. Some spinel compounds accommodate a large degree of cationic disorder. The cationic disordering naturally affects the structural properties of the spinels. For example, magnesium aluminate (MgAl_2O_4) and nickel aluminate (NiAl_2O_4) spinels are generally known as normal and inverse spinel structures, respectively. However, their inversion degrees for synthetic specimens were also reported to be fluctuating between 0 and 1, respectively, due to the cationic disordering. Recently, the structure of $\text{Mg}_{1-x}\text{Ni}_x\text{Al}_2\text{O}_4$ was reported using neutron total scattering to understand the cationic disordering process [1]. X-ray absorption spectroscopy (XAS) is a powerful structure characterization method that uses an X-ray probe to reveal local atomic coordination and electronic structures. In this study, we focus on the local structures in MgAl_2O_4 – NiAl_2O_4 solid solutions, particularly cationic-disordered structures.

The polycrystalline samples of $\text{Mg}_{1-x}\text{Ni}_x\text{Al}_2\text{O}_4$ ($x = 0.0, 0.05, 0.2, 0.5, 0.8, 1.0$) were synthesized by a solid-state reaction. They were sintered in air at 1300 °C for 10 h followed by furnace. Mg and Al *K*-edge XANES measurements were performed on BL2A beamline at UVSOR Synchrotron Facility, Okazaki, Japan, using the partial fluorescence yield method. A KTiOPO_4 double-crystal monochromator gives Mg and Al *K*-absorption edges in the energy regions 1290 – 1340 eV and 1540 – 1610 eV, respectively. The measurements of Mg and Al *K*-edge XANES spectra were carried out in vacuum at a pressure and temperature of 1×10^{-4} Pa and 20 °C, respectively. Fluorescence X-rays of Mg K_α and Al K_α were collected utilizing an energy-dispersible silicon drift detector.

The Al *K*-edge XANES spectra for $\text{Mg}_{1-x}\text{Ni}_x\text{Al}_2\text{O}_4$ are shown in Fig. 1 with the composition values $x = 0, 0.05, 0.2, 0.5, 0.8,$ and 1.0 . The intensity of each spectrum was normalized to a value of 1 at the photon energy of 1588 eV after the removal of the background intensity. The spectral shapes of the Al *K*-edge XANES clearly changed depending on the Ni content x in $\text{Mg}_{1-x}\text{Ni}_x\text{Al}_2\text{O}_4$. It is seen that the identical peak appeared at the absorption edge as indicated by an arrow in Fig. 1, and its intensity increased with the increasing x . Alternatively, in the higher energy region, the large peak at 1579 eV broadened with the increasing x or Ni content. Such spectral changes suggest

that the Al at tetrahedral sites increased with increasing Ni concentrations instead of Al at octahedral sites.

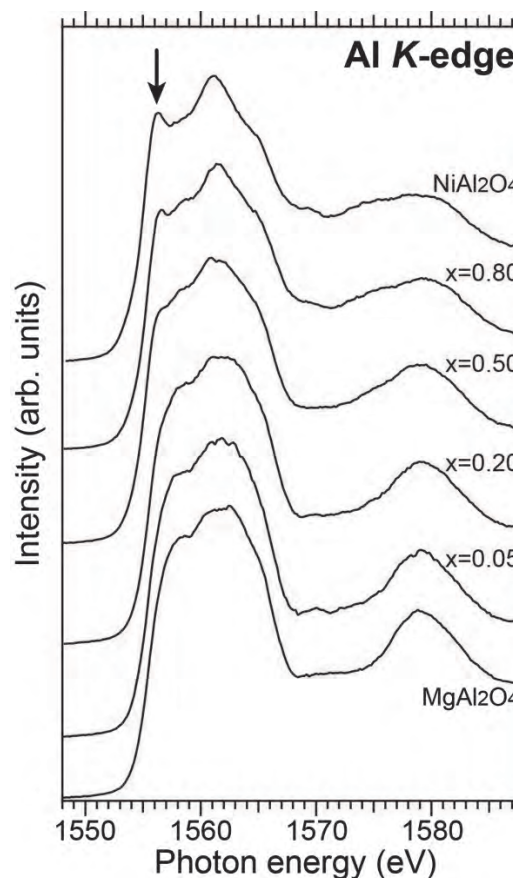


Fig. 1. Al *K*-edge XANES spectra of $\text{Mg}_{1-x}\text{Ni}_x\text{Al}_2\text{O}_4$.

[1] E. O'Quinn *et al.*, *J. Am. Chem. Soc.* **139** (2017) 10395.

BL2A

X-ray Absorption Fine Structure Measurements of Sulphur Chain Encapsulated in Carbon Nanotubes

H. Ikemoto¹ and T. Miyanaga²¹Department of Physics, University of Toyama, Toyama 930-8555, Japan² Department of Mathematics and Physics, Hirosaki University, Hirosaki 036-8561, Japan.

Chalcogen atoms are bonded with two-fold covalent bonds, and form rings or chains. They bind each other with inter-ring or inter-chain interactions. The chalcogen atoms form isolated chains within narrow space, such as, carbon nanotube, morodenite, and so on [1-3]. In this study, we are studying structure of sulfur chain in the CNT (S@CNT) with X-ray absorption fine structure (XAFS) measurements.

The XAFS measurements of crystalline S (c-S) and S@CNT were done at BL2A in UVSOR with total electron yield and SDD detectors. Intensity of incident X-ray were observed with Au or Cu meshes. Figure 1 shows spectrum of S@CNT with Au mesh. A sharp white line of S K-edge and XAFS oscillations were observed. Unfortunately, steps were observed around 2.5 and 2.9 keV. The steps may be brought about by monitoring of the intensity of the incident X-ray with Au mesh.

Figure 2 shows extended X-ray absorption fine structure (EXAFS) oscillations reduced from the spectrum of Fig. 1 with miXAFS code [4]. EXAFS oscillation is obtained. It contains steps around 8.5 and 11.5 Å⁻¹, which correspond with the steps of Fig. 1.

Figure 3 shows Fourier transform of EXAFS oscillation to account for backscattering form factor, phase shift calculated with FEFF code. There is a main peak around 2.0 Å, which is close to the covalent bond length of c-S. The position of the peak coincident with the covalent bond length of c-S. However, it is necessary to verify whether the peak position is coincidental because the correct EXAFS function is obtained, or whether they coincide by chance.

The EXAFS spectra were obtained, but the qualities were not sufficient for the EXAFS analysis to obtain the structural parameters, such as, interatomic distances, coordination numbers, and so on. To obtain the structure parameters of S@CNT much improvements may be required, such as, monitoring of the intensity of the incident X-ray, increment of the intensity above 3.0 keV.

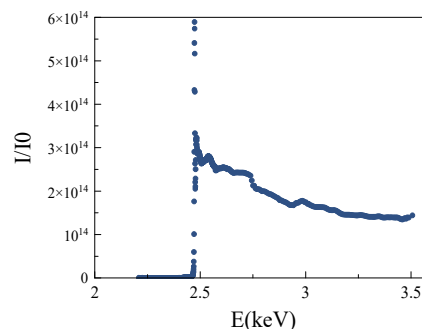


Fig. 1. Spectrum of S K-edge for S@CNT.

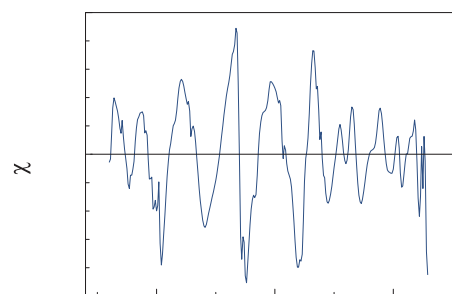


Fig. 2. EXAFS oscillation of S@CNT.

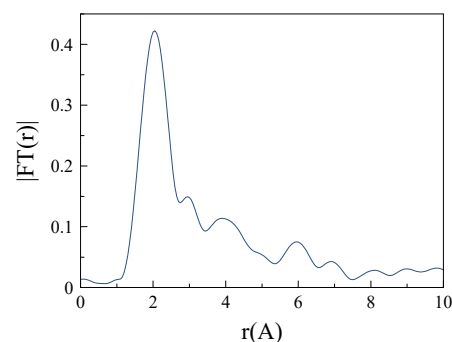


Fig. 3. Fourier transform of EXAFS oscillation of S@CNT.

- [1] T. Fujimori *et al.*, ACS Nano **7** (2013) 5607.
- [2] M. Inui *et al.*, J. Phys. Soc. Jpn. **57** (1988) 553.
- [3] H. Ikemoto *et al.*, J. Phys. Chem. C **124** (2020) 26043.
- [4] H. Ikemoto, J. Synchrotron Rad. **25** (2018) 61.

BL3U

First Trial of Precise Analysis of Super-structures of Chiral Smectic Liquid Crystals by Resonant Soft X-ray Scattering (RSoXS) at UVSOR

Y. Takanishi¹, F. Araoka² and H. Iwayama^{3,4}¹Faculty of Science, Kyoto University, Kyoto 606-8502, Japan²RIKEN Center for Emergent Matter Science, Wako 351-0198, Japan³UVSOR Synchrotron Facility, Institute for Molecular Science, Okazaki 444-8585, Japan⁴School of Physical Sciences, The Graduate University for Advanced Studies, SOKENDAI, Okazaki 444-8585, Japan

Smectic liquid crystals have one-dimensional positional order, so-called layer structures. In particular, chiral tilted chiral smectic phases have attracted much attention because molecular clinicity in neighboring layers influence the macroscopic polarity; ferroelectric and antiferroelectric order appears in synclinic and anticlinic structures, respectively. Furthermore, the successive phase transition between synclinic SmC* and anticlinic SmCA* is one of the most interesting subjects, in which the appearance of some subphases due to the competition between SmC* and SmCA* has been experimentally determined and the existence of further subphases has been theoretically predicted based on the long-range interlayer interaction and the frustration of clinicity (synclinic or anticlinic). Conventional X-ray diffraction is a powerful tool for studying the layer structure, but difficult to distinguish the difference of the clinicity because the electron density along the layer normal of left and right tilting molecules are the same.

This subject was resolved by resonant X-ray scattering. In this technique, by using X-ray whose energy is coincident with a certain atom absorption edge, the structure factor becomes a tensor instead of the scalar in conventional X-ray diffraction. As a result, scattering intensity is sensitive for the system symmetry, and also molecular orientation. In this technique, the structure analysis of tilted chiral phase has dramatically evolved. So far, however, sample compounds have to possess an atom with the same absorption energy as the used X-ray, and such atoms as sulphur, selenium, chlorine and bromine. Recently, carbon K edge resonant scattering has been applied to study, and successful in obtaining the precise structures of polymer blends, block copolymer, and liquid crystals. Hence this time we tried to perform this technique, and to investigate the precise structures of chiral liquid crystals.

The experiment was performed at BL3U of UVSOR (Okazaki). For the measurement, a new vacuum chamber was created, as shown in Fig. 1. Liquid crystals was filled in the isotropic phase between two pieces of 100 nm-thick Si₃N₄ membranes (NTT-AT). The scattering was detected by CCD (ANDOR DO940P-BN). Incident X-ray beam was tuned between 270~300 eV. Typical absorption spectrum was shown in inset of Fig. 1; in this compound, carbon K-edge energy is 286 eV.

Figure 2 shows the first obtained results of RSoXS. When the incident energy E_0 is 285 eV(a), clear scattering

peaks are observed at wider angle, while these peaks disappear at $E_0=270$ eV. Center position of two peaks just corresponds to twice of the fundamental layer spacing of this chiral smectic SmCA* phase, which proves the anticlinic bilayer structure. Furthermore, two resonant peaks comes from the macroscopic helical structure of SmCA*, and splitting width corresponds to ca. 250 nm, which is coincident with the obtained helical pitch from the optical measurement.

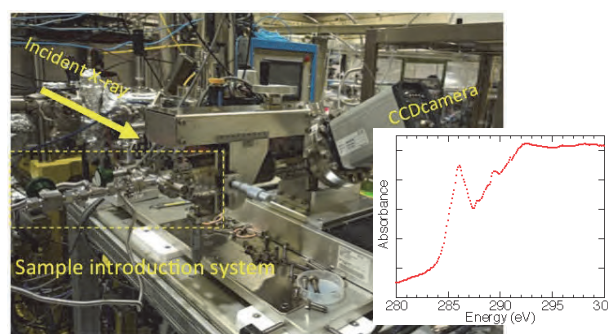


Fig. 1. Photo of experimental setup & absorption spectrum of chiral liquid crystals.

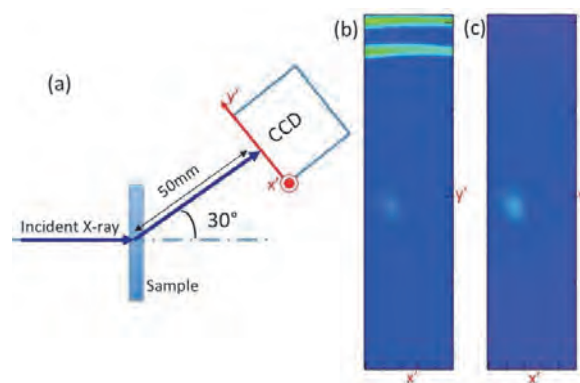


Fig. 2. Schematic image of experimental geometry(a), and obtained 2D scattering image at $E_0=285$ eV(on resonance) (b) and $E_0=270$ eV(off resonance)(c).

BL3B

Intrinsic Luminescence from Self-trapped Excitons in BaMBe₂(BO₃)₂F₂ (M=Mg,Ca) Crystals with Two-dimensional Single Layers upon VUV Excitation

N. Kodama and T. Takahashi

Faculty of Engineering and Resource Science, Akita University, Akita 010-8502, Japan

Mixed anion compounds have gained increasing attention recently from the point of view of their increased degree of freedom regarding parameters such as electric charge, electronegativity, polarizability, and orbital energy, arising from the coordinated anions. The formation energy and luminescence properties of excitons are considered to depend on the degree of two-dimensionality or two-dimensional modulation. To date, very little research has focused on the formation of self-trapped excitons (STEs) in terms of the dimensionality and modulation of the structure. Fluorine-beryllium borates BaMBe₂(BO₃)₂F₂ (M = Mg, Ca) have a layered structure which consists of flexible two-dimensional [Be₃B₃O₆F₃]_∞ single layers. [1] We examined the correlation between the intrinsic luminescence intensity and the degree of two-dimensionality in BaCaBe₂(BO₃)₂F₂ (BCBF) and BaMgBe₂(BO₃)₂F₂ (BMBF) crystals. We discuss the structural correlation of the intrinsic luminescence intensity from STEs.

Under VUV excitation at 50 and 160 nm, intrinsic luminescence from STEs was observed in these crystals. The excitation spectral intensity for BCBF and BMBF increased rapidly below about 180-200 nm. These observations support the conclusion that the luminescence band originates from STE formed by band-gap excitations, or to molecular transitions in the BO₃³⁻ group.

Figures 1(a) and 1(b) show the luminescence spectra for BCBF and BMBF excited at 160 nm in the range of 13-293 K. One luminescence band with a peak at 305-340 nm associated with STE appears for BCBF, and the corresponding peak appears at 310-320 nm for BMBF. In BCBF, the STE intensity decreases gradually from 13 K to 193 K. The BMBF crystal exhibited an STE intensity that increased gradually as the temperature increased to 125 K, above which the intensity decreased. These decreases in the intensity of STE luminescence likely resulted from a thermal quenching process. The peaks of the STE emission band in the two samples shifted to slightly shorter wavelengths with increasing temperature from 13 to 293 K.

Figure 2 shows the luminescence spectra for BCBF and BMBF excited at 160 nm at 13 K. The dependence of the intensity and bandwidth of the intrinsic luminescence on the substitutional effects of Ca²⁺ for Mg²⁺ was examined for these crystals. As an example, Fig. 2 shows the luminescence spectra for BCBF and BMBF excited at 160 nm in the range of 13 K. We found the intensity of the STE for BCBF to be greater than that for

BMBF under excitation at 160 nm as seen in Fig. 2. The same is true for luminescence under excitation at 50 nm. There are two plausible explanations for the dependence of luminescence intensity on the Ca²⁺-substitution for Mg²⁺, involving (i) a two-dimensional effect or (ii) an incommensurate structural modulation effect. The magnitude of two-dimensionality is defined as the ratio of the interlayer distance to the intralayer distance. Here, the magnitude of two-dimensionality can be expressed by the *c/a* axis ratio. The magnitude of two-dimensionality for BCBF with *c/a* ratio of 3.42 is higher than that for BMBF with the *c/a* ratio of 3.34, with the increase being due to the larger ionic radius of Ca²⁺ than of Mg²⁺. Taking into account the above result, the dependence of the STE intensity on Ca²⁺ substitution can be explained in terms of a two-dimensional effect. The other possible explanation is that the structural modulation effect increases the number of local sites with larger distortion potentials. These structural changes would result in broadening of the luminescence. This possibility is unlikely because there is no significant difference in the STE bandwidth between the BCBF and BMBF crystals.

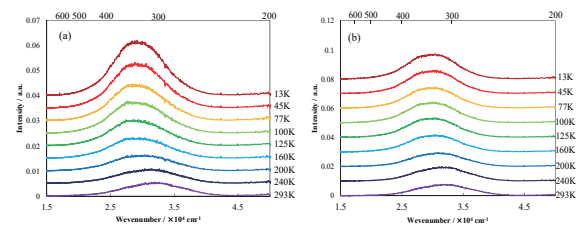


Fig. 1. Temperature dependence of luminescence spectra of (a) BaCaBe₂(BO₃)₂F₂ and (b) BaMgBe₂(BO₃)₂F₂ excited at 50 nm in the range of 13-293 K.

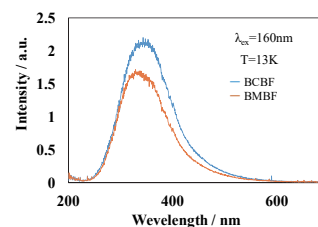


Fig. 2. The luminescence spectra for BaCaBe₂(BO₃)₂F₂ and BaMgBe₂(BO₃)₂F₂ excited at 160 nm at 13 K.

[1] S.Guo, X.Jiang, M.Xia, L.Liu, Z.Fang, Q.Huang, R. Wu, X. Wang, Z. Lin, C. Chen, *Inor. Chem.Phys.* **56** (2017) 11451.

BL3B

Intrinsic Nature of Luminescence Bands for undoped and Sn doped β -Ga₂O₃ Crystals

R. Tarukawa¹, M. Kitaura¹, K. Miki², A. Ohnishi¹, K. Sasaki³ and A. Kuramata³

¹Faculty of Science, Yamagata University, Yamagata 990-8560, Japan

²Graduate School of Engineering, University of Hyogo, Himeji 671-2280, Japan

³Novel Crystal Technology Inc., Sayama 350-1328, Japan

β -Ga₂O₃ is a wide-gap semiconductor with the band-gap of 4.8 eV. Tetravalent cations doping causes the n-type conductivity in β -Ga₂O₃. The electric properties are changed by high-temperature annealing under various atmospheres. The high-temperature annealing under nitrogen atmosphere (nitrogen annealing) remarkably lowers the electrical resistance of β -Ga₂O₃, resulting in high electrical conductivity. The oxygen annealing keeps the electric insulation with high electrical resistance. Because high-temperature annealing varies lattice defects, it is likely that the change in electrical resistance of β -Ga₂O₃ is caused by the interaction of tetravalent cations with lattice defects. Such lattice defects influence luminescence properties of β -Ga₂O₃. So far, there are many studies on luminescence properties of β -Ga₂O₃. Luminescence spectra exhibited a prominent band at around 400 nm. Bient *et al.* were assigned the 400 nm band to an intrinsic nature due to radiative annihilation of relaxed excitons or radiative recombination between donor-acceptor pairs [1]. Usui *et al.* assigned the 400 nm band to an extrinsic origin associated with Sn 5s-5p transitions [2]. Thus, the nature of the 400 nm band still remains unclear.

In the present study, luminescence properties of undoped and Sn-doped β -Ga₂O₃ crystals were investigated at the BL3B beamline [3]. Here, an undoped crystal, and Sn-doped crystals annealed under oxygen and nitrogen atmosphere were named as #1, #2, and #3 samples, respectively. Figure 1 shows absorption spectra of #1-#3 samples, measured at 15 K. The absorption spectra exhibit a stepwise structure at around 260 nm, which corresponds to the indirect absorption edge of β -Ga₂O₃ crystals. Luminescence spectra of #1-#3 samples were measured at 15 K under excitation above the indirect absorption edge. The results are shown in Fig. 2. The photon energy was 200 nm. A prominent band appears at around 400 nm. A weak band is also observed at around 340 nm. These bands were effectively excited in the region above the indirect absorption edge. This feature indicates that the 340 and 400 nm bands are of intrinsic feature in β -Ga₂O₃ crystals. Other bands are seen in the long wavelength side of the 400 nm band. Because they were excited at the longer wavelength side than the indirect edge, they are attributed to extrinsic origins.

Luminescence spectra of #1-#3 samples were measured under two-photon excitation (TPE) with THG pulses from a Nd:YAG laser system. The TPE luminescence spectra of #1 and #2 samples exhibited the 340 and 400 nm bands. The intensities of the 340

and 400 nm bands increased in proportion to the square of the laser power. It is therefore concluded that the 340 and 400 nm bands are intrinsic origins in β -Ga₂O₃. Further experiments are needed to identify the origins of the 340 and 400 nm bands.

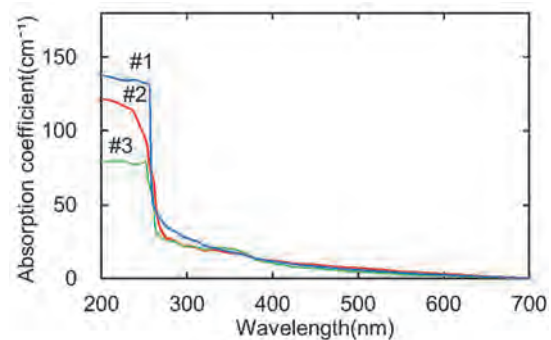


Fig. 1. Absorption spectra of #1-#3 samples, measured at 15 K.

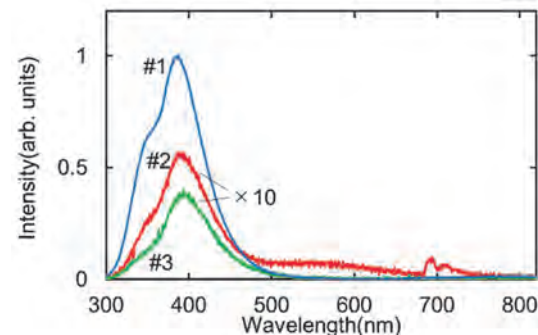


Fig. 2. Luminescence spectra of #1-#3 samples, measured at 15 K under excitation with 200 nm photons. The intensities for #2 and #3 samples were multiplied by 10.

- [1] L. Binet *et al.*, J. Phys. Chem Solid **59** (1998) 1241.
 [2] Y. Usui *et al.*, J. Phys. Chem Solid **117** (2018) 36.
 [3] K. Fukui *et al.*, J. Synchrotron Rad. **21** (2014) 452.

BL3B

Temperature Dependence of Ce-doped CaHfO₃ Crystals Synthesized by the Core Heating Method

Y. Kurashima¹, S. Kurosawa^{1,2} and A. Yamaji^{1,2}¹Institute for Materials Research, Tohoku University, Sendai 980-8577, Japan²New Industry Creation Hatchery Center, Tohoku University, Sendai 980-8579, Japan

High-melting-point oxides are frontier and attractive materials for scintillators with higher gamma-ray stopping power. Although the Skull-melting process is commercial use to grow such materials, growth time was too long to feedback the growth conditions or parameters in the research and development phase. Thus, we developed a novel crystal growth method, Core Heating (CH) method. In previous research, we reported the CH method is available for the material quick search [1, 2].

In this report, we focused on Ce-doped CaHfO₃ (Ce:CHO) as a first step of crystal growth of high melting point materials by the CH method. Ce:CHO has a melting point of 2440 °C, and higher gamma-ray stopping power than conventional scintillators such as Ce:(Lu,Y)₂SiO₅ because of the highly effective atomic number (65).

We succeeded in growing transparent (>50%) Ce:CHO samples by the CH method for the first time. The use of transparent samples is expected to determine the scintillation light output with more accuracy when compared to non-transparent samples such as ceramics.

Optical and radio photoluminescence spectra of Ce:CHO crystals were similar to the low transparency Ce:CHO samples or powders. However, the light outputs of our crystals were smaller than previous studies with that of 4,000-5,000 photons/MeV [3,4] at room temperature (RT).

One of the possible reasons for the low light output is the thermal quenching of Ce³⁺ 5d-4f emission in Ce:CHO at RT, so that we measured the temperature dependence (TD) of photoluminescence (PL) spectra of Ce:CHO at the UVSOR-III facility. TD of PL emission for the main emission band located at ~ 400 nm was measured with a CCD SPEC-10 (Roper Scientific) at the beamline BL3B operating in a multi-bunch mode. Additionally, the TD of PL decay times were also measured under the single-bunch mode.

Figure 1 shows the TD of emission intensity for Ce:CHO excited with 193 and 330-nm photons. Each emission intensity was calculated by integrating the emission spectra. The TD results showed different behavior clearly between two excitation energy; The emission intensity for Ce:CHO excited at 193 nm continuously increased from 150 to 300K, and decreased above 300K.

Figure 2 shows TD of PL decay times of Ce:CHO excited with 193 and 330-nm photons; The decay times of Ce:CHO excited 193 nm rapidly increased at 200 and 250K, while at over 300K, the times were

almost the same value as that at low temperature. Meanwhile, decay times excited at 330 nm were stable from 10 to 250K, and gently decreased above 250K.

These results of TDs suggested (i) thermal quenching of Ce³⁺ 5d-4f emission is not the main reason for the low scintillation light yield at RT, (ii) the sample had additional trap level(s) related to defect(s) corresponding to 200-300K at TD of emission intensity and decay time. Moreover, One of the possible causes for the low output of Ce:CHO is due to such trap(s).

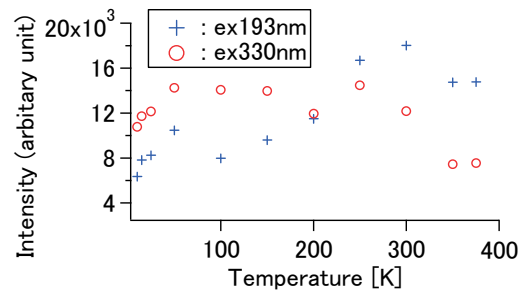


Fig. 1. TD of emission intensity of Ce-doped CaHfO₃ excited at 193 and 330 nm.

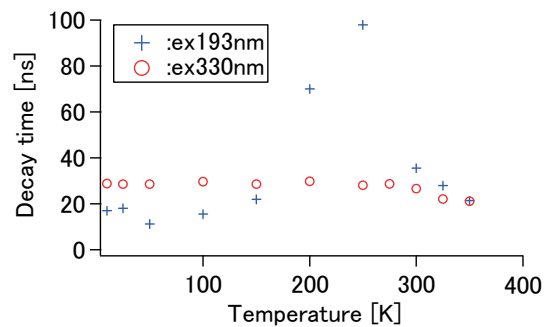


Fig. 2. TD of PL decay times of Ce-doped CaHfO₃ excited at 193 and 330 nm.

[1] Y. Kurashima *et al.*, *Cryst. Growth Des.* **21** (2021) 572.

[2] Y. Kurashima *et al.*, *UVSOR Activity Report 2019* **47** (2020) 58.

[3] S. Kurosawa *et al.*, *Radiat. Meas.* **56** (2013) 155.

[4] H. Chiba *et al.*, *Radiat. Meas.* **90** (2016) 287.

BL3B

Temperature Dependence of Photoluminescence Properties of Cs₂HfCl₃Br₃

S. Kodama¹, S. Kurosawa², A. Yamaji², M. Yoshino¹, T. Hanada¹, S. Toyoda², H. Sato²,
Y. Ohashi², K. Kamada^{2,3}, Y. Yokota¹ and A. Yoshikawa^{1,2,3}

¹Institute for Materials Research, Tohoku University, Sendai 980-8577, Japan

²New Industry Creation Hatchery Center, Tohoku University, Sendai 980-8579, Japan

³C&A Corporation, Sendai 980-0811 Japan

Intrinsic-luminescence halide scintillators with the chemical formula of A_2BX_6 (A : alkali metal, B : tetravalent ion, X : halogen ion) have been reported to exhibit the excellent scintillation performances such as Cs₂HfCl₆ with the blue emission around ~400 nm [1] and Cs₂HfBr₆ with the emission peak at ~450 nm [2]. We developed Cs₂HfI₆ as the novel red-emitting scintillator with the emission peak around ~700 nm [3]. Above studies imply the emission peak shifts towards the longer wavelength depending on the host X ion (Cl < Br < I).

The emission mechanism of A_2BX_6 halides is still unclear. To reveal the luminescence phenomena in A_2BX_6 halides, the relationship of the host ions, structures and luminescence properties should be understood. As a first step, the halogen-mixture compound Cs₂HfCl₃Br₃ was studied in this study.

Cs₂HfCl₃Br₃ crystal was grown by the vertical Bridgman method. The crystal structure was analyzed by the single-crystal X-ray diffraction to be cubic (space group: $Fm\bar{3}m$) which is the same as that of Cs₂HfCl₆ and Cs₂HfBr₆ [4]. The photoluminescence properties were evaluated in BL3B. The temperature dependences were measured at 10, 50, 100, 150, 200, 250, 300 and 350 K.

Figure 1 shows the photoluminescence excitation and emission spectra of Cs₂HfCl₃Br₃. The excitation and emission spectra were illustrated as the dashed and solid lines, respectively. At 300K, Cs₂HfCl₃Br₃ had two photoluminescence bands. One band with the blue emission peak at ~435 nm was excited by ~270 nm. The other band had the broad green emission at ~515 nm excited by 315 nm. These two photoluminescence bands stably existed at the whole temperature range. The emission intensities of such blue- and green-emission bands gradually increased as cooled down from 350K to 10K. The emission peak wavelengths of both bands shifted towards the longer wavelengths from 350K to 10K.

The photoluminescence emission wavelength of Cs₂HfCl₆, Cs₂HfCl₃Br₃, Cs₂HfBr₆ were summarized in Table 1. Cs₂HfCl₃Br₃ rather had the quite similar emission wavelength to Cs₂HfBr₆ than the medium wavelength between Cs₂HfCl₆ and Cs₂HfBr₆. Therefore, the emission wavelength of A_2BX_6 halides might be determined by the host halogen ion X . For further study, more crystals with the different Cr/Br ratios, Br-I mixture and Cl-I mixture compounds are synthesized, and the photoluminescence properties should be evaluated.

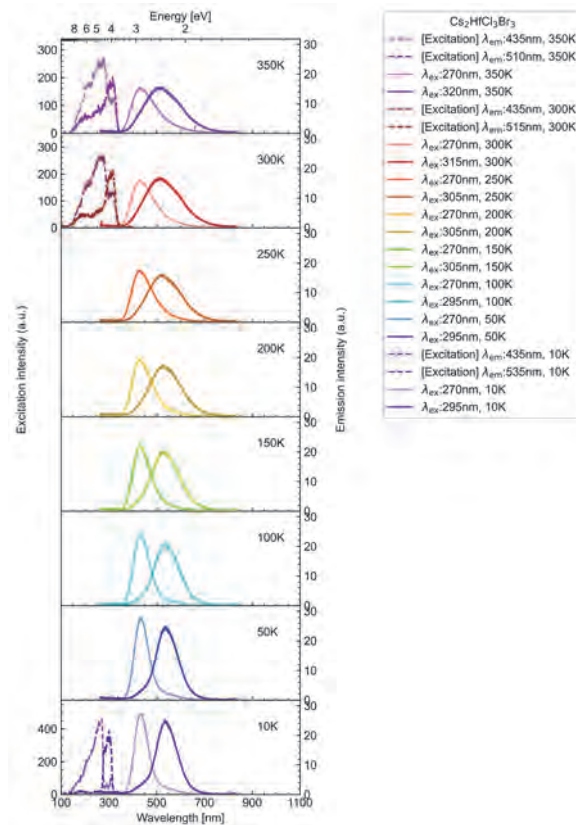


Fig. 1. Temperature dependence of photo-luminescence excitation and emission spectra of Cs₂HfCl₃Br₃.

Table 1. Photoluminescence emission peaks

Compounds	Emission wavelength at 300K
Cs ₂ HfCl ₆	375nm, 440 nm [5]
Cs ₂ HfCl ₃ Br ₃	435 nm, 515 nm
Cs ₂ HfBr ₆	435nm, 525 nm [2]

- [1] A. Burger *et al.*, Appl. Phys. Lett. **107** (2015) 34.
 [2] K. Saeki *et al.*, Jpn. J. Appl. Phys. **57** (2018) 030310.
 [3] S. Kodama *et al.*, Radiat. Meas. **124** (2019) 54.
 [4] S. Kodama *et al.*, Opt. Mater. **106** (2020) 109942.
 [5] K. Saeki *et al.*, Appl. Phys. Express. **9** (2016) 042602.

BL3B

Emission Spectra of Pr-doped $Y_3Ga_{5-x}Zn_xO_{12-\delta}$

M. Yoshino and J. Sugiyama

Graduate School of Engineering, Nagoya University, Nagoya 464-8603 Japan

In this study, the excitation spectra and emission spectra of Pr^{3+} in $Y_3Ga_5O_{12}$ crystal have been measured and changes in the spectra with doping of Zinc and hydration are examined. The samples are synthesized by solid state reactions followed by annealing in N_2-H_2 atmosphere in order to reduce Pr^{4+} to Pr^{3+} . The oxygen vacancies are created in Zn-doped $Y_3Ga_5O_{12}$ and protons are incorporated by hydration of the vacancies. The concentration of Pr is 0.5 mol% and that of Zn are 3, 10 and 15 mol%. The Zn-doped samples are hydrated at 523 K in humidified N_2 . The emission spectra and excitation spectra are measured at 30 K.

The emission spectra of $Y_3Ga_{5-x}Zn_xO_{12-\delta}:Pr$ at 275 nm excitation are shown in Fig. 1. The sharp peaks around 500-700 nm originate from $4f-4f$ transitions of Pr^{3+} . The emissions of $5d-4f$ transitions are not observed in Zn-doped samples as in the case of $Y_3Ga_5O_{12}:Pr$. The emission intensities of Pr^{3+} increase with 3 mol% Zn doping, but they do not increase monotonically and decrease above 10 mol%. Figure 2 shows the excitation spectra of Pr^{3+} in $Y_3Ga_{5-x}Zn_xO_{12-\delta}$ at 485 nm. The host absorption band (~220 nm) and $4f-5d$ absorption band (230-300 nm) are observed in each sample. The absorption spectrum of $Y_3Ga_{5-x}Zn_xO_{12-\delta}$ shows that the band gap becomes smaller with the addition of Zn. The decrease in the emission intensity of Pr^{3+} with Zn addition shown in Fig. 1 may relate to the change in the energy difference between band gap and the $4f-5d$ transition. Since the addition of Zn promotes the formation of oxygen vacancies, there should also be a contribution of the defect level in the band gap in the emission decrease. The excitation spectrum of $Y_3Ga_{5-x}Zn_xO_{12-\delta}:Pr$ ($x = 0.75$) at 485 nm and 617 nm are shown in Fig. 3 and Fig. 4. The emission changes before and after hydration are found to be different for host and $4f-5d$ excitation. These characteristic changes can be attributed to the defect levels of oxygen vacancy and hydrogen, respectively.

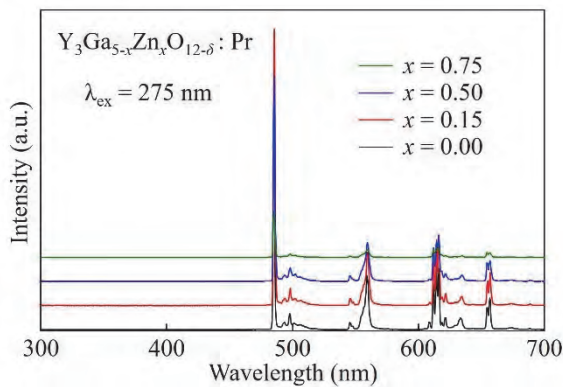


Fig. 1. Emission spectra of $Y_3Ga_{5-x}Zn_xO_{12-\delta}:Pr$ at 30 K ($\lambda_{ex} = 275$ nm).

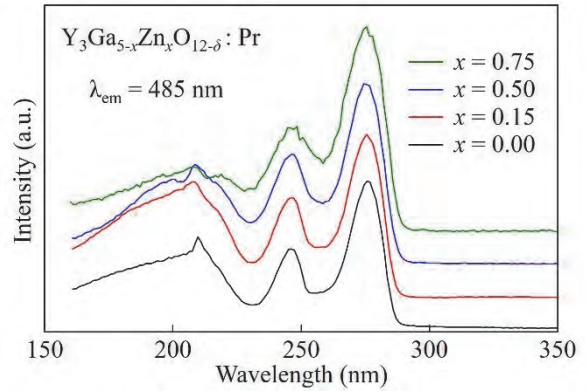


Fig. 2. Excitation spectra of $Y_3Ga_{5-x}Zn_xO_{12-\delta}:Pr$ at 30 K ($\lambda_{em} = 485$ nm).

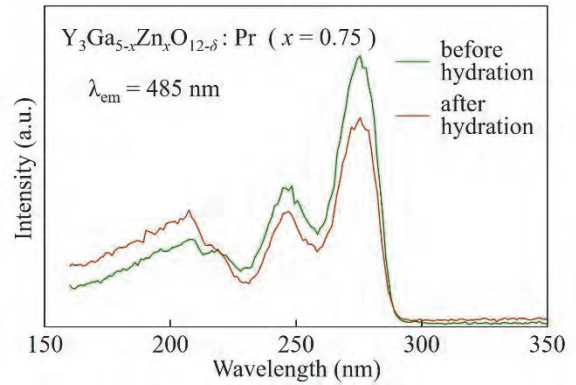


Fig. 3. Change in the excitation spectra with hydration in $Y_3Ga_{4.25}Zn_{0.75}O_{12-\delta}:Pr$ ($\lambda_{em} = 485$ nm).

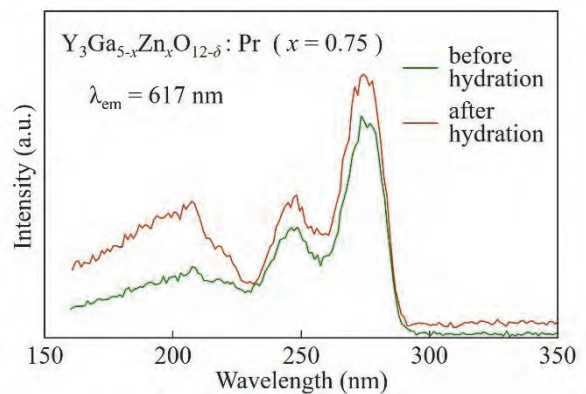


Fig. 4. Change in the excitation spectra with hydration in $Y_3Ga_{4.25}Zn_{0.75}O_{12-\delta}:Pr$ ($\lambda_{em} = 617$ nm).

BL3B

Optical Conductivity Spectra of a Locally Noncentrosymmetric Material LaRh₂As₂

S. Kimura^{1,2,3}, A. Goto¹, J. Sichelschmidt⁴ and S. Khim⁴¹Graduate School of Frontier Biosciences, Osaka University, Suita 565-0871, Japan²Department of Physics, Graduate School of Science, Osaka University, Suita 565-0871, Japan³Institute for Molecular Science, Okazaki 444-8585, Japan⁴Max Planck Institute for Chemical Physics of Solids, 01187 Dresden, Germany

Recently, noncentrosymmetric crystal structure and inversion symmetry breaking at crystal surfaces have attracted attention for physical properties combined with spin-orbit interaction (SOI). By using the SOI and the electric field gradient generated by the spatial symmetry breaking, spin-polarized current originating from spin-polarized bands is generated and is regarded to be useful for spintronics applications.

The breaking of the spatial inversion symmetry also generates a Cooper pair with a helical spin structure, which produces a superconducting state with a high critical field. Actually, the heavy-fermion superconductor CePt₃Si ($T_c \sim 0.75$ K) has an extremely high upper critical field H_{c2} as high as 5 T has been observed [1].

Recently, CeRh₂As₂ was discovered as a new heavy fermion superconductor ($T_c = 0.26$ K) with the local inversion symmetry breaking while overall crystal structure remains centrosymmetric [2]. RM_2X_2 ($R =$ rare earth, $M =$ transition metals, $X =$ Si, Ge) compounds usually have a tetragonal ThCr₂Si₂-type crystal structure with inversion symmetry ($I4/mmm$), CeRh₂As₂, however, crystallizes in the CaBe₂Ge₂-type structure, which lacks local inversion symmetry as the Ce and one of Rh and As sites ($P4/nmm$) as shown in Fig. 1. This results in a local electric field at the Ce site. Therefore, the Ce band undergoes Rashba splitting. It is necessary to investigate how this Rashba splitting affects the electronic structure. In this study, we measured the optical conductivity [$\sigma(\omega)$] spectra of LaRh₂As₂, a reference material without $4f$ electrons, and compared them with the LDA band calculations to investigate the electronic structure without spatial inversion symmetry.

In the experiment, the vacuum-ultraviolet reflectivity spectrum measured at BL3B was connected to the infrared THz spectrum measured in the laboratory, and the $\sigma(\omega)$ spectrum was obtained by using the Kramers-Kronig analysis.

Figure 2 shows the experimental $\sigma(\omega)$ spectrum of LaRh₂As₂ (Experiment, dotted line). The interband transition part of the $\sigma(\omega)$ spectra subtracted by the Drude fitting curve is the thick line. Calculated $\sigma(\omega)$ spectra with and without spin-orbit interaction are shown by red and blue lines, respectively. The calculated spectrum with the $I4/mmm$ crystal structure is also plotted as a dashed line.

of $P4/nmm$ explains the experimental results well. In particular, the experimental 0.4-eV peak can be explained by the calculation. This peak is hardly observed in $I4/mmm$ structure, which suggests a unique electronic structure in the $P4/nmm$ structure.

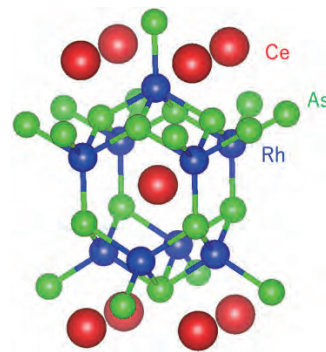


Fig. 1. Crystal structure of RRh_2As_2 ($R =$ La, Ce).

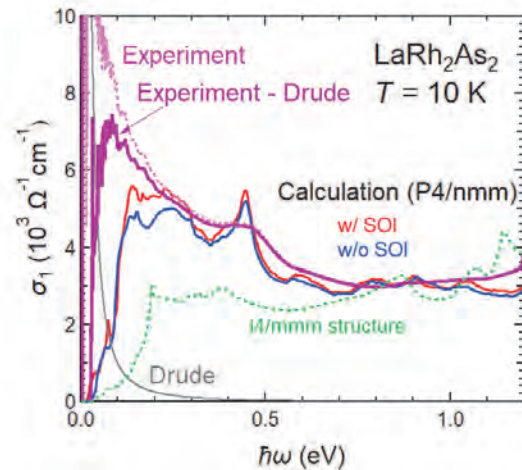


Fig. 2. Optical conductivity [$\sigma(\omega)$] spectrum of LaRh₂As₂ (Experiment, dotted line). The interband transition part of the $\sigma(\omega)$ spectra subtracted by the Drude fitting curve is the thick line. Calculated $\sigma(\omega)$ spectra with and without spin-orbit interaction are shown by red and blue lines, respectively. The calculated spectrum with the $I4/mmm$ crystal structure is also plotted as a dashed line.

[1] E. Bauer *et al.*, Phys. Rev. Lett. **92** (2004) 027003.

[2] S. Khim *et al.*, arXiv: **2101** (2021) 09522.

BL3B

Optical Investigation on Fluoro-olefins in Vacuum-Ultraviolet for New Refrigerant Gas Development

K. Yamanoi^{1,2}, Y. Sakata¹, H. Iwayama³, Y. Hasumoto^{1,2}, T. Takakuwa^{1,2}, O. Yamamoto^{1,2} and M. Noumi^{1,2}

¹Osaka university, Suita 565-0871, Japan

²DAIKIN Industries Ltd, Settsu 566-8585, Japan

³UVSOR Synchrotron Facility, Institute for Molecular Science, Okazaki 444-8585, Japan

Chlorofluorocarbon (CFC), hydrochlorofluorocarbon (HCFC), and hydrofluorocarbon (HFC) have been used as a refrigerant. These gases have high global warming potential (GWP) over 100. Recently, the hydrofluoroolefin (HFO) gases are expected as new low environmental load refrigerant due to its low GWPs since olefin gas is unstable and easily decompose by ultraviolet light in nature. In order to put HFO into practical use as a refrigerant, it is necessary to clarify the physical characteristics of HFO such as UV absorption and decomposition process. In this study, we measured the vacuum ultraviolet (VUV) light induced decomposition of HFO.

The decomposition spectra measurements were carried out in BL3B in UVSOR facility. $C_2H_2F_2$ gas was flowed into vacuum chamber through the capillary tube. The pressure in vacuum chamber was kept less than 3×10^{-4} Pa. The VUV light from 12 to 30 eV was irradiated on sample gas and the ionized molecular fragments were detected TOF-mass spectrometer shown in Fig. 1.

Figure 2 shows the decomposition spectra of $C_2H_2F_2$. We could clearly observe the ionization energies of each fragments. The ionization threshold of C_2HF_2 , C_2H_2F , C_2HF , CH_2F , and C_2F_2 were 12.8 eV, 14.2 eV, 14.4 eV, 14.8 eV, and 17 eV, respectively. From our previous results, the $C_2H_2F_2$ has the absorption from 135 nm (9.2 eV) to 190 nm (6.5 eV) as shown in Fig. 3. The absorption at 145 nm is attributed to the stretching and twisting of carbon double band and the 190 nm is the transition from π to π^* in C=C bonds, respectively [1]. However the ionization threshold is quite higher than these absorption.

In conclusion, we could observe the optical properties and ionization energy of decomposition process of $C_2H_2F_2$ in VUV region. The results let us know the UV- or VUV-induced decomposition dynamics of fluoro-olefins as refrigerant in next-generation.

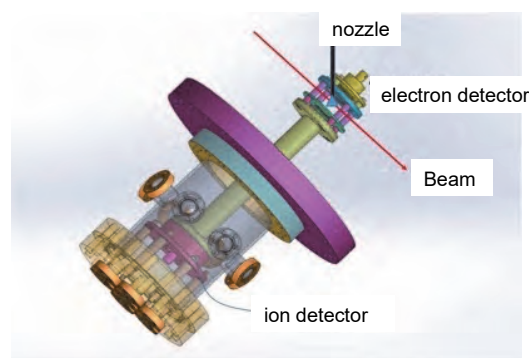


Fig. 1. Schematic image of the experimental setup in BL3B.

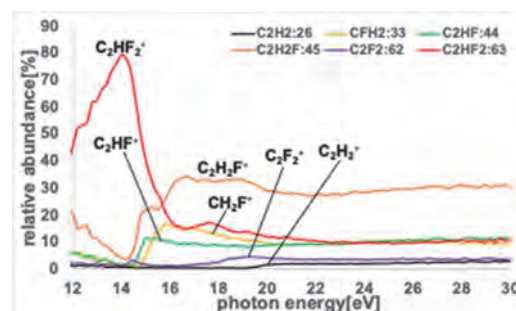


Fig. 2. Decomposition spectra of $C_2H_2F_2$

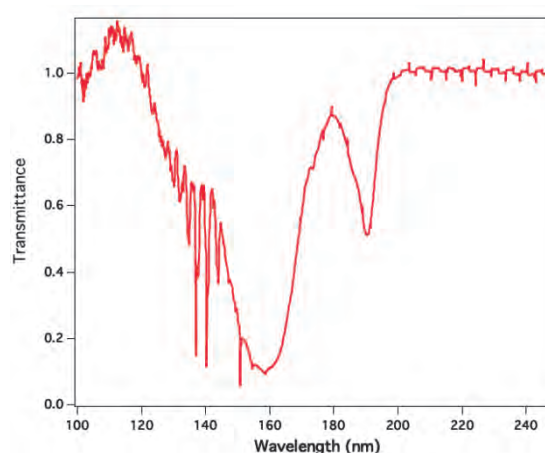


Fig. 3. Absorption spectrum of $C_2H_2F_2$.

[1] G. Belange *et al.*, J. Chem. Phys. **55** (1971) 2055.

BL3B

Absorption Bands of Tl^+ Centers in $KCaCl_3$ and $CsCaCl_3$ Crystals

T. Kawai and K. Kubota

Graduate School of Science, Osaka Prefecture University, Sakai 599-8531, Japan

Tl^+ centers in alkali halide crystals exhibit the optical bands called A, B, and C, which are attributed to intra-ionic transitions from the $^1A_{1g}$ ground state to the $^1T_{1u}$, $^3T_{2u} + ^3E_u$, and $^3T_{1u}$ excited states, respectively [1-3]. Though the optical properties of the Tl^+ centers in alkali halide crystals have been studied for a long time, there have been few reports on the Tl^+ centers in ternary halide compounds, which recently have attracted attention as host crystals of new scintillator materials [4,5]. In this study, we focused on Tl^+ centers in ternary halide crystals of $KCaCl_3$ and $CsCaCl_3$.

$KCaCl_3:Tl^+$ and $CsCaCl_3:Tl^+$ crystals were grown by the Bridgman method from the starting material powders. The optical measurements were performed at low temperatures at the BL3B line of UVSOR.

Figure 1 shows the absorption spectra of (a) $KCaCl_3:Tl^+$ and (b) $CsCaCl_3:Tl^+$ crystals at 10K. The several absorption bands are observed in the transparent energy region below the respective fundamental absorption edge. These absorption bands exhibit no simple Gaussian shape.

Owing to the dynamical Jahn-Teller effect, the A and C bands of the Tl^+ centers in alkali halide crystals often exhibit the double or triple structures, respectively [1-3]. We resolved the absorption bands observed in $KCaCl_3:Tl^+$ and $CsCaCl_3:Tl^+$ into two or three Gaussian shapes. As shown by thin curves in Fig.1, the absorption bands located around 5.4 eV for $KCaCl_3:Tl^+$, and 5.6 eV for $CsCaCl_3:Tl^+$ can be resolved into two Gaussian shapes. The intense absorption bands around 6.8 eV for $KCaCl_3:Tl^+$, and 7.1 eV for $CsCaCl_3:Tl^+$ can be resolved into three Gaussian shapes. Thus, the absorption bands at 5.4 eV for $KCaCl_3:Tl^+$, and 5.6 eV for $CsCaCl_3:Tl^+$ are assigned to the A band of the Tl^+ centers, and the absorption bands at 6.8 eV for $KCaCl_3:Tl^+$, and 7.1 eV for $CsCaCl_3:Tl^+$ are assigned to the C band of the Tl^+ centers. Furthermore, a small absorption band is observed at 6.4 eV in $KCaCl_3:Tl^+$ and the shoulder structure is observed at 6.6 eV in $CsCaCl_3:Tl^+$. The absorption band and the shoulder structure are assigned to the B band of the Tl^+ centers.

On the basis of a theoretical treatment for the Tl^+ centers [1-3], the relative positions of the absorption bands and their relative intensity ratios are determined by the Coulomb energy F , the exchange energy G between the s- and p-electron, the spin-orbit interaction energy ζ of the p-electron and the King-Van Vleck factor λ , which account for the differences between the radial wave functions of the p-electron in the triplet and singlet states. These parameters F , G , ζ and λ can be evaluated from the energy positions of the center of the A, B and C absorption bands and the dipole strength ratio R of the C to A bands. These parameters characterizing the Tl^+ centers were estimated by analyzing our experimental

data, as shown in Table I. In the same Table, similar data for the Tl^+ centers doped in alkali chloride crystals are also presented. From a comparison of these values, it is found that our assignment of the absorption bands observed in the $KCaCl_3:Tl^+$ and $CsCaCl_3:Tl^+$ crystals is reasonable.

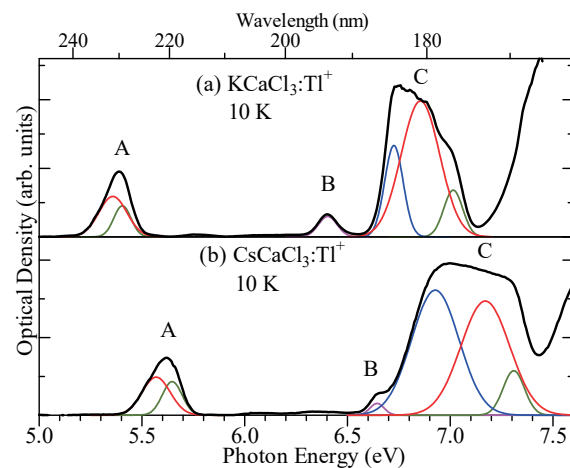


Fig. 1. Absorption spectra of (a) $KCaCl_3:Tl^+$ and (b) $CsCaCl_3:Tl^+$ crystals at 10K. The thin curves represent Gaussian components decomposing the absorption bands.

Table 1. Parameters characterizing the Tl^+ centers. Except for λ , all parameters are in eV.

Crystals	F	G	ζ	λ	Ref.
$KCaCl_3:Tl^+$	5.9	0.25	0.72	1.2	
$CsCaCl_3:Tl^+$	6.1	0.31	0.83	0.89	
$NaCl:Tl^+$	5.7	0.26	0.66	1.1	[1]
$KCl:Tl^+$	5.7	0.28	0.7	0.99	[1]

- [1] A. Fukuda, *Sci. Light (Tokyo)* **13** (1964) 64.
- [2] A. Ranfagni, *et al.*, *Advance in Physics* **32** (1983) 823.
- [3] P.W.M.Jacobs, *J. Phys. Chem. Solids* **52** (1991) 35.
- [4] M. Tyagi, *et al.*, *J. Appl. Phys.* **113** (2013) 203504.
- [5] N.V. Rebrova, *et al.*, *J. Lumin.* **182** (2017) 172.

BL3B

Influence of Crystal Structures of $\text{CsCaI}_3:\text{Tl}^+$ and $\text{Cs}_4\text{CaI}_6:\text{Tl}^+$ on Absorption Bands

S. Ito and T. Kawai

Graduate School of science, Osaka Prefecture University, Sakai 599-8531, Japan

Thallium impurity centers in alkali halides, which are binary compounds, have been extensively investigated [1]. However, thallium impurity centers in ternary compounds, which have attracted attention as scintillator materials, have been less reported. In this study, we investigated absorption bands of $\text{CsCaI}_3:\text{Tl}^+$ and $\text{Cs}_4\text{CaI}_6:\text{Tl}^+$.

The single crystals of $\text{CsCaI}_3:\text{Tl}^+$ and $\text{Cs}_4\text{CaI}_6:\text{Tl}^+$ were prepared by a cell method [2]. The quartz-cells with the narrow gap are made of a pair of two quartz plates. The melt of the starting materials was percolated into the gap of the quartz-cells through capillary action and thin crystals were grown in the gap by natural cooling.

Figure 1 shows the absorption spectra of $\text{CsCaI}_3:\text{Tl}^+$ and non-doped CsCaI_3 crystals. In the non-doped CsCaI_3 crystal, no absorption bands are observed in the energy region below the fundamental absorption edge of 5.7 eV. On the other hand, the three absorption bands are observed in $\text{CsCaI}_3:\text{Tl}^+$.

Figure 2 shows the absorption spectrum of $\text{Cs}_4\text{CaI}_6:\text{Tl}^+$ crystals. The five absorption bands are observed in $\text{Cs}_4\text{CaI}_6:\text{Tl}^+$. That is to say, the appearance of the absorption bands of $\text{Cs}_4\text{CaI}_6:\text{Tl}^+$ is complicated than those of $\text{CsCaI}_3:\text{Tl}^+$.

In both crystals, the Tl^+ ions replaced the Cs^+ ions because of the equal valance of both ions. Thus, the nearest neighbor ion of the Tl^+ ion is iodide ions. In $\text{CsCaI}_3:\text{Tl}^+$, the Tl^+ ion is surrounded with a distorted square antiprism geometry by eight iodide ions [3]. In $\text{Cs}_4\text{CaI}_6:\text{Tl}^+$, on the other hand, there are two types of Tl^+ -occupied sites: one with a distorted square antiprism geometry and another with a trigonal prism geometry. In the site with the trigonal prism geometry, the Tl^+ ion is surrounded by six iodide ions [4]. The Tl^+ ions occupied two types of sites exhibit the diverse absorption bands. Thus, the appearance of the absorption bands of $\text{Cs}_4\text{CaI}_6:\text{Tl}^+$ becomes complex as against those of $\text{CsCaI}_3:\text{Tl}^+$.

In the case of the Tl^+ centers in alkali halides, the absorption bands often exhibit the double or triple structures due to the Jahn-Teller effect. The double or triple structures due to the Jahn-Teller effect become conspicuous with increasing temperature. The band-shape of the absorption bands in $\text{Cs}_4\text{CaI}_6:\text{Tl}^+$ may be seen as the double structures. However, the band-shape of the absorption bands in $\text{Cs}_4\text{CaI}_6:\text{Tl}^+$ did not become conspicuous with increasing temperature. Thus, the complicated absorption bands in $\text{Cs}_4\text{CaI}_6:\text{Tl}^+$ do not come from the Jahn-Teller effect.

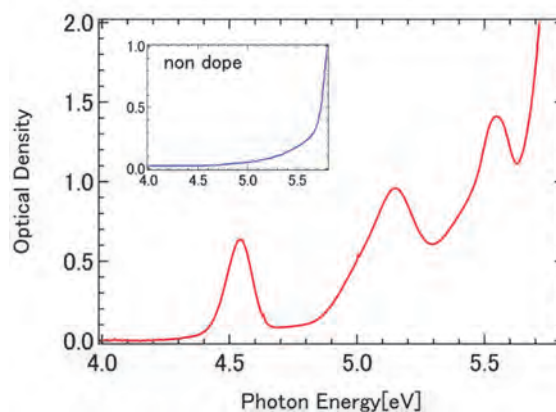


Fig. 1. Absorption Spectrum of $\text{CsCaI}_3:\text{Tl}^+$ at 10K. Insert shows an absorption spectrum of non-doped CsCaI_3 at 25K.

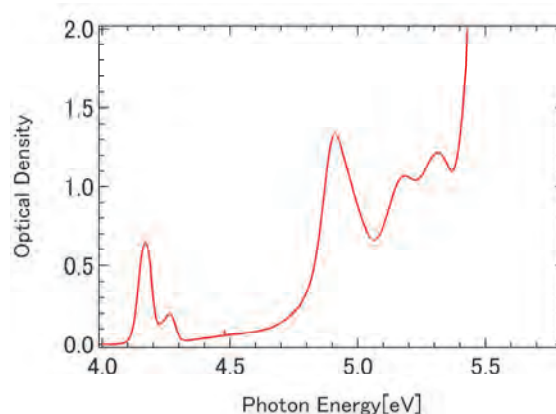


Fig. 2. Absorption Spectrum of $\text{Cs}_4\text{CaI}_6:\text{Tl}^+$ at 10K

[1] A. Ranfagni, *et al.*, *Advances in Physics*, **32** (1983) 823

[2] S. Hashimoto and M. Itoh, *Jpn. J. Appl. Phys.* **27** (1988) 726.

[3] M. Tyagi, *et al.*, *J. Appl. Phys.* **113** (2013) 203504.

[4] L. Stand, *et al.*, *J. Cryst. Growth*, **486** (2018) 162.

BL3B

Photoluminescence and Scintillation of CsCl-based Ternary Crystals

M. Koshimizu¹, K. Takahashi¹, Y. Fujimoto¹, T. Yanagida² and K. Asai¹

¹Department of Applied Chemistry, Graduate School of Engineering, Tohoku University, Sendai 980-8579, Japan

²Division of Materials Science, Nara Institute of Science and Technology, Ikoma 630-0192, Japan

Auger-free luminescence (AFL) is caused by the radiative transition of a valence electron to a core hole state. The transition is competitive with the Auger process, which is a much faster process, efficient AFL cannot be observed in many compounds. In other words, efficient AFL has been observed in limited compounds such as alkaline- or alkaline-earth fluorides or CsCl-based compounds.

AFL has been applied to fast scintillators owing to its fast decay. A representative one is BaF₂; however, CsCl-based compounds have an advantage of long emission wavelength appropriate for detection with a photomultiplier tube. Thus far, we have developed fast scintillators based on ternary CsCl-based compounds [1-2]. In this report, we present some results on the photoluminescence properties with VUV excitation and scintillation properties of several CsCl-based ternary compounds.

Crystal samples of the ternary CsCl-based compounds were fabricated using a self-seeding solidification method and the Bridgman method. Raw materials were mixed in a stoichiometric ratio. The mixed powders were poured into quartz ampoules and heated at 350 °C in vacuum for 1 day to remove adsorbed water. For the self-seeding solidification method, the quartz ampoule was set in a tubular furnace, and the furnace was heated to 950 °C for 12 h and subsequently cooled to room temperature over 72 h. For the Bridgman method, the ampoule was set in a Bridgman furnace. The temperatures of the upper and lower heaters in the furnace were set at 950 °C and 750 °C, respectively, during crystal growth, and the ampoules were lowered at a rate of 1.5 mm/h.

The luminescence properties were characterized with vacuum ultraviolet (VUV) light as an excitation source. Measurements were performed at BL3B for temporal profiles at the UVSOR facility at the Institute for Molecular Science, Japan, using a time-correlated single photon counting.

Photoluminescence temporal profiles of the CsCl-based ternary compounds are presented in Fig. 1. The excitation wavelength was 84 nm, whose photon energy corresponds to the excitation from the outermost core level to the bottom of the conduction band. The emission wavelengths correspond to the emission peak whose excitation spectra have a step at around 84 nm, which strongly suggests that the emission is owing to the AFL. The decay behavior shown in Fig. 1 was fitted with an exponential decay function. The decay time constants were 0.8 – 1.2 ns, which are typical for the AFL. Scintillation temporal profiles of the CsCl-based ternary compounds are presented in Fig. 2. The decay behavior is similar to those of the photoluminescence, which

indicates that the scintillation of these compounds is mainly of AFL.

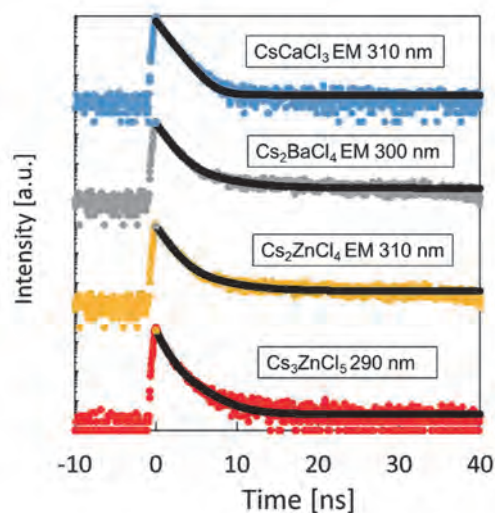


Fig. 1. Photoluminescence temporal profiles of CsCl-based ternary compounds.

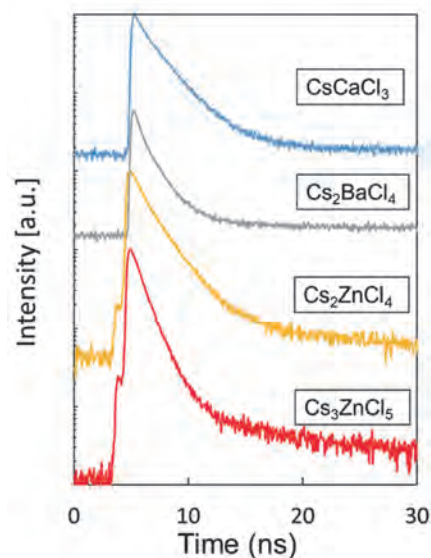


Fig. 2 Scintillation temporal profiles of CsCl-based ternary compounds.

[1] K. Takahashi *et al.*, Jpn. J. Appl. Phys. **59** (2020) 032003.

[2] K. Takahashi *et al.*, Jpn. J. Appl. Phys. **59** (2020) 072002.

BL4U

Microscopic Evidence of Complex Cobalt Oxides Electrodeposited on Graphene Window

C. H. Chuang¹, J.-J. Velasco Velez², Yi-Ying Chin³, W. F. Pong¹, T. Ohgashi⁴ and N. Kosugi⁴¹Department of Physics, Tamkang University, Tamsui 251, Taiwan²Max Planck Institute for Chemical Energy Conversion, Mülheim 45470, Germany³Department of Physics, National Chung Cheng University, Chiayi 62102, Taiwan⁴UVSOR Synchrotron Facility, Institute for Molecular Science, Okazaki 444-8585, Japan

The X-ray-in (electron-in) and electron-out techniques [1,2] using the surface-sensitive analysis are quite important for the electrochemical interface. Graphene as an early example of two-dimensional materials has been received a lot of attentions i.e. a promising use of window membrane, because of the remarkable points (such as vacuum-liquid environment separation, thinnest thickness, and X-ray/electron transparency). Studies for an essential role of graphene-based working electrode are still missing in the wide-range applications due to the difficulties in solid-liquid phase and nanoscale-resolved approaching. The electrocatalytic project is one of interests of energy materials; thus, the critical factor and diverse function are devoted for the heterogeneous system owing to the interface correlation.

In the work, we have investigated various oxidation states of electrodeposited Co and underlying graphene window by using scanning transmission X-ray microscopy (STXM) at BL4U. The electronic structure and bonding configuration of electrodeposited Co layer were studied to solve the answer of the catalytic synergy of oxygen evolution reaction. The electrochemical reduction and deposition of the aqueous Co^{2+} ions were formed on the graphene electrode through the cathodic electron reduction in the CoSO_4 solution. Diverse lattice structures of cobalt nanoparticles (Co-NPs) grown on the graphene electrode were characterized through transmission electron microscopy (TEM) measurement, shown in Fig. 1(a)–(c). High-magnified TEM images highlights the local region (green squares) of Co-NPs for the ordered particle size ranging from 5 to 10 nm for the initial stage and the amorphous structure for the later and thick stage. The inset images of Fig. 1(d)–(f) were taken at the pre-edge energy to observe the background images, which consistent with the same area of TEM image. The X-ray absorption (XA) spectra at C *K*-edge in Fig. 1(d) show absorption peaks at photon energies (PEs) of 284.9, 286.6, 288.4, 290.2, and 292.5 eV, which are known for $\pi^*(\text{C}=\text{C})$, $\pi^*(\text{C}-\text{OH})$, $\pi^*(\text{C}=\text{O}$ in $\text{HO}-\text{C}=\text{O})$ or defect, $\pi^*(\text{O}-\text{C}(\text{O})-\text{O}$ or $\text{C}=\text{O}$ at the edge), and $\sigma^*(\text{C}=\text{C})$ bonds [3,4]. The spectral evidences between region 1, 2, and 3 reflect the oxidation evolution of graphene with a function of Co NPs thickness. The XA spectra at O *K*-edge in Fig. 1(e) indicate three π^* resonances (530.8, 532.4, and 534.0 eV) and two σ^* resonances (536.8 and 538.9 eV), corresponding to the oxidation states of the graphene electrode and the electrodeposited Co-NPs [4,5]. The hybridized O *2p*-Co *3d* states [6] are located at two peaks at PEs of 532.4 and 534.0 eV, and the hybridized O

2p-Co *4s* state are located at the broad peak at PE of 538.9 eV [6].

In Fig. 1(e), the multiple features of the Co XA spectra at the *L*₃- and *L*₂-edges were divided into two regions (774–781 eV and 789–795 eV), which are involved by the oxidation state, crystal field splitting, and low/high spin states of Co *3d* [6]. Our theoretical simulation indicated three components (Metal Co^0 , Oct. symmetrical Co^{2+} , and Oct. symmetrical Co^{3+} species) existed in region 1, 2, and 3, depending on the linear combination of three reference spectra through the lowest deviation between the experimental and fit data. The curve-fitting statistics reflects the increasing metal Co^0 and Oct. Co^{2+} state by the elimination of Oct. Co^{3+} state for the mixing state of Co NPs in region of 1, 2, and 3.

Through STXM, the multiple carbonyl-like states (C–OH, HO–C=O, and O–C(O)–O/C=O) and multiple Co states (Co^0 , Co^{2+} , and Co^{3+}) were found on the surface. Our chemical mapping evidence signified the bonding tendency of graphene and de-oxidation stages of Co-NPs, which accounts for the synergistic reason of Co-based energy materials.

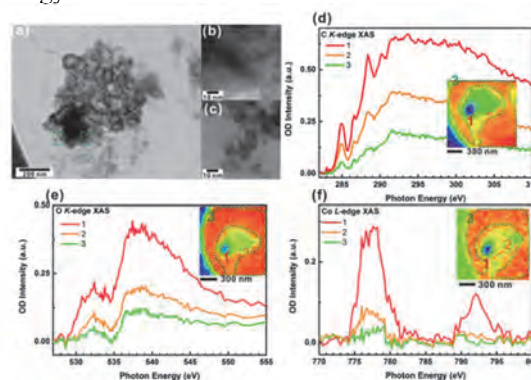


Fig. 1 (a)–(c) High-resolution TEM images of electrodeposited Co-graphene membranes. (d)–(f) Selected areas of the XA spectra of the C *K*-edge, O *K*-edge, and Co *L*-edge and the corresponding averaged areas (insets) of the element maps.

- [1] D. Waldmann *et al.*, ACS Nano 7 (2013) 4441.
- [2] M. Krueger *et al.*, ACS Nano 5 (2011) 10047.
- [3] Y. Wang *et al.*, Sci. Rep. 5 (2015) 15439.
- [4] L. R. De Jesus *et al.*, J. Phys. Chem. Lett. 4 (2013) 3144.
- [5] J. G. Zhou *et al.*, J. Mater. Chem. 21 (2011) 14622.
- [6] J. Wang *et al.*, Energy Environ. Sci. 6 (2013) 926.

BL5U

High-resolution ARPES Study of Topological Dirac-semimetal Candidates

D. Takane¹, Y. Kubota¹, K. Nakayama^{1,2}, S. Souma^{3,4}, K. Sugawara^{1,2,3,4}, T. Takahashi^{1,3,4}, K. Segawa⁵ and T. Sato^{1,3,4}

¹Department of Physics, Tohoku University, Sendai 980-8578, Japan

²Precursory Research for Embryonic Science and Technology (PRESTO), Japan Science and Technology Agency (JST), Tokyo 102-0076, Japan

³Center for Spintronics Research Network, Tohoku University, Sendai 980-8577, Japan

⁴WPI Research Center, Advanced Institute for Materials Research, Tohoku University, Sendai 980-8577, Japan

⁵Department of Physics, Kyoto Sangyo University, Kyoto 603-8555 Japan

The search for novel fermions, which has long been an important research target in elementary-particle physics, is recently becoming an exciting challenge in condensed-matter physics, as highlighted by the discovery of two-dimensional (2D) Dirac fermions in graphene and helical Dirac fermions at the surface of three-dimensional (3D) topological insulators. The recent discovery of 3D topological Dirac semimetals (TDSs) that host massless Dirac fermions further enriches the category of exotic fermions. TDSs show exotic quantum phenomena such as high carrier mobility and giant linear magnetoresistance governed by the linearly dispersive Dirac-cone energy band. Also, TDS can be switched to other novel topological phases, e.g., by breaking the time-reversal/crystalline symmetry or by chemical substitution. Therefore, TDS provides a fertile playground for realizing a variety of topological phases. However, despite many theoretical predictions for TDS candidates, TDSs that have been experimentally verified are still rare. In addition, well-known TDSs, Na₃Bi and Cd₃As₂ [1-3], are not well suited for the physical-property measurements and device applications because Na₃Bi is extremely active in the air and there exists a critical controversy between experiments and theories in Cd₃As₂ on the Dirac-cone states. Thus, it is highly desirable to explore new TDS materials that overcome such difficulties.

It was recently predicted that BaMg₂Bi₂ is a TDS [4]. In BaMg₂Bi₂, Ba atoms can be easily replaced with other elements, so this system seems suitable for manipulating topological and physical properties. In this study, we performed high-resolution angle-resolved photoemission spectroscopy (ARPES) of BaMg₂Bi₂. By utilizing energy tunable photons, we mapped out the band structure over the entire 3D Brillouin zone [Fig. 1(a)] to search for the Dirac-cone band dispersions.

High-quality single crystals of BaMg₂Bi₂ were synthesized by the self-flux method. ARPES measurements were performed with micro-focused VUV synchrotron light at BL5U. Samples were cleaved *in situ* along the (0001) plane of the hexagonal crystal in an ultrahigh vacuum.

Figure 1(b) shows the 2D ARPES intensity plot at E_F measured at $k_z \sim 0$, where the presence of Dirac-cone bands is predicted by the band calculations. One

can find a circular Fermi surface centered at the Γ point. This Fermi surface originates from the E_F crossing of a holelike band that shows linear dispersions, as seen from Fig. 1(c). We doped electrons to the crystal surface by alkaline-metal deposition and searched for a predicted point touching between the valence and conduction bands due to the Dirac-cone band formation. The present study lays the foundation for understanding the topological property of BaMg₂Bi₂.

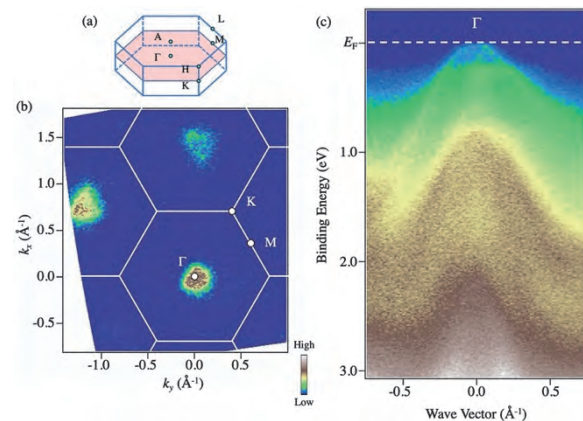


Fig. 1. (a) 3D bulk Brillouin zone of BaMg₂Bi₂. (b) ARPES intensity at E_F plotted as a function of 2D wave vector. (c) ARPES-intensity plot measured along a momentum cut crossing the Γ point.

- [1] Z. K. Liu *et al.*, Science **343** (2014) 864.
- [2] M. Neupane *et al.*, Nat. Commun. **5** (2014) 3786.
- [3] Z. K. Liu *et al.*, Nat. Mater. **13** (2014) 677.
- [4] Z. Zhang *et al.*, J. Phys. Chem. Lett. **9** (2018) 6224.

BL5U, BL7U

Determination of Contribution of Atomic Orbital to the Valence Band in SnS

I. Suzuki¹, S. Kawanishi¹, L. Zexin¹, T. Omata¹ and S. Tanaka²¹Institute of Multidisciplinary Research for Advanced Materials, Tohoku University, Sendai 980-8577, Japan²The Institute of Scientific and Industrial Research, Osaka Univ., Ibaraki 567-0047, Japan

SnS is a compound semiconductor with a band gap of ~ 1.2 eV, which is expected as a novel absorber material for the thin-film solar cells due to being composed of abundant and safe elements. Therefore, SnS solar cells have been actively studied for decades, whereas there has been limited experimental studies on the electronic structures of SnS. Since the electronic structure at the band edge is largely responsible for the optical and electrical properties of the material, it is important to understand them by experimental approach as well as by the theoretical analysis considering its application to the optoelectronic devices. In this study, we have experimentally determined the contribution of atomic orbital to the valence band using difference of each atomic orbital in the photoionization cross section (Fig. 1).

The electronic structure of the valence band of SnS was observed by high-resolution angle-resolved photoemission spectroscopy (ARPES) at BL5U and BL7U. Single crystalline Br-doped SnS grown by flux method [1] were subjected to the measurement after being cleaved in the measurement chamber prior to the measurement. First-principles calculations of the electronic structure of SnS were performed using the Quantum Espresso package.

Figure 2 shows the band dispersion in the Γ -Z direction measured with excitation energies of 60 eV (BL7U) and 21 eV (BL5U). It is indicated that the valence band maximum (VBM) is located at a k -point slight offset from the Z-point to Γ -point as reported in the previous first-principles calculations [2]. The relative intensity of each band differs depending on the excitation energies. For a simple comparison, Fig. 3(a) shows the energy distribution curve, which is integrated over the whole wavenumber space, where the intensity was normalized at -4 eV. The valence band is composed of three major bands (Band I, II and III), which is well reproduced in the partial density of states (PDOS) obtained by first-principles calculation (Fig. 3(b)). In the measurement with excitation energy of 21 eV, the intensities of band I and III were obviously lower than those of 60 eV. Since the photoionization cross section is small only for Sn 5s at 21 eV compared to other atomic orbitals (Fig. 1), it is suggested that Sn 5s orbital strongly contributes to the band I and II. This is well consistent with the calculated PDOS. In conclusion, it is experimentally clearly shown that the VBM is mainly composed of Sn 5s orbitals.

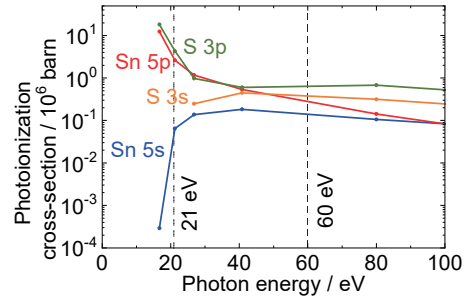


Fig. 1. Photoionization cross-section of each atomic orbital in SnS [3].

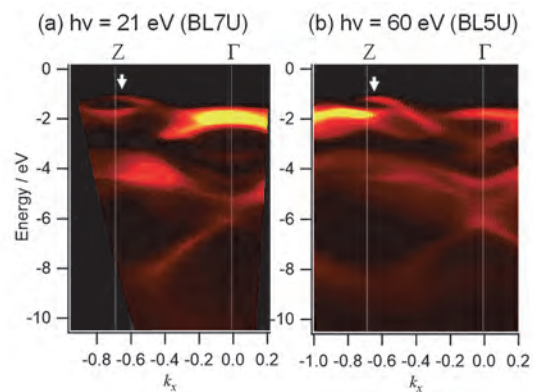


Fig. 2. E- k plot of SnS measured with an excitation energy of (a) 21 eV and (b) 60 eV. The white arrows in the figures indicate the location of the VBM.

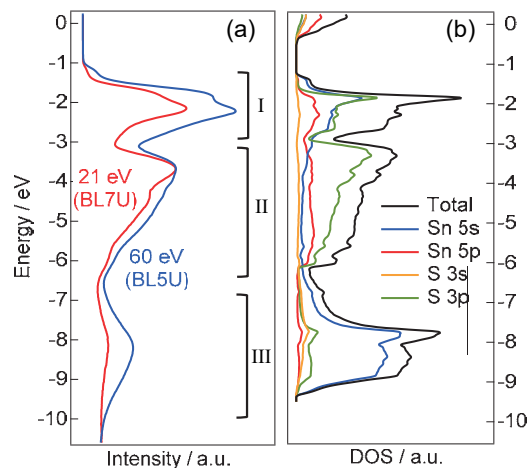


Fig. 3. (a) EDC and (b) PDOS plots of the SnS.

[1] S. Kawanishi *et al.*, Cryst. Growth Des. **20** (2020) 5931.

[2] J. Vidal *et al.*, Appl. Phys. Lett. **100** (2012) 032104.

[3] J. J. Yeh *et al.*, At. Data Nucl. Data Tables **32** (1985) 1.

BL5U

Band Dispersion Unique to the Cobalt Intercalation in the Noncentrosymmetric Antiferromagnet CoNb_3S_6

H. Tanaka¹, S. Okazaki², K. Kuroda¹, S. Ideta³, K. Tanaka³, T. Sasagawa² and T. Kondo¹

¹*Institute for Solid State Physics, The University of Tokyo, Kashiwa 277-8581, Japan*

²*Materials and Structure Laboratory, Tokyo Institute of Technology, Yokohama 226-8503, Japan*

³*UVSOR Synchrotron Facility, Institute for Molecular Science, Okazaki 444-8585, Japan*

CoNb_3S_6 is a transition metal dichalcogenide NbS_2 with cobalt intercalation. Neutron scattering experiments have revealed that intercalated Co atoms emerge collinear antiferromagnetic structure along in-plane direction [1]. Furthermore, weak ferromagnetism along out-of-plane direction and anomalous Hall effect have been observed recently [2]. However, the anomalous Hall response is giant even though the ferromagnetic moments are weak, and the mechanism of this giant anomalous Hall effect has been undiscovered.

We studied the electronic structure of CoNb_3S_6 by comparing with that of NbS_2 without the intercalation. Single crystals of CoNb_3S_6 and NbS_2 were synthesized by chemical vapor transport method. Angle-resolved photoemission spectroscopy (ARPES) measurements using the vacuum ultraviolet (VUV) light were performed at BL5U of UVSOR. We used the 120 eV photons, and the energy resolution was 45 meV. The measurement temperature was kept at 20 K, lower than $T_N \sim 28$ K. All samples were cleaved *in situ* along the (001) direction at an ultrahigh vacuum of 4.0×10^{-9} Pa.

Figure 1(a) shows Fermi surfaces of NbS_2 and CoNb_3S_6 . NbS_2 has pockets around the Γ and K points. These pockets are hole pockets, as revealed in Fig. 1(b) left panel. These dispersions were also observed in the band dispersion of CoNb_3S_6 , as highlighted by pink dashed rectangles in Fig. 1(b). In CoNb_3S_6 , these dispersions were shifted down, because of the electron doping from Co cations. This band shift is also observed as a smaller hole pocket around the Γ point in CoNb_3S_6 [Fig. 2]. Furthermore, an additional band dispersion appeared near the Fermi level [blue dashed rectangles in Fig. 1(b) right panel]. This dispersion seems to come from Co atoms, because such a band dispersion does not exist in NbS_2 , even if the band shift is considered. The additional band dispersion of intercalated atoms crossing the Fermi level is not reported in the ARPES study of CrNb_3S_6 [3], which has the same crystal structure as CoNb_3S_6 . Therefore, we conclude that this electronic structure is unique to the cobalt intercalation, and possibly responsible for the particularly large anomalous Hall effect of CoNb_3S_6 .

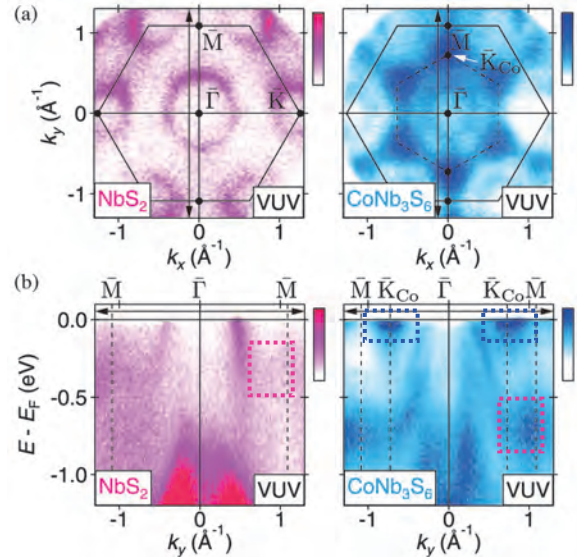


Fig. 1. VUV-ARPES measurements of NbS_2 and CoNb_3S_6 . (a) Fermi surfaces of NbS_2 and CoNb_3S_6 . Solid and dashed hexagons represent the Brillouin zones of NbS_2 and CoNb_3S_6 , respectively. (b) Band dispersion along the k_y direction [black arrows in (a)].

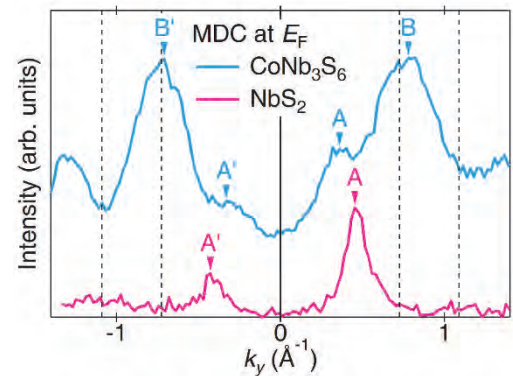


Fig. 2 Momentum distribution curves (MDCs) of NbS_2 (pink) and CoNb_3S_6 (light blue) along the k_y direction at the Fermi level. Spectrum peaks corresponding to the hole pocket around the Γ point are labeled by A and A'.

[1] S. S. P. Parkin, *et al.*, J. Phys. C: Solid State Phys. **16** (1983) 2765.

[2] N. J. Ghimire *et al.*, Nat. Commun. **9** (2018) 3280.

[3] N. Sirica *et al.*, Phys. Rev. B **94** (2016) 075141.

BL5U

Orbital-resolved 3d Band Structure of Fe Layers

J. Okabayashi¹, K. Tanaka² and S. Mitani³

¹Research Center for Spectrochemistry, The University of Tokyo, Tokyo 113-0033, Japan

²UVSOR Synchrotron Facility, Institute of Molecular Science, Okazaki 444-8585, Japan

³National Institute for Materials Science, Tsukuba 305-0047, Japan

Iron-based materials have been widely investigated for the practical uses and fundamental science. For the spintronics device applications, Fe-based alloys facing on other materials have a high potential for producing functional properties such as perpendicular magnetic anisotropy derived from the symmetry broken spin-orbit effects at the film interfaces. On the other hand, clean Fe surface is required for the development of the spin- and angle-solved photoemission spectroscopy (ARPES) system as a target material of spin detector using very-low energy electron diffraction. In order to develop the researches and applications, a fundamental knowledge about the fundamental Fe 3d orbital-resolved band structures is necessary.

Density-functional-theory (DFT) calculation in the bcc Fe bulk exhibits the band dispersions along the Γ - Δ -H symmetric line in Fe [001] direction [1,2]. The dispersion in the Δ_1 band is well known as a fully spin polarized band which corresponds to the coherent tunneling phenomena in tunneling magnetoresistance devices. However, there are few reports detecting the band dispersions directly with orbital resolutions in ARPES. In these motivations, we aim to access the linear polarization dependence in ARPES to detect the orbital-resolved 3d states in Fe which is comparable with the band-structure calculation in the momentum space.

Sample was prepared on MgO (001) substrate using Fe electron-beam evaporation. The MgO substrate was cleaned by annealing at 800 °C. Then, after cooling to room temperature, Fe was deposited in the growth rate of 0.015 nm/min to 100-nm thickness. Post-annealing at 800 °C was performed to obtain clear LEED pattern. After the sample was introduced from the air condition, the sample surface was cleaned by Ar-ion sputtering to remove the oxide contamination and by annealing at 800 °C.

ARPES was performed at BL5U, UVSOR, where photoemission chamber is connected to the sample preparation chamber. The measurement conditions were set at 15 meV energy resolution and 10 K. Linear polarized beams of *s*- and *p*-polarization were used to detect the orbital symmetry. We employ the photon energy of 60 eV to enhance the Fe 3d photo-ionization cross section, where the Γ -H line is scanned by the angular mode of $\pm 15^\circ$.

For the Fe 3d states, *s*- and *p*-polarized beams (vertical and horizontal) probe the wave functions in odd (*xy*, *yz*) and even symmetry (*zx*, x^2-y^2 , z^2) along the mirror plane, respectively [3]. Considering the effect of matrix element in photoemission process, *s*- and *p*-

polarization enhances the *yz* and *zx* orbitals, respectively.

Figures 1(a) and 1(b) show the energy-momentum *E*-*k* curves in ARPES using *p*- and *s*-polarized beams, respectively, with different momentum points along Γ - Δ -H symmetric line. At the Γ point, specific feature is obtained such as parabolic band from the energy of 0.2 eV. The states near the Fermi level (E_F) appear in the Δ line, which is enhanced in *p*-polarization and $3z^2-r^2$ orbital contributes to the crossing of the E_F . In Fig. 1(b), the dispersion feature is different. Specific features of the changes of dispersion curvatures are explained by the DFT calculation results as the spin majority- and minority-band mixing. These will be resolved by spin-resolved ARPES. Therefore, the *E*- k_x - k_y three-dimensional detection of band dispersions for Fe bulk is achieved, which brings the future developments for high-quality crystal growth and spin detector for spin-resolved ARPES system.

This work was partly supported by KAKENHI Kiban(S) and Toyota-Riken projects.

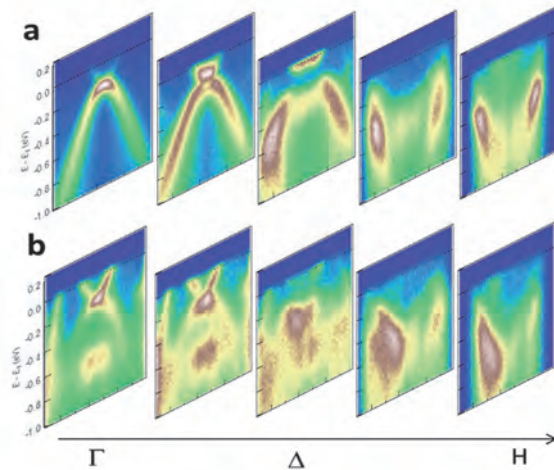


Fig. 1. Polarization dependent APRES images of 100-nm thick Fe film taken at 60 eV for (a) *p*-polarization and (b) *s*-polarization. Each image consists of energy and in-plane momentum. Another in-plane axis is shown in other panel along Γ -H line in the bcc Brillouin zone.

[1] J. Schafer *et al.*, Phys. Rev. B **72** (2005) 155115.

[2] M.Dabrowski *et al.*, Phys. Rev. Lett. **113** (2014) 067203.

[3] Y. Zhang *et al.*, Phys. Rev. B **83** (2011) 054510.

BL5U

Angle-resolved Photoemission Study of *i*-MAX Phase Compound (Mo_{2/3}Ho_{1/3})₂AlC₂

T. Ito^{1,2}, K. Furuta², D. Pinek³, M. Nakatake⁴, S. Ideta⁵, K. Tanaka⁵ and T. Ouisse³¹Nagoya University Synchrotron radiation Research center (NUSR), Nagoya University, Nagoya 464-8603, Japan²Graduate School of Engineering, Nagoya University, Nagoya 464-8603, Japan³Grenoble Alpes, CNRS, Grenoble INP, LMGP, F-38000 Grenoble, France⁴Aichi Synchrotron Research Center, Seto 489-0965, Japan⁵UVSOR Synchrotron Facility, Institute for Molecular Science, Okazaki 444-8585, Japan

MAX phase compounds, i.e., M_{n+1}AX_n where M is a transition metal, A belongs to groups 13-16 and X is the C or N element, have recently been attracted much attention due to their possible application for new class of two-dimensional systems called MXenes by removing A atoms [1]. Among MAX phases, RE-*i*-MAX phase (RE = rare earth), with the general formula (M_{2/3}RE_{1/3})₂AC, was recently synthesized system where the emergence of magnetic phase transition has been reported [2]. In this study, we have performed angle-resolved photoemission spectroscopy (ARPES) on RE-*i*-MAX phase compound (Mo_{2/3}Ho_{1/3})₂AlC (T_N = 7.8 K) to directly investigate the electronic structure of this system, especially the role of 4*f* electrons on its physical properties.

ARPES measurements were performed at the UVSOR-III BL5U. Data were acquired at T = 20 K with hν = 96 eV and 83 eV. It should be noted that the measured axis is defined on the (001)-projected surface hexagonal Brillouin zone (BZ) (Fig. 1(c)).

Figure 1(a) show the ARPES image along the $\overline{\Gamma}$ KM line of (Mo_{2/3}Ho_{1/3})₂AlC at the wide valence band region. PES spectrum obtained by integrating the ARPES intensity over the whole k_x region is shown in Fig. 1(b). It has been found that the electronic structure of (Mo_{2/3}Ho_{1/3})₂AlC is characterized by the non-dispersive bands at the high binding energy of 4-13 eV and the highly-dispersive bands near the Fermi level (E_F), respectively. Since the relative energy positions and intensities of the former are similar with the calculated Ho³⁺ final state multiplets when taking account of the bulk and surface components, the former can be attributed to the localized Ho 4*f* states.

Figures 2(a) and (b) show the band structure near E_F along the $\overline{\Gamma}$ M and $\overline{\Gamma}$ KM lines, respectively. Clear dispersive features matching with the BZ symmetry have been observed clearly. From the comparison with DFT+U calculation (U = 3 eV) along the $\overline{\Gamma}$ FZ and $\overline{\Gamma}$ XY lines, we have found that the observed dispersive features were mostly well reproduced by the calculation. To pursue into the characteristic properties of this system, further studies across the magnetic phase transition are intended.

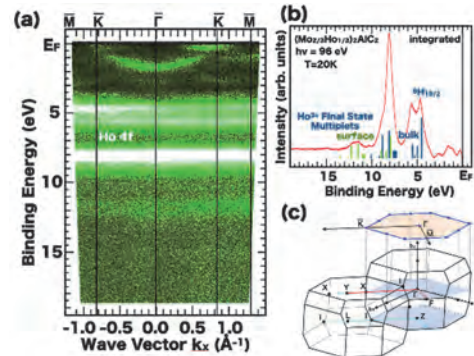


Fig. 1. (a,b) Wide valence band ARPES image along $\overline{\Gamma}$ KM line (a) and AIPES spectrum (b) of (Mo_{2/3}Ho_{1/3})₂AlC acquired with hν = 96 eV. Blue and green vertical bars indicate Ho³⁺ final state multiplets of bulk and surface states, respectively [3]. (c) The monoclinic C2/c BZ of (Mo_{2/3}Ho_{1/3})₂AlC in the extended zone scheme. Red lines are $\overline{\Gamma}$ F and $\overline{\Gamma}$ XY lines. Orange shaded area is projected surface hexagonal BZ.

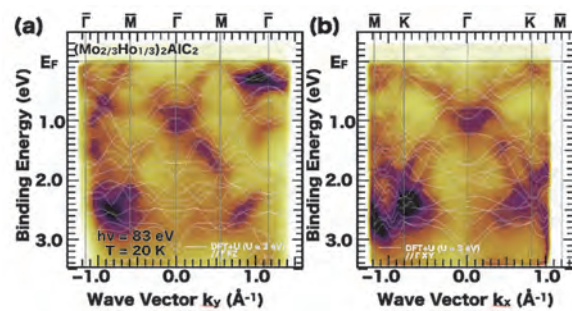


Fig. 2. (a,b) ARPES image of the dispersive features along $\overline{\Gamma}$ M (a) and $\overline{\Gamma}$ KM line (b) of (Mo_{2/3}Ho_{1/3})₂AlC acquired with hν = 83 eV. The white lines in Fig. 2(a) and (b) are DFT+U calculations (U = 3 eV) along the $\overline{\Gamma}$ FZ and $\overline{\Gamma}$ XY lines on the bulk BZ, respectively.

[1] M. Barsoum, MAX phases (Wiley, Weinheim 2013).

[2] Q. Tao, *et al.*, Chem. Mater. **31** (2019) 2476.

[3] J.K. Kang *et al.*, J. Phys. F:Met. Phys. **11** (1981) 121.

BL5U

Change of Fermi Surface Topology in $\text{NdFeAs}_{1-x}\text{P}_x\text{O}_{0.9}\text{F}_{0.1}$ Observed by Angle-Resolved Photoemission Spectroscopy

 S. Miyasaka¹, N. Katayama¹, K. Yoshino¹, Z. H. Tin¹, S. Ideta^{2,3} and K. Tanaka^{2,3}
¹Department of Physics, Graduate School of Science, Osaka University, Toyonaka 560-0043, Japan

²UVSOR Synchrotron Facility, Institute for Molecular Science, Okazaki 444-8585, Japan

³School of Physical Sciences, The Graduate University for Advanced Studies, SOKENDAI, Okazaki 444-8585, Japan

Since the discovery of iron-based superconductors (IBSs), many experimental and theoretical studies have been performed, but the superconducting mechanism of this system has not yet been clarified. The IBSs are multiband systems with several two-dimensional Fermi surfaces (FSs). In this work, we have studied the change of FS topology by P-doping in $\text{NdFeAs}_{1-x}\text{P}_x\text{O}_{0.9}\text{F}_{0.1}$ by angle-resolved photoemission spectroscopy (ARPES). The present system $\text{NdFeAs}_{1-x}\text{P}_x\text{O}_{0.9}\text{F}_{0.1}$ is one of famous IBSs, where P doping induces the change of local crystal structure around Fe site concomitantly with the gradual decrease of critical temperature T_c from 55 K ($x=0$) to 4 K ($x=1.0$) [1,2].

In the present work, we synthesized the single crystals of $\text{NdFeAs}_{1-x}\text{P}_x\text{O}_{0.9}\text{F}_{0.1}$ with various P concentration x s using high pressure technique. The ARPES measurements have been performed in BL5U at Institute of Molecular Science. We have measured ARPES spectra using P- and S-polarization geometries of incident beam to clarify the orbital characters of FSs and electronic bands.

Figure 1 shows the in-plane FS mapping for $x=0, 0.2, 0.4,$ and 0.6 . We observed several FSs around Brillouin zone (BZ) center ($k_x=k_y=0$) and zone corner ($k_x=k_y=\pi$). In this work, we focused the FSs around BZ center. All samples have a large hole FS around BZ center, which is observed in P-polarization and has $3z^2-r^2$ character. In addition, the middle hole FS with xz/yz character is observed in S-polarization in all P concentrations. Only in $x=0.4$ and 0.6 , the additional FS with small size appears.

We have carefully measured polarization dependence of hole bands at BZ center. Figure 2 shows the schematic band dispersions and their orbital characters around BZ center for each P concentration samples. Below Fermi level, we have observed the xy band, and this band has shifted down with increasing P content. On the other hand, the most inner xz/yz band shifts up with increasing x , and this band makes FS above $x=0.4$. This band shows anomalous feature that the orbital character is xy at band top and xz/yz in other parts. In addition, the present results of polarization dependence show the P-doping-induced change of orbital character in the inner and middle hole bands from xz/yz to $(xz+yz)/(xz-yz)$, as shown in Fig. 2.

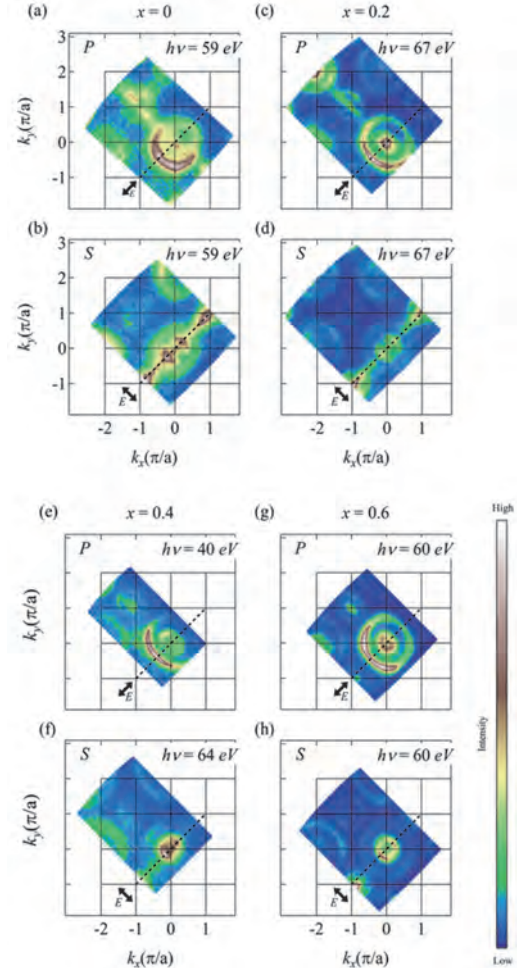


Fig. 1. In plane ARPES intensity mapping for (a, b) $x=0$, (c, d) $x=0.2$, (e, f) $x=0.4$, and (g, h) $x=0.6$ in $\text{NdFeAs}_{1-x}\text{P}_x\text{O}_{0.9}\text{F}_{0.1}$.

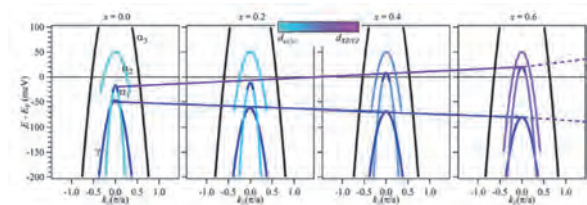


Fig. 2. Schematic band dispersions for $x=0-0.6$ in $\text{NdFeAs}_{1-x}\text{P}_x\text{O}_{0.9}\text{F}_{0.1}$.

[1] A. Takemori *et al.*, Phys. Rev. B **98** (2018) 100501.

[2] S. Miyasaka *et al.*, J. Phys. Soc. Jpn. **82** (2013) 124706.

BL5U

Doping and Temperature Dependence of the Nodal Spectral Weight in Bi2212

 S. Ideta^{1,2}, S. Ishida³ and K. Tanaka^{1,2}
¹UVSOR Synchrotron Facility, Institute for Molecular Science, Okazaki 444-8585, Japan

²School of Physical Sciences, The Graduate University for Advanced Studies, SOKENDAI, Okazaki 444-8585, Japan

³National Institute of Advanced Industrial Science and Technology, Tsukuba 305-8568, Japan

Which momentum space on Fermi surfaces (FSs) contributes to superconductivity is one of the important issues to elucidate the mechanism of high- T_c superconductivity. According to the Fermi arc picture [1], carrier concentration is proportional to the Fermi arc length and the effective SC gap scales with T_c [1,2]. These results suggest that the superconductivity near the nodal direction plays an important role of superconductivity in cuprates. On the other hand, there is a report that spectral weights (SWs) which are distributed over the FSs, observed by angle-resolved photoemission spectroscopy (ARPES) would contribute to high- T_c superconductivity in cuprates [3]. Therefore, it has been unclear which parameters contribute to superconductivity dominantly so far.

In the present report, we studied that to what extent the nodal region on FSs contributes to superconductivity in the cuprate superconductors. We have performed an ARPES experiment to investigate doping and temperature dependence of SW in the nodal direction.

High-quality single crystals of underdoped (UD), optimally doped (OPT), and overdoped (OD) $\text{Bi}_2\text{Sr}_2\text{CaCu}_2\text{O}_{8+\delta}$, Bi2212 ($T_c = 70, 92,$ and 75 K) were grown by the TSFZ method. ARPES experiments were carried out at BL5U of UVSOR-III Synchrotron. Clean sample surfaces were obtained for the ARPES

measurements by cleaving single crystals *in-situ* in an ultrahigh vacuum better than 5×10^{-9} Pa, and total energy resolution was set at 15 meV. The measurements were performed at 20 K – 110 K.

Figures 1(a)-1(c) show AREPS spectra of symmetrized energy-distribution curves (EDCs) in the nodal direction taken at $T = 20$ K, 90 K, and 110 K for OD75, OPT92, and UD70 samples. EDCs are subtracted as shown in Figs. 1(d)-1(f) to see the change of SW in the SC and normal states. The difference is shown by blue shaded area in Figs. 1(d)-1(f) and the area is plotted in Fig. 1(g). In contrast with the speculation that the nodal momentum region is related with T_c , the nodal SW is almost independent of hole concentration and T_c . The present result suggests that we need to study the momentum dependence of SW on entire FSs in future work.

- [1] M. Oda *et al.*, Phys. Soc Jpn. **69** (2000) 983.
- [2] S. Ideta *et al.*, Phys. Rev. B **85** (2012) 104515.
- [3] T. Kondo *et al.*, Nature **457** (2009) 296.
- [4] M. R. Norman *et al.*, Phys. Rev. B **57** (1998) R11093.
- [5] D.A. Shirley, Phys. Rev. **55** (1972) 4709.

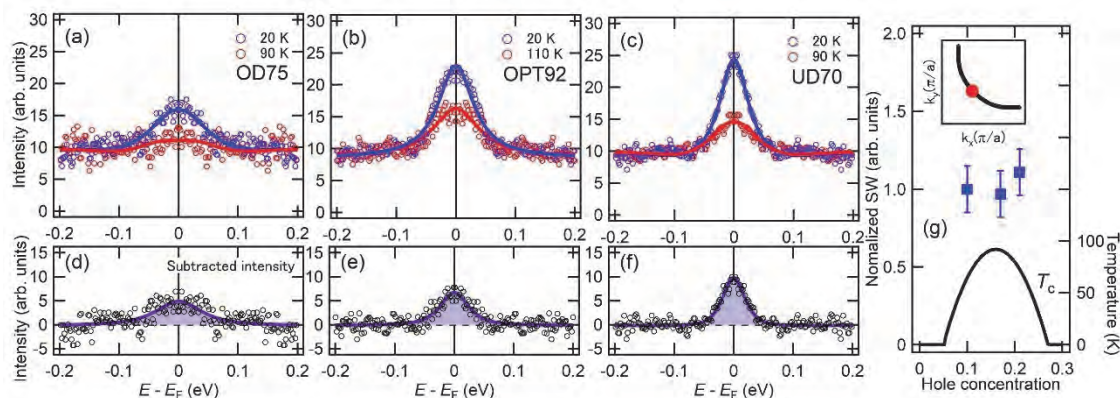


Fig. 1. Doping and temperature dependence of double-layer cuprate Bi2212. (a)-(c) Temperature dependence of symmetrized EDCs in the SC and normal states. The data is fitted by phenomenological function [4] including Shirley-type background [5]. (d), (e), and (f) are symmetrized EDCs obtained from subtraction of EDC in the SC and normal states shown in (a), (b), and (c), respectively. Shaded area shown in panels (d)-(f) is plotted in panel (g) with the T_c dome of Bi2212 as a function of hole concentration.

BL6B

Infrared Reflectivity Spectra for Undoped and *n*-type Mg₂Si Crystals

T. Tanimoto¹, M. Kitaura², H. Udono³ and A. Ohnishi²

¹Graduate School of Science and Engineering, Yamagata University, Yamagata 990-8560, Japan

²Faculty of science, Yamagata University, Yamagata 990-8560, Japan

³Ibaraki University, College of Engineering, Hitachi 316-8511, Japan

Mg₂Si belongs to the cubic system with the space group Fm-3m, and it has anti-fluorite structure [1]. This material is called environmentally-friendly semiconductor, because it is composed of nontoxic and earth-abundant elements. Mg₂Si attracts much attentions as optoelectronic and thermoelectric substance. The band-gap energy is reported 0.61 eV [2], and thus Mg₂Si can respond to the illumination of mid-infrared (MIR) light [3]. This feature opens the way to apply to a MIR detector. Actually, pn-junction Mg₂Si diodes were fabricated, and they showed a clear response for photons with the energies above 0.6 eV [3]. Despite an industrially important material, free carrier behaviors in Mg₂Si have been little studied so far. Plasma oscillation is regarded as a fingerprint for the creation of free carriers in semiconductors. The information on such plasma oscillation can be obtained from the measurement of reflectivity in the infrared region. In the present study, we have measured reflectivity spectra of undoped and *n*-type Mg₂Si crystals at various temperatures. Because low grade reagents were used as starting materials, carriers were naturally introduced, resulting in *n*-type Mg₂Si crystals. The carrier concentrations of undoped and *n*-type Mg₂Si crystals were 1.8×10^{15} and 2.2×10^{18} cm⁻³. The surfaces of crystals were mechanically polished.

Figure 1 shows reflectivity spectra of an undoped *n*-Mg₂Si crystal. Red and blue lines indicate reflectivity spectra at 20 and 300 K, respectively. A prominent peak due to Reststrahlen band is observed around 300 cm⁻¹, in good agreement with the previous paper [4]. The spectral shape was approximated by a Lorentz oscillator model. No Drude peak due to the plasma oscillation of free carriers is found in the wavenumber region below the Reststrahlen band. The reflectivity spectrum at 20 K is slightly changed with increasing temperature.

Figure 2 shows reflective spectra of an *n*-type Mg₂Si crystal. Red and blue lines indicate reflectivity spectra at 20 and 300 K, respectively. The Reststrahlen band deforms compared to that for the undoped crystal. Furthermore, a spectral change in the low-wavenumber region of the Reststrahlen band is conspicuous. Because of high-carrier concentration in the *n*-type Mg₂Si crystal, the Drude peak due to plasma oscillation of free carriers appears in the low-wavenumber region of the Reststrahlen band. The reflectivity spectrum at 20 K is slightly changed with increased temperature. This result implies that the carrier concentration is independent of temperature.

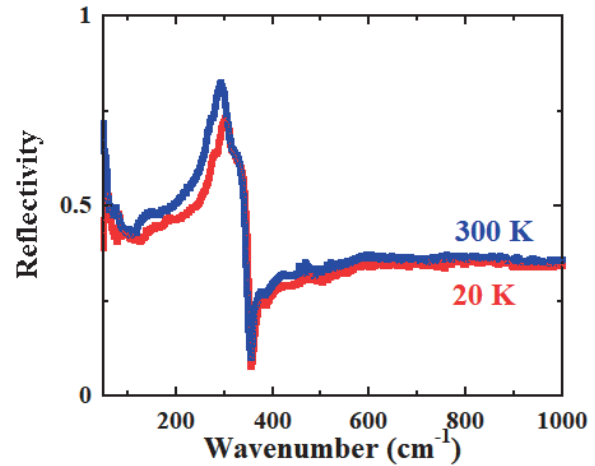


Fig. 1. Reflective spectra of an undoped Mg₂Si crystal. Red and blue lines indicate reflectivity spectra at 20 and 300 K, respectively.

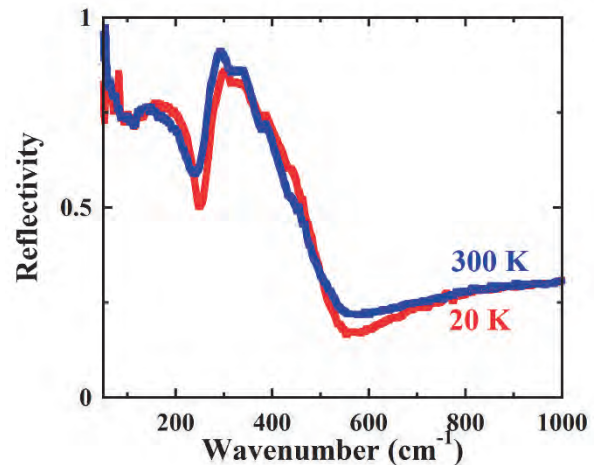


Fig. 2. Reflective spectra of an *n*-type Mg₂Si crystal. Red and blue lines indicate reflectivity spectra at 20 and 300 K, respectively.

- [1] N. V. Morozova *et al.*, J. Appl. Phys. **115** (2014) 213705.
- [2] K. Sekino *et al.*, Physics Procedia, **11** (2011) 171.
- [3] H. Udono *et al.*, Jpn. J. Appl. Phys. **54** (2015) 07JB06.
- [4] D. McWilliams *et al.*, Phys. Rev. **130** (1963) 2248.

BL6B

Optical Evidence of Current-Induced Local-to-Nonlocal Transition of SmS

 H. Watanabe^{1,2}, S. Tatsukawa², K. Imura³, H. S. Suzuki⁴, N. K. Sato³ and S. Kimura^{1,2,5}
¹Graduate School of Frontier Biosciences, Osaka University, Suita 565-0871, Japan

²Department of Physics, Graduate School of Science, Osaka University, Toyonaka 560-0043, Japan

³Department of Physics, Graduate School of Science, Nagoya University, Nagoya 464-8602, Japan

⁴Institute for Solid State Physics, The University of Tokyo, Kashiwa 277-8581, Japan

⁵Institute for Molecular Science, Okazaki 444-8585, Japan

Samarium monosulfide SmS is a black-colored semiconductor with an energy gap of about 0.1 eV at ambient pressure. Applying pressure above 0.7 GPa, the electronic properties changes to a golden-colored metallic one with the change of Sm valence, namely Black-to-Golden phase Transition (BGT) [1,2]. The origin of the BGT is now still under debate. However, one possibility of the transition between Bose-Einstein condensation (BEC) and BCS state of excitons is discussed [3], but no definitive evidence has been obtained.

Recently, Ando *et al.* reported that the nonlinear relation between the voltage (V) and electric current (I) with increasing current at lower temperatures than 100 K, which suggests the electrical resistivity changes discontinuously [4]. To investigate the origin of the nonlinear V/I curve and the relation to the BGT, we measured the current and temperature dependence of the reflectivity spectrum in the THz region using the THz microscope at BL6B to detect the current-induced electronic structural change.

The single crystalline SmS with the typical sample size of $1 \times 1 \times 1 \text{ mm}^3$ was mounted in a liquid-helium-cooled cryostat and connected to the current source. Figure 1 shows the I -dependence of the reflectivity spectrum at temperatures (T) of 60 K and 150 K. At $T = 60 \text{ K}$ and $I = 0.0 \text{ A}$, only a large peak originating from a TO-phonon was observed at 200 cm^{-1} , which suggests carriers do not exist. With increasing electric current, the reflectivity intensity at the lowest wavenumber increases suggesting the Drude weight and the carrier density increase. At $T = 150 \text{ K}$, the Drude weight is visible even at $I = 0.0 \text{ A}$. To evaluate the effective carrier density N^* ($= N_0 m_0 / m^*$, where N_0 is the carrier density, and m_0 and m^* the rest mass and the effective mass of an electron), we fitted the reflection spectra [$R(\omega)$] by the Drude-Lorenz function shown below.

$$R(\omega) = c \left| \frac{1 - \sqrt{\tilde{\varepsilon}(\omega)}}{1 + \sqrt{\tilde{\varepsilon}(\omega)}} \right|^2,$$

$$\tilde{\varepsilon}(\omega) = \varepsilon_\infty - \frac{(\omega_p^f)^2}{\omega^2 - i\omega\Gamma_f} + \frac{(\omega_p^b)^2}{(\omega_0^2 - \omega^2) - i\omega\Gamma_b},$$

where c is the fitting constants of reflectivity, ε_∞ the background of dielectric constant, ω_p^f (ω_p^b) and Γ_f (Γ_b) the plasma frequency and damping constant of free carriers (phonons). Figure 2 shows the current dependence of the ω_p^{f2} , which is proportional to N^* . ω_p^{f2} as well as N^* increase with applied current both at

60 K and 150 K, which suggests the current-induced local-to-nonlocal transition of SmS.

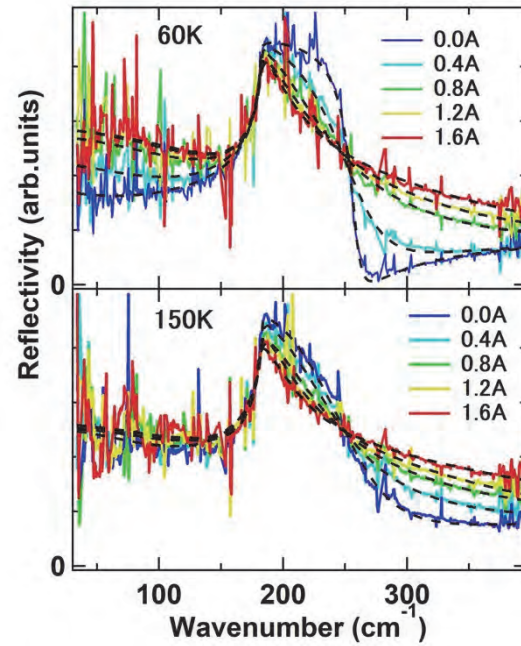


Fig. 1. Current dependence of THz reflectivity spectra at 60 K and 150 K. The dashed black lines result from the Drude-Lorenz function fitting.

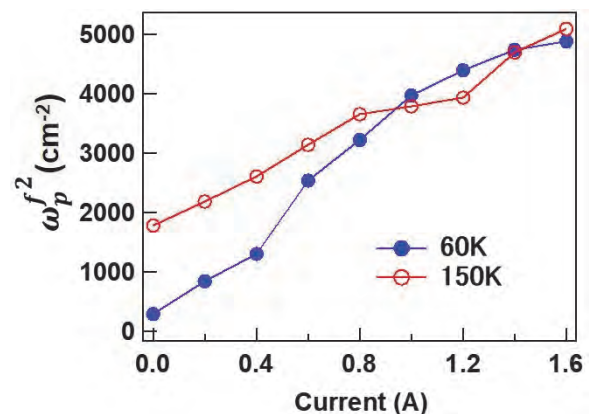


Fig. 2. The current dependence of the square of plasma frequency of carriers.

- [1] A. Jayaraman *et al.*, PRL **25** (1970) 1430.
- [2] T. Mizuno *et al.*, JPSJ **77** (2008) 113704.
- [3] B. I. Halperin and T. M. Rice, RMP **40** (1968) 755.
- [4] H. Ando *et al.*, JPS Conf. Proc. **30** (2020) 011132.

BL6B

Development of an Infrared Spectro-microtomography Using a Mid-IR Supercontinuum Laser: Preliminary Report

H. Yabuta¹, Y. Ikemoto², F. Teshima³ and K. Tanaka³

¹Department of Earth and Planetary Systems Science, Hiroshima University, Higashi-Hiroshima 739-8526, Japan

²Japan Synchrotron Radiation Research Institute (JASRI), Sayo 679-5198, Japan

³UVSOR Synchrotron Facility, Institute for Molecular Science, Okazaki 444-8585, Japan

This study aims to develop a three-dimensional infrared spectro-microtomography using a mid-infrared supercontinuum laser, for investigating the three-dimensional spatial distributions of micron-sized organic materials and hydrous minerals of extraterrestrial samples and for understanding the chemical history in the early Solar System.

The first step for establishing the element techniques of three-dimensional infrared spectro-microtomography was to introduce a laser optical system in a FTIR Linear Array Imaging Microscope (JASCO) at an IR BL6B, UVSOR. For this purpose, we purchased a mid-infrared supercontinuum laser (fiber laser) (NOVAE, Coverage, 782 mW, 1.9-3.9 μm) (Fig. 1) in September, 2019 (Hiroshima University). As the infrared laser is invisible and it is not easy to check its optical path, a red semiconductor laser (5 mW) was firstly used as an external light to check the shape and size of the laser. Introduction of the red laser in the spectroscopy was confirmed by detection of a sharp absorption peak at 14850 cm^{-1} in an FTIR spectrum (Fig. 2). Introduction of the red laser in the center of the field of view of the infrared microscopy was confirmed as well by optimization of spectral intensity and adjusting the laser position. However, an absorption peak was not detected at 14850 cm^{-1} sedue to the detection upper limit (7800 cm^{-1}) of the MCT detector. After these test experiments using a red laser, a fiber laser was introduced in the infrared microscopy (its intensity was reduced to 3 mW). The infrared spectrum of the fiber was detected, but, a spectrum at the longer wavelength (< 3500 cm^{-1}) was not detected, probably due to absorption by a quartz window and/or CaF beam splitter.

In order to solve the problem, a quartz window and CaF beam splitter were replaced with a BaF₂ window and KBr beam splitter, respectively. As a result, the fiber laser-derived absorption was detected in the range of 8000-2000 cm^{-1} by the infrared microscope (Fig. 3). The laser spectral intensity was also improved. Under the laser condition, an FTIR spectrum of CaCO₃ powder was preliminarily obtained.

In future, we will set up a rotation stage and try to acquire the 3D FTIR spectra of several extraterrestrial samples by using a newly-upgraded fiber laser.



Fig. 1. Photo of the mid-infrared supercontinuum laser (Fiber laser) (NOVAE, Coverage, 782 mW, 1.9 - 3.9 μm) introduced in a BL6B, UVSOR.

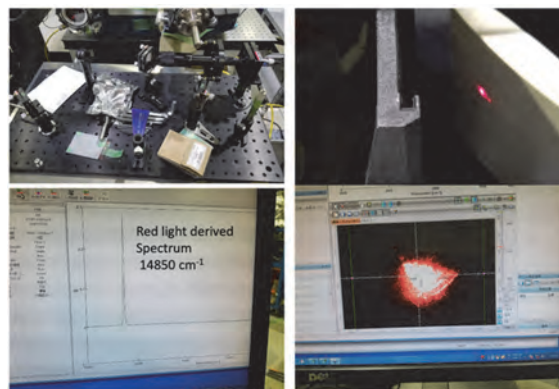


Fig. 2. Optical system using a red semiconductor laser (upper left), introduction of the red laser in the spectroscopy (upper right) and microscopy (bottom right), and FTIR spectrum of the red laser at 14850 cm^{-1} (bottom left).

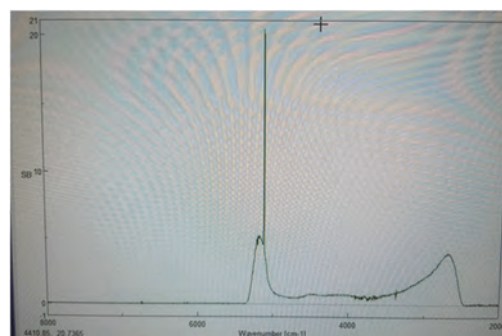


Fig. 3. FTIR spectrum of the mid-infrared supercontinuum laser acquired by the infrared microscopy.

Acknowledgement: This work was supported by JSPS KAKENHI Grant Number JP 19H01954

BL6B

Far-infrared Absorption Measurements on Single Crystal Pentacene

Y. Nakayama and J. Miyamoto

Department of Pure and Applied Chemistry, Faculty of Science and Technology, Tokyo University of Science, Noda 278-8510, Japan

Coupling of lattice- as well as molecular-vibrations with the electronic states is a crucial factor for dominating the charge carrier transport in crystalline organic semiconductors. In fact, it has been clearly demonstrated that both intra- and inter-molecular vibrations deforms the valence bands of single crystal rubrene, a representative p-type organic semiconductor material exhibiting the charge carrier mobility over $10 \text{ cm}^2 \text{ V}^{-1} \text{ s}^{-1}$ [1]. In order to understand the natures of such electron-phonon (vibration) coupling, experimental measurements not only for the electronic (band) structures but also for the inter- and intra-molecular vibrational modes has been demanded.

Pentacene is another representative p-type organic semiconductor material of considerable charge carrier mobility. In its single crystal phase, energy-momentum dispersion relationships have been demonstrated by angle-resolved photoelectron spectroscopy [2]. The inter-molecular vibrational modes and their coupling strength with the electronic states have been predicted theoretically [3]. Experimentally, Raman spectroscopy measurements were conducted on the single crystal pentacene to characterize the symmetric lattice and low-frequency molecular vibrational modes [4]. In the present work, we attempted far-infrared absorption measurements on the single crystal pentacene for complementation of its vibrational characteristics.

Far-infrared absorption spectra were obtained at BL6B by using a Michelson-type interferometer (Bruker Vertex70v) and a bolometer (Infrared Laboratories). A pentacene single crystal (PnSC) sample was fixed on a CVD diamond plate (thickness 0.4 mm) and was attached to a home-made sample holder for adjustment of the in-plane azimuthal angle (Fig. 1(a)). The crystallographic orientation of the PnSC sample was settled using the polarized optical microscopy (Fig. 1(b)). The spectra were collected in a transmission geometry. All the measurements were conducted at room temperature.

Figure 2(a) shows far-infrared absorbance spectra of the PnSC and blank diamond samples. Although the signal intensity was small, spectral contribution of PnSC could be extracted by dividing the absorbance of the PnSC/diamond sample by that of blank sample, as shown in Fig. 2(b). A peak in 450 - 500 cm^{-1} can be assigned to low-frequency intra-molecular vibration modes (Fig. 2(c)). On the other hand, whereas the signal in the inter-molecular phonon range was faint, intensity in 100 - 200 cm^{-1} may be attributed to a_u lattice vibration modes predicted theoretically [3].

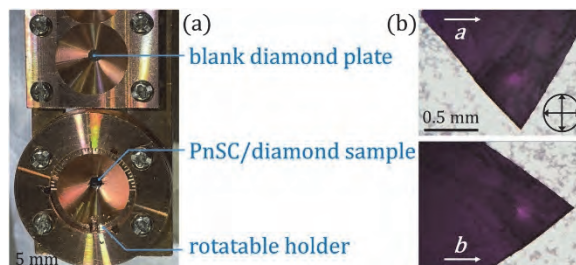


Fig. 1. (a) Photograph of the sample holder used in this work. (b) Polarized micrographs of the sample.

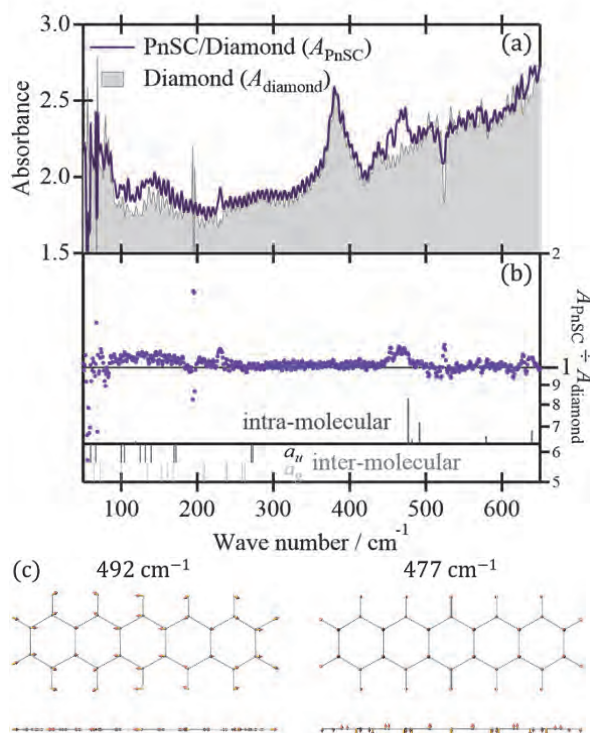


Fig. 2. (a) Far-infrared absorbance of the PnSC/diamond and (blank) diamond plate samples. (b) $A_{\text{PnSC}}/A_{\text{diamond}}$ spectrum where the background oscillation was reduced by Fourier filtering. Dipole moment for intra-molecular vibrations (calculated with Gaussian09, b3lyp, 6-31g*) and wave number distributions for inter-molecular vibrations in the symmetry a_g and a_u [3] are also shown. (c) Calculated intra-molecular vibration for 492 cm^{-1} and 477 cm^{-1} .

- [1] F. Bussolotti *et al.*, Nat. Commun. **8** (2017) 173.
 [2] Y. Nakayama *et al.*, J. Phys. Chem. Lett. **8** (2017) 1259; *ibid.*, J. Mater. Res. **33** (2018) 3362.
 [3] A. Girlando *et al.*, J. Chem. Phys. **135** (2011) 084701.
 [4] R. Valle *et al.*, J. Phys. Chem. B **108** (2004) 1822.

BL7U

Energy Shift of Dirac Point in $\text{Ni}_{1-x}\text{Pd}_x\text{Te}_2$ Observed by Angle-Resolved Photoemission Spectroscopy

S. Miyasaka¹, K. Yoshino¹, N. Katayama¹, S. Ideta^{2,3} and K. Tanaka^{2,3}¹Department of Physics, Graduate School of Science, Osaka University, Toyonaka 560-0043, Japan²UVSOR Synchrotron Facility, Institute for Molecular Science, Okazaki 444-8585, Japan³School of Physical Sciences, The Graduate University for Advanced Studies, SOKENDAI, Okazaki 444-8585, Japan

Transition metal dichalcogenides with layered structures show a variety of physical phenomena such as the charge density wave, superconductivity and so on. Recent experimental studies on Pd and Pt dichalcogenides with CdI_2 -type structure have indicated that these systems have new exotic electronic state, type II Dirac fermion state [1-3]. The results of angle resolved photoemission spectroscopy (ARPES) have revealed that the Dirac point exists at $(0,0,k_z)$ and the Dirac cone is strongly tilted along Γ -A direction (k_z -direction) in the Pd and Pt dichalcogenides. In these compounds, the Dirac point is located below Fermi level. For example, one of the target materials in the present work, PdTe_2 , the energy level of Dirac point is about -0.6 eV below Fermi level. On the other hand, the theoretical study has demonstrated that another end member NiTe_2 has Dirac point just above Fermi level (about +0.02 eV).

In the present work, we have tried to control the energy level of Dirac point in NiTe_2 - PdTe_2 solid solution system. In this system $\text{Ni}_{1-x}\text{Pd}_x\text{Te}_2$, we expected that the Dirac point energy shifts from +0.02 eV to -0.6 eV with increasing Pd doping level. We have performed the measurements of ARPES in $\text{Ni}_{1-x}\text{Pd}_x\text{Te}_2$ to observe the electronic structure and Dirac cone directly. The single crystals of $\text{Ni}_{1-x}\text{Pd}_x\text{Te}_2$ were grown by Te flux method. The ARPES experimental was carried out at BL7U in UVSOR Facility, Institute for Molecular Science.

The band calculation in consideration of spin-orbit interaction has indicated that as well as Pd and Pt systems, NiTe_2 is the type II Dirac fermion system with the Dirac point at $(0,0,k_z)$. The results of ARPES also suggested the existence of Dirac point at $(0,0,k_z)$. We measured the band dispersion along $k_{//}$ ($k_{//} \perp k_z$) at different k_z . At $k_z=0$, there are several hole-like bands around Γ points. With increasing k_z , the energy level of the hole band around Γ point shifts down, and the top of this band is located just above Fermi level at $k_z \sim 0.37c^*$. (Fig. 1(a)) At this k_z , the band dispersion shows a linear $k_{//}$ -dependence around Brillouin zone center. This result has suggested that Dirac point exists very near Fermi level at $(0,0, \sim 0.37c^*)$ in NiTe_2 . The observed band dispersion is roughly consistent with the band calculation, as shown in Fig. 1(a).

By Pd doping, the electronic band around Brillouin zone center shifts down at the same k_z ($\sim 0.37c^*$). As presented in Fig. 1(b), the crossing point of the linear band dispersion, i.e. Dirac point has been observed just below Fermi level at Pd-doping level $x=0.04$. With

increasing Pd-doping level x , the energy of Dirac point shifts down to deeper binding energy region, as shown in Figs. 1(c) and (d). The present results indicate that the Dirac point energy level can be continuously controlled by Pd substitution of Ni site in NiTe_2 .

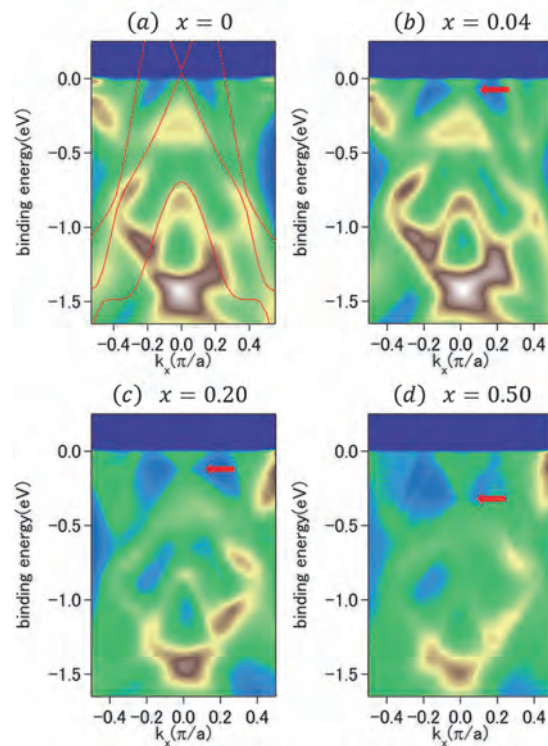


Fig. 1. ARPES intensity plot along $k_{//}$ (parallel to Γ -M direction) at $(0, 0, 0.37c^*)$ for (a) $x=0$, (b) $x=0.04$, (c) $x=0.20$, and (d) $x=0.50$ in $\text{Ni}_{1-x}\text{Pd}_x\text{Te}_2$. In panel (a), the calculated band dispersion is also shown by red solid lines. Red arrows indicate the position of Dirac point in panels (b), (c) and (d).

[1] H.-J. Noh *et al.*, Phys. Rev. Lett. **119** (2017) 016401.[2] K. Zhang *et al.*, Phys. Rev. B **96** (2017) 125102.[3] B. Ghosh *et al.*, Phys. Rev B **100** (2019) 195134.

BL7U

Reconstruction of the Electronic Structure in FeSe_{1-x}Te_x/CaF₂

K. Nakayama^{1,2}, R. Tsubono¹, F. Nabeshima³, N. Shikama³, T. Ishikawa³, Y. Sakishita³,
A. Maeda³, T. Takahashi^{1,4,5} and T. Sato^{1,4,5}

¹Department of Physics, Tohoku University, Sendai 980-8578, Japan

²Precursory Research for Embryonic Science and Technology, Japan Science and Technology Agency,
Tokyo 102-0076, Japan

³Department of Basic Science, the University of Tokyo, Tokyo 153-8902, Japan

⁴Center for Spintronics Research Network, Tohoku University, Sendai 980-8577, Japan

⁵WPI Research Center, Advanced Institute for Materials Research, Tohoku University, Sendai 980-8577, Japan

Iron selenide FeSe, a superconductor with the critical temperature T_c of ~ 8 K, is recently attracting great attention because of the structural simplicity and various exotic properties such as anisotropic superconductivity and electronic nematicity without long-range magnetic order. These properties are sensitive to chemical substitution, high-pressure application, and/or carrier doping. Therefore, one can investigate the interplay between nematicity and superconductivity while controlling some physical parameters. In this respect, isovalent-substituted FeSe_{1-x}Te_x films grown on CaF₂ substrate (FeSe_{1-x}Te_x/CaF₂) offer an excellent platform because nematicity is realized in FeSe/CaF₂ ($x=0$) as in bulk FeSe and the highest T_c of 23 K among non-carrier-doped FeSe-based compounds has been reported at the critical Te concentration x_c of ~ 0.2 at ambient pressure [1-3]. Also, FeSe_{1-x}Te_x/CaF₂ is a candidate to realize 'high- T_c ' topological superconductivity hosting Majorana fermions because possible topological superconductivity has been proposed for the bulk counterpart.

In this study, we performed systematic angle-resolved photoemission spectroscopy (ARPES) measurements of FeSe_{1-x}Te_x/CaF₂ with a series of different x values, and determined the evolution of the electronic structure across $x_c = 0.2$ [4].

High-quality compressive-strained FeSe_{1-x}Te_x thin films with the thicknesses of approximately 400 layers were grown on CaF₂ substrate by pulsed laser deposition. High-resolution ARPES measurements were performed by using a MBS-A1 spectrometer at BL7U with linearly-polarized energy-tunable photons of 7-25 eV.

Figure 1 shows a comparison of the electronic structure between $x = 0$ and 0.4. At $x = 0$, The near- E_F band structure around the Γ point consists of two highly dispersive bands and a relatively flat band [red curves in Fig. 1(b)], which are ascribed to the Fe $3d_{xz}/d_{yz}$ orbitals and the Fe $3d_{xy}$ orbital, respectively. Around the M point, there are two holelike bands [Fig. 1(c)], which are attributed to the d_{xz}/d_{yz} -derived bands originating from the lifting of orbital degeneracy by nematicity. Due to the nematicity, the Fermi surface shape around the M point is elongated along k_x [Fig. 1(a)]. On the other hand, the Fermi surface around the M point is more rounded for $x = 0.4$ [Fig. 1(d)]. This result signifies the absence of nematicity for $x = 0.4$ [Fig. 1(f)]. In addition, a

remarkable x dependence beyond the effect of nematicity manifests itself in the band dispersion around the Γ point [Fig. 1(e)]. Namely, the top of the d_{xy} band shifts upward and nearly touches E_F at $x = 0.4$, resulting in an increase of the density of states. The appearance of the d_{xy} orbital character around the Γ point also modifies an interband (intraorbital) scattering between the hole and electron pockets, which has been proposed as a key to controlling the superconducting and nematic properties. Our systematic measurements revealed that these changes in the electronic structure occur in the close vicinity of x_c , where the T_c shows a large jump. The present results provide important insights into the interplay among high- T_c superconductivity, nematicity, and orbital degrees of freedom.

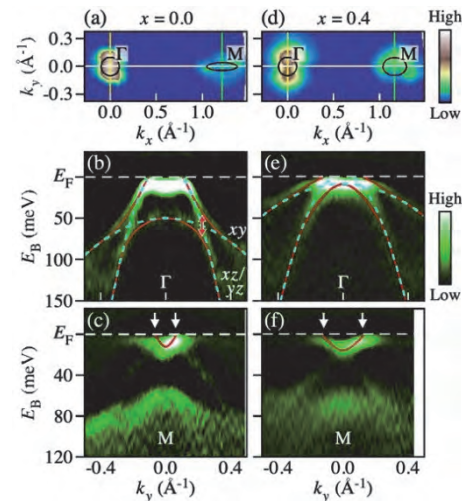


Fig. 1. (a)-(c) Fermi surface and the band dispersions around the Γ and M points for FeSe/CaF₂. (d)-(f) Same as (a)-(c) but for FeSe_{0.6}Te_{0.4}/CaF₂.

- [1] F. Nabeshima *et al.*, Appl. Phys. Lett. **103** (2013) 172602.
- [2] Y. Imai *et al.*, Proc. Natl. Acad. Sci. USA **112** (2015) 1937.
- [3] Y. Imai *et al.*, Sci. Rep. **7** (2017) 46653.
- [4] K. Nakayama *et al.*, Phys. Rev. Research **3** (2021) L012007.

BL7U

Temperature Dependence of Nodal Spectral Weight in High- T_c Cuprate Superconductor Bi2212

 S. Ideta^{1,2*}, S. Ishida³ and K. Tanaka^{1,2}
¹UVSOR Synchrotron Facility, Institute for Molecular Science, Okazaki 444-8585, Japan

²School of Physical Sciences, The Graduate University for Advanced Studies, SOKENDAI, Okazaki 444-8585, Japan

³National Institute of Advanced Industrial Science and Technology, Tsukuba 305-8568, Japan

Angle-resolved photoemission spectroscopy (ARPES) is a powerful tool to investigate the electronic structure in the normal and superconducting states of superconductors [1-3]. The essential origin of superconductivity is coupled electrons so-called ‘‘Cooper pairs’’, and these coupled electrons condense into the ground state. The volume of the condensed electrons, namely, the superfluid density, is strongly related to the spectral weight (SW) obtained by ARPES. Temperature dependence of SW might give information of an important role of superconductivity in strongly electron correlated system [4].

According to the 2-dimensional t - J models [4], SW abruptly changes upon a transition from the projected Fermi-liquid (pFL) state with electron correlation to the resonating valence bond (RVB) state. In the present study, we have performed an ARPES experiment to investigate temperature dependence of SW in the nodal direction in order to understand the electron correlation of the double-layer $\text{Bi}_2\text{Sr}_2\text{CaCu}_2\text{O}_{8+\delta}$, (Bi2212) as reported in the previous ARPES study [5,6].

High-quality single crystals of optimally doped Bi2212 ($T_c = 92$ K) were grown by the TSFZ method. ARPES experiments were carried out at BL7U of UVSOR-III Synchrotron. Clean sample surfaces were obtained for the ARPES measurements by cleaving single crystals *in-situ* in an ultrahigh vacuum better than 7×10^{-9} Pa, and total energy resolution was set at 6-8 meV. The measurements were performed at 20 K – 108 K.

Figure 1 shows the ARPES result of temperature dependence of the nodal SW in Bi2212 taken at $h\nu = 8$ eV. In order to estimate the change of SW, we have measured the temperature dependence from well below (20 K) to above T_c (108 K) as shown in Fig. 1(a). Energy-distribution curve (EDC) at the nodal point on the Fermi surface (FS) are extracted and symmetrized to remove the contribution from Fermi-Dirac function. As shown in Fig. 1(b), difference of the intensity for EDC, $I - I_{108\text{K}}$, at certain temperature is estimated from subtraction by using the EDC at 108 K, $I_{108\text{K}}$. We estimated SW obtained from Fig. 1(b) and the result is plotted as a function of temperature in Fig. 1(c). One can see that SW abruptly changes at the superconducting phase transition shown by a dotted line. Therefore, the temperature dependence of the nodal SW is related with the superfluid density and is consistent with the previous ARPES study of triple-layer cuprate $\text{Bi}_2\text{Sr}_2\text{Ca}_2\text{Cu}_3\text{O}_{10+\delta}$ [5]. This result suggests that the suppression of SW

would be universal behavior in the strongly electron correlated system. In addition, the present result is consistent with the RVB picture based on the 2-dimensional t - J model. We will study the temperature dependence of SW on the entire FS as future work.

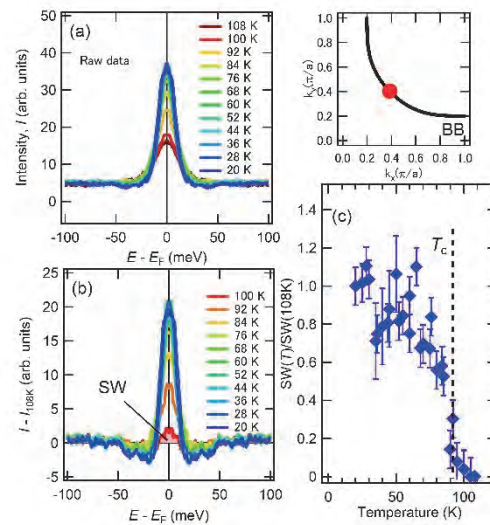


Fig. 1. Temperature dependence of optimally doped Bi2212 in the nodal direction. (a) Raw symmetrized ARPES spectra well below and above T_c . (b) Subtracted symmetrized EDC. As an example of the spectral weight (SW), shaded area (red) at 100 K is shown. (c) SW is plotted as a function of temperature. Several experiments are demonstrated in Bi2212 to confirm the data accuracy. BB shown in the schematic FS is the bonding band in Bi2212

- [1] Z.-X. Shen *et al.*, Phys. Rev. Lett. **70** (1993) 1553.
 - [2] A. Lanzara *et al.*, Nature **412** (2001) 510.
 - [3] M. R. Norman *et al.*, Phys. Rev. B **63** (2001) 148508 (R).
 - [4] C-P. Chou, T. K. Lee and C-M. Hou, Journal of Physics and Chemistry of Solids **69** (2008) 2993.
 - [5] S. Kudo *et al.*, Phys. Rev. B **92** (2015) 195123.
 - [6] S. Kudo, Master Thesis, Tokyo University (2008).
- *Present address: Hiroshima Synchrotron Radiation Center, Hiroshima University 739-0046

BL7U

Angle-resolved Photoemission Study of Solid Electrolytes $\text{Li}_x\text{La}_{(1-x)/3}\text{NbO}_3$ Bulk Single Crystal

T. Ito^{1,2}, R. Yamamoto², M. Nakatake³, S. Ideta⁴, K. Tanaka⁴, Y. Fujiwara⁵ and Y. Iriyama²¹Nagoya University Synchrotron radiation Research center (NUSR), Nagoya University, Nagoya 464-8603, Japan²Graduate School of Engineering, Nagoya University, Nagoya 464-8603, Japan³Aichi Synchrotron Research Center, Seto 489-0965, Japan⁴UVSOR Synchrotron Facility, Institute for Molecular Science, Okazaki 444-8585, Japan⁵Faculty of Engineering, Shinshu University, Nagano 380-8553, Japan

In recent years, as the use of secondary Li-ion batteries has expanded, the development of all-solid batteries using solid electrolytes has progressed to realize greater safety, wider thermal stability range, easier material handling. To understand their electronic properties and transport characteristics, the electronic structure is essentially important. However, there are few examples of experimental observations on solid electrolytes. In this study, we performed direct observation of the electronic structure of $\text{Li}_x\text{La}_{(1-x)/3}\text{NbO}_3$ (LLNO; $x = 0.07 - 0.08$) bulk single crystals [1,2] by using angle-resolved photoemission spectroscopy (ARPES) in order to clarify the electronic structure of solid electrolytes, especially the electronic band structure.

ARPES measurements were performed at the UVSOR-III BL7U. Data were acquired with $h\nu = 18$ eV at room temperature. To minimize photoirradiation damage, photon flux was sufficiently reduced during all measurements. Single crystals were cleaved *in situ* along (001) plane, where partially occupied (A1) and unoccupied cation layers (A2) appear alternately (Fig.1(b)).

Figure 1(a) shows the ARPES spectra along ion-conducting [100] axis of LLNO. At $k = 0 \text{ \AA}^{-1}$ (Γ), two peaks around 5 (α) and 6 eV (β) appear dominantly relative to 9 eV feature (δ). On the other hand, the former becomes smaller than the latter at $k = -0.4 \text{ \AA}^{-1}$ (X), following the additional feature around 7 eV (γ). Furthermore, it has been found that the feature γ shows clear dispersion from 6 eV splitting from the peak β along the Γ X line.

To show the observed features clearly, we show the band structure obtained by mapping the ARPES intensity in Fig. 2. It has been found that the electronic structure around the valence band maximum of LLNO seems to be characterized by the band gap of 2~3 eV formed by the edge of almost non-dispersive α band. In addition, highly dispersive feature γ appears among the non-dispersive β and δ bands. We expect that the present result is the first experimental observation of the band structure of solid electrolytes for Li-ion battery.

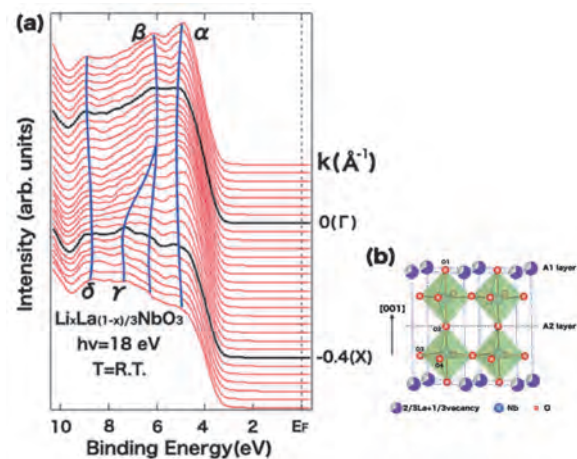


Fig. 1. (a) ARPES spectra along the Γ X line of $\text{Li}_x\text{La}_{(1-x)/3}\text{NbO}_3$. Solid lines are guides for eyes. (b) Average crystal structure of $\text{Li}_x\text{La}_{(1-x)/3}\text{NbO}_3$. The alternating partially occupied and unoccupied cation layers parallel to the c axis are labeled as A1 and A2 layer, respectively [2].

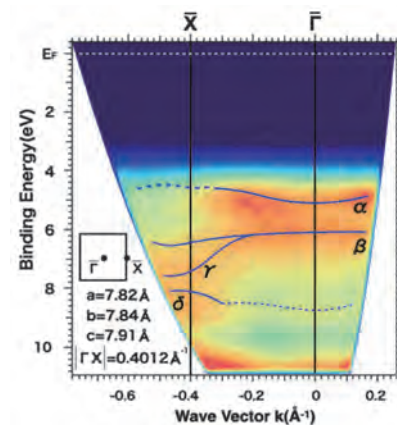


Fig. 2. Valence band structure along the Γ X line of $\text{Li}_x\text{La}_{(1-x)/3}\text{NbO}_3$. Solid and dashed lines are guides for eyes.

[1] Y. Fujiwara, K. Hoshikawa and K. Kohama, *J. Cryst. Growth* **433** (2016) 48.

[2] Y. Fujiwara, T. Taishi, K. Hoshikawa, K. Kohama and H. Iba, *Jpn. J. Appl. Phys.* **55** (2016) 090306.

BL7B

Evaluation of Optical Properties of Glass Materials in the VUV Region

T. Shimizu¹, M. J. F. Empizo¹, K. Shinohara¹, D. Umeno¹, N. Sarukura¹ and T. Murata²

¹Institute of Laser Engineering, Osaka University, Suita 565-0875 Japan

²Faculty of Advanced Science and Technology, Kumamoto University, Kumamoto 860-8555, Japan

Recently, neutron detection is required in inertial confinement fusion research and infrastructure inspection. The ratio of primary neutron and scattered neutron corresponds to the density and radius parameter of fusion plasma. Additionally, neutron detection is considered as one of the nondestructive methods for inspecting the form of infrastructure.

Scintillator materials which are able to detect and discriminate neutrons should then be developed to be able to satisfy the technological demand.

Previously, we have developed co-dope 20Al(PO₃)₃-80LiF (APLF) glass with Pr and Ce for improvement of decay times and conversion efficiencies and investigated the optical properties of Pr/Ce-doped APLF glasses with different concentrations. As a result, both radiative and non-radiative energy transfers from Pr³⁺ to Ce³⁺ are observed. These results present exciting prospects for APLF80 as a response time improved scintillator.

In this study, Nd³⁺-doped APLF glasses were investigated as potential vacuum ultraviolet (VUV) scintillator materials. Nd³⁺ is used as dopant in laser materials and optical property of that are largely analyzed from the UV to the near-infrared regions (200–1500 nm), but rarely in the VUV region (170–190 nm). Although absorption and emission properties in the VUV region are always difficult to measure due to the spectral limit of many devices.

We performed absorption and emission spectroscopic analysis to investigate the optical properties of the Nd³⁺-doped APLF glass at the BL7B solid-state spectroscopy beamline of UVSOR [1-3].

Figure 1 shows the VUV absorption spectra of the undoped APLF glass at RT and the 1.0 mol% Nd³⁺-doped APLF glass at different sample temperatures. The undoped glass has a room-temperature absorption edge in the VUV region around 162.2 nm (61650 cm⁻¹). In contrast, the Nd³⁺-doped glass exhibits an absorption edge at 300 K (RT) around 191.8 nm which corresponds to the interconfigurational transition from the 4I9/2 ground state of the 4f3 configuration to the 4f25d excited state configuration of Nd³⁺ ions. The absorption edge shifts with temperature and is located at 189.7 nm (52710 cm⁻¹), 190.1 nm (52600 cm⁻¹), 190.4 nm (52520 cm⁻¹), and 191.8 nm (52140 cm⁻¹) at 20 K, 100 K, 200 K, and 300 K, respectively.

These absorption edges are determined by generating the first derivative of the absorbance with respect to wavelength and then identifying the position of the absolute minima, i.e., the wavelength where the decrease in the absorbance is the highest. The shifting

of the absorption edge with sample temperature indicates the temperature broadening of the interconfigurational 4f25d transition which is associated with the population of the Stark components (Z1, Z2, etc.) of the 4I9/2 ground state of the Nd³⁺ ions' 4f3 configuration and which is often observed in Nd³⁺-doped crystals and glasses. Additionally, the low-temperature absorption spectra suggest that the lowest energy level of the 4f25d excited state configuration of Nd³⁺ ions in APLF glass is estimated to be at a position higher than 52710 cm⁻¹ (6.54 eV).

We have successfully investigated the absorption and emission properties of Nd³⁺-doped APLF glasses at different sample temperatures and with different doping concentrations mainly for potential neutron scintillator applications. Further development of these glasses as VUV scintillator materials is then anticipated in the future.

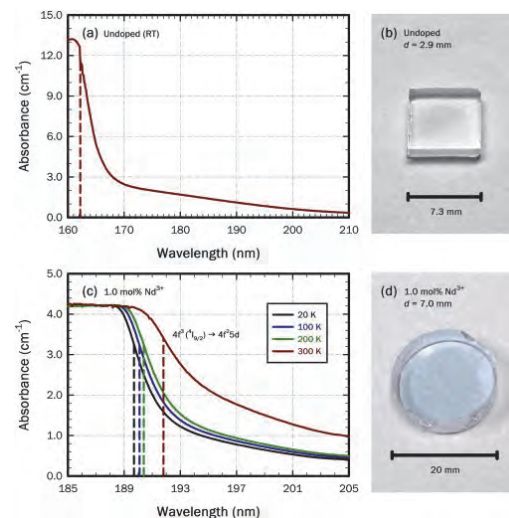


Fig. 1. VUV absorption spectra of (a,b) undoped APLF glass at RT and (c,d) 1.0 mol% Nd³⁺-doped APLF glass at 20 K, 100 K, 200 K and 300 K (RT)[3].

- [1] T. Shimizu *et al.*, UVSOR Activity Report 2018 **46** (2019) 107.
- [2] Y. Minami *et al.*, J. Noncryst. Solids **521** (2019) 119495.
- [3] Y. M. J. F. Empizo *et al.*, J. Alloys Compd. **856** (2021) 158096.

III-3

Chemistry

BL1U

Tracking Few-Femtosecond Auger Decay by Synchrotron Radiation

T. Kaneyasu¹, Y. Hikosaka², M. Fujimoto^{3,4}, H. Iwayama^{3,4} and M. Katoh^{5,3}¹SAGA Light Source, Tosu 841-0005, Japan²Institute of Liberal Arts and Sciences, University of Toyama, Toyama 930-0194, Japan³UVSOR Synchrotron Facility, Institute for Molecular Science, Okazaki 444-8585, Japan⁴The Graduate University for Advanced Studies, SOKENDAI, Okazaki 444-8585, Japan⁵Hiroshima Synchrotron Radiation Center, Hiroshima University, Higashi-Hiroshima 739-0046, Japan

The sequential interaction of a pair of time-separated pulses with an atomic or molecular system results in quantum interference between the resulting atomic/molecular wave packets. In this work, we use the recently disclosed ability of synchrotron light sources to perform wave packet interferometry experiments [1,2]. By using soft x-ray radiation wave packets with attosecond-controlled spacing, we observed the time-domain interferogram due to the interference between electron wave packets launched from the inner-shell 4d orbital of the Xe atom [3]. The time-domain approach presented here enables us to control the quantum interference in atomic inner-shell processes and to track the femtosecond decay of the short-lived excited state.

The experiment was carried out at beamline BL1U. The light source of BL1U consists of twin APPLE-II undulators. The electrons passing through the undulators emit pairs of 10-cycle radiation wave packets [Fig. 1]. The temporal duration and spectral width of the radiation wave packets were about 2 fs and 3 %, respectively. The peak photon energy of the 3rd harmonic radiation was adjusted close to the energy of the 4d_{5/2}-16p resonance. In order to monitor the population of the 4d_{5/2}-16p excited state, we detected visible fluorescence photons of 460-nm-wavelength emitted from singly-charged ionic states formed via spectator resonant Auger decay.

Figure 2(a) shows the fluorescence yields measured as a function of time delay over a range from 0 to 21 fs. The time spectrum shows rapid oscillations, with a period of approximately 63 as. This can be understood as “time-domain Ramsey fringes”, which arise from the quantum interference of electron wave packets launched at different times. Here the oscillation period corresponds to the transition frequency of the Xe 4d_{5/2}-16p inner-shell excited state.

It is clear that the amplitude of the Ramsey fringes decreases with increasing time delay. This can be explained by considering the time evolution of the first electron wave packet during the sequential interaction. Assuming a 6 fs lifetime for the 4d_{5/2}-16p state, the time-damped Ramsey fringe spectrum can be calculated. Figure 2(b) shows the calculated spectrum, taking into account the temporal resolution of the delay control. The good agreement between experiment and calculation confirms that the reduction in fringe amplitude does indeed arise from the excited state

lifetime, proving the time-domain access to femtosecond Auger decay processes. While the temporal resolution in synchrotron experiments has been thought to be limited by the electron bunch length, the present study clearly shows that processes in much shorter timescale can be accessed by the use of the longitudinal coherence between radiation wave packets.

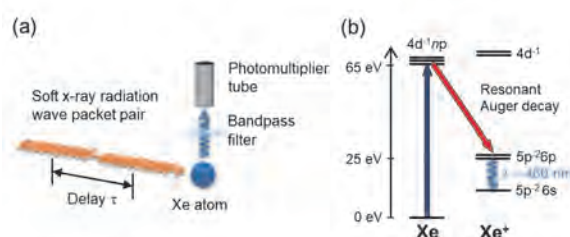


Fig. 1. (a) Experimental scheme for wave packet interferometry. (b) Energy level diagram of Xe atom.

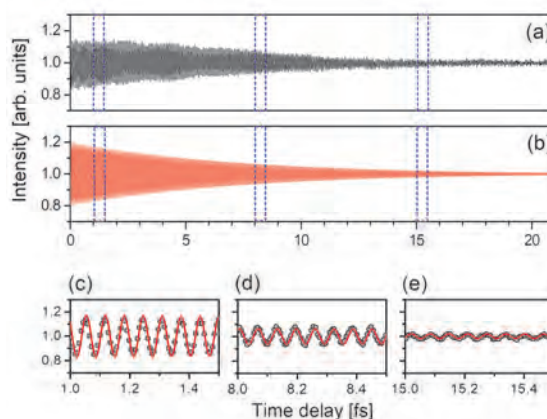


Fig. 2. (a) Fluorescence yield measured as a function of time delay. (b) Calculated spectrum. (c)-(e) Comparison between the experimental and calculated spectra.

[1] Y. Hikosaka *et al.*, Nat. Commun. **10** (2019) 4988.

[2] T. Kaneyasu *et al.*, Phys. Rev. Lett. **123** (2019) 233401.

[3] T. Kaneyasu *et al.*, Phys. Rev. Lett. **126** (2021) 113202.

BL1U

Polarization Control in a Crossed-Undulator without a Monochromator

T. Kaneyasu¹, Y. Hikosaka², M. Fujimoto^{3,4}, H. Iwayama^{3,4} and M. Katoh^{5,3}

¹SAGA Light Source, Tosu 841-0005, Japan

²Institute of Liberal Arts and Sciences, University of Toyama, Toyama 930-0194, Japan

³UVSOR Synchrotron Facility, Institute for Molecular Science, Okazaki 444-8585, Japan

⁴The Graduate University for Advanced Studies, SOKENDAI, Okazaki 444-8585, Japan

⁵Hiroshima Synchrotron Radiation Center, Hiroshima University, Higashi-Hiroshima 739-0046, Japan

The crossed undulator scheme for synchrotron radiation is a powerful method to produce light beams of various polarization states. In this study, we demonstrate that the polarization control of light from a crossed undulator can be achieved using the material response, without any prior monochromatization [1].

Figure 1 compares the polarization control of light from a crossed undulator by a conventional system and by the present method. A relativistic electron that passes through the undulators emits a pair of horizontally and vertically polarized radiation wave packets which are separated by time delay τ . In a conventional system, the radiation wave packets are temporally stretched by a monochromator which allows an interference between the two radiation fields. Various polarization states can be obtained by tuning the time delay using a phase shifter magnet that controls the electron orbit between the two undulators. On the other hand, when an atom is directly irradiated by non-monochromatized radiation from the crossed undulator, it absorbs specific frequency component. Therefore, the resonant photoabsorption is expected to reflect the polarization determined by the interference of radiation fields at the resonant frequency.

A proof-of-concept experiment was performed at BL1U. The light source of BL1U comprises a twin APPLE-II undulators. The upstream and downstream undulators were set in the vertical and horizontal linear polarizations, respectively. The UVSOR-III synchrotron was operated in the single bunch mode during the measurements. The non-monochromatized undulator radiation interacted with He atoms. The polarization property of the light was investigated by observing the Zeeman quantum beat in the fluorescence decay of the $1s6p\ ^1P$ excited state [2]. Fluorescence photons with a wavelength of 345 nm, which were emitted by the decay from $1s6p$ to $1s2s$ states, were detected using a photomultiplier tube equipped with a bandpass filter.

Figure 2 shows the fluorescence decay curves measured at different settings of time delay. The corresponding phase difference between the radiation fields was tuned from π to $9\pi/2$ with a step of approximately $\pi/2$. The shapes of beat structures change according to the phase difference, reflecting the polarization state of light. The observed beat structures are well reproduced by the calculation curves. This result verifies that polarization control in the crossed undulator can be achieved using atomic response.

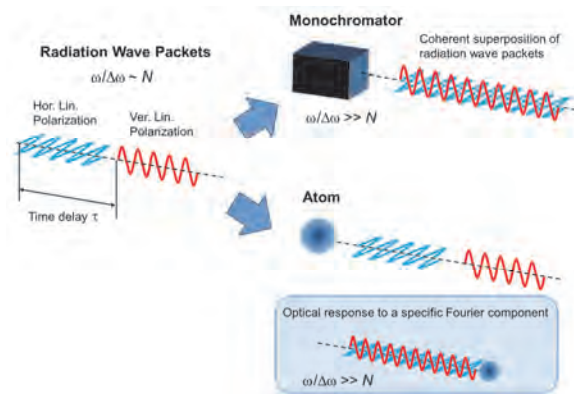


Fig. 1. Polarization control in a crossed undulator.

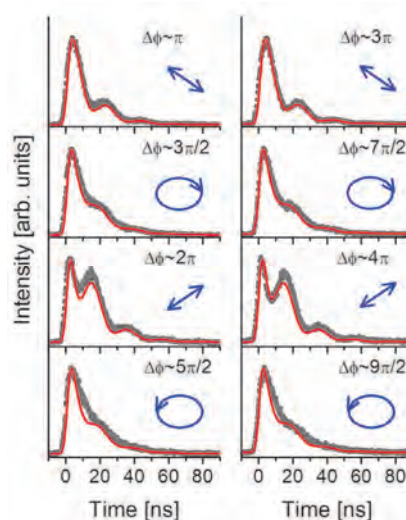


Fig. 2. Zeeman quantum beat measured for fluorescence decay of $1s6p$ state. The gray circles and red curves represent measured and calculated results, respectively. The polarization ellipse and vectors assumed in the calculation are shown.

[1] T. Kaneyasu *et al.*, *New J. Phys.* **22** (2020) 083062.

[2] Y. Hikosaka *et al.*, *J. Synchrotron Radiat.* **27** (2020) 675.

BL1U

Energy-Dependence of Photoelectron Circular Dichroism of Chiral Molecules

H. Kohguchi¹, Y. Hikosaka², T. Kaneyasu³, S. Wada¹, M. Fujimoto⁴, M. Katoh⁴
and Y-I. Suzuki⁵

¹Graduate School of Advanced Science and Engineering, Hiroshima University, Higashi-Hiroshima 739-8526, Japan

²Institute of Liberal Arts and Sciences, University of Toyama, Toyama 930-0194, Japan

³SAGA Light Source, Tosu 841-0005, Japan

⁴UVSOR Synchrotron Facility, Institute for Molecular Science, Okazaki 444-8585, Japan

⁵School of Medical Technology, Health Sciences University of Hokkaido, Tobetsu 061-0293, Japan

Our group started a research project of photoelectron circular dichroism (PECD) of chiral molecules with BL1U beamline in 2020 February. Photoelectron scattering images exhibiting PECD, which appears as forward-backward asymmetry of the photoelectron angular distributions with respect to the propagation direction of circularly polarized light for ionization, have been measured for various typical chiral molecules. Methyl oxirane is one of the typical PECD molecules, by which we confirmed feasibility of our experimental setup to measure PECD [1]. In this research project, we have searched novel chiral species showing PECD.

We conducted theoretical calculations based on multiple scattering theory to predict the energy-dependence of PECD of polyaromatic molecules. The theoretical results of some chiral systems yielded a certain amount of PECD parameters (β_1) that are measurable with our experimental setup consisted of a velocity-mapping imaging (VMI) apparatus with the undulator light source at BL1U. Availability of samples is practically important for PECD study since each enantiomer is required for measurement. Most of promising candidates found in terms of theoretical β_1 values and availability were solid compounds at room temperature. We used a gas inlet nozzle with a heater to introduce isolated chiral molecules into the vacuum chamber. An example of the result (dimethyl binaphthyl) is shown in Fig. 1; mass signals of the higher mass > 60 amu with elevated nozzle temperature served as a good monitor for gas-phase samples in the detection zone. The photoelectron signal with irradiation of the VUV light increased as the growth of the high-mass peaks, indicating photoionization of the chiral molecules. We obtained the photoelectron images with a characteristic ring-like structure in the outer region (Fig. 2). The multiple rings, which could correspond to the band structure of the photoelectron spectrum, disappeared at the higher photon energy. The present experimental condition with linearly polarized light is applicable to the circularly polarization measurement. Additional calculation for the excited and ionized electronic states will provide an solid assignment of the photoelectron spectrum, which is a fundamental spectroscopic data for PECD measurements.

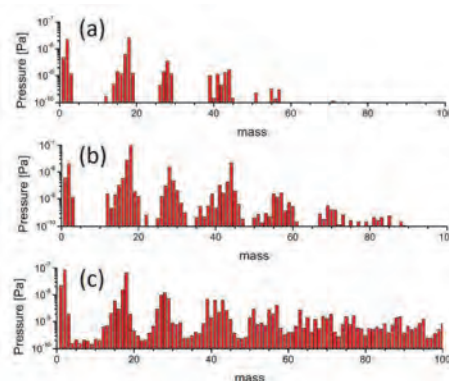


Fig. 1. Mass spectra of vaporized dimethyl binaphthyl at several nozzle temperatures with a heat nozzle. (a) room temperature, (b) nominal nozzle temperature of 50 °C, (c) 80 °C.

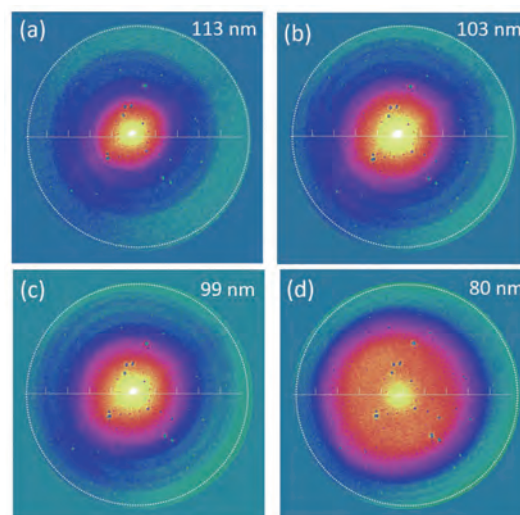


Fig. 2. Photoelectron images of dimethyl binaphthyl at several ionization wavelengths: (a) $h\nu = 11.0$ eV, (b) $h\nu = 12.3$ eV, (c) $h\nu = 12.5$ eV, (d) $h\nu = 15.5$ eV (expanded). White dotted circles define the detector edge.

[1] H. Kohguchi, Y. Hikosaka, T. Kaneyasu, S. Wada and Y-I. Suzuki, UVSOR Activity Report 2019 **47** (2020) 107.

BL1B, BL6B

Low-Frequency and THz Region Spectroscopy on Various Organic Molecules to Elucidate Microwave-Enhanced Organic Reactions

H. Takaya¹, K. Tanaka², F. Teshima², T. Yamada³, M. Nishioka⁴ and K. Kashimura⁴¹International Research Center for Elements Science, Institute for Chemical Research, Kyoto University, Uji 611-0011, Japan²UVSOR Synchrotron Facility, Institute for Molecular Science, Okazaki 444-8585, Japan³Faculty of Science and Engineering, Keio University, Yokohama 223-8522, Japan⁴Faculty of Engineering, Chubu University, Kasugai 487-0025, Japan

THz and Low-frequency region spectroscopic analysis was performed on various organic compounds to investigate the dynamic behavior of organic molecules under microwave (MW) irradiation.

MW-enhanced chemical process has been recently focused intensely because the high-speed and high-selective molecular conversion provide a highly efficient chemical processes which never accessible by using the conventional heating techniques such as oil bath and electric heater. In this research, we conducted development of a BL1B/BL6B-based terahertz spectroscopic system which can be used under microwave irradiation to detect the molecular dynamics under oscillating electromagnetic field.

Our research group found that various organic and inorganic reactions can be drastically accelerated under microwave irradiation with high selectivity and low energy consumption. For direct observation of the MW-induced molecular dynamics in these reactions by THz spectroscopy at BL1B/BL6B, we designed a in situ THz measurement system as shown in Fig 1 (left),

where a newly developed small size MW resonant cavity is inserted into the optical path of sample chamber of 1B. As shown in the picture of Fig 1 (right), the setting of MW resonant cavity having a pair of light path port was succeeded to detect reference THz light under MW irradiation condition. We also designed PEEK-made sample holder where a low-dielectric loss factor material of PEEK is almost transparent toward MW with negligible absorbance at 2.45 GHz frequency of MW.

In the 2021 research project, we planed to perform in situ THz spectroscopic experiments using this system to investigate the effects of microwaves on 1) the racemization reaction of biaryl compounds where the racemization proceeds intramolecularly through the rotation around the biaryl axial linkage and 2) microwave-specific selective heating of nitrobenzenes in toluene solution. First of all detection of characteristic absorption bands (peaks) induced by MW irradiation will be the main goals of this project.

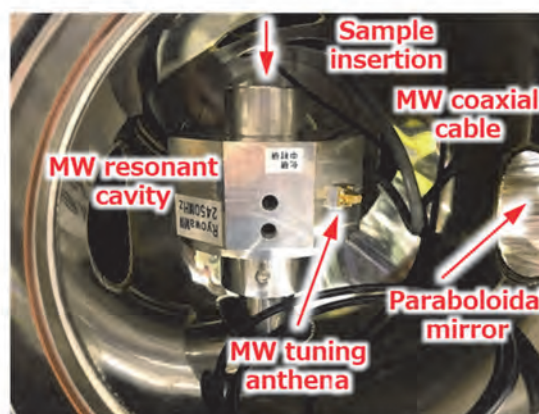
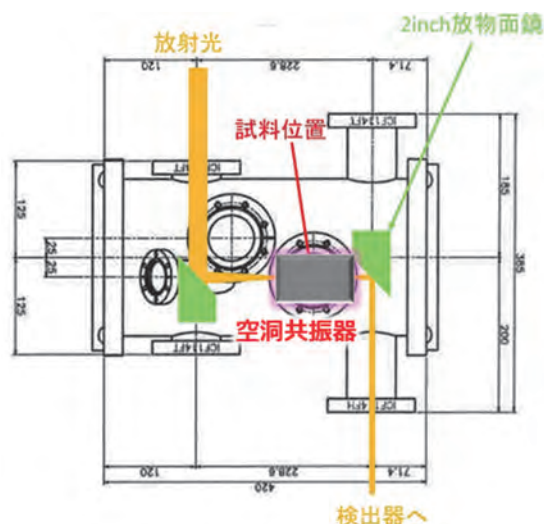


Fig. 1. The layout of microwave reaction system in the measurement chamber of BL1B THz optic system (left) and a picture of MW resonant cavity with the related electrical system inserted in the chamber of BL1B (right).

BL3U

XAS Measurements for Sugar Molecules in Aqueous Solutions

T. Sasaki and D. Akazawa

*Department of Complexity Science and Engineering, Graduate School of Frontier Sciences,
The University of Tokyo, Kashiwa 277-8561, Japan*

In recent years, attention has been paid to biomass conversion using water or an ionic liquid as a solvent without using an organic solvent. There have been many studies on biomass-related compounds in solution, but there are few reports on their molecular theory. We have studied the conversion process by dehydration reaction of polyalcohol as models of sugar molecules and found that the solvation structure with water molecules and the interaction with protons are important for the reaction process [1,2].

The purpose of this study is to explore the solvation structure of sugar molecules in aqueous solution, which is important in the conversion process from cellobiose to glucose, that is typical of biomass conversion process using water or ionic liquids. Cellobiose, a disaccharide, is taken up as a model substance for cellulose, which is one of the starting materials in biomass conversion. Of these, cellobiose can be hydrolyzed by the ionic liquid 1-ethyl-3-methyl-imidazolium chloride (EmimCl) to produce glucose [3]. These are typical routes for obtaining useful compounds from cellulose. A typical biomass conversion and utilization of glucose can be facilitated by elucidating the solvation structures and conversion mechanisms for related compounds.

In aqueous solutions, the dependence of temperature, pressure, and acidity will be investigated to elucidate the roles of hydrogen bond networks and protons surrounding sugar alcohol molecules. For ionic liquid aqueous solutions, the effect of polarity and viscosity will be elucidated by investigating the ionic liquid carbon chain length dependence. In this way, the entire molecular mechanism of sugar alcohol conversion using aqueous solutions and ionic liquid solutions will be elucidated, and the possibility of a more efficient sugar alcohol conversion route will be explored.

XAS measurements for liquid samples were conducted at UVSOR BL3U using facilities developed by Nagasaka et al [4]. The liquid sample cell with Si₃N₄ membranes was adopted, where the thickness of the liquid layer was controlled by the He gas pressure around the cell. The photon energy was calibrated by using the C-K edge XAS spectrum of the proline thin layer.

Figure 1 shows C-K edge XAS spectra for glucose and cellobiose aqueous solutions with concentrations specified in the figure. Molecular dynamics calculations for the solutions and the XAS simulations are under way to interpret the XAS spectra to explore the solvation structures of sugar molecules.

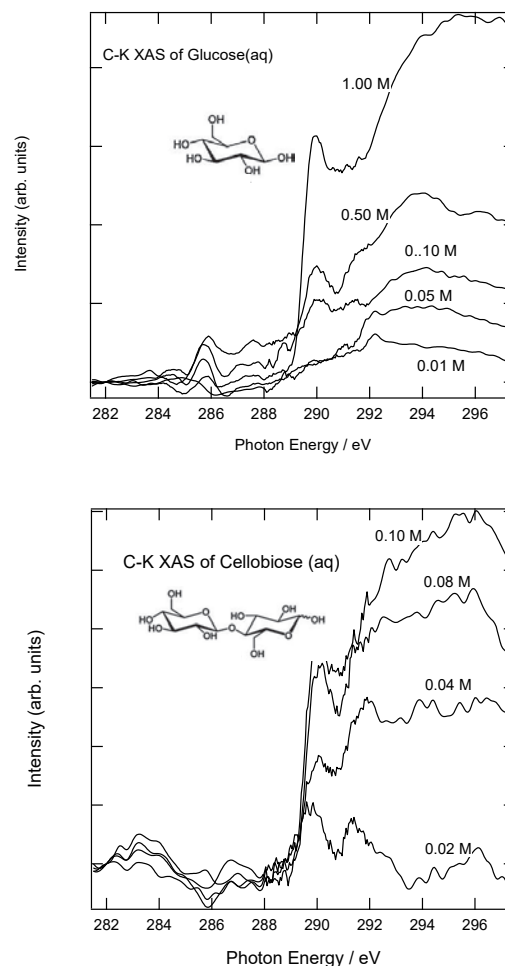


Fig. 1. C-K XAS spectra for glucose (upper panel) and cellobiose (lower panel) aqueous solutions.

- [1] Y. L. Chang *et al.*, *J. Phys. Chem. B.* **123** (2019) 1662.
- [2] T. Kondo *et al.*, *J. Computational Chem.* **42** (2021) 156.
- [3] Vanoye *et al.*, *Green Chem.* **11** (2009) 390.
- [4] M. Nagasaka *et al.*, *J. Electrosc. Relat. Phenom.* **200** (2015) 293.

BL3U

Nitrogen K-edge X-ray Absorption Spectroscopy of Metal Protoporphyrin IX Complexes in Aqueous Solutions

M. Nagasaka^{1,2}¹Institute for Molecular Science, Okazaki 444-8585, Japan²The Graduate University for Advanced Studies, SOKENDAI, Okazaki 444-8585, Japan

Iron porphyrin complex is a model of Cytochrome P450 that is important for enzyme reaction such as secondary metabolism. Chlorophyll *a* complex is used as a light-harvesting antenna for photosynthetic reaction. Thus, the electronic structural analysis of a metal complex is important for chemistry and biology. X-ray absorption spectroscopy (XAS) in the hard X-ray region extensively studied the electronic structures of central metals in metal complexes during a metal to ligand charge transfer process with photoirradiation [1]. The electronic structure of the central metal is also investigated by Fe L-edge XAS (700 eV) in the soft X-ray region [2]. Fe L-edge XAS is effective for the observation of the interactions between central metals and ligands since Fe L-edge is more sensitive for the measurements of valence and spin states than Fe K-edge in the hard X-ray region [3]. On the other hand, C and N K-edge XAS is necessary for investigating the electronic structures of ligands in metal complexes. Recently, Golnak et al. discuss the difference between liquid and solid states of hemin, which is also known as iron Protoporphyrin IX (FePPIX) complex, by using N K-edge XAS in fluorescence yield [4]. In this study, we have investigated interaction between metal and PPIX ligand from N K-edge XAS spectra of FePPIX, CoPPIX, and PPIX complexes in aqueous solution in transmission mode.

The experiments were performed by using a transmission-type liquid cell settled at BL3U [5]. The liquid layer is sandwiched between two SiC membranes and the liquid thickness is optimized to obtain appropriate absorbance of metal PPIX peaks. 50 mM FePPIX, CoPPIX, and PPIX in 0.5 M NaOH solutions were prepared. Although these complexes show dimer structure in aqueous NaOH solution, the interaction between metal and ligand would not be influenced in the dimer structures.

Figure 1 shows N K-edge XAS spectra of FePPIX, CoPPIX, and PPIX complexes in aqueous solutions. Sharp peaks around 398 eV and 400 eV are observed in the spectra of PPIX complex. In CoPPIX complex, the first peak shows a higher energy shift, and the second peak shows a lower energy shift compared to those in PPIX complex. These peaks are overlapped in the XAS spectrum. The XAS spectrum of FePPIX also shows same spectral features although the shoulder at the high energy side is smaller than that of CoPPIX. The peak around 403 eV in PPIX complex is also observed in CoPPIX complex, but it is not observed in FePPIX complex. In the future, we will discuss the

metal-ligand delocalization in metal PPIX complex more precisely with the help of quantum chemical inner-shell calculations.

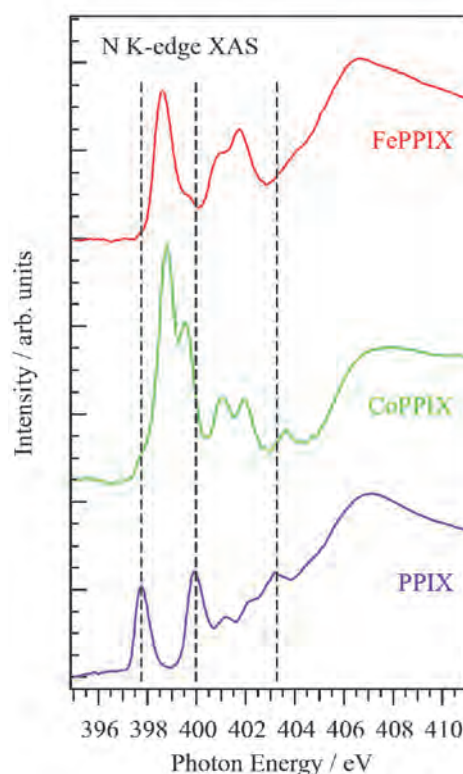


Fig. 1. N K-edge XAS spectra of FePPIX, CoPPIX, and PPIX complexes with the molar concentration of 50 mM in 0.5 M aqueous NaOH solutions. The dashed lines indicate the peak positions of PPIX.

[1] C. J. Milne, T. J. Penfold, M. Chergui, *Coord. Chem. Rev.* **277** (2014) 44.

[2] N. Huse *et al.*, *J. Am. Chem. Soc.* **132** (2010) 6809.

[3] S. A. Wilson *et al.*, *J. Am. Chem. Soc.* **135** (2013) 1124.

[4] R. Golnak *et al.*, *Phys. Chem. Chem. Phys.* **17** (2015) 29000.

[5] M. Nagasaka, H. Yuzawa and N. Kosugi, *Anal. Sci.* **36** (2020) 95.

BL3U

XAS Study of a High Valent Oxo Species of a μ -Nitrido-Bridged Iron Phthalocyanine Dimer Deposited on a Graphite Surface

Y. Yamada^{1,2,3} and M. Nagasaka⁴¹Department of Chemistry, Graduate School of Science, Nagoya University, Nagoya 464-8602, Japan²Research Center for Materials Science, Nagoya University, Nagoya 464-8602, Japan³PRESTO/JST, Kawaguchi 332-0012, Japan⁴Institute for Molecular Science, Okazaki 444-8585, Japan

Methane has long been expected as a next-generation carbon resource because it is abundant in nature as natural gas or methane hydrate. However, its high C-H bond dissociation energy prevent the development of the catalyst that can convert methane into more valuable raw chemicals under mild reaction conditions. μ -Nitrido-bridged iron phthalocyanine dimer **1** (Fig. 1) is one of a few molecular catalysts for direct C-H activation of methane.[1,2] It is reported that treatment of **1** with H_2O_2 in an acidic aqueous solution produce high valent iron-oxo species $\mathbf{1}_{\text{oxo}}$ possessing a strong methane oxidation activity. However, the electronic structure of $\mathbf{1}_{\text{oxo}}$ have never been investigated by XAS presumably because of its high reactivity. In this study, we attempted to observe $\mathbf{1}_{\text{oxo}}$ directly by XAS by using a highly oriented pyrolytic graphite (HOPG) substrate on which **1** was deposited (**1**/HOPG in Fig. 2(a)). We assumed that $\mathbf{1}_{\text{oxo}}$ generated on a HOPG substrate is stable enough for XAS measurement as long as any organic substrates do not coexist.

Beforehand of this study, we confirmed that **1** was adsorbed on a highly oriented pyrolytic graphite to prepare **1**/HOPG successfully by treatment of a HOPG with the $1e^-$ -oxidized monocationic species of **1** ($\mathbf{1}^+$) in an organic solvent. O K-edge and Fe L-edge XAS measurements were performed at the soft X-ray beamline BL3U of UVSOR.[3] For these measurements, **1**/HOPG was fixed with double-sided conductive carbon tape onto a stainless sample holder. In order to generate $\mathbf{1}_{\text{oxo}}$ on HOPG substrate, **1**/HOPG was treated with 35% aqueous H_2O_2 just before measurement. The holder with a HOPG sample was fixed on a rotatable linear and installed into a vacuum chamber ($< 1 \times 10^{-5}$ Pa). The XAS spectra were obtained in total electron yields by measuring a sample drain current.

Figure 2b shows a comparison of the O K-edge XAS spectra obtained for **1**/HOPG and **1**/HOPG treated with H_2O_2 . It was found that the peak at around 532 eV was significantly increased after treatment with H_2O_2 . DFT calculation for $\mathbf{1}_{\text{oxo}}$ adsorbed on a graphene suggested that the peak assignable to the excitation of $\text{O}1s - \pi^*$ of $\text{Fe}=\text{O}$ for $\mathbf{1}_{\text{oxo}}$ should appear at around 529 eV, whereas the peaks for **1** with a coordinating H_2O on a graphene were calculated to appear at higher than 534 eV as shown in Fig. 2(c). On the other hand, Fe L-edge XAS spectra of **1**/HOPG after H_2O_2 treatment

showed slight high energy shifts compared to that before treatment. Taking that $\mathbf{1}_{\text{oxo}}$ was observed by MALDI-TOF MS by using **1**/HOPG treated with H_2O_2 , it is considered that the spectra shown in Fig. 2 indicates that $\mathbf{1}_{\text{oxo}}$ was actually observed by XAS.

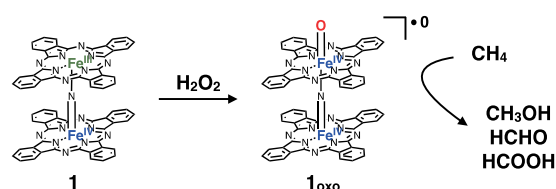


Fig. 1. Formation of a high valent iron-oxo species $\mathbf{1}_{\text{oxo}}$ having methane oxidation activity.

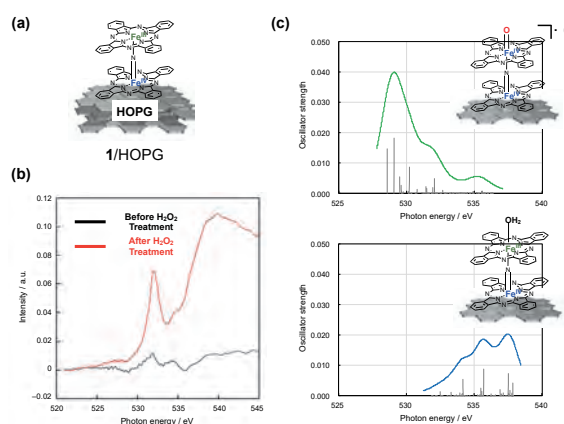


Fig. 2. (a) Structure of **1**/HOPG, (b) Comparison of O K-edge XAS spectra of **1**/HOPG before and after treatment with H_2O_2 . (c) DFT-calculated O K-edge XAS spectra for $\mathbf{1}_{\text{oxo}}$ on a graphene surface (upper) and **1**(OH_2) on a graphene surface (bottom).

[1] P. Afanasiev and A. B. Sorokin, *Acc. Chem. Res.* **49** (2016) 583.

[2] Y. Yamada, K. Morita, N. Mihara, K. Igawa, K. Tomooka and K. Tanaka, *New J. Chem.* **43** (2019) 11477.

[3] T. Hatsui, E. Shigemasa, N. Kosugi, *AIP Conf. Proc.* **705** (2004) 921.

BL3U

Mechanistic Investigation of Homogeneous Nickel-Catalyzed Organic Reactions Based on Solution-Phase L-edge XAS

H. Takaya^{1,2}, M. Nagasaka² and K. Kashimura³

¹International Research Center for Elements Science, Institute for Chemical Research, Kyoto University, Uji 611-0011, Japan

²Institute for Molecular Science, Okazaki 444-8585, Japan

³Faculty of Engineering, Chubu University, Kasugai 487-8501, Japan

We have found that iron complexes of NiX₂ (phosphine) (X = Cl or Br) bearing various phosphine ligands showed excellent catalytic activities toward the coupling of organometallic reagents of Mg, B, Al, and Zn with various aryl halides [1]. Such nickel-based catalysts for organic reactions alternative to the conventional precious metal catalysts has been intensively investigated for the development of future sustainable production of chemical compounds. Solution-phase XAS analysis is highly useful for the mechanistic study of iron-catalyzed organic reactions to identify the catalytically active organoiron species with their electronic and molecular structures, because the conventional solution-phase NMR analysis cannot be used due to the paramagnetic nature of organoiron species along with the large paramagnetic shift and peak broadening in NMR spectrum. L-edge XAS of transition-metal catalysts has been expected to be highly useful to investigate the electronic structure of 3d orbitals which provide essential information to elucidate how to work the catalyst. However, solution-phase L-edge XAS measurement is generally difficult because the measurement has to be performed under a vacuum condition where the solution sample is vaporized with vigorous boiling. In this project, we used the specially designed flow-cell for the solution-phase L-edge XAS measurement of homogeneous organic solution of nickel complex catalysts. In BL3U beamline, a stainless-steel flow cell has been used for various experiments, but we should carefully avoid contamination of iron species from the environment. For this reason Prof. Nagasaka newly designed and prepared PEEK-made flow cell bearing ultra-thin 100 nm Si₃N₄ membrane X-ray window (Fig. 1. left). The solvent-resistant PEEK made body worked well with an excellent chemical resistance toward the various organic solvents such as THF, CH₂Cl₂, toluene, and benzene, these often used in nickel-catalyzed coupling reactions. However, the static electrical charge generated by the frictional interactions between PEEK wall and organic solvents caused undesired baseline shifts in the NEXAFS spectrum. To solve this problem, a gold-made electrode was attached to the Si₃N₄ membrane with earth connection (Fig. 1. right). This flow cell was introduced into the He-filled chamber which inserted into the X-ray optics line, and connected to a syringe pump through a Teflon tube. The toluene solution samples of nickel phosphine

catalyst of NiCl₂(PPh₃)₂ **1** was prepared in an argon-filled glovebox, because the solution of iron complexes are quite sensitive to oxygen and water, and immediately react to give iron oxide and hydroxide. The XAS measurement was successfully carried out under a flow condition (flow rate: 50–200 μL/h) to give L-edge NEXAFS of **1** without the undesired baseline shift by the static electricity (Fig. 2.). However, the penetration of helium gas into the cell causing a bubbling noise could not be perfectly controlled. To solve this problem, Viton O-ring is changed to a fluorosilicone polymer with improving the flow line design and tube connection. This improved cell is testing in 2021 experiment.

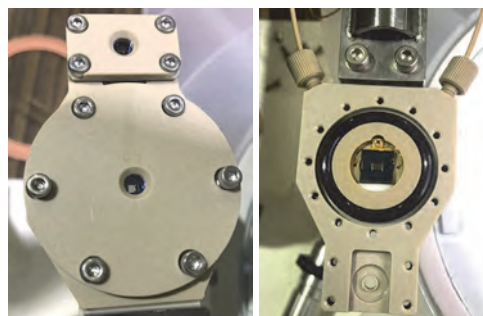


Fig. 1. Photos of the PEEK-made flow cell.

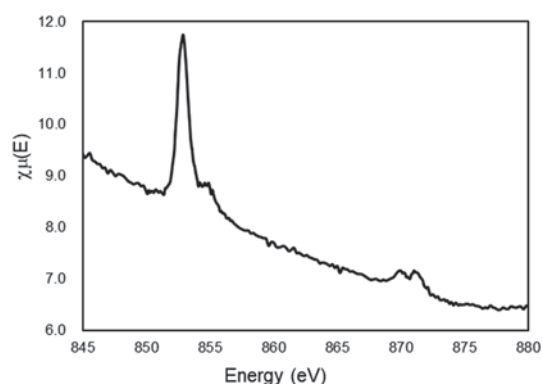


Fig. 2. Solution-phase L-edge XAFS spectrum of NiCl₂(PPh₃)₂ in toluene.

[1] JP Patent 2020-016437 (Feb. 3, 2020).

BL3U

Complex Formation in Glycine Betaine Saline Solution Revealed by the Deconvolution of Its Soft X-Ray Absorption Band

S. Ohsawa¹, N. Fukuda¹, H. Iwayama^{2,3}, M. Nagasaka^{2,3} and K. Okada^{1,4}

¹Graduate School of Science, Hiroshima University, Higashi-Hiroshima 739-8526, Japan

²Institute for Molecular Science, Okazaki 444-8585, Japan

³School of Physical Sciences, The Graduate University for Advanced Studies, SOKENDAI, Okazaki 444-8585, Japan

⁴Graduate School of Advanced Science and Engineering, Hiroshima University, Higashi-Hiroshima 739-8526, Japan

Living cells adapt to various environments, such as drought and high salinity, by regulating the concentration of solutes termed osmolytes [1], because an increase in extracellular salinity can cause water efflux and cell shrinkage. Among the most common organic osmolytes is glycine betaine. The amount of glycine betaine has been found to correlate with external salinity for several shoots of halophytes [2] and for halophilic eubacteria [3]. Altering the hydration structure of glycine betaine by salt addition presumably plays an important role in protecting the secondary structure of proteins, but the molecular level understanding of the hydration structure is not yet fully explored [4]. In this report O 1s absorption spectra were recorded for various concentrations of glycine betaine and sodium chloride, to extract the hydrated and bulk water components by a peak deconvolution technique.

Photoabsorption spectra of the solutions in the oxygen K-edge region were measured on the soft X-ray beamline, BL3U. A pair of windows made of thin silicon nitride membrane was used for the sample cell. The incident photon energy was calibrated to the peak at 530.88 eV of a polymer film [5]. Peak deconvolution was applied to the 4a₁ resonance band of water into five components: one for the water hydrated to anions, three for the bulk water and one for the water hydrated to cations.

Figure 1 displays the peak area of the component for the water hydrated to cations versus the concentration of either glycine betaine or sodium chloride. The data for the betaine- and NaCl-only solutions align linearly, indicating the correctness of the present analysis. For mixed solutions of glycine betaine and sodium chloride, the data are plotted for the set of the varying NaCl concentration with the glycine betaine concentration constant (blue) and for the set of vice versa (green). The area for the former set decreases up to about 0.55 mol/dm³. The slope corresponds to the consumption of about 1.5 times the NaCl concentration. The decrease in area can be interpreted to be caused by the loss of water molecules hydrated to the solute due to the strong interaction between glycine betaine and sodium chloride. Above 0.55 mol/dm³ the area keeps nearly constant, which infers that different components of ion pairs exist in the solution. The data in green color behave similarly but have different slope. These results show that depending on the salt concentration the

betaine·Na⁺ complex with varying composition from 2:1 to 1:2 exists in glycine betaine saline solutions. We can therefore safely conclude that this provides the osmoregulation function in living cells against salinity.

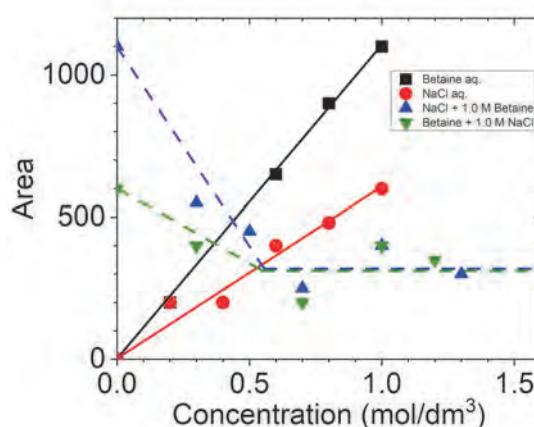


Fig. 1. Peak area of the water component hydrated to the sodium cation or cationic part of glycine betaine plotted against concentration.

- [1] P. H. Yancey, M. E. Clark, S. C. Hand, R. D. Bowlus and G. N. Somero, *Science* **217** (1982) 1214.
 [2] R. Storey and R. G. Wyn Jones, *Plant Sci. Lett.* **4** (1975) 161.
 [3] J. F. Imhoff and F. Rodriguez-Valera, *J. Bacteriol.* **160** (1984) 478.
 [4] S. Ohsawa, N. Fukuda, H. Iwayama, H. Yuzawa, M. Nagasaka and K. Okada, *UVSOR Activity Report 2018* **46** (2019) 115.
 [5] M. Nagasaka, H. Yuzawa, T. Horigome and N. Kosugi, *J. Elec. Spectrosc. Relat. Phenom.* **224** (2018) 93.

BL4U

Analysis of One-dimensional Single-crystalline Cathode Materials for Secondary Batteries by Scanning Transmission X-ray Microscopy

E. Hosono^{1,2,3}, W. X. Zhang^{3,4}, D. Asakura^{1,2,3}, Y. Harada^{3,4}, H. Yuzawa⁵ and T. Ohgashi^{5,6}

¹Global Zero Emission Research Center, National Institute of Advanced Industrial Science and Technology, Tsukuba 305-8568, Japan

²Research Institute for Energy Conservation, National Institute of Advanced Industrial Science and Technology, Tsukuba 305-8568, Japan

³AIST-UTokyo Advanced Operando-Measurement Technology Open Innovation Laboratory (OPERANDO-OIL), National Institute of Advanced Industrial Science and Technology (AIST), Kashiwa 277-8565, Japan.

⁴Institute for Solid State Physics, The University of Tokyo, Sayo 679-5148, Japan

⁵UVSOR Synchrotron Facility, Institute for Molecular Science, Okazaki 444-8585, Japan

⁶School of Physical Sciences, The Graduate University for Advanced Studies, SOKENDAI, Okazaki 444-8585, Japan

Development of innovative technologies for clean energy devices is desired to realize sustainable society with preventing global warming, and development of high-performance secondary batteries for electric vehicle applications and grid introduction through large-scale power storage in renewable energy power plants is attracting much attention.

In secondary battery materials, when Li or Na ions diffuse into or out of the host crystal, the crystal axis along the diffusion path becomes clearer. However, the redox reaction is still unclear. The electronic-structure change in transition metals and oxygen of the host crystal due to the insertion or extraction of Li or Na in the single-crystal active material should be unveiled in detail. It is desirable to clarify the distribution of the electronic state using a position sensitive analysis with high spatial resolution. The knowledge of Li or Na diffusion with the electronic-structure change of the host structure is important for the understanding of cathode materials for secondary batteries from a viewpoint of basic science.

These discussions are directly related to the crystal structure change (volume change) and charge-discharge cycle characteristics related with fast ionic diffusion. If we clarify the battery characteristics from the electronic state, we can establish a strategy for innovative material design.

Here, we show a result of STXM for LiMn_2O_4 single-crystalline nanowire. Figure 1 shows the STXM image measured with an excitation energy of 525 eV. Nanowire image of LiMn_2O_4 was obtained by STXM. An O K -edge absorption spectrum of a selected region is shown in Fig. 2. The pre-edge region from 528 to 534 eV is attributed to the Mn $3d$ -O $2p$ hybridization.

In the near future, we will establish *operando* STXM measurement system.

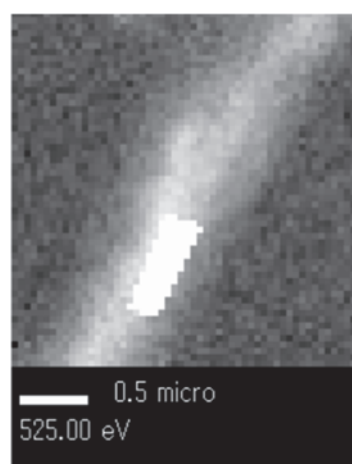


Fig. 1. A STXM image of the LiMn_2O_4 single-crystalline nanowire.

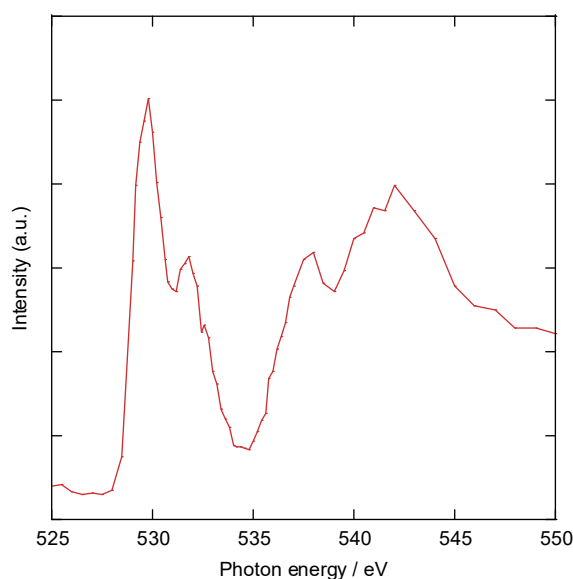


Fig. 2. O K -edge absorption spectrum of a selected region.

BL4U

Analysis of High Active Photocatalytic Materials by Scanning Transmission X-ray Microscope

Y. Miseki^{1,2}, E. Hosono^{1,3,4}, D. Asakura^{3,4}, H. Yuzawa⁵ and T. Ohigashi^{5,6}

¹Global Zero Emission Research Center, National Institute of Advanced Industrial Science and Technology, Tsukuba 305-8568, Japan

²Research Center for Photovoltaics, National Institute of Advanced Industrial Science and Technology, Tsukuba 305-8565, Japan

³Research Institute for Energy Conservation, National Institute of Advanced Industrial Science and Technology, Tsukuba 305-8568, Japan

⁴AIST-UTokyo Advanced Operando-Measurement Technology Open Innovation Laboratory (OPERANDO-OIL), National Institute of Advanced Industrial Science and Technology (AIST), Kashiwa 277-8565, Japan.

⁵UVSOR Synchrotron Facility, Institute for Molecular Science, Okazaki 444-8585, Japan

⁶School of Physical Sciences, The Graduate University for Advanced Studies, SOKENDAI, Okazaki 444-8585, Japan

The conversion of solar energy into chemical energy by artificial photosynthetic reactions is being studied as a candidate technology for realizing a sustainable low-carbon society. For the widespread use of this technology in society, it is important to establish design strategy for innovative photocatalytic materials that are significantly superior to the current performance. Since the photocatalytic reaction proceeds by redox reaction at the interface, it is necessary to establish appropriate design method for the reaction field, especially technology to control the crystallinity and crystal plane of the material.

However, since each catalytic material has a different active surface, it is important to confirm which surface is the active surface, as a preliminary step for precise control. Comparing the electronic states of the active surface with those of other surfaces and element-selectively/orbital-selectively understanding the mechanism of high activity is expected to lead to design strategy for the development of innovative materials.

To establish the high-level crystal growth techniques and morphology control methods, theoretical understanding from a viewpoint of electronic structure by using synchrotron radiation soft X-rays is necessary. Scanning Transmission X-ray Microscope (STXM) is most suitable to reveal the electronic structure information with spatial information (minimum spatial resolution is ca. 30 nm).

We have tried the preparation of *operando* measurement system for crystal growth in STXM. Figure 1 shows the optical microscope image of Mn²⁺ solution with agar gel sandwiched by Si chips with Si₃N₄ windows. One of the major features of STXM is that it is possible to obtain a spectrum of the solution by sandwiching it between the Si₃N₄ windows.

Figure 2 shows the spectrum of Mn. In the near future, we will establish in-situ measurement system.

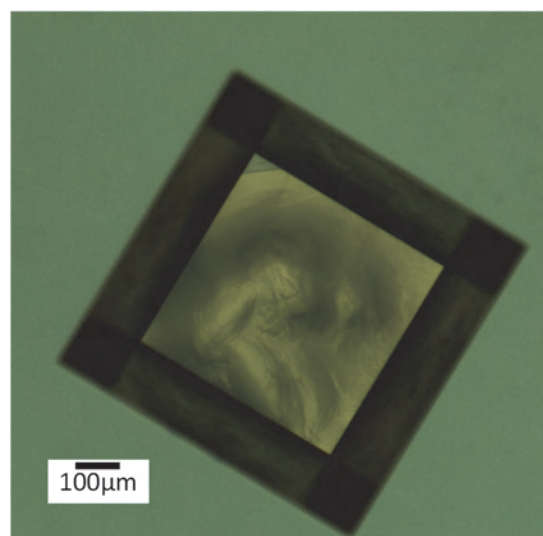


Fig. 1. Optical microscope image of Mn solution with agar gel.

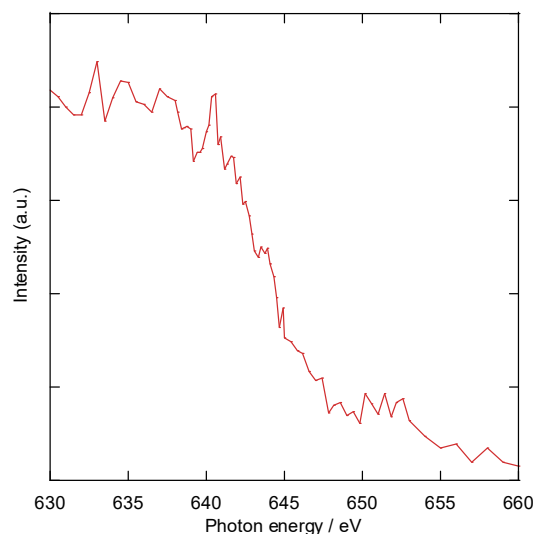


Fig. 2. Absorbance spectrum of Mn.

BL4U

Chemical State Mapping of a Heterostructured Oxygen Catalyst using STXM

J. Wang, J. Chung and J. Lim

Department of Chemistry, College of Science, Seoul National University, Seoul, 08826, Republic of Korea

Water electrolysis is regarded as one of the most promising methods for clean hydrogen production [1], where the sluggish kinetics of oxygen evolution reaction (OER) at the anode of a water electrolyzer compromised the energy efficiency [2]. For the purpose of boosting the OER rate, we proposed a new heterostructured OER catalyst by mating MoS₂ dichalcogenide with layered LiCoO₂ oxide. The as-prepared hybrid catalyst (MML) outperformed the commercial RuO₂ in catalyzing the OER and demonstrated remarkable stability. However, it is well known that both MoS₂ and LiCoO₂ are inert in OER activity. In order to look into the mechanism behind the synergistic performance enhancement, we applied scanning transmission X-ray microscopy (STXM) with several in-situ/ex-situ techniques to probe the dynamic structural change and to clarify the actual active species of the catalyst during the reaction.

The chemical state of MML sample before and after the OER was mapped around the Co L-edge and Mo M-edge at the BL4U beamline of the UVSOR. Hybridization with MoS₂ was found to lower the Co valence state of LiCoO₂, as clearly visualized from the mapping in Fig. 1 and supported by the representative line-cut spectra showing the negative shift of the Co L-edge spectrum of MML relative to that of pristine LiCoO₂. In addition, the homogenous distribution of Co valence states within the MML particle suggested the thorough mixing of the MoS₂ and LiCoO₂ components, which is expected to be beneficial to maximize the heterointerface density and tune the electronic structure. The maintenance of Mo in MML is confirmed by the Mo M-edge spectrum. However, it is challenging to judge the Mo valence state change from this soft XAS spectrum. To supplement this Mo data, XAFS around the K-edge was scanned, which demonstrated the reduced Mo in MML. From the oxygen K-edge spectrum, the hybridization of MoS₂ with LiCoO₂ led to the formation of oxidized oxygen moieties, which can be explained by the coordination of Co with S after the hybridization. Replacement of oxygen with less electronegative ligands (i.e., S) potentially activated the oxygen redox.

The MML sample after the catalysis was also investigated. From the valence state mapping, Co was oxidized during the OER, leading to a higher valence state. The oxidized Co in LiCoO₂ was accompanied by the leaching of Li, which process led to the structural reconstruction of LiCoO₂ forming the cobalt

oxyhydroxide. This deduction was also supported by various other techniques including in-situ XAFS, online ICP-MS, post-mortem TEM, etc. Without forming the heterointerface, the surface of pristine LiCoO₂ was transformed into spinel LiCo₂O₄, resulting in an inferior OER activity. This work highlighted the role of heterointerface in modulating the dynamic structural reconstruction of catalysts during water electrolysis. The corresponding manuscript is under draft now and will be submitted soon.

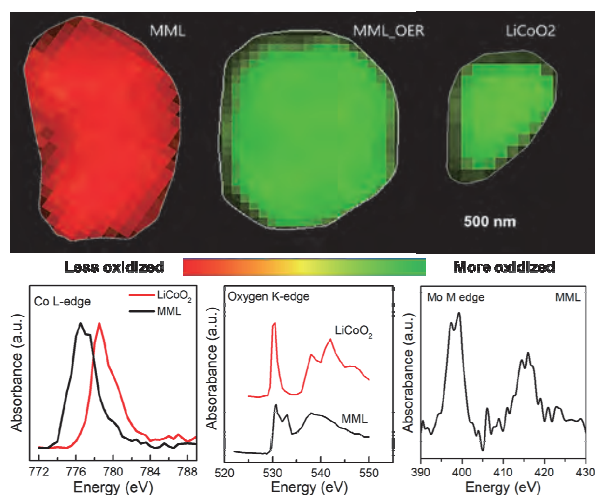


Fig. 1. Chemical state mapping around the Co L-edge of MML particle before and after the OER. A LiCoO₂ particle is also provided as a reference. The representative line-cut spectra of the MML sample around the Co L-edge, O K-edge, and Mo M-edge are shown below.

[1] Wang J, Gao Y, Kong H, Kim J, Choi S, Ciucci F, Hao Y, Yang S, Shao Z, Lim J. *Chem. Soc. Rev.* **49** (2020) 9154.

[2] Wang J, Kim SJ, Liu J, Gao Y, Choi S, Han J, Shin H, Jo S, Kim J, Ciucci F, Kim H, Li Q, Yang W, Long X, Yang S, Cho S, Chae K. H, Kim M. G, Kim H, Lim J. *Nat. Catal.* (2021) <https://doi.org/10.1038/s41929-021-00578-1>.

BL4B

Detection Efficiency of a Funnel MCP Estimated for Its Use in a Magnetic Bottle Electron Spectrometer

Y. Hikosaka

Institute of Liberal Arts and Sciences, University of Toyama, Toyama 930-0194, Japan

Magnetic bottle electron spectrometer, utilizing an inhomogeneous magnetic field to capture electrons formed by photoionization, is a very efficient electron spectroscopic tool and enabling one to perform multielectron coincidence spectroscopy very effectively. The electrons captured over 4π -steradian solid angle are guided to a detector (usually a microchannel plate (MCP) detector) ending a long flight path. Ions formed together with electrons can be detected with the same detector, by applying a pulsed electric field to the photoionization region [1-3]. The ion detection capability thus added to a magnetic bottle electron spectrometer leads to efficient coincidence measurements of multi-electrons and ions. The coincidence efficiency for the multiple particles is the product of the detection efficiencies for individual particles. Thus, gaining higher detection efficiency for each particle is crucial in achieving more effective coincidence measurements.

A standard MCP detector of 32-mm active diameter and 60% open area ratio had been employed in our previous multielectron-ion coincidence measurements [3]. For the electron detection, the coincidence efficiency limited by the detection efficiency of the MCP was practically observed [3,4]. In this work, we have newly introduced an MCP detector (40-mm active diameter) consisting of funnel micropores, instead of the previous one. The MCP has a large open area ratio (90%), and high detection efficiencies for electrons and ions are expected.

The detection efficiency of the funnel MCP for detections of electrons and ions was estimated on its use in the magnetic bottle electron spectrometer. A single mesh of 88% transmission was placed in front of the MCP, to avoid a leak of the electric potential of the MCP front. The electron detection efficiency, estimated from the number of Auger electrons from Ar 2p core-hole measured in coincidence with the relevant 2p photoelectron, is presented in Fig. 1 as a function of kinetic energy. The electron detection efficiency, observed to be constant around 0.7, is quite favorable, though it does not reach the open area ratio of the funnel MCP. The detection efficiency for ions, plotted in Fig. 2, was determined from the numbers of electrons ejected in known ionization paths in coincidence with the formed Xe ion. While the detection efficiency for the singly charged Xe ion is not very favorable on the present extraction pulse (2 kV height), those for highly-charged Xe ions are close to the value reflecting the open area ratio of the MCP. The present study proves that the use of the funnel

MCP is promising in achieving more efficient multielectron-ion coincidence measurements.

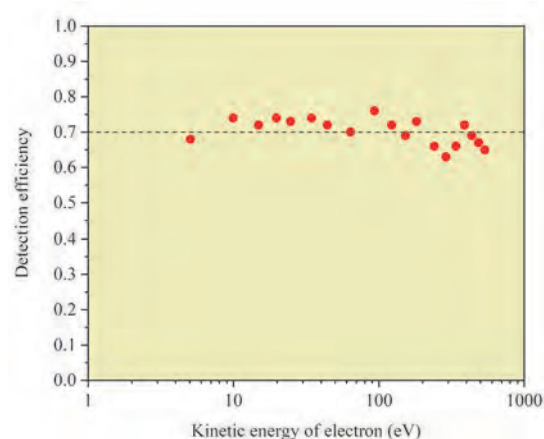


Fig. 1. Electron detection efficiency of the funnel MCP estimated as a function of kinetic energy.

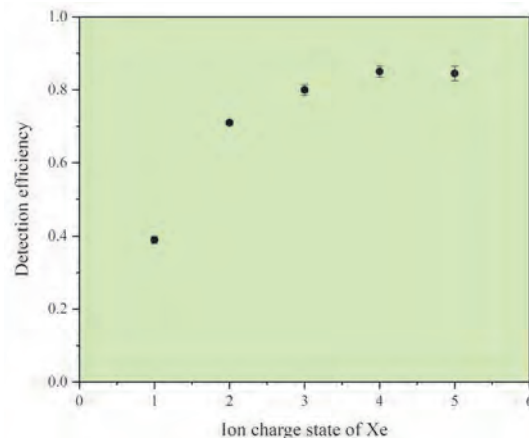
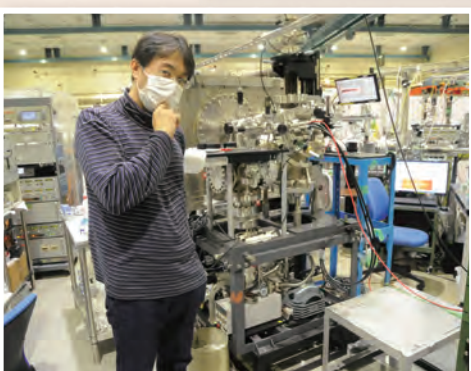
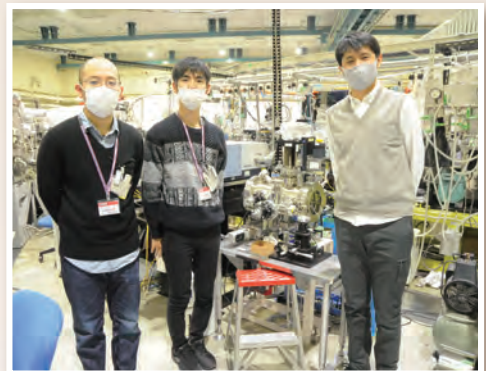
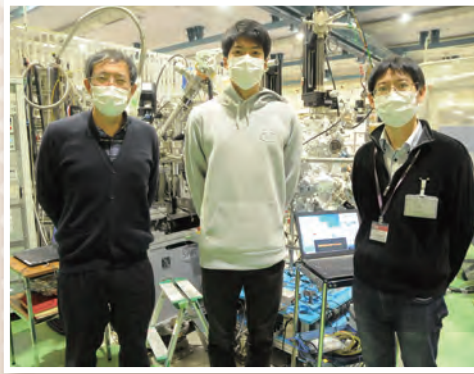
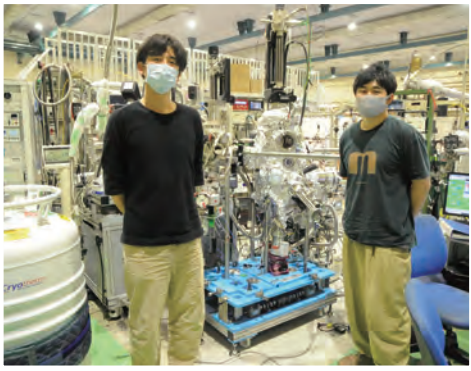


Fig. 2. Detection efficiency of the funnel MCP for Xe ions.

- [1] A. Matsuda, M. Fushitani, C.-M. Tseng, Y. Hikosaka, J.H.D. Eland, and A.Hishikawa, *Rev. Sci. Instrum.* **82** (2011) 103105.
- [2] J.H.D. Eland, P. Linusson, M. Mucke, and R. Feifel, *Chem. Phys. Lett.* **548** (2012) 90.
- [3] Y. Hikosaka and E. Shigemasa, *Int. J. Mass Spectrom.* **439** (2019) 13.
- [4] Y. Hikosaka, M. Sawa, K. Soejima, and E. Shigemasa, *J. Electron Spectrosc. Relat. Phenom.* **192** (2014) 69.

UVSOR User 5



The background is a solid purple color with several abstract geometric elements. A large, semi-transparent circular graphic is centered on the right side, featuring concentric rings and a dashed outer boundary. Diagonal lines and bands of varying shades of purple sweep across the page. At the bottom, there is a grid of small, light-colored dots.

III-4

Surface,
Interface and
Thin Films

BL2A

Zn L_3 -edge XANES of ZnO Powder

E. Kobayashi¹, S. Yoshioka² and K. K. Okudaira³

¹Kyushu Synchrotron Light Research Center, Tosu 841-0005, Japan

²Graduate School of Engineering, Kyushu University, Fukuoka 819-0395 Japan

³Graduate School of Science and Engineering, Chiba University, Chiba 263-8522, Japan

Zinc oxide (ZnO) is an important material in device [1] because of its wide band gap 3.37 eV and has a relatively large exciton binding energy of 60 meV. In recent years, organic photovoltaic (OPV) has been attracting attention as a low-cost, lightweight battery that replaces conventional solar cells. ZnO plays an essential role as an electron transporting layer (ETL) material. In order to further improve the characteristics of ETL, it is necessary to understand the electronic states. Near-edge X-ray absorption fine structure (NEXAFS) spectroscopy is a powerful tool for investigating the electronic structures of materials.

In this report, we investigated the electronic structure of ZnO powder by means of XANES using fluorescence yield method.

Zn L_3 -edge XANES measurements were performed at the BL2A beamline of UVSOR Okazaki, Japan, using the partial fluorescence yield method (PFY). A Beryl double crystal monochromator defined Zn L absorption edges in the energy region from 1000 to 1090 eV. Fluorescence X-rays were collected using an energy dispersible silicon drift detector (SDD). All measurements of XANES spectra were carried out at room temperature.

Figure 1 shows the Zn L -edge NEXAFS spectra of ZnO powder and ZnO/Si film obtained from TEY.

The peak A provides information both about the forbidden electron transitions, which does not obey dipole selection rules and disorder in the crystal geometry [2]. The peak B and C are related to the transition of 2p core electrons to the Zn4p levels [2].

The spectral feature marked as A in Zn L -edge NEXAFS spectra of ZnO powder is almost the same as that of ZnO / Si film, while the peaks B and C in Zn L -edge NEXAFS of ZnO powder are difference from those of ZnO / Si film. This suggests that the surface state of ZnO powder is different from that of ZnO / Si film since TEY is sensitive to the surface electronic states.

Figure 2 shows the Zn L -edge NEXAFS spectra of ZnO powder obtained from PFY. PFY (Zn L) is almost the same as the result of TEY, but PFY (O $K\alpha$) is different. This suggests that the surface and bulk of ZnO particles may have different electronic states of oxygen.

Next, we will clarify how this electronic state changes when an organic layer is placed on ZnO.

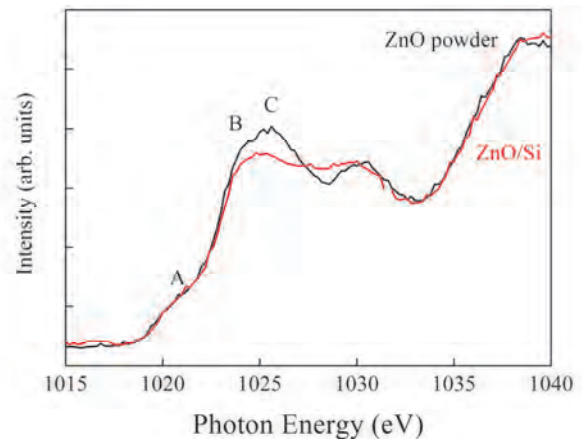


Fig. 1. Zn L -edge XANES spectra of ZnO obtained from TEY. ZnO powder (black) and ZnO/Si film (red) spectrum.

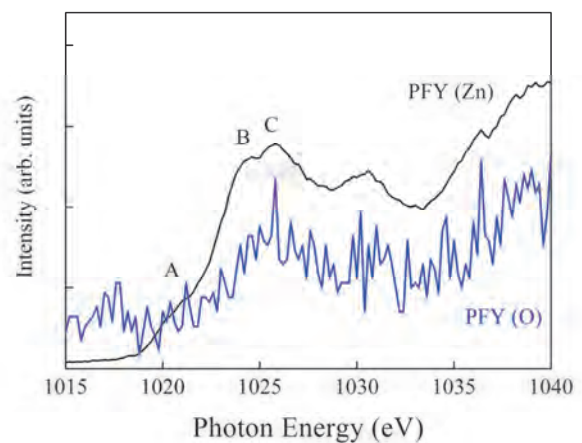


Fig. 2. ZnO L -edge XANES spectra of ZnO powder obtained from PFY. PFY (Zn L) (black) and PFY (O $K\alpha$) (blue) spectrum of ZnO.

[1] F. Quaranta, A. Valentini, F. R. Rizzi, and G. Gasamassima, *J. Appl. Phys.* **74** (1993) 224.

[2] O. M. Ozkendir, S. Yildirimcan, A. Yuzer, K. Ocakoglu, *Progress in Natural Science: Materials International* **26** (2016) 347.

BL2B

Electronic Structure of ZnO Nanoparticles as an Electron Extraction Layer for Organic Solar Cells

K. K. Okudaira and T. Kikuchi

Association of Graduate Schools of Science and Technology, Chiba University, Chiba 263-8522, Japan

Organic devices such as organic photovoltaic cells have been attracting interest concerning both fundamental research and practical application for low-cost, large-area, lightweight and flexible devices. Conjugated polymer solar cells are attractive as a source of renewable energy due to the low cost by using roll-to-roll-printing processes. The most polymer solar cells have bulk heterojunction (BHJ) morphology. At this morphology, one of materials consisting of BHJ contacts directly the undesired electrode. To fabricate inverted polymer solar cells, one widely used approach is to deposit a thin film of zinc oxide (ZnO) nanoparticles as an electron extraction layer and a hole-blocking layer on top of a transparent indium tin oxide coated substrate [2].

For nanoparticles, the contribution of surface to their electronic and optical properties is expected to be significant, because of their large surface area-to-volume ratio.

In this work we deposited ZnO nanoparticles (NPs) using spin-casting method on indium tin oxide (ITO) substrate and estimated the electronic structure of ZnO NPs by ultraviolet photoelectron spectroscopy (UPS) measurements with different exciting energies due to the photoionization cross-section.

UPS measurements were performed at the beam line BL2B of the UVSOR storage ring at the Institute for Molecular Science at the photon energy ($h\nu$) of 28 eV and 40 eV. ZnO NPs with uniform shape and highly dispersed were synthesized using zinc acetate dihydrate ($\text{Zn}(\text{CH}_3\text{COO})_2 \cdot 2\text{H}_2\text{O}$) and potassium hydroxide (KOH) as a precursor and absolute ethanol as solvent via solvothermal method [3]. The thin films of ZnO NPs were deposited on ITO by spin casting (as-grown ZnO NP). The films were annealed at 140 °C in the atmosphere for 10 minutes (annealed ZnO NPs). The mean size of synthesized ZnO NPs was about 7 nm using TEM measurements.

We observed UPS of as-grown ZnO NPs and annealed ZnO NPs at $h\nu$ of 28 eV and 40 eV (Fig. 1). The peak at binding energy (E_b) of about 10 eV at $h\nu$ of 40 eV appears more clearly than that at $h\nu$ of 28 eV. The calculated photoionization cross-section of Zn 3d at $h\nu$ of 40.8 eV is much larger than that at $h\nu$ of 26.8 eV, while that of O 2p at $h\nu$ of 40.8 eV is smaller than that of 26.8 eV [4]. The peak at E_b of about 10 eV can be assigned to Zn-3d. The broad feature at E_b about 7 eV and 4 ~ 5 eV are attributed to mainly Zn-4s electrons and O-2p electrons, respectively [5]. The UPS structure at E_b about 5 eV changes by annealing. The O-2p states would be affected by annealing, due to disappearance of oxygen vacancies and/or formation of hydroxyl

groups at the surface of nanoparticles. Furthermore, the work-function of as-grown ZnO NPs can be estimated to 3.92 eV, which is lower than that of ITO (about 4.6 eV). This value is closer to the electron affinity of PCBM (3.82 eV) [6], which is a typical electron acceptor material in BHJ. It is expected that the ZnO NP is good electron extraction layer for polymer solar cells.

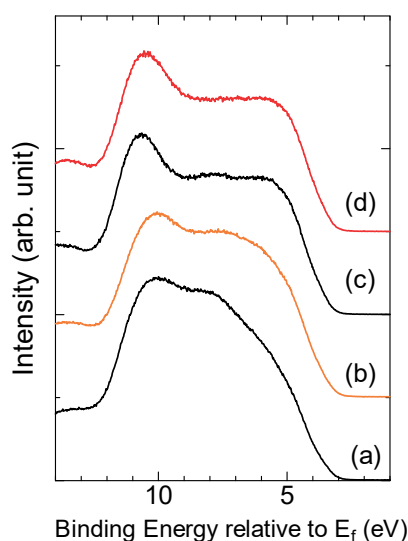


Fig. 1. UPS of (a) as-grown ZnO NPs at $h\nu = 28$ eV, (b) annealed ZnO NPs at $h\nu = 28$ eV (c) as-grown Zn NPs at $h\nu = 40$ eV, (d) annealed ZnO NPs at $h\nu = 40$ eV.

- [1] X. Gu *et al.* *Adv. Energy Mater.* **7** (2017) 1602742.
- [2] S. Kim *et al.* *Chem. Commun.* **49** (2013) 6033.
- [3] N. M. Shamhari *et al.* *Acta Chim. Slov.* **65** (2018) 578.
- [4] Atomic Calculation of Photoionization Cross-Sections and Asymmetry Parameters, J. -J. YEH, 1993, AT & T.
- [5] W. Ranke, *Solid state commun.* **19** (1976) 685.
- [6] H. Yoshida, *J. Phys. Chem. C*, **118** (2014) 24377.

BL3U

Layered Manganese Oxide Electrocatalyst Containing K⁺ Cation for Water Oxidation Studied by Operando XAFS Observations

S. Tsunekawa¹, M. Nagasaka², H. Yuzawa² and M. Yoshida¹¹*Yamaguchi University, Tokiwadai, Ube 755-8611, Japan*²*Institute for Molecular Science, Okazaki 444-8585, Japan*

Energy consumption is increasing in proportion to the world's population. This large energy consumption is leading to serious problems such as depletion of fossil fuels and increase in carbon dioxide emissions. In recent years, hydrogen production has been attracting attention as a CO₂-free energy source that does not rely on fossil fuels, and a hydrogen production process by water electrolysis using renewable energy sources has been proposed. However, the insufficient efficiency of oxygen evolution reaction (OER) restricts the efficiency of overall water splitting. In this situation, a potassium-including manganese oxide (K:MnO_x) was developed by Nocera group [1], and they reported that K:MnO_x could decompose water to oxygen gas efficiently. Thus, we have investigated the structure and function of the K:MnO_x catalysts during water splitting by operando soft, tender, and hard X-ray XAFS measurements.

The electrochemical cell was used with a Pt counter and an Ag/AgCl reference electrode. The K:MnO_x catalyst was prepared by electrodeposition on Au thin film in a solution containing MnCl₂ and K⁺ cation. Under electrochemical control, the operando Mn K-edge and K K-edge XAFS were measured by fluorescence mode in the PF BL-9A, and the operando O K-edge XAFS was measured by transmission mode at BL3U in the UVSOR Synchrotron.

First, we checked the OER activity and found that K:MnO_x function as highly efficient water splitting catalyst. The surface morphology and chemical composition were investigated by SEM, EDX and XPS. The Faraday efficiency for catalyst was estimated as about 100 % for production of oxygen and hydrogen gasses by quadrupole mass spectrometry.

Next, operando O K-edge XAFS was measured under electrochemical control, and the peak top position and shape of the spectra for the K:MnO_x suggested that the electronic state of Mn species in the catalyst was similar with δ-MnO₂ (Fig. 1.). Then, operando Mn K-edge XAFS measurements showed that most of the Mn species were oxidized from Mn³⁺ to Mn⁴⁺ at 1.0V, although small amount of Mn³⁺ remained. Furthermore, the curve fitting of the Fourier transform of k³ weighted EXAFS oscillation exhibited that the local structure of Mn species in the catalyst composed of δ-MnO₂ structure, which was similar to the conclusion of the operando O K-edge XAFS. On the other hand, operando K K-edge XAFS measurements showed that the hydrated K⁺ intercalated between the δ-MnO₂ layers. It is reported that the water splitting reaction proceeds at a Mn³⁺ sites in the δ-MnO₂ structure [2-4]. Thus, we

also suggest that the Mn³⁺ in the δ-MnO₂ layers function as the active sites for OER process [5].

In conclusion, we investigated the electronic state and local structure of K:MnO_x electrocatalyst by operando O K-edge, Mn K-edge and K K-edge XAFS measurements. The result elucidates that the catalyst composed of δ-MnO₂ with layered structures containing hydrated alkali metal ion, and suggested that the water splitting reaction efficiently proceeded at the active sites of Mn³⁺.

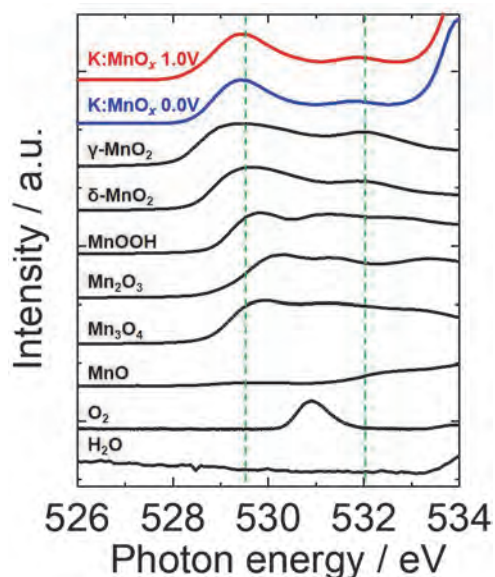


Fig. 1. Operando O K-edge XAFS spectra for K:MnO_x and references.

- [1] M. Huynh, D. Bediako and D. Nocera, *J. Am. Chem. Soc.* **136** (2014) 6002.
- [2] T. Takashima, K. Hashimoto and R. Nakamura, *J. Am. Chem. Soc.* **134** (2012) 1519.
- [3] M. Huynh, C. Shi, S. Billinge and D. Nocera, *J. Am. Chem. Soc.* **137** (2015) 14887.
- [4] Y. Gorlin, B. Kaiser, J. Benck, S. Gul, S. Webb, V. Yachandra, J. Yano and T. Jaramillo, *J. Am. Chem. Soc.* **135** (2013) 8525.
- [5] S. Tsunekawa, F. Yamamoto, K. Wang, M. Nagasaka, H. Yuzawa, S. Takakusagi, H. Kondoh, K. Asakura, T. Kawai and M. Yoshida, *J. Phys. Chem. C.* **124** (2020) 23611.

BL3B

Control of Growth Orientation and Evaluation of Film Quality of UV Emitting Zinc Aluminate Phosphor Thin Films

H. Kominami¹, M. Endo², T. Kawashima², N. Sonoda², A. Fujii¹, K. Inoue¹,
N. Uesugi¹, K. Nie¹, A. Dorokhina³ and S. Kurosawa^{4,5}

¹Graduate School of Integrated Science and Technology, Shizuoka University, Hamamatsu 432-8651, Japan

²Faculty of Engineering, Shizuoka University, Hamamatsu 432-8651, Japan

³Graduate School of Science and Technology, Shizuoka University, Hamamatsu 432-8651, Japan

⁴New Industry Creation Hatchery Center (NICHe), Tohoku University, Sendai 980-8579, Japan

⁵Faculty of science, Yamagata University, Yamagata 990-8560, Japan

The global pandemic of COVID-19 has led to frequent disinfection of hands and everywhere they can touch, and the pharmaceutical industry is rapidly developing vaccines. A “new normal” has been advocated, and it has become necessary not only to wear face masks and secure social distance, but also lifestyle habits including dietary habits that improve immune function are emphasized, and how to protect ourselves from viruses is important. It has become a re-concern in people's lives.

The UV light is used for various applications depending on the wavelength as well as the sterilization described above. The lights of 200-280nm (UV-C) region as for the sterilization, 280-320nm (UV-B) region as the treatment of the skin disease, 320-400nm (UV-A) region as application of purification of water and air, and photocatalysts. Recently, from the viewpoint of consideration to the environment, the mercury free UV emission devices have been demanded for the application of catalyst and medical situations. In our previous work, it was clarified that ZnAl_2O_4 phosphor was suitable for the UV field emission lamp because of its stability and luminescent property. It shows strong UV emission peaked around 250 nm which suitable for sterilization.

In this research, ZnAl_2O_4 layer were prepared by thermal diffusion of ZnO and sapphire substrate for new UV devices. To obtain ZnAl_2O_4 thin film with high quality, we explore optimum condition of thermal annealing, such as annealing temperature, atmosphere, and annealing time. From the experiment, optimum annealing conditions were obtained 990 °C for 50 hours.

Figure 1 shows PLE spectra of ZnAl_2O_4 thin films prepared on 2 types of sapphire substrate, one-side polished and both-side polished. PL intensity of one-side polished substrate was higher than the both-side polished. It is thought that the possibility of total internal reflection occurs inside the board of the substrate. Therefore, it is necessary to determine the film thickness by fully considering the light extraction efficiency.

Figure 2 shows transmittance spectra of ZnAl_2O_4 thin film, compared with sapphire substrate. Excitation edges were observed around 180 nm and 380 nm. The edge of 180 nm was caused from ZnAl_2O_4 , it consistent with the transmittance results. However, the edge of 380

nm was caused from slightly residual ZnO phase. In order to suppress the residual zinc oxide, it is necessary to carefully examine the film thickness of ZnO.

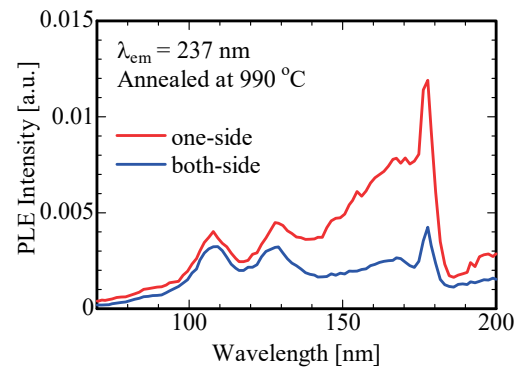


Fig. 1. PLE spectra of ZnAl_2O_4 thin films prepared on sapphire substrate of one-side polished and both-side polished.

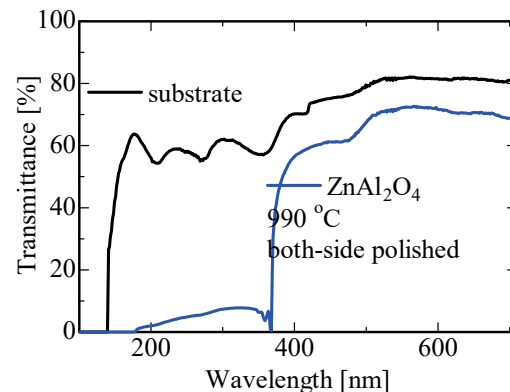


Fig. 2. Transmittance spectra of ZnAl_2O_4 thin film.

BL4B

Characterization of Amorphous Arsenic, Selenium and Arsenic Triselenide by Vacuum Ultraviolet Transmission Spectroscopy

K. Hayashi

Department of Electrical, Electronic and Computer Engineering, Gifu University, Gifu 501-1193, Japan

Amorphous chalcogenide semiconductor materials are very expected as a potential material for optoelectronic devices. Because, in these materials are very sensitive to the light, and show a variety of photoinduced phenomena [1-3]. Although many studies have been done on the photoinduced phenomena of these materials, little is known about the details of these mechanisms. These phenomena were studied by exciting outer core electrons with the irradiation of light with the energy corresponding to the optical bandgap or sub-bandgap. The interest has been attracted for the change of the optical properties in the energy region of the visible light. We are interesting for the changes of the optical properties in the higher energy region. To obtain a wide knowledge of the photoinduced phenomena, it is necessary to investigate to the photoinduced and annealing effects on wide energy region. In this report, we report the VUV transmission spectra of amorphous compound semiconductors and their constituent elements.

Samples used for the measurement of the VUV transmission spectra were amorphous arsenic, selenium and arsenic triselenide thin films prepared onto thin aluminum films by conventional evaporation technique. The sample thicknesses ranged between 100 and 200 nm. The aluminum film of the thickness of 200 nm was used to eliminate the higher order light from the monochromator in the VUV region. These measurements were carried out at room temperature at the BL4B beam line of the UVSOR facility of the Institute for Molecular Science. The spectrum was measured by using the silicon photodiode as a detector. Two pinholes of 1.5 mm in a diameter were inserted between the monochromator and sample to remove stray light. The intensity of the VUV light was monitored by measuring the TPEY of a gold mesh. The positions of the core levels for the samples were calibrated by referencing to the 2p core level absorption peak of the aluminum film.

Figure 1 shows the VUV transmission spectra of amorphous arsenic (a-As), selenium (a-Se) and arsenic triselenide (a-As₂Se₃) thin films. Two main absorption peaks were observed in this wavelength region for amorphous As₂Se₃. One absorption peak around 22nm corresponds to the 3d core level of Se atom. Another absorption peak around 28 nm corresponds to the 3d core level of As atom. As shown in the figure, each spectrum is very broad and multiple shoulders are observed. The absorption spectrum observed in the amorphous As₂Se₃ is roughly consistent with the previous report [4]. On the other hand, VUV

transmission spectra of amorphous As and Se are different from the previous report. Although the wavelength resolutions in the spectral measurements are all the same, the spin-orbit splitting of the 3d_{5/2} and 3d_{3/2} level of each atom is clearly resolved in amorphous As₂Se₃, while in amorphous As and Se are not clearly resolved. It is not clear about the origin of broad spectra and shoulders. I think that these origins are related to the local structures of the amorphous network. Therefore, it seems that it depends on the preparation method and the presence or absence of annealing. The detailed experiments and analysis will be done in the next step. More detailed experiments are necessary to clarify the origin of the VUV transmission spectra.

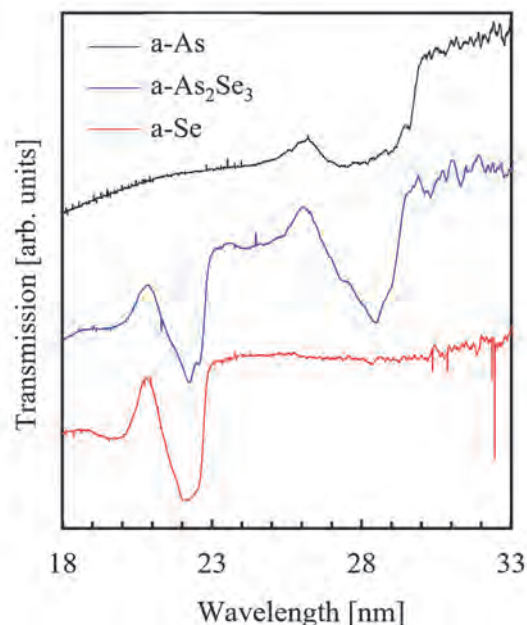


Fig. 1. VUV transmission spectra of a-As, a-Se, and a-As₂Se₃ thin films.

- [1] K. Tanaka, Rev. Solid State Sci. **4** (1990) 641.
- [2] K. Shimakawa, A. Kolobov and S. R. Elliott, Adv. Phys. **44** (1995) 475.
- [3] K. Tanaka, Encyclopedia of Nanoscience and Nanotechnology **7** (2004) 629.
- [4] J. Bordas and J. B. West, Phil. Mag. **34** (1976) 501.

BL4B

Structural and Magnetic Properties of FeCo Alloy Multilayer Thin Films Grown by Nitrogen Surfactant Epitaxy on Cu(001)

T. Miyamachi¹, K. Yamamoto^{2,3}, T. Koitaya^{2,3} and T. Yokoyama^{2,3}¹The University of Electro-Communications, Chofu 182-8585, Japan²Institute for Molecular Science, Okazaki 444-8585, Japan³The Graduate University for Advanced Studies, SOKENDAI, Okazaki 444-8585, Japan

An L1₀-type FeCo ordered alloy attracts much attention as a rare-earth free magnetic material due to its large magnetic anisotropy, large magnetic moment, and high Curie temperature. Intensive works has been carried out to fabricate L1₀-FeCo phase with uniaxial anisotropy. Using pulsed laser deposition, the growth of FeCo thin films with alternating Fe and Co atomic layers was investigated [1]. However, the L1₀ structure is a non-equilibrium state of FeCo phase and hence its fabrication method has not been established yet. The main problem could be caused by the atomic-scale disorder at the Fe/Co interface during growth processes, which suggests the importance of microscopic characterizations of structural, electronic and magnetic properties of L1₀-FeCo.

To improve the quality of FeCo alloy thin films, we intend to incorporate nitrogen surfactant effects of monatomic layer magnetic nitrides into the alternate atomic-layer Fe and Co deposition. In this method, the nitrogen surfactant epitaxy of monatomic layer magnetic nitride with high lateral lattice stability can suppress the interdiffusion at the Fe/Co interface during the deposition and annealing processes, which results in atomically flat surface/interface. The important role of the nitrogen surfactant effect on the fabrication of high quality L1₀-type alloy thin films has been demonstrated for FeNi alloy thin films [2].

In this study, we here performed combined study of scanning tunneling microscopy (STM) and x-ray absorption spectroscopy/x-ray magnetic circular dichroism (XAS/XMCD) to investigate structural, electronic and magnetic properties of FeCo alloy multilayer thin films by the nitrogen surfactant epitaxy. This complementary experimental approach enables to link macroscopic observations of element specific and quantitative electronic and magnetic properties by XAS/XMCD with microscopic origins of the Fe/Co interface characteristics revealed by STM [3]. FeCo alloy multilayer thin films was grown on Cu(001) in the following processes: (1) the monatomic layer iron nitride (Fe₂N) was first grown on Cu(001) [4], (2) 1 ML Co was deposited at a low temperature (~ 150 K) and annealed at room temperature, (3) alternating layer deposition of Fe and Co was repeated to fabricate multilayers.

XAS/XMCD measurements were performed at BL4B in UVSOR by total electron yield mode at B = 0 - ± 5 T and T = 7.3 K. The XMCD spectra are obtained at the normal (NI: θ = 0°) and the grazing (GI: θ = 55°)

geometries by detecting $\mu_+ - \mu_-$, where μ_+ (μ_-) denotes the XAS recorded at Fe and Co L adsorption edges with the photon helicity parallel (antiparallel) to the sample magnetization. Note that θ is the angle between the sample normal and the incident x-ray. Magnetization curves were recorded by plotting the L₃ XAS intensity normalized by the L₂ one as a function of the magnetic field.

We first confirmed from XMCD measurements the strong in-plane magnetic anisotropy of bare Fe₂N as previously reported [4]. STM measurements revealed that adding Co 1 ML on Fe₂N results in the formation of Co₂N/Fe/Cu (001) via nitrogen surfactant effect. Accordingly, relative increase in the out-of-plane magnetization of Fe to the in-plane magnetization was observed. We found from thickness dependence of Fe magnetization curves that the out-of-plane magnetization of Fe was further increased by repeating alternative depositions of Fe and Co. The results possibly reflect the intrinsic out-of-plane magnetization of L1₀ FeCo and indicate that the nitrogen surfactant effect efficiently suppress the interdiffusion at the Fe/Co interface and keep atomically flat surface/interface in FeCo atomic layers.

[1] H. Ito *et al.*, AIP Advances **9** (2019) 045307.[2] K. Kawaguchi *et al.*, Phys. Rev. Materials, **4** (2020) 054403.[3] S. Nakashima *et al.*, Adv. Funct. Mater. **29** (2019) 1804594.[4] Y. Takahashi *et al.*, Phys. Rev. B **95** (2017) 224417.

BL4B

Ground State and Magnetic Properties of Iron Phthalocyanine Thin Films Grown on a Monolayer Graphene Sheet

S. Ohno¹, I. Sakaida¹, K. Yamamoto^{2,3}, T. Koitaya^{2,3} and T. Yokoyama^{2,3}¹College of Engineering Science, Yokohama National University, Yokohama 240-8501, Japan²Institute for Molecular Science, Okazaki 444-8585, Japan³The Graduate University for Advanced Studies, SOKENDAI, Okazaki 444-8585, Japan

Iron phthalocyanine (FePc) is one of the prototype molecules to study magnetic properties of molecular thin films. It is a planar molecule which has an Fe²⁺ iron at the center. The ground state of an FePc molecule has been a controversial issue. Density functional theory (DFT) calculations showed that the calculated density of states (DOS) at the valence band region agree well with the experimental data [1]. However, it was found to be quite difficult to determine the ground state symmetry unambiguously because of the similarity of the calculated DOS even for the ground states with different symmetries. X-ray absorption spectroscopy study suggested that the ³E_g ground state with the half-filled e_g state at the Fermi level is plausible for FePc thin films grown on gold surfaces [2]. In the present work, we focused on the ground state and magnetic properties of FePc thin films grown on a monolayer graphene sheet, which is produced by chemical vapor deposition (CVD) and transported onto the silicon oxide substrate (Gr/SiO₂).

BL4B soft X-ray beamline was used for X-ray Absorption Near Edge Structure (XANES) spectroscopy measurements in N K-edge and Fe L-edge regions, and X-ray Magnetic Circular Dichroism (XMCD) measurements in Fe L-edge region.

We have reported on our previous results for FePc thin films grown on passivated silicon surfaces as well as a graphene sheet [3]. Here, we report on our new results on the high-resolution XANES spectra, and some further analysis on the magnetic properties.

Figures 1 (a) and (b) show XANES spectra taken at the incident angle of $\theta = 0^\circ$ and 65° , respectively. These results agree well with the previous assignment of the spectral components based on the ³E_g ground state [2].

Tilt angle of the molecular plane of FePc can be evaluated based on the conventional analysis method[4]. The obtained value is $\sim 24^\circ$ in the present case. The applicability of the full analysis using the sum rules is based on the assumption that the FePc molecule takes the adsorption configuration of the flat-lying orientation and has D_{4h} symmetry in the point group representation [2]. Present XANES spectra shown in Fig. 1 is quite similar to those in the other reports[2,5], suggesting that the sum rules can be applied approximately.

Thus, we could have obtained a series of physical

quantities related to the magnetic properties of FePc. For example, the ratio of the orbital moment in the molecular plane (m_L^y) and the spin moment (m_s) is evaluated to be ~ 1.0 , even larger than the reported value of ~ 0.8 [2]. This indicates that the enhancement of the orbital moment is promoted by the contact with the graphene sheet.

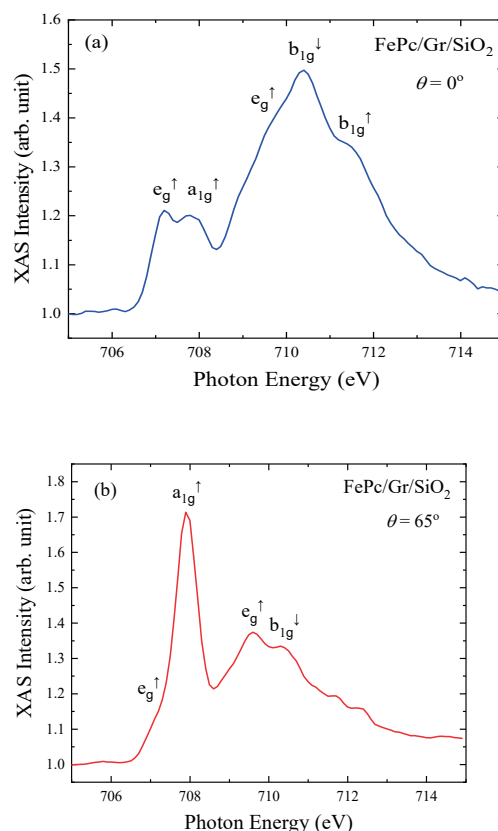


Fig. 1. Angle-dependent linearly polarized XANES spectra for FePc/Gr/SiO₂.

- [1] N. Marom *et al.*, Appl. Phys. A **95** (2009) 165.
- [2] J. Bartolomé *et al.*, Phys. Rev. B **81** (2010) 195405.
- [3] S. Ohno *et al.*, UVSOR Activity Report 2019 **47** (2020) 133.
- [4] J. Stöhr, "NEXAFS Spectroscopy" (Springer).
- [5] S. Lisi *et al.*, J. Phys. Chem. Lett. **6** (2015) 1690.

BL5U

Observation of Electronic Band Structure in Two-dimensional WSe₂ Flake

M. Sakano¹, Y. Tanaka¹, S. Masubuchi², S. Okazaki³, K. Watanabe⁴, T. Taniguchi⁵,
T. Sasagawa³, T. Machida² and K. Ishizaka¹

¹Quantum-Phase Electronics Center and Department of Applied Physics, The University of Tokyo,
Tokyo 113-8656, Japan

²Institute of Industrial Science, The University of Tokyo, Tokyo 153-8505, Japan

³Materials and Structures Laboratory, Tokyo Institute of Technology, Yokohama 226-8503, Japan

⁴Research Center for Functional Materials, National Institute for Materials Science, Tsukuba 305-0044, Japan

⁵International Center for Materials Nanoarchitectonics, National Institute for Materials Science,
Tsukuba 305-0044, Japan

Development of fabrication techniques for exfoliated two-dimensional (2D) flakes enables us to investigate the physical properties of the 2D materials. In 2D materials, peculiar physical phenomena that do not appear in bulk crystals are realized because the electronic band dispersion discretely changes as the layers decrease to the monolayer limit. However, due to the limited size of the flake samples (typically $\sim 10 \mu\text{m}$), it is a challenging task to precisely determine the electronic structures of various two-dimensional materials.

In our study, we have developed a procedure to fabricate flake samples that can be adapted to various 2D materials and investigated the electronic band dispersions of monolayer WSe₂ by performing micro-focused angle-resolved photoelectron spectroscopy (micro-ARPES).

The samples were fabricated by an all-dry pick-up and flip method (see ref. [1] for details). As shown in Fig. 1 (a), the monolayer WSe₂ is encapsulated with graphene to prevent oxidation of the WSe₂, and electrically contacts to an Au electrode fabricated on a SiO₂/Si substrate through graphite to prevent charging up. The fabricated sample is pumped and sealed in an ICF-70 nipple with a gate valve, and transported to the ultrahigh vacuum chamber. Before the micro-ARPES measurement, the sample is annealed around 200 °C for ~ 10 hours in the ultrahigh vacuum.

Figure 1 (b) shows an obtained ARPES image. Unfortunately, although we could observe the photoelectron intensities of the graphene and/or graphite, but not observe those of the monolayer WSe₂. After the measurement, the spot size of the synchrotron light was evaluated and found to be much larger than the size of the WSe₂ flake ($\sim 20 \mu\text{m}$) in the setup at that time. For future measurements, it is necessary to make the spot size of the synchrotron light comparable to the size of the fabricated sample before performing the ARPES measurement.

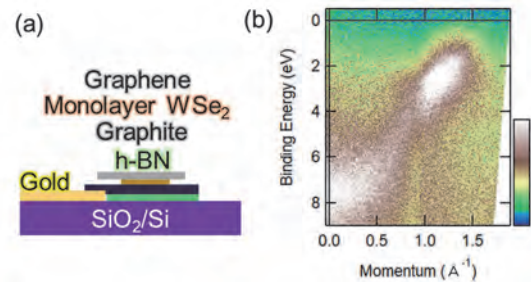


Fig. 1. (a) A schematic of a fabricated monolayer WSe₂ flake (typical size $\sim 20 \mu\text{m}$) sample for micro-ARPES measurement. The monolayer WSe₂ electrically connects to an Au electrode fabricated on a SiO₂/Si substrate through graphite. To prevent oxidation of the WSe₂ flake, the topmost is covered by graphene (typical size $\sim 100 \mu\text{m}$). The detailed fabrication process is written in ref. [1]. (b) Obtained ARPES image. The photoelectron intensities from the graphene and/or graphite can be observed, but not clearly from the monolayer WSe₂.

[1] M. Sakano *et al.*, arXiv:2103.11885 (2021).

BL5U

Electronic Structures of Transition Metal Phosphide (TMP) Thin Films on TMP Substrates

N. Maejima^{1,2}, T. Yoshida¹, Y. Shimato¹ and K. Edamoto^{1,2}

¹Coll. Sci., Rikkyo Univ., Tokyo 171-8501, Japan

²Research Center for Smart Molecules, Rikkyo Univ., Tokyo 171-8501, Japan

Transition metal phosphides (TMPs) have attracted much attention because of their high catalytic activities for hydrodesulfurization (HDS). Among TMPs studied thus far, Ni₂P shows the highest catalytic activity while that of Fe₂P is extremely low [1]. Recently it has been found that, when some of Ni atoms in Ni₂P are substituted by Fe atoms (denoted as NiFeP, hereafter), the reaction path is changed from a hydrogenation path to a direct desulfurization path [2]. Such a change in selectivity should be closely related to the change in the electronic structure of active Ni sites due to the charge transfer between Ni, Fe and P atoms. In this study, we investigate the electronic structures of Ni_xP/Fe₂P and Fe_xP/Ni₂P, which can be viewed as model systems to reveal the charge transfer in NiFeP.

Experiments were performed at BL5U of the UVSOR facility. Ni₂P(10-10) and Fe₂P(10-10) were cleaned by cycles of Ar⁺ ion sputtering (0.5 keV) and annealing (600 °C and 750 °C, respectively). The cleaned surfaces showed c(2x4) and c(2x2) LEED patterns, respectively. Fe (Ni) atoms were deposited on the Ni₂P (Fe₂P) clean surface at room temperature and the films were post annealed at 350 °C (550 °C), which induces phosphorization of the film owing to surface segregation of P atoms from the bulk [3,4]. The prepared Fe_xP/Ni₂P and Ni_xP/Fe₂P samples showed 1x2 and c(2x2) LEED patterns, respectively. Ni 3p, P 2p, Fe 3p and valence band photoelectron spectroscopy (PES) measurements were performed by an MBS A-1 analyzer.

The Fe 3p spectra of Fe₂P, Ni_xP/Fe₂P and Fe_xP/Ni₂P are shown in Fig.1 (a). The analyses of angle resolved Fe 3p spectra revealed that the 3p level of Fe atoms in the interface region of Ni_xP/Fe₂P located at 54.5 eV. This is slightly higher than that observed for a Fe₂P substrate. The Ni 3p spectra of Ni₂P, Ni_xP/Fe₂P and Fe_xP/Ni₂P are shown in Fig.1 (b). Ni 3p peak of Ni_xP/Fe₂P was shifted to the lower binding energy side from that of the Ni₂P substrate. The results showed that Fe 3p and Ni 3p peaks were shifted due to the interaction between the Ni₂P thin film and the Fe₂P substrate. On the other hand, these peaks showed little shifts in the case of Fe_xP/Ni₂P. These results suggest that the Ni_xP film is chemically bound to the Fe₂P substrate while the interaction between the film and the substrate is weak in the case of Fe_xP/Ni₂P.

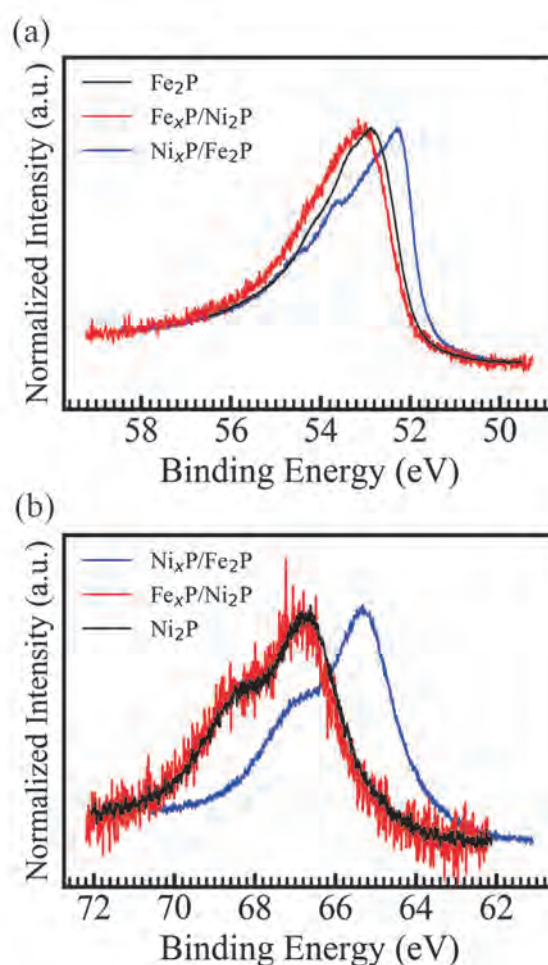


Fig. 1. (a) Fe 3p and (b) Ni 3p photoelectron spectra of Fe₂P, Ni₂P, Fe_xP/Ni₂P and Ni_xP/Fe₂P

- [1] S. T. Oyama *et al.*, *J.Catal.* **216** (2003) 343.
- [2] S. T. Oyama *et al.*, *J.Catal.* **285** (2012) 1.
- [3] S. Imanishi *et al.*, *e-J. Surf. Sci. Nanotech.* **10** (2012) 45.
- [4] Y. Sugizaki *et al.*, *Jpn. J. Appl. Phys.* **57** (2018) 115701.

BL5U

Electronic Band Structure of Novel Se-containing Phases on SrTiO₃

 B. Lin^{1,2}, C. Y. Hong^{1,2}, Z. Song^{1,2}, P. X. Ran^{1,2} and R.-H. He²
¹Department of Physics, Fudan University, Shanghai 200433, China

²School of Science, Westlake Institute for Advanced Study, Westlake University, Hangzhou 310064, China

Searching for novel quantum materials and understanding their properties have been a major theme in condensed matter physics. Se substitution in SrTiO₃ has revealed multiple electronic phases with peculiar band structures that were initially observed using our home-based ARPES with Helium lamp.

To further study the electronic band structure of one of the phases (Phase #1), we performed systematic ARPES measurements at the BL5U of UVSOR. A series of Fermi surface maps and cuts along high-symmetry directions were measured with photons of linearly horizontal (LH) and linearly vertical (LV) polarization and energy ($h\nu$) from 42 eV to 180 eV at $T=5.8$ K. Figures 1(a) and (b) are, respectively, an iso-energy contour and the band dispersion along Cut#1 through Γ point obtained with $h\nu = 160$ eV (LH). Figure 2 are Cut#1 taken with a series of photon energies between 57 eV and 67 eV with LH & LV polarization, which suggests a negligible k_z dependence.

We also studied another phase (Phase #2) in Se-substituted SrTiO₃ that is different from the one above. Figure 3 compare the cuts measured near Γ point between Phase #1 and Phase #2 with $h\nu = 60$ eV at $T = 5.8$ K. Our measurements of Phase #2 show the photon energy dependence from 110 eV to 125 eV (See Fig. 4).

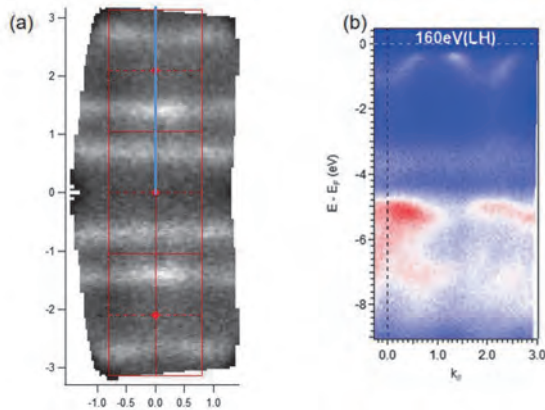


Fig. 1. Iso-energy contour and momentum cut obtained with $h\nu = 160$ eV at $T = 5.8$ K. (a) Integrated spectral intensity in the momentum space of Phase 1 over a small energy window $[-0.21$ eV, -0.19 eV]. (b) Band dispersion image along Cut #1 as marked in Fig. 1(a).

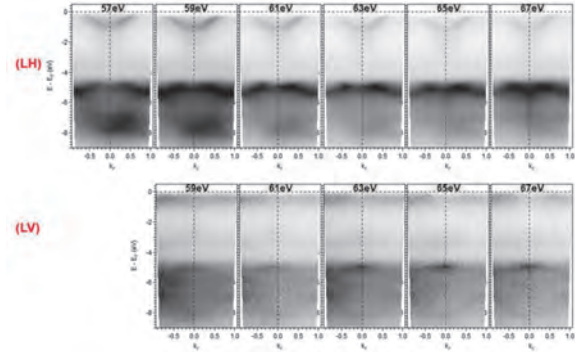


Fig. 2. Cut #1 in Fig. 1(a) measured with a series of photon energies between 57 eV and 67 eV with LH & LV polarization at $T = 5.8$ K.

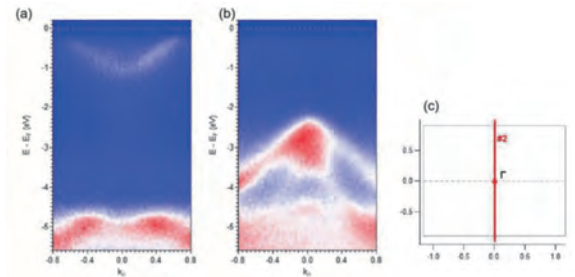


Fig. 3. Band dispersion image measured with $h\nu = 60$ eV at $T = 5.8$ K for (a) Phase #1 and (b) Phase #2 along Cut #2 as marked in Fig. 3(c).

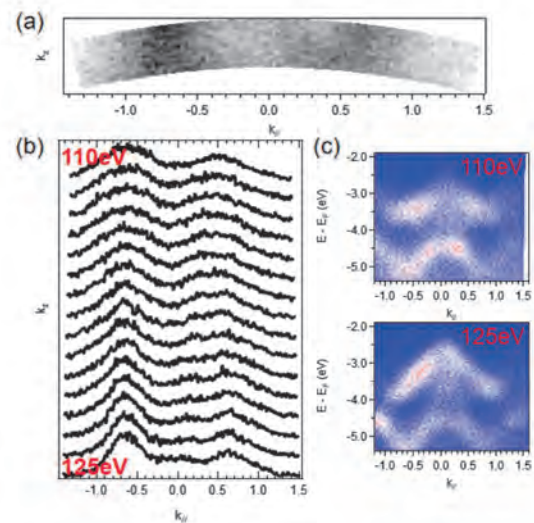


Fig. 4. k_z dependence of Phase #2. (a) Iso-energy map in the k_x - k_z plane and (b) stacked momentum distribution curves (MDCs) at energy -3.5 eV. (c) Band dispersion image along Cut #2 as marked in Fig. 3(c) with $h\nu = 110$ eV & 125 eV.

BL5B

Reflectance Measurements of Al/TiO₂ Bilayers in the 10–30 eV Region at BL5B, UVSOR

T. Hatano¹, Y. Matsuda² and T. Ejima¹¹IMRAM, Tohoku University, Sendai 980-8577, Japan²Department of Chemistry, Graduate School of Science, Tohoku University, Sendai 980-8578, Japan

VUV of a photon energy of 12.4 eV from Ar excited by laser pulse is a high potential source when it is focused by a suitable condenser optics. Al is known as the best material for normal incidence mirror if its surface is not covered by oxide layer. As a capping layer material to prevent the surface oxidation of Al, we have chosen TiO₂ considering its low refractive index at 12.4 eV, 0.63 [1]. By bilayer model of 2 or 4 nm thick TiO₂ on a thick Al, normal incidence reflectance can be expected as 68 % or 52 %, respectively. We have fabricated Al/TiO₂ bilayer on SiO₂ substrates by three methods: (1) Al (100 nm)/TiO₂ (2 and 4 nm) by consecutive thermal evaporation deposition, (2) Al (200 nm) thermal evaporation deposition, transfer to another vacuum chamber, Al surface oxide layer milling and TiO₂ (2 and 4 nm) magnetron sputtering deposition, and (3) Al (200 nm)/TiO₂ (0–14 nm gradient) consecutive ion beam sputtering deposition.

Reflectance measurements were performed at BL5B, UVSOR. The grating and mirror combination was G3M5. The angle of incidence was 11.6°.

Figure 1 shows the measured spectral reflectance of evaporated Al (100 nm)/TiO₂ (2 and 4 nm) bilayers. Oscillation structure appeared through 9–31 eV. The period did not depend on the thickness of TiO₂, which means the oscillation was caused by interference of substrate-Al interface reflection and Al-TiO₂ interface reflection. The spectral shape in 9–15 eV looks like a reduced-size copy of that in 18–30 eV. It is because of the second order diffraction of the monochromator [2]. As a result, reflectances at 12.4 eV were quite low.

Figure 2 shows the measured spectral reflectance of evaporated Al (200 nm)/sputtered TiO₂ (2 and 4 nm) bilayers. The thickness of Al layer is uncertain because of the oxide layer removal before TiO₂ deposition. The result that the periods of the oscillation structure were shorter than those of Fig. 1 means the Al layer was thicker than 100 nm.

Figure 3 shows the measured spectral reflectance of sputtered Al (200 nm)/TiO₂ (0–14 nm) bilayer. Measurement points was shifted by 8 mm to change TiO₂ thickness by 2 nm. The plot raveled by 0 nm shows an Al with surface oxide layer. The reflectance in low energy region was unexpectedly low [3]. The reason could be attributed to the second and higher order diffraction or low energy scattering of the gating could be attributed.

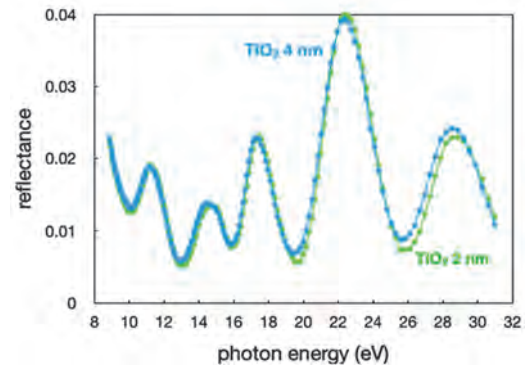


Fig. 1. Spectral reflectances of evaporated Al (100 nm)/TiO₂ (2 and 4 nm) bilayers.

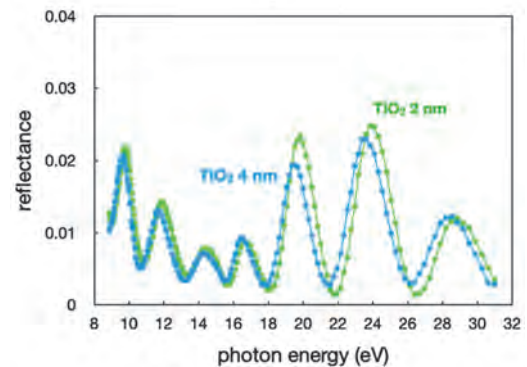


Fig. 2. Spectral reflectances of evaporated Al (200 nm)/sputtered TiO₂ (2 and 4 nm) bilayers.

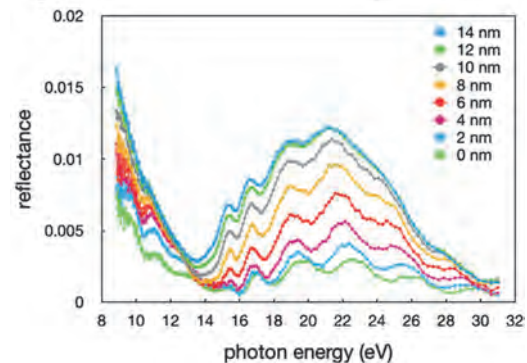


Fig. 3. Spectral reflectances of sputtered Al (200 nm)/TiO₂ (0–14 nm) bilayer.

[1] *Handbook of Optical Constants of Solids* (Ed. by Edward D. Palik, Academic Press, Inc., 1985).

[2] T. Hatano *et al.*, UVSOR Activity Report 2019 **47** (2020) 41

[3] G. Hass and R. Tousey, *J. Opt. Soc. Am.* **49** (1959) 539.

BL5B

Measurement of Soft X-Ray Resonant Magneto-Optical Kerr Effect for GdFe(Co) and TbFe

T. Sumi¹, M. Horio¹, S. E. Moussaoui¹, E. Nakamura², S. Makita^{2,3}, K. Tanaka^{2,3}, A. Tsukamoto⁴ and I. Matsuda¹

¹The Institute for Solid States Physics, The University of Tokyo, Kashiwa 277-8581, Japan

²Institute for Molecular Science, Okazaki 444-8585, Japan

³the Graduate University for Advanced Studies, SOUKENDAI, Okazaki 444-8585, Japan

⁴College of Science and Technique, Nihon University, Funabashi 274-8501, Japan

In the advanced information society today, spintronic devices have attracted great interests due to the fast-processing speed [1]. The material is complicated and composed of multi-element, it has been demanded to track their spin dynamics at individual magnetic elements. Recently, we have developed an experimental technique of the resonant magneto-optical Kerr effect (RMOKE) in soft X-ray region and succeeded in element-selectively tracing spin-states of d-electrons at transition metal atoms, *e.g.* Fe [1-5]. In the present research, we extended our spintronics research to the f-electronic system, such as in rare-earth elements, by the RMOKE experiment.

We prepared two ferrimagnetic samples: Gd₂₃Fe₆₇Co₁₀ crystal and Tb₂₀Fe₈₀ crystal. The direction of spontaneous magnetization was perpendicular to the surface. The experiments were carried out at soft X-ray beamline BL5B. The beam is irradiated on the sample with an angle of 67.5 degrees with respect to the surface normal. The specular beam after the reflection was led to a unit of the rotating analyzer ellipsometry (RAE) for analyses of the light polarization, *i.e.* the Kerr rotation angle. The RAE system was composed of a multilayer mirror and a detector of microchannel plate. By rotating the unit with respect to the beam direction, the Kerr rotation angle θ_K was determined by $\theta_K = -(\chi_+ - \chi_-) / 2$, where χ_+ and χ_- are the rotation angle which is the measured at the intensity maximum of the ellipsometry curves under the positive and negative magnetic field, respectively.

Figure 1 shows photon energy spectra of the Kerr rotation angle for crystals of Gd₂₃Fe₆₇Co₁₀ and Tb₂₀Fe₈₀. The degree of Kerr rotation angle corresponds to magnetizations at each element. Therefore, we found that the spin directions of f-electrons system are opposite to those of d-electrons system in both GdFe(Co) and TbFe. This result is consistent to the spin configuration in a ferrimagnetic material and it demonstrates that our RMOKE can be applied to the f-electronic systems.

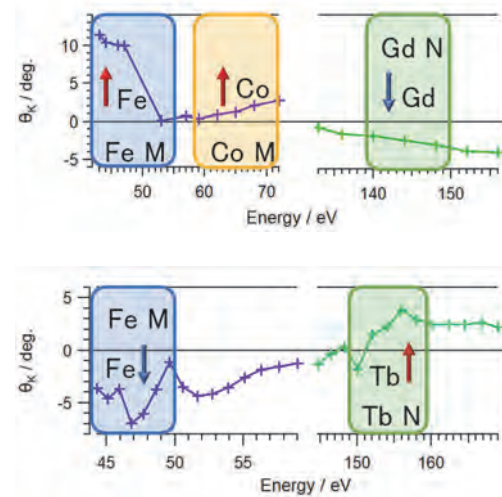


Fig. 1. Photon energy dependence of Kerr rotation angle for crystals of (top) Gd₂₃Fe₆₇Co₁₀ and (bottom) Tb₂₀Fe₈₀ crystal. The solid squares correspond to the absorption edge of each elements.

[1] C. D. Stanciu *et al.*, Phys. Rev. Lett. **99** (2007) 047601.

[2] Sh. Yamamoto *et al.*, Phys. Rev. B **89** (2014) 064423.

[3] Sh. Yamamoto and I. Matsuda, Appl. Sci. **7** (2017) 662.

[4] Sh. Yamamoto *et al.* Rev. Sci. Instrum. **86** (2015) 083901.

[5] K. Yamamoto *et al.* Appl. Phys. Lett. **116** (2020) 172406.

BL6U

Domain Distribution in the Monolayer CVD Graphene Sheet Observed with Photoelectron Momentum Microscope

Y. Aoyagi¹, S. Ohno¹ and F. Matsui²¹Graduate School of Engineering Science, Yokohama National University, Yokohama 240-8501, Japan²UVSOR Synchrotron Facility, Institute for Molecular Science, Okazaki 444-8585, Japan

Photoelectron Momentum Microscope (MM) is considered as a promising means to explore orbital tomography of organic molecules as well as various nanostructures such as a graphene nanolayer [1]. In the present work, we focused on the graphene monolayer produced by chemical vapor deposition (CVD) and subsequently transferred to the silicon oxide substrate.

Experiments were performed at BL6U of UVSOR III. Band dispersion data of CVD monolayer graphene were obtained over a wide reciprocal range. Figure 1 shows the typical result obtained near Fermi level. This indicates that a single-domain structure is formed within the accuracy of the spatial resolution of the present measurements. Based on this type of the data, we can easily recognize the orientation of the monolayer graphene sheet. In contrast, we observed ring-like pattern at some part of the sample. We deduce that several domains coexist at such a position. In other words, density of the domain boundary is larger, resulting in the isotropic electronic states within the monolayer graphene sheet at such a location. In order to clarify further the two-dimensional distribution of the single-domain structure, we conducted the measurements of the two-dimensional mapping as shown in Fig. 2. We found that single-domain with several equivalent directions coexist within the measured area ($70 \times 500 \mu\text{m}^2$). This indicates that there should be a preferred direction of the domain boundary line between the single-domain structures. Our atomic force microscopy (AFM) study showed that many boundary lines should exist inside of the single-domain region, although the band dispersion is well retained as shown in Fig. 1. Our present results indicate that the macroscopic self-organization process should exist during the growth of CVD monolayer graphene sheet so that the three single-domain structures preferentially coexist in a macroscopic range. We deduce that not only the local electronic structure at the atomic scale but also that at the submicron scale should be assessed more carefully to grasp the spatial distribution of the domains with a typical band dispersion or isotropic electronic state.

In the study of two-dimensional materials, it is well recognized that the effect related to the domain boundary should be carefully assessed [2]. Here, we propose that MM will become a useful means to relate the microscopic knowledge with macroscopic transport property and other physical properties.

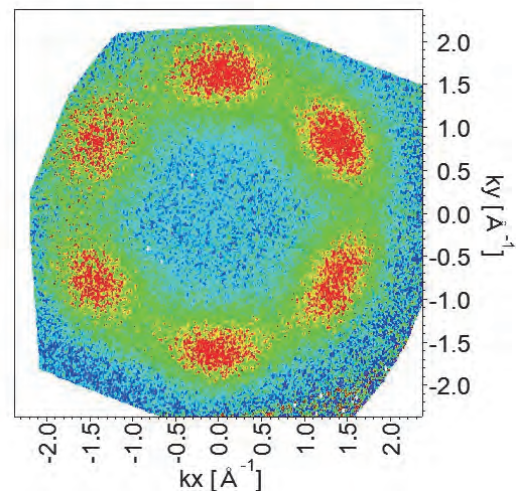


Fig. 1. Isoenergy cross section of the valence band dispersion of CVD graphene monolayer near Fermi level. Photoelectron peaks appeared at the K points.

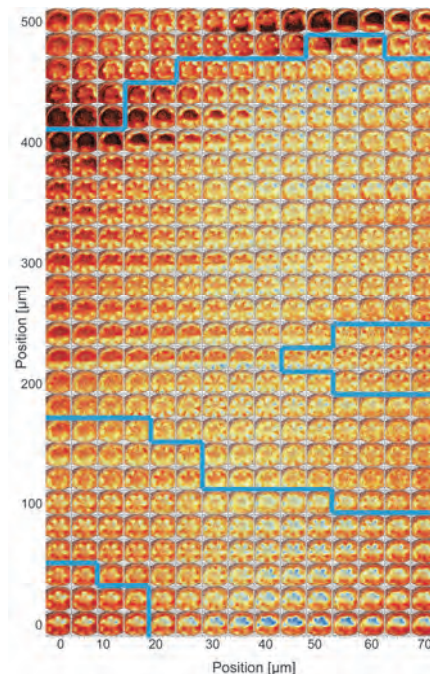


Fig 2. The Fermi surface patterns from two-dimensionally scanned positions.

[1] F. Matsui *et al.*, Jpn. J. Appl. Phys. **59** (2020) 067001.

[2] S. M. Hus *et al.*, Prog. Surf. Sci. **92** (2017) 176.

BL6U

Electronic Structures of 1T-TaS₂ Studied by a Momentum Microscope

 S. Suga¹, T. Kobayashi², E. Iwamoto², K. Sakamoto² and F. Matsui³
¹ISIR, Osaka University, Ibaraki 567-0047, Japan

²Graduate School of Engineering, Osaka University, Suita 565-0871, Japan

³UVSOR Synchrotron Facility, Institute for Molecular Science, Okazaki 444-8585, Japan

Among various transition metal dichalcogenides, 1T-TaS₂ shows the richest phase diagram including a pronounced metal to insulator phase transition (MIT) and a sequence of different charge density wave (CDW) transformation. With lowering temperatures, incommensurate CDW (ICCDW) is observed below 550K and then nearly commensurate phase (NC-CDW) is seen below 350 K. Further a commensurate CDW (CCDW) is realized below 180 K.

This material is cleaved in UHV and the angle resolve photoemission spectra in a wide wave vector space were measured at various E_B by use of synchrotron radiation (SR) by a newly installed momentum microscope (MM) at BL6U of UVSOR.

The advantage of MM is that without any rotation of the sample, photoemission intensity at more than several thousand multichannels of wide (k_x, k_y) can be simultaneously recorded by a 2D detector in the form of $E_B(k_x, k_y)$. Therefore the sample-rotation dependent intensity normalization, slight shift of the measured area on the sample surface as well as the consideration of the change of the measurement configurations are not at all required for analyses.

As soon as a flat and clean sample surface is obtained, one should locate the sample just in front of the PEEM objective lens by use of delicate sample manipulator. Then one can obtain huge amount of data set within a short time. Partial results are shown in Figs. 1 (a)-(d). These results are obtained at $T=50$ K in the CCDW phase by use of monochromatized synchrotron radiation light at $h\nu=66$ eV. The binding energies E_B correspond to (a) 0 eV, (b) 0.5 eV, (c) 1.0 eV and (d) 1.5 eV. Each data is integrated within ± 0.15 eV for realizing enough statistics.

The detailed behavior of the Ta 5d orbitals is clearly recognized around the $k_x=0, k_y=0$ point in the data (a)-(c). Since even the 2nd Brillouin zone is imaged, the hole pocket resulting from the S 3p orbital can be recognized in Fig(d) near $k_x=0, k_y=2\text{\AA}^{-1}$.

The band dispersions can be then easily revealed not only along the k_y axis but also any k_x - k_y axes by comparing the data selected from a huge data set integrated at different temperatures.

Thus high potential of MM for studying detailed $I(E_B(k_x, k_y))$ is clarified [1]. $I(E_B(k_x, k_y, k_z))$ measurement is also possible by use of SR.

[1] S. Suga, A. Sekiyama and C. Tusche, Photo-electron Spectroscopy, Springer Series in Surface Sciences 72 (2021), in press.

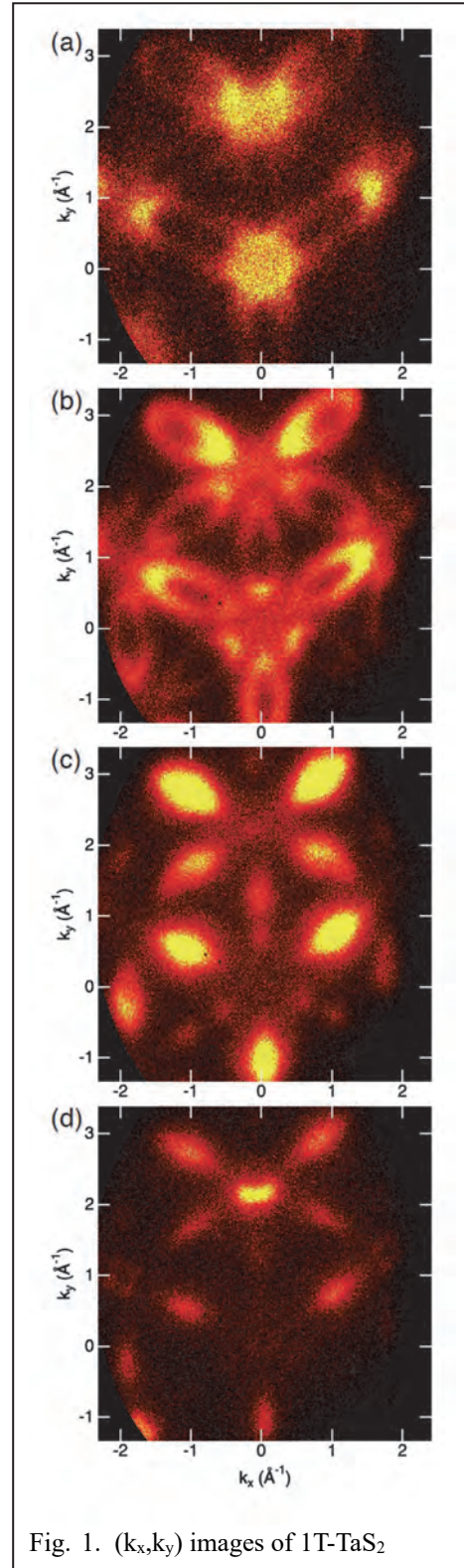


Fig. 1. (k_x, k_y) images of 1T-TaS₂

BL6U

Momentum Microscopy of Highly Oriented Dph-BTBT Film on Ag(110)

M. Iwasawa¹, Y. Hasegawa², F. Matsui³, S. Kera³ and Y. Yamada¹

¹Faculty of Pure and Applied Sciences, University of Tsukuba, Tsukuba 305-8573, Japan

²Institute for Molecular Science, Okazaki 444-8585, Japan

³UVSOR Synchrotron Facility, Institute for Molecular Science, Okazaki 444-8585, Japan

While devices based on [1]benzothieno[3,2-b] [1] benzothiophene (BTBT) derivatives, which exhibit strong intermolecular interactions and atmospheric stability, have achieved mobility in excess of 30 cm²/Vs, the origin of their efficient conduction is still not fully understood. Although the mobility of many organic semiconductors has been understood by the energy and spatial distribution of HOMO, a recent study has shown that the contribution of HOMO-1 is significant in BTBT derivatives [1]. In this study, we focused on Dph-BTBT, one of the BTBT derivatives, and analyzed the energy states and the photoelectron angular distribution (PAD) of HOMO and HOMO-1.

For the detailed measurement and the analysis of PAD, a molecular layer with single domain structure is required. We have recently shown that well-ordered Dph-BTBT film can be realized on metal(111) surface [2]. However, Dph-BTBT film on metal(111) has multi-domain structure, which is not suitable for the PAD measurement. Therefore, we have further demonstrate that, by using anisotropic Ag(110) surface, a nearly one-dimensionally oriented film of Dph-BTBT can be fabricated. Here, we tried to measure the photoelectron momentum map of the single-domain, multilayer film of Dph-BTBT on Ag(110).

The one-dimensionally oriented Dph-BTBT film were fabricated by supplying 10 nm of Dph-BTBT on clean Ag(110). The molecular structure of the Dph-BTBT film was examined using a scanning tunneling microscope (STM) and low energy electron diffraction (LEED). The PAD measurements were performed using momentum microscope at BL6U of UVSOR.

Figure 1 shows the STM image and LEED pattern of Dph-BTBT film on Ag(110). It is seen that the molecular long axis is almost along with the [1-10] direction of the substrate, indicating the formation of nearly one-dimensional structure. Although it was not a completely single-domain structure, it is a suitable sample for the measurement of PAD.

Figure 2(a) shows the energy distribution curve (EDC) of Dph-BTBT film on Ag(110). It is found that both HOMO and HOMO-1 are energetically broadened. Here, each orbital can be fitted with two Gaussian functions, suggesting that orbital splitting due to the overlap of neighboring (upper and lower) molecules. Then, we examined PAD patterns of each orbital as shown in Fig. 2(b, c). It is recognized that both PAD patterns of HOMO and HOMO-1 have strong intensity in k_x direction, which is in general agreement with the simulation by means of FFT of molecular orbital. For the detail analysis, we focus on the energy dependence

of the peak location and the width at half maximum (FWHM) of the intensity at around k_x = 1.5 ~ 1.7 Å⁻¹ as illustrated with arrows in Fig. 2(b). As for the peak location (blue dots in Fig. 2(a)), there is no change in the HOMO region, but a gradual shift to the lower-momentum side is seen in the HOMO-1 region. On the other hand, the FWHM shows little change in the k_x direction (orange dots), but a significant change in the k_y direction (green dots) in the HOMO region.

Thus, by means of PAD using the momentum microscope at BL6U, we were able to experimentally detect the subtle changes in the wavefunction of Dph-BTBT in the condensed state, which was difficult by the conventional techniques.

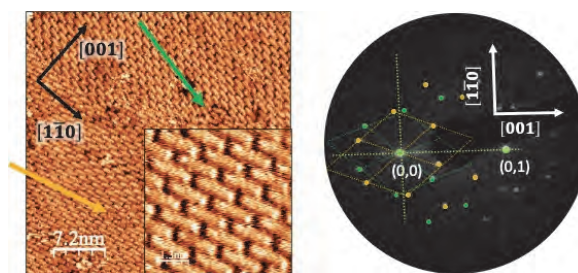


Fig. 1. STM image and LEED pattern of Dph-BTBT/Ag(110).

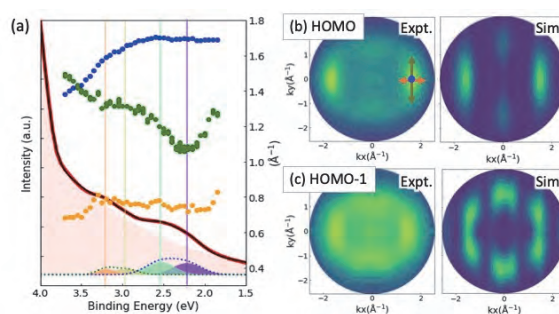


Fig. 2. (a) EDC plotted with peak location and FWHM of PAD. (b, c) PAD patterns of HOMO and HOMO-1 of Dph-BTBT.

[1] Y. Kuroda *et al.*, Jpn. J. Appl. Phys. **58** (2019).

[2] Y. Yamada *et al.*, UVSOR Activity Report 2019 **47** (2020) 137.

BL6U

PEEM-mode Magnification Parameters for Photoelectron Momentum Microscopy

F. Matsui¹, S. Makita¹, H. Matsuda¹, Y. Okano¹, T. Yano¹, E. Nakamura¹ and S. Kera^{1,2}

¹UVSOR Synchrotron Facility, Institute for Molecular Science, Okazaki 444-8585, Japan

²The Graduate University for Advanced Studies, SOKENDAI, Okazaki 444-8585, Japan

As reported in the previous activity report, new experimental station for momentum microscopy was constructed and is currently operating at the BL6U, an undulator-based soft X-ray beamline [1,2]. The photoelectron momentum microscope is a unique multifunctional system for characterizing the electronic properties of μm - and nm -scale structures. A spectro-microscopy (PEEM) mode in real space and micro-spectroscopy (momentum) mode in reciprocal space are available.

Calibration and lens parameter optimization are important issues for high quality data acquisition, so we use checkered-patterned samples for this purpose.

The spatial distribution of elements can be mapped using photoelectrons from the core level. On the other hand, the contrast in valence photoelectron images varies from case to case. In a recent paper [3], we reported on a detailed study of contrast formation. The photoelectron intensity of the gold region near the Fermi level was higher than that of the silicon substrate region, while the inverted contrast images were obtained at lower kinetic energies. The contrast inversion in the photoelectron images by mercury (Hg) lamp excitation is due to the differences in work functions specific to materials and surface conditions, and that of synchrotron radiation excitation is due to the difference in the density of states between gold and silicon substrate.

The following is an overview of the magnification modes available in PEEM mode. Figure 1 shows an example of observing a checkerboard pattern in various magnification modes. Hg lamp excitation was used. The largest field of view (ϕ 140 μm) is achieved by Mag.1 mode. Note that the irradiation spot on the sample is smaller than the field of view in the present case. The intensity ratios of different magnifications are indicated together. In higher magnification modes, the flux density per pixel is reduced, resulting in lower photoelectron intensity. Since the momentum of photoelectrons excited by the Hg lamp is smaller than the acceptance cone of the PEEM lens, all photoelectrons are detected. In the case of synchrotron radiation excitation, it is needed to be considered that the acceptance cone in the momentum space limits the photoelectrons in low magnification mode.

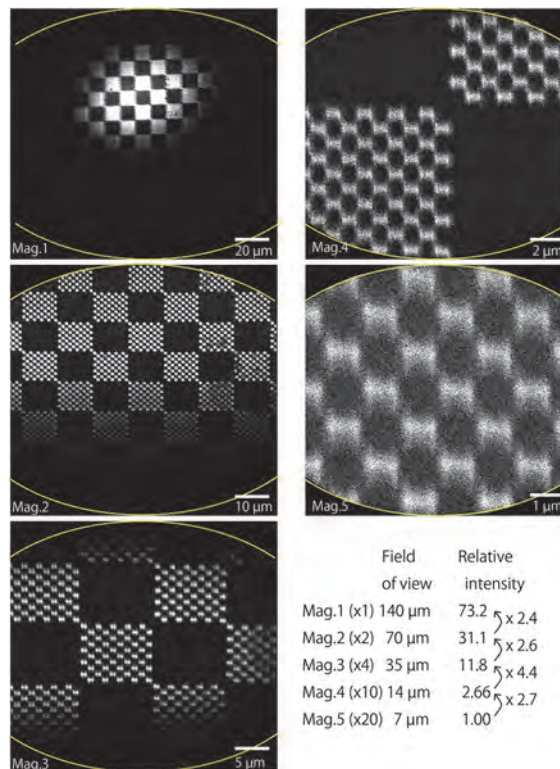


Fig. 1. A checkered pattern observed by the photoelectron momentum microscope in various magnification modes. The Hg lamp was used for excitation.

[1] F. Matsui, S. Makita, H. Matsuda, T. Yano, E. Nakamura, K. Tanaka, S. Suga, and S. Kera, *Jpn. J. Appl. Phys.* **59** (2020) 067001.

[2] F. Matsui, S. Makita, Y. Okano, H. Matsuda, and S. Kera, *Vacuum and Surface Science* accepted (2021).

[3] S. Makita, H. Matsuda, Y. Okano, T. Yano, E. Nakamura, Y. Hasegawa, S. Kera, S. Suga, and F. Matsui: *e-J. Surf. Sci. Nanotech.* accepted (2021).

BL7U

Study of Electronic Band Structure of Li- and Ca-Intercalated Graphene

S. Ichinokura¹, M. Hashizume¹, K. Horii¹, R. Fukushima¹, M. Toyoda¹, S. Ideta²,
K. Tanaka², R. Shimizu³, T. Hitosugi³, S. Saito¹ and T. Hirahara¹

¹Department of Physics, Tokyo Institute of Technology, Tokyo 152-8551, Japan

²UVSOR Synchrotron Facility, Institute for Molecular Science, Okazaki 444-8585, Japan

³Department of Applied Chemistry, Tokyo Institute of Technology, Tokyo 152-8550, Japan

Graphene is known as the most promising nanomaterial for the post-silicon electrical industry. The remarkable high-carrier mobility in graphene originates from its characteristic band structure called the Dirac cone. When the Fermi energy in graphene locates near the Dirac cone crossing (Dirac point), graphene has a massless carrier due to its linear and steep band dispersion.

Many-body interaction in graphene materials is also a target of intensive research. The band structure of monolayer graphene has a saddle point at the M point of the Brillouin zone. The dispersion near this point is flat, leading to the heavy effective mass and divergent density of states. This is called Van Hove singularity (VHS), expected to drive unconventional superconductivity. It is known that deposition of alkali- and alkaline earth-metals tunes the Fermi energy to the VHS point upon electron doping [1,2]. Recently, this VHS filling has attracted renewed interest due to the emergence of superconductivity in twisted bilayer graphene, which also originated from the VHS at the Fermi level [3].

In our group, a comprehensive study on alkali- and alkaline earth-doped graphene is carried out by a combination of *in situ* angle-resolved photoemission spectroscopy (ARPES) and electrical transport measurements in ultrahigh vacuum (UHV). By comparing band structures and the transport properties, we are investigating the many-body interaction in graphene.

In the present study, we prepared monolayer graphene on SiC(0001) substrates. Li and Ca were doped by vapor deposition and annealing in UHV, followed by *in situ* ARPES measurements. In Fig. 1, we show the band structure of (a) as-grown, (b) Li- and (c) Ca-doped graphene. The Brillouin zone (BZ) of the graphene is drawn in Fig. 1(d). Fig. 1(a) was collected around K point, parallel to the direction shown as the solid green line in Fig. 1(d). The slightly n-doped single Dirac cone centered at the K point is seen, typical for the monolayer graphene. On SiC, such high-quality epitaxial growth of graphene is possible because of the underlying buffer layer, which terminates the dangling bonds of the SiC(0001) surface.

Figures 1(b) and (c) were taken at the Γ point along the Γ -K line, shown as the solid magenta line in Fig. 1(d). In both spectra, steep band dispersions are seen. We conclude that these bands are two pairs of Dirac bands (denoted as π_1^* and π_2^*). In Ref. [4], it was reported that Li intercalates into both sides of the buffer layer. Consequently, the atomic structure of the

system is changed into a layered one shown in Fig. 1(e); Li terminates the substrate dangling bonds and decouples the buffer layer from the substrate. Further deposited Li intercalates between the lifted graphene and the top one, forming the $\sqrt{3}\times\sqrt{3}$ periodicity. The heavily-doped two Dirac bands observed around Γ in Fig. 1(b) perfectly match this picture. Besides, the π_2^* band reaches the Fermi level at its flat part at the M point of $\sqrt{3}\times\sqrt{3}$ BZ, which satisfies the VHS.

We newly found that similar structural change takes place in Ca-doped graphene, with further charge transfer to π_1^* and π_2^* bands. In Fig. 1(c), another band with a parabolic shape can be seen. This free-electron (FE) like characteristic corresponds to the interlayer band of superconducting Ca-intercalated graphite [5].

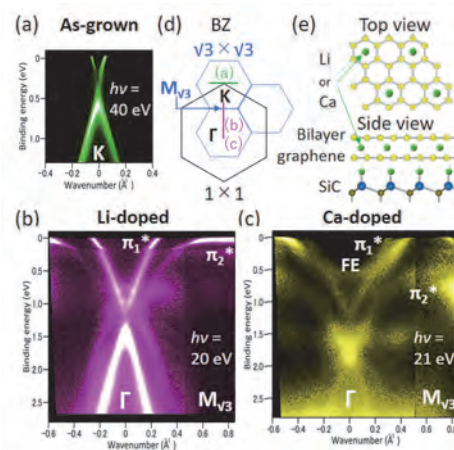


Fig. 1. (a)-(c) Band structure of (a)As-grown, (b) Li-doped and (c) Ca-doped graphene. ARPES measurements were performed with $h\nu=20-40$ eV p-polarized light under $T=11-13$ K. (d) Schematic of 1×1 and $\sqrt{3}\times\sqrt{3}$ BZ. Measurement directions of (a)-(c) are drawn as solid green and magenta lines. (e) Schematic atomic model of Li- and Ca-doped graphene.

[1] J. L. McChesney *et al.*, Phys. Rev. Lett. **104** (2010) 136803.

[2] P. Rosenzweig *et al.*, Phys. Rev. Lett. **125** (2020) 176403.

[3] Y. Cao *et al.*, Nature **556** (2018) 43.

[4] S. Fiori *et al.*, Phys. Rev. B **96** (2017) 125429.

[5] K. Sugawara *et al.*, Nat. Phys. **5** (2009) 40.

BL7U

Low-kinetic Energy and Low-temperature Measurements to Unveil the Impact of Weak Interaction: a Machine Status of the BL7U

Y. Hasegawa¹, S. Ideta¹, K. Tanaka^{1,2} and S. Kera^{1,2}¹Department of Photo-molecular science, Institute for Molecular Science, Okazaki 444-8585, Japan²School of Physical Sciences, The Graduate University for Advanced Studies, SOKENDAI, Okazaki 444-8585, Japan

The purpose of this study is to clarify the impacts on the electronic state of the organic/inorganic interface stabilized by weak interaction such as van der Waals force. We have studied the oriented-monolayer film of pentacene on graphite so far and realized the emergence of a dispersive band utilizing low-energy excitation angle-resolved photoelectron spectroscopy (LE-ARPES). The dispersive band appears at the kinetic energy of 1 to 2 eV where the secondary electron is a non-negligible and constant final state (CFS) feature is overlapping with the non-dispersive molecular orbital states. The CFS band could be originated from a newly-formed conduction band at the weakly bounded interface visualized by high-resolution angle-resolved secondary electron emission [1], demonstrating that the impact of weak interaction would appear much stronger in unoccupied states by a larger spread of an electron cloud. During the experiment at BL7U, however, we encountered technical issues to measure this system at low-kinetic energy and low temperature this time.

A single crystalline graphite (SCG) as the substrate was cleaned by annealing at 600 K for 2 h. A pentacene film of 4.1 Å was deposited onto the SCG at room temperature in a custom UHV chamber designed for organic layer deposition. After the deposition, a rapidly cooled sample below the phase transition temperature [2] was measured.

Figure 1 shows LE-ARPES image of the SCG taken at $h\nu$ of 7.4 eV on the same day. In the image, the signal lacks at the lower right, and the energy and angle positions are different from each other. There was no choice to optimize the image distortion properly by arranging the experimental setup, a measurement position, a sample preparation, and so on. This curve appears nearly the same position at a different excitation energy of 7.2 eV and 8.0 eV because the photoemission is mainly from a secondary electron. This kind of time-dependent phenomenon has never been found at BL7U, therefore, the artifact was caused by changes of the present analyzer condition, unfortunately.

Figure 2 shows ARPES of pentacene/SCG taken at $h\nu = 40$ eV with decreasing the temperature from 50 K to 10 K. Upon the cooling, a new feature appears at around binding energy of -11 eV at 10 K. According to the previous report, it is caused by adsorbing Ar atoms on the surfaces [3]. Evolution of the Ar 3p peak with the cooling is observed and the feature is completely recovered at 50 K by annealing (not shown). The molecular film structure (packing or orientation) is easily affected by adding such a weak perturbation of the gas adsorption [4]. To discuss the modification of the

electronic state of the molecular interfaces by the weak interaction, the low-temperature experiments are mandatory to monitor the effects of decreasing the distance between a molecule and the surface. We will improve the present machine status at BL7U for standing a severe experiment.

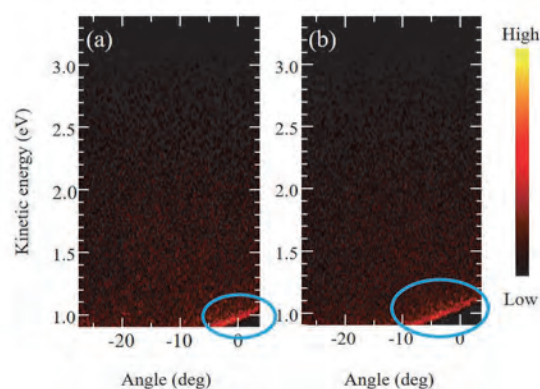


Fig. 1. (a) and (b) are LE-ARPES images of the same SCG taken at $h\nu = 7.4$ eV which show different lacked areas indicated by blue ovals.

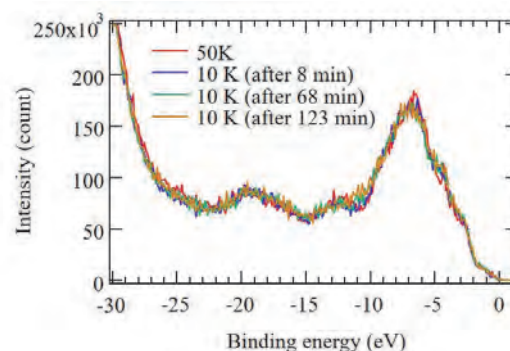


Fig. 2. ARPES spectra of pentacene/SCG measured with decreasing the temperature.

[1] T. Yamaguchi *et al.*, UVSOR Activity Report 2018 **46** (2019) 148.

[2] Y. Hasegawa *et al.*, UVSOR Activity Report 2019 **47** (2020) 140.

[3] F. Carnovale *et al.*, J. Chem. Phys. **90** (1989) 1452.

[4] F. Bussolotti *et al.*, Phys. Rev. Lett. **110** (2013) 267602.

BL7U

Hybridization between π Band of Graphene and 6sp Band of Hex-Au(001) Reconstructed Structure

T. Terasawa^{1,2}, S. Tanaka³, K. Matsunaga⁴, T. Ito^{4,5}, S. Yasuda¹, S. Machida¹, M. Yano¹ and H. Asaoka¹

¹Advanced Science Research Center, Japan Atomic Energy Agency, Tokai 319-1195, Japan

²Institute of Industrial Science, The University of Tokyo, Tokyo 153-8505, Japan

³The institute of Scientific and Industrial Research, Osaka Univ., Ibaraki 567-0047, Japan

⁴Graduate School of Engineering, Nagoya University, Nagoya 464-8603, Japan

⁵Nagoya University Synchrotron radiation Research center (NUSR), Nagoya University, Nagoya 464-8603, Japan

The interface between graphene and Au has attracted much attention since the large Rashba splitting of 100 meV in the π band of graphene/Au/Ni structure was discovered in 2012 [1]. As one of the graphene and Au interfaces, graphene on Hex-Au(001) reconstructed surface has also been studied. The quasi-one-dimensional periodic potential in this structure is considered to replicate graphene π band to open a new bandgap at the Brillouin zone boundary [2]. However, the electronic structure of this system has not been reported yet. In this study, we have performed angle-resolved photoemission spectroscopy (ARPES) on graphene grown on the Hex-Au(001) surface to directly investigate this system's electronic structure.

Graphene was prepared on Hex-Au(001) substrate using chemical vapor deposition in Japan atomic energy agency [3]. Hex-Au(001) spontaneously formed during the graphene growth. Low energy electron diffraction measurements indicated that the sample surface and the interface were unchanged during the transport under ambient conditions. ARPES measurements were performed at the UVSOR-III BL7U after the sample annealing in the pre-chamber by an IR-heater. Data were acquired at room temperature with $h\nu = 9 - 40$ eV. We changed the photon energy and polarization to visualize graphene and Au bands and their replicas.

Figure 1 shows the ARPES image on a Γ -X(Au)-K (graphene) line. Two sharp bands and one faint band were observed. The linear band dispersion from $k = 1.7 \text{ \AA}^{-1}$ (K point of graphene) was assigned to the graphene π band. This band shows a mini-gap at the binding energy of about 0.9 eV. The other linear band crossing the Fermi energy at $k = 1.2 \text{ \AA}^{-1}$ close to the X point of Au was assigned to the Au 6sp band, according to the previous report about the electronic structure of Hex-Au(001) [4]. An electron pocket around the X point was also consistent with the previous report [4].

The faint linear band comes from $k = 1.47 \text{ \AA}^{-1}$ at the Fermi energy and crosses the top edge of the mini-gap. This band crossing suggests that this linear band is the origin of the mini-gap formation in the graphene π band. Accounting for the periodicity of the Hex-Au(001) surface of 1.44 nm, the reciprocal vector of this structure is 0.44 \AA^{-1} [2,4]. Thus the original band of this band should begin from $k = 1.47 \pm n \times 0.44 \text{ \AA}^{-1}$

at the Fermi energy. While this value does not match the graphene K point, $k = 1.7 \text{ \AA}^{-1}$, $k = 1.47 - 0.44 = 1.03 \text{ \AA}^{-1}$ is reasonable for the Au 6sp band. Such the replicated Au 6sp band was observed for Hex-Au(001) in the previous report [4]. We concluded that the Au 6sp band hybridized with the graphene π band to form the mini-gap in the graphene π band. We expect this hybridization changes the electronic structure and the spin characteristics of graphene, similar to the hybridization between graphene and Au in the graphene/Au/Ni system reported in 2012 [1].

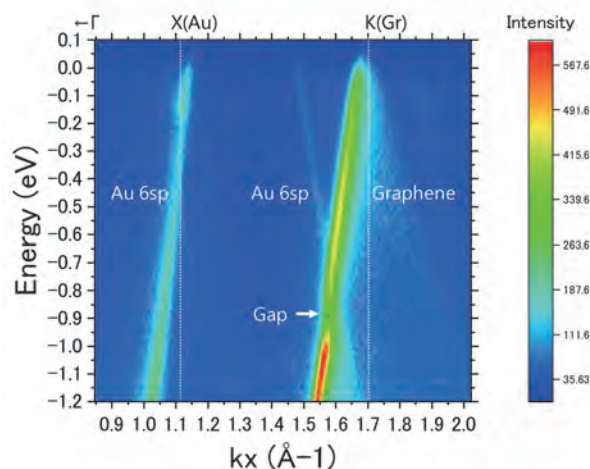


Fig. 1. Band structure of graphene grown on hex-Au(001) substrate. An energy gap of 150 meV was observed in the graphene π band.

[1] D. Marchenko, *et al.*, Nat. Commun. **3** (2012) 1232.

[2] X. Zhou, *et al.*, ACS Nano **10** (2016) 7550.

[3] T. Terasawa, *et al.*, Jpn. J. Appl. Phys. **58** (2019) SIIB17.

[4] S. Bengió, *et al.*, Phys. Rev. B **86** (2012) 045426.

BL7U, BL5U

Topological Electronic Structure of the Interface between α -Sn and InSb

 T. Nakaya¹, Y. Ohtsubo^{2,1}, T. Nakamura¹ and S. Kimura^{2,1,3}
¹Department of Physics, Graduate School of Science, Osaka University, Toyonaka 560-0043, Japan

²Graduate School of Frontier Biosciences, Osaka University, Suita 565-0871, Japan

³Department of Materials Molecular Science, Institute for Molecular Science, Okazaki 444-8585, Japan

Among the topological materials [1], α -Sn [2,3] is gathering much attention because of its possible spintronic application, as reported to exhibit spin to charge conversion due to the inverse Edelstein effect even at room temperature [4]. The next barrier for the new-generation spintronic devices is to realize the interface between TIs and normal semiconductors in order to make the spin-polarized topological electronic states available for them. Along this line, to make the junction between TI and normal semiconductor hosting the topological “interface” state is awaited. In this study, we have tried to grow normal semiconductor InSb, which has a small lattice mismatch to a topological material α -Sn (0.14%), on α -Sn(111) ultrathin films and observed its surface and interface electronic structure by angle-resolved photoelectron spectroscopy (ARPES).

The InSb(111) substrates were cleaned by repeated cycles of Ar⁺ sputtering (0.5 keV) and annealing up to 600 K in an ultra-high vacuum chamber. Then, homo-epitaxial growth of InSb was performed to obtain the clean surface of the InSb(111) substrates. α -Sn films with the thickness of 8 bi-atomic layers (BL) were obtained by evaporating Sn from a home-made evaporator. The evaporation rates of In, Sb, and Sn were monitored *in-situ* from the intensity oscillation of the electron diffraction patterns. After the growth, (1×1) periodic structure of α -Sn was observed, consistent with the earlier report [6]. On such α -Sn(111) films, In and Sb were deposited and the InSb layer with the thickness of ~1BL was grown there. The surface periodicity remained after the growth of InSb without in-plane lattice distortion.

Figure 1 shows the band dispersion of the InSb(~1BL)/ α -Sn(8BL)/InSb(111)B observed by ARPES. A linear Dirac cone like dispersion (guided by dashed white lines), which is a typical behavior of the topological electronic states, was observed around the center of the surface Brillouin zone ($k_x = 0.0 \text{ \AA}^{-1}$) after the deposition of the InSb layer. This result suggests that the topological surface state of α -Sn is transplanted to the interface with InSb, a normal semiconductor. Further analysis to understand the spin texture of the interface electronic states between α -Sn and InSb is in progress.

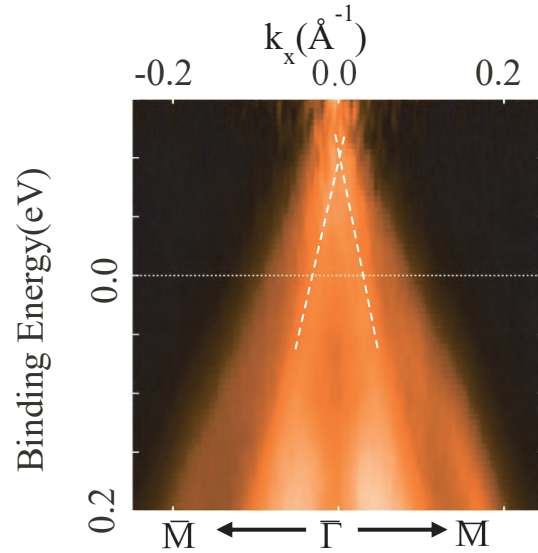


Fig. 1. Band dispersion of InSb/ α -Sn/InSb(111)B by observed by ARPES ($h\nu = 16\text{eV}$). The measurement was taken at room temperature and normalized by the Fermi distribution function.

- [1] M. Z. Hasan and C. L. Kane, Rev. Mod. Phys. **82** (2010) 3045.
- [2] Y. Ohtsubo *et al.*, Phys. Rev. Lett. **111** (2013) 216401.
- [3] A. Barfuss *et al.*, Phys. Rev. Lett. **111** (2013) 157205.
- [4] J-C Rojas-Sanchez *et al.*, Phys. Rev. Lett. **116** (2016) 09602.
- [5] Q. Barbedienne *et al.*, Phys. Rev. B **98** (2018) 195445.
- [6] H. Omi *et al.*, Phys. Rev. Lett. **72** (1994) 2596.

The background is a solid purple color with several abstract geometric elements. A large, semi-transparent circular graphic is centered on the right side, featuring concentric rings and a dotted border. Diagonal lines and a grid of small dots are also visible, creating a sense of depth and movement.

III-5

Life, Earth and
Planetary Sciences

BL3U

Measurement and Assignment of X-ray Absorption Spectra of Lipid Bilayer Membranes in Aqueous Solutions

R. Tero¹, W.-Z. Goh¹ and M. Nagasaka²¹Toyohashi University of Technology, Toyohashi 441-8580, Japan²Institute for Molecular Science, Okazaki 444-8585, Japan

The lipid bilayer is a self-assembled structure of amphiphilic lipid molecules and is the fundamental structure of biomembranes such as cell membranes. Internal structures of lipid bilayers, such as two-dimensional domains and hydrophobic thickness, and physical properties affect the transportation of materials, information, and energy through the biomembranes. All these physiological reactions proceed in the presence of ions. Ions in the aqueous solution significantly influence to these structures and properties of lipid bilayers. Phosphatidylcholine (PC) is the most abundant lipid of eukaryotic cell membranes. Cations bind to the phosphate and carbonyl groups of PC. However, affinity of cations to PC, and also other lipids, are still controversy especially in the fields of theoretical simulations [1]. We aim to determine the binding affinity of cations to lipids in aqueous solutions experimentally, by means of X-ray absorption spectroscopy (XAS) [2, 3].

Supported lipid bilayers (SLBs) of dioleoyl-PC (DOPC), dioctadecenyl-PC (dietherPC), and digalactosyldiacylglycerol (DGDG) were formed on the Si₃N₄ membranes of the XAS flow cell [2] by the vesicle fusion method. We prepared SLBs with few residual vesicles as shown in Fig. 1. Fluorescence recovery after photobleaching observation showed that fluid and continuous SLB covered the whole Si₃N₄ membrane surface. O-K edge XAS spectra of the Si₃N₄ membrane before and after formation of SLB were obtained in a buffer solution (NaCl 100 mM, HEPES 25 mM/ pH 7.4 NaOH) which thickness was controlled to be ~100 nm. The XAS spectrum of the Si₃N₄ membrane without SLB was subtracted from that with SLB.

The O-K-edge spectrum of DOPC, which has phosphate and carbonyl groups on its headgroup, appeared at 531 - 533 eV (Fig. 2a, black dotted line). Removing residual vesicles from SLBs drastically improved the S/N ratio [2]. Figure 2b shows the XAS spectrum of dietherPC, which have only the phosphate group. We attributed the components of the dietherPC spectrum to $1s \rightarrow \pi^*$ transitions of P=O and P-O-Na at 531.5 eV and 532.3 eV, respectively, based on the inner shell calculation. We assigned the single component at 532.0 eV in the DGDG spectrum (Fig. 2c) to C=O. Based on these assignments, we deconvoluted the DOPC spectrum to P=O, C=O, and P-O-Na (Fig. 2a, dashed lines).

In conclusion, we obtained O-K edge XAS spectra of SLBs in an aqueous solution with a sufficient S/N ratio to identify the components in the spectra. We will

investigate the effects of the cation concentration and species on the XAS components in SLBs.

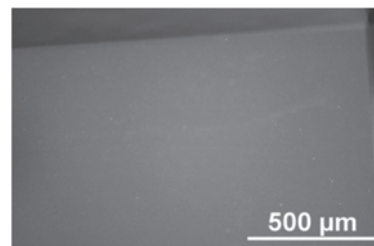


Fig. 1. Fluorescence image of DOPC-SLB on the Si₃N₄ membranes of the XAS flow cell.

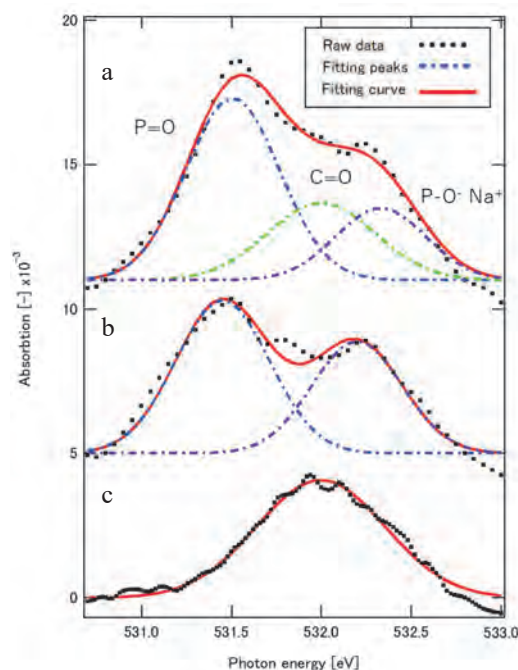


Fig. 2. O K-edge spectra of (a) DOPC-, (b) dietherPC-, and (c) DGDG-SLBs. Black dotted curves show raw data. Dashed curves and red solid curves show deconvoluted components and their summation, respectively.

[1] T. B. Woolf, *Biophys. J.* **104** (2013) 746; A. Catte, *Phys. Chem. Chem. Phys.* **18** (2016) 32560.

[2] M. Nagasaka, H. Yuzawa, T. Horigome, and N. Kosugi, *J. Electron Spectros. Relat. Phenomena* **224** (2018) 93.

[3] R. Tero, W.-Z. Goh and M. Nagasaka, *UVSOR Activity Report 2019* **47** (2020) 145.

BL4U

Improvement of Molecular Mapping for Thin Sections of Isolated Mammalian Nuclei Embedded in Resin Using STXM

A. Ito¹, K. Shinohara², A. Matsuura³, S. Toné⁴, M. Torigata¹, K. Tohya⁵, H. Yuzawa⁶
and T. Ohigashi^{6,7}

¹*School of Engineering, Tokai University, Hiratsuka 259-1292, Japan*

²*Graduate School of Health Sciences, Fujita Health University, Toyoake 470-1192, Japan*

³*Research Integrity Office, Fujita Health University, Toyoake 470-1192, Japan*

⁴*School of Science and Engineering, Tokyo Denki University, Hatoyama 350-0394, Japan*

⁵*Kansai University of Health Sciences, Kumatori-cho 590-0482, Japan*

⁶*UVSOR Synchrotron Facility, Institute for Molecular Science, Okazaki 444-8585, Japan*

⁷*School of Physical Sciences, The Graduate University for Advanced Studies, SOKENDAI, Okazaki 444-8585, Japan*

Spectromicroscopy using a scanning transmission X-ray microscope (STXM) has been widely accepted as a useful tool to visualize molecular distribution in specimens. Using STXM installed at BL4U, we have been developing an image processing procedure for the quantitative mapping of biomolecules, and successfully applied to the distribution of nucleic acids (DNA and RNA) and proteins such as histone and bovine serum albumin (BSA) in biological specimens using combined NEXAFS at the C, N and O-K absorption edges [1-3].

In continuing effort to obtain molecular distribution of thick biological specimen, we used thin-sectioned specimen to ensure sufficient transmitted X-ray photons [4]. However, the morphology of the specimen was not properly imaged to identify the inner structure of the nucleus. In the present study, we tried the following issues to explore a proper analysis procedure for molecular distributions in isolated mammalian nuclei embedded in agarose and resin: 1) the sectioning method to attain thinner specimen with high quality and 2) analytical procedure to obtain maps of biological molecules in the presence of agarose and organic resin.

Isolated nuclei from human HeLa S3 cells were fixed with glutaraldehyde followed by mixing with agarose to confine to limited volume, and then embedded in Quetol-812 epoxy resin with curing agents and a curing promoter as described previously [4]. The resin section of 0.2 μm thickness was made by a microtome with a diamond knife in place of a glass knife used before. The section was attached directly on an address mesh (HF-15, Nissin EM) without any supporting membrane such as collodion to avoid the complexity of analytical procedure by the additional organic compound.

We applied our method to calculate the distributions of nucleic acids and proteins [3] with some modifications for the resin-embedded section specimens. In order to estimate the stack files of agarose and resin, we adopted an iteration procedure: First, the tentative stack files of agarose and resin were obtained with the SVD (Singular Value Decomposition) method applied to the observed data with the spectra for nucleic acids, proteins, agarose

and resin. After subtracting stack files of agarose and resin, residual stack files including nucleic acids and proteins were calculated by our method [3]. The stack files of these biomolecules were used to obtain the secondly approximated stack files of agarose and resin. By using thus obtained stack files of agarose and resin, the improved stack files of biomolecules were calculated. The above procedure was repeated.

Figure 1 shows the X-ray image of the isolated nucleus at 398 eV (panel a), where the dense area in the center of nucleus is probably assigned as a nucleolus. The quality of the image was much better than the previous one [4]. Molecular images of DNA, RNA, and histone were shown in the panel b, c and d, respectively. DNA and histone seem to be preferentially co-localized in the nucleolus, while RNA had significant distribution all over the nucleus.

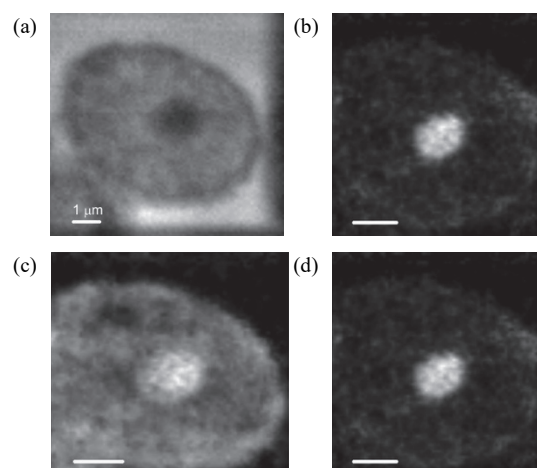


Fig. 1. Isolated nucleus of human HeLa S3 cell. (a) X-ray image at 398 eV, (b-d) Molecular distribution of DNA, RNA and histone.

[1] K. Shinohara *et al.*, *Ultramicrosc.* **194** (2018) 1.

[2] K. Shinohara *et al.*, *J. X-Ray Sci. Technol.* **26** (2018) 877.

[3] K. Shinohara *et al.*, *Cells* **8** (2019) 8.

[4] A. Ito *et al.*, *UVSOR Activity Report* 2019 **47** (2020) 148.

BL4U

Nano-Structural and Chemical Analysis of Structural Color on an Elytron of a Jewel Beetle

T. Ohigashi^{1,2} and H. Yuzawa¹¹UVSOR Synchrotron Facility, Institute for Molecular Science, Okazaki 444-8585, Japan²School of Physical Sciences, The Graduate University for Advanced Studies, SOKENDAI, Okazaki 444-8585, Japan

Structural color is not a real color but an optical phenomenon such as reflection, diffraction and interference. Some kinds of animals, birds, clam shells, squids and insects, have the structural color caused by fine periodic structures, whose size is nearly wavelength of visible light. The structural color often shows shiny and metallic color and is different from pigment color. Therefore, the animals with the structural color are sometimes treated as jewelry. A jewel beetle, *Chrysochroa fulgidissima* (Fig. 1), shows structural color, green with a red line, on its elytron and is used as ornaments on *Tamamushi no zushi* as a national treasure in Japan (made in 7th c.). On the other hand, the structural color is attracting the attention in industries as an ecological painting method because the structural color does not use pigments. In this research, the fine structures of the elytron of the jewel beetle are analyzed to understand origin of the structural color. Then, scanning transmission X-ray microscopy (STXM) is a powerful tool to analyze chemical and morphological information of the sample with high spatial resolution.

As a sample preparation, the elytron of the jewel beetle, which was captured in Ishikawa prefecture, is embedded in NER-814 epoxy resin (Nisshin EM Co. Ltd.) without chemical fixation and staining. Thin sections of thickness of 150 nm were cut by using ultra-microtome and set on a TEM grid with a support membrane. An energy stack of surface of the elytron with the embedded resin, was acquired with C 1s regime (280 ~ 300 eV). Then, dwell time was 3 ms and scanning pitch was 30 nm step for each pixel, respectively. A STXM images (transferred as optical density) at 282, 286, 288 and 300 eV in X-ray energy and localized X-ray absorption spectra (XAS) are shown in Fig. 2. Positions of the XAS spectra are indicated in Fig. 2(b) as corresponded colors. The multilayers can be clearly distinguished only in a small energy region, from 285 to 287 eV and is probably 14 layers. A top layer, which decides color of the elytron (orange in Fig. 2(b)), shows the lowest optical density in the observed region [1]. XAS of the darker layer (pink) is almost coincident with a substrate of the elytron (green). Therefore, the brighter layers (blue) with different chemical state are considered to be formed on the substrate layer during metamorphosis. From comparison of optical density for the excitation to continuum level between the two layers, difference of density is ~6%. Even though this difference is small, the pair of the layers works as a multilayer to form structural color. For the next step, polarization of molecules of the elytron will be studied [2].



Fig. 1. Photo of a jewel beetle, *Chrysochroa fulgidissima*

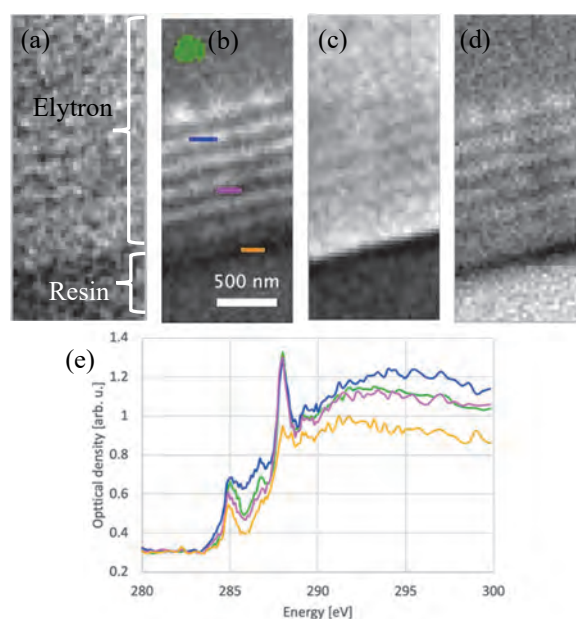


Fig. 2. Optical density images at X-ray energies of (a) 282, (b) 286, (c) 288 and (d) 300 eV and (e) localized X-ray absorption spectra of the elytron of the jewel beetle.

[1] S. Yoshioka, S. Kinoshita, H. Iida and T. Hariyama, *J. Phys. Soc. Jpn.*, **81** (2012) 054801.

[2] T. Ohigashi, M. Nagasaka, T. Horigome, N. Kosugi, S. M. Rosendahl and A. P. Hitchcock, *AIP Conf. Proc.*, **1741** (2016) 050002.

BL4U

Analysis of 3D Structure of Extraterrestrial Organic Materials Using Combination of STXM-NEXAFS and SR Nano-tomography

M. Uesugi¹, M. Ito², K. Tomioka², Y. Kodama³, T. Ohigashi^{4,5} and H. Yuzawa⁴

¹Japan synchrotron radiation research institute (JASRI/SPring-8), Sayo 679-5198, Japan

²Kochi Institute for Core Sample Research, Japan Agency for Marine-Earth Science Technology (JAMSTEC), Nankoku 783-8502, Japan

³Marine Works Japan Ltd., Yokosuka 237-0063, Japan

⁴UVSOR Synchrotron Facility, Institute for Molecular Science, Okazaki 444-8585, Japan

⁵School of Physical Sciences, The Graduate University for Advanced Studies, SOKENDAI, Okazaki 444-8585, Japan

Unique structure of organic compounds in extraterrestrial materials, spherical in sub- μm radius and sometime accompanying with hollow structure, is considered to be informative about their origin and evolutionary history [1,2]. In previous studies, most of such globules, called hollow organic nano-globules, were found in insoluble organic matter (IOM), which was extracted as residual of acid treatment of meteorites, to remove rocky materials. Content of organic matter in meteorites is up to 2 % for carbonaceous chondrite, and it is difficult to determine the organic globules in rocky meteorites by in situ analysis in previous studies. Thus, analyzing organic matters in IOM seems to be reasonable for previous studies.

However, organic materials were damaged and averaged, and their nature was lost by acid treatment of meteorites. For example, origin of hollow structure is uncertain, because materials inside the globule would be lost during the acid treatment. Molecular structure is also changed due to averaging.

Recently, we obtained the distribution of organic component by in situ observation of ultrathin sections of meteorites, using scanning transmission x-ray microscopy and near edge x-ray absorption fine structure (STXM-NEXAFS) analysis, equipped at BL4U of UVSOR in previous studies [3]. The organic globules distribute widely in meteorites, and their number density was much higher than expected before, and reduced due to aqueous alteration.

In this experiment, we aim to obtain 3D shape and structure of the organic globules, using in situ observation with combination of the high resolution (HR) nano tomography developed at SPring-8, and STXM-NEXAFS. Pixel size of HR-nano tomography at SPring-8 is around 10 nm, and is enough to resolve the organic globules, although it is difficult to observe carbonaceous materials inside the rocky material due to large difference of linear attenuation coefficient (rocky material: 200 - 500 cm^{-1} , carbonaceous materials: 10 - 20 cm^{-1}). In this study, we determined position of spherical holes in meteoritic samples using in HR-nano tomography at first. Then an ultrathin section around the largest hole was extracted by Focused ion beam (FIB). Figure shows mapping of C-NEXAFS of the ultrathin section extracted from A 12169 (CM) meteorite. It shows multiple small objects, which show organic

globules. Unfortunately, the globules were very small, less than 100 nm, and could not be resolved even by HR nano tomography. Although we tried to make an ultrathin section of the largest globules observed in HR-nano tomography, FIB fabrication with accuracy less than a micron meter was failed in this case.

In future work, we plan to improve accuracy of the FIB work. By putting marks on the surface of sample using FIB, we can determine the position of the largest globule in the sample with higher accuracy. In addition, the thin section was deformed and tilted slightly during thinning of the sample. Then objective organic globules could not be included in the thin section. We can fix the problem by holding both sides of the section by FIB grid.

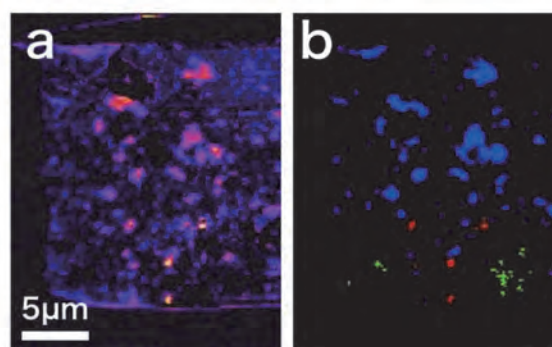


Fig. 1. (a) mapping of intensity of carbon absorption (b) mapping with 3 phases blue: matrix, red: organic globules, green: carbonate. Some of tiny spots of high carbon absorption in (a) are coupled with red area of (b), suggesting that they are organic globules. However, their size is less than 100 nm and could not be resolved by HR-nano tomography, in this time.

[1] L.A. Garvie, P. R. Buseck *Earth. Planet. Sci. Lett.* **224** (2004) 431

[2] T. Matsumoto *et al.*, *Geochim. Cosmochim. Acta* **116** (2013) 84.

[3] M. Uesugi *et al.*, JpGU meeting, abstract (2019).

BL4U

Assessing the Debris Generated by the Small Carry-on Impactor Operated from the Hayabusa2 Mission

M. Ito¹, Y. Takano², Y. Kebukawa³, T. Ohigashi⁴, M. Matsuoka⁵, K. Kiryu³, M. Uesugi⁶, T. Nakamura⁷, H. Yuzawa⁴, K. Yamada⁸, H. Naraoka⁹, T. Yada⁵, M. Abe⁵, M. Hayakawa⁵, T. Saiki⁵, S. Tachibana^{5,10} and Hayabusa2 Project Team

¹Kochi Institute for Core Sample Research, JAMSTEC, Nankoku 783-8502, Japan

²Biogeochemistry Program, JAMSTEC, Yokosuka 237-0061, Japan

³Yokohama National University, Yokohama 240-8501, Japan

⁴UVSOR Synchrotron Facility, Institute for Molecular Science, Okazaki 444-8585, Japan

⁵ISAS-JAXA, Sagami-hara 252-5210, Japan

⁶JASRI/SPring-8, Sayo-cho 679-5198, Japan

⁷Tohoku University, Sendai 980-8577, Japan

⁸Tokyo Institute of Technology, Yokohama 226-0026, Japan

⁹Kyushu University, Fukuoka 819-0395, Japan

¹⁰University of Tokyo, Tokyo 113-0033, Japan

The JAXA planetary exploration mission Hayabusa2 (to the near-Earth C-type asteroid (162173) Ryugu) is a combination of an asteroidal sample-return mission and detailed spectroscopic observations designed to improve our understanding of Solar System evolution from the point of view of organics and water (as hydrous minerals). The Hayabusa2 spacecraft is to have obtained Ryugu samples successfully (with a total amount of ~ 5.4 g) from surface and subsurface regions [1]. To obtain fresh subsurface samples from the Ryugu asteroid, a small carry-on impactor (SCI) was used to generate an artificial crater on the surface (e.g., [2,3]). Since very-high-explosive energy was required for the cratering operation of the Hayabusa2 mission, the SCI system contained HMX (the high-melting-point explosive cyclotetramethylenetetranitramine, C₄H₈N₈O₈) and other combustion chemicals. HMX is a typical high explosive that is used to produce a momentary driving force (e.g., [4]).

Because these materials may be possible contaminants in the subsurface samples, they must be investigated prior to analysis of the Ryugu samples. They may have been scattered around the surface of the Ryugu asteroid, including at the second touchdown site, and then have been collected into the sample container together with the asteroidal subsurface samples during touchdown sampling. We therefore set up an engineering model of the SCI experiment using an HMX mixture containing HTPB, IDP, and IPDI in an Ar atmosphere at ambient temperature and pressure in a closed system.

In this work, we report chemical and isotopic studies of the carbonaceous-based explosion products in addition to those presented by [5]. We used both non-destructive and destructive analytical techniques to identify the chemical nature of the materials. From SEM-EDS, we found the materials to be composed mainly of carbon, nitrogen, and oxygen, with a detectable amount of metals. Suitable parameters for identifying these materials are a FTIR peak at 1520 cm⁻¹, low reflectance and gentle red slope of FTIR spectrum compared with a Murchison CM2 chondrite,

the Raman D and G bands, and the H, C, and N isotopic compositions and their spatial distributions. The STXM-XANES results (Fig. 1) provided the molecular nature of these highly aromatic materials, which was supported by results from TD-GC/MS. These results suggest that it is possible to distinguish either Ryugu samples or SCI materials as potential contaminants in a sample container by using proper combinations of analytical techniques. This assessment provides information useful for the analysis of the Ryugu asteroidal samples.

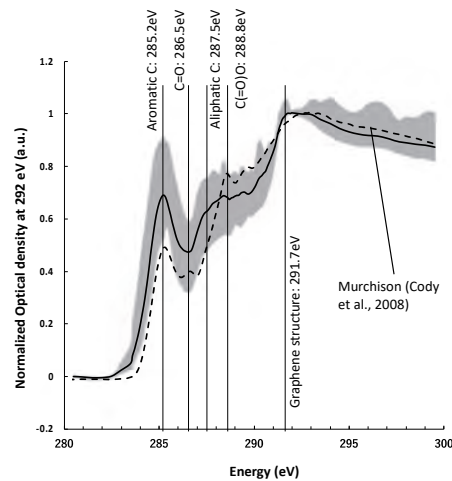


Fig. 1. Carbon-XANES of carbonaceous grains. Solid line is average of measured spectra together with spectrum of Murchison IOM (dotted line [6]). Grey area is a range of maximum and minimum absorptions observed among all spectra of each measurement.

- [1] T. Yada *et al.*, 52nd LPSC (2021) LPI Contrib. No. 2548.
- [2] S. Tachibana *et al.*, *Geochem. J.* **48** (2014) 571.
- [3] M. Arakawa *et al.*, *Science* **368** (2020) 67.
- [4] P.A. Snyder *et al.*, *Org. Mass Spectrom.* **26** (1991) 1109.
- [5] Y. Takano *et al.*, *Earth Planets Space.* **72** (2020) 97.
- [6] G.D. Cody *et al.*, *EPSL* **272** (2008) 446.

BL4U

Penetration of Redox-Sensitive Nanocarriers in Human Skin Ex Vivo

G. Germer¹, T. Ohigashi², H. Yuzawa², K. Rajes³, R. Haag³, F. Rancan⁴, A. Vogt⁴ and E. Rühl¹

¹Physical Chemistry, Freie Universität Berlin, Arnimallee 22, 14195 Berlin, Germany

²UVSOR Synchrotron Facility, Institute for Molecular Science, Okazaki 444-8585, Japan

³Organic Chemistry, Freie Universität Berlin, Arnimallee 22, 14195 Berlin, Germany

⁴Charité Universitätsmedizin, 10117 Berlin, Germany

Redox-sensitive nanocarriers transporting drugs into human skin have been investigated. The goal of this research is to use local changes in the redox state of inflamed skin for controlled drug release. This requires redox-sensitive nanocarriers transporting the drugs over the skin barrier, which have recently been characterized by *in vitro* and *ex vivo* studies [1]. These core-multishell nanocarriers (CMS) contain dendritic architectures with sizes below 20 nm. Key is redox-sensitive sites that can lead upon oxidation to changes in local polarity of the sulfur sites (osCMS) or upon reduction to the cleavage of disulfides (rsCMS). In a first step skin penetration of these redox-sensitive nanocarriers has been investigated by scanning transmission X-ray microscopy (STXM). The challenge of these studies was the selective probing of the nanocarriers, since there is no distinct chemical shift compared to the majority species contained in the EPON fixed human skin samples. This required the use of a recently developed procedure of data reduction by singular value decomposition [2].

The present studies on human skin *ex vivo* consider changes induced by the topically applied oxidizer dibenzoyl peroxide (DBPO, 40 mg/mL dissolved in a 1:1 mixture of acetone/propyl myristate), which was applied to one half of the samples for 16 h prior to topical application of rapamycin-loaded nanocarriers (rapamycin: C₅₁H₇₉NO₁₃, M = 914.13 g/mol). The nanocarrier samples (rsCMS (5 mg/mL, rapamycin loading: 2.7 %); osCMS (5 mg/mL) 0.5 % rapamycin loading) were formulated in HEC gel and 40 μ L of this formulation were topically applied for 10, 100, and 1000 min to the skin samples, respectively. The final drug concentrations were 1 μ g/cm² (osCMS) and 5.4 μ g/cm² (rsCMS), respectively. The experiments were performed at the BL4U beamline of UVSOR III. They mostly rely on scanning of the photon energy in the O 1s regime (520 – 565 eV), allowing for the acquisition of stacks of images by concentrating on the stratum corneum, the top horny layer of skin. Selected results are shown in Fig. 1, where a comparison is made between a skin sample initially not exposed to DBPO (A) and another one with pretreatment (B). The skin samples were subsequently exposed for 1000 min to drug-loaded rsCMS. The top of each plot shows (a) an X-ray micrograph recorded at 532.04 eV. The skin surface is located at the right hand side of each micrograph. Clearly, the stratum corneum (SC) with its layered structure is visible besides the viable

epidermis (VE). The spatial distribution of rsCMS is shown in (b). Less nanocarriers are found in the non-pretreated skin sample (A), which indicates that DBPO enhances the skin penetration of the nanocarriers. This becomes clearly visible from the integrated rsCMS signals as a function of depth. In the case of the not pre-treated skin sample only weak intensity is observed, whereas for the DBPO-treated sample (B) shows an enhanced rsCMS concentration. Integrations also show that the maxima of the local rsCMS concentration are correlated with narrow regions that are assigned to the lipid regions between the corneocytes. This is similar to earlier work on CMS nanocarriers that were not redox-sensitive [3]. Note that the present results could only be derived by singular value decomposition derived from data stacks containing the full spectral information in each pixel of the micrographs, whereas the previously used pairs of photon energies for probing the nanocarriers (cf. [3]) did not yield reliable results. Furthermore, the local rapamycin concentration was too low in the present samples to be detected. Subsequent work is required with enhanced drug loading to probe the redox-triggered drug release.

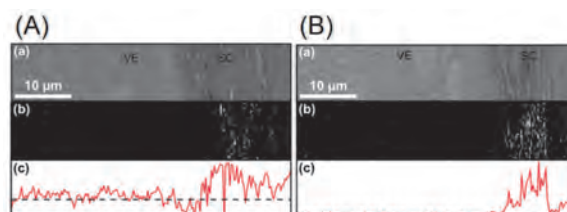


Fig. 1. Results from STXM of the top skin layers of fixed human skin without (A) and with (B) primary treatment with DBPO for 16 h followed by 1000 min exposure to reduction-sensitive nanocarriers (rsCMS): (a) X-ray scanning micrograph recorded at 532.04 eV; (b) spatial distribution of rsCMS; (c) integrated concentration of rsCMS.

[1] K. Rajes *et al.*, *Pharmaceutics* **13** (2021) 37; K. Rajes *et al.*, *Biomater. Sci. Engin.*, accepted (2021).

[2] G. Germer *et al.*, *ACS Omega*, accepted (2021).

[3] K. Yamamoto *et al.*, *J. Control. Release* **242** (2016) 64.

BL4U

Chemical Mapping of Particulate Matter from a Marine Test-bed Engine with Varying Sulfur Content Fuels and a Laboratory Wet-Scrubber

X. Kong¹, L. F. E. D. Santos¹, J. Noda², T. Ohigashi³, K. Salo⁴ and E. Thomson¹

¹Department of Chemistry and Molecular Biology, University of Gothenburg, 412 96 Gothenburg, Sweden

²School of Veterinary Medicine, Rakuno Gakuen University, Ebetsu 069-8501, Japan

³UVSOR Synchrotron Facility, Institute for Molecular Science, Okazaki 444-8585, Japan

⁴Maritime Environment, Shipping and Marine Technology, Chalmers University of Technology, SE-412 96 Gothenburg, Sweden

The marine shipping sector remains a large source of anthropogenic particle emissions [1]. In order to reduce particle emissions from ships, the international maritime organization (IMO) has implemented regulations that offer ship operators two primary options for compliance. They can either use marine low sulfur content fuels or high sulfur content fuels in conjunction with wet scrubbers as exhaust abatement system [2]. It is of large interest to investigate how both compliance measures affect physicochemical properties of exhaust particles and thus their potential role(s) within the climate system.

In June 2019 laboratory measurements investigating the effects of fuel sulfur content (FSC) and wet scrubbing on the droplet forming potential of exhaust particles from a marine diesel engine were performed using a cloud condensation nuclei counter (CCNC, DMT Inc.). Three different marine distillate fuels including a high sulfur content fuel, heavy gas oil (HGO), with a FSC of 0.86 wt % and two IMO compliant fuels with a FSC of <0.003 wt %, marine gas oil (MGO) and hydrotreated vegetable oil (HVO), were used in a four-stroke marine test-bed engine. HGO was also used in conjunction with a laboratory wet scrubber which itself was operated using both fresh as well as seawater. While a reduction in FSC decreased the ability of the exhaust particles to act as CCN, wet scrubbing facilitated droplet formation significantly. Figure 1 shows the critical supersaturations, *i.e.*, the supersaturations needed to activate particles into cloud droplets, of exhaust particles for different mobility diameters.

STXM measurements of exhaust particles collected during a second campaign in 2020 helped to identify chemical information (*e.g.*, functional groups) of the particles, which indicates the mechanism causing the differences observed in CCN activity. The STXM results presented in this study were obtained at the BL4U beamline at UVSOR.

Figure 2 shows C K-edge NEXAFS spectra of 4 cases, *i.e.*, HGO (2 samples), MGO, seawater and freshwater scrubbing cases. Interestingly, the two HGO and seawater scrubbing cases show almost identical spectra, and the MGO and freshwater scrubbing cases are similar in line shapes. This indicates the different organic species and abundance of these 4 cases. In addition to the carbon edge, we also acquired N K-edge, S L-edge, O K-edge and Cl L-edge spectra. Further

analysis of this STXM dataset and comparison with gas (*e.g.*, SO₂) and particle emission results is currently ongoing. A manuscript is in preparation.

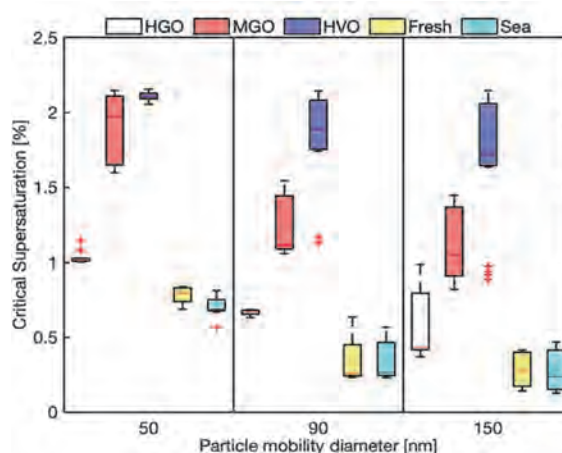


Fig. 1. Critical supersaturations measured for exhaust particles of three different mobility diameters. The colors represent the different fuel types, “Fresh” and “Sea” designate wet scrubbed exhaust particles using fresh and seawater, respectively.

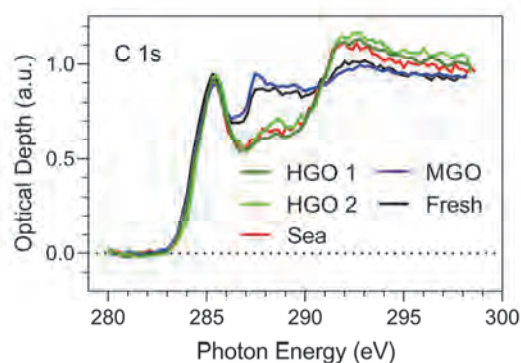


Fig. 2. Carbon K-edge NEXAFS spectra of sampled particles from HGO, MGO, seawater scrubber and freshwater scrubber cases.

[1] N. Kuittinen *et al.*, *Environ. Sci. Technol.* **55**, 1 (2021) 129.

[2] IMO, Resolution MEPC.176(58) (Revised MARPOL Annex VI), 2008.

BL5B

Study on Reflectance Characteristics of Mirror-polished Meteorite Fragments in the EUV Region

Y. Suzuki¹, K. Yoshioka^{1,2}, M. Kuwabara³, S. Nishimura¹ and T. Kosugi²

¹Department of Earth and Planetary Science, Graduate School of Science, The University of Tokyo, Tokyo 113-0033, Japan

²Department of Complexity Science and Engineering, Graduate School of Frontier Sciences, The University of Tokyo, Kashiwa 277-8561, Japan

³Institute of Space and Astronautical Science, Japan Aerospace Exploration Agency, Sagami-hara 252-5210, Japan

We study the transition of the reflection spectrum in the UV region when the meteorites are exposed to solar UV for a long time. In preparation for the measurement of meteorites, we, in this time, measured the reflectance of mirrors with higher reflectance, since it is easier to be measured. The principle of reflectance measurement, such as decreasing higher-order rays and the design of jigs, is the same for meteorites and mirrors. These mirrors are also to be used for the Hydrogen Imager (HI) onboard Comet Interceptor (CI) mission launched in 2028. In this experiment, the transmittance of filters used for the same mission was also measured. Evaluation of the wavelength dependence and the incidence angle dependence of the mirrors' reflectance and the filters' transmittance is also important in estimating the radiance expected in CI/HI observations.

We estimated the mirror's reflectance (or the filter's transmittance) by calculating the ratio of the radiance when a mirror was placed on the main stage (or a filter was placed on the filter stage) to it when nothing was placed on the optical path (Fig. 1). Wavelength scan was performed from 110 nm to 140 nm in 0.2 nm step with summing 5 using G3M4 grating. A photo-diode was used as a detector. The slit width and the pinhole diameter were set to 0.5 mm and 1 mm, respectively. Two types of filters are used: named (f1) and (f2) here, whose transmission peak are around 122 nm and 120 nm, respectively. We also used two kinds of mirrors: (m1) and (m2), an aluminum mirror and a multilayer dielectric-coated mirror, respectively. Measurements were repeated several times. Dark current measurements were performed each time the position of the stages or the detector was moved.

As a result, the transmittance of the filters and the reflectance of the mirrors at an incident angle of 5 degree are as shown in Fig. 2.

Both filters had a maximum transmittance just under 10 %. Their spectra are so similar that no significant performance difference was found in this experiment. The reflectance of (m2) at an incident angle of 5 deg was found to be 3 times higher than that of (m1). However, when the incident angle was 10 deg, the reflectance of (m2) became 250 % at maximum (the figure is omitted). Although we re-measured in another day, the reflectance was still up to 200 %. It is possible that stray light has occurred in the experimental system.

The further optimization (stray light cut or noise reduction) for the setting are needed.

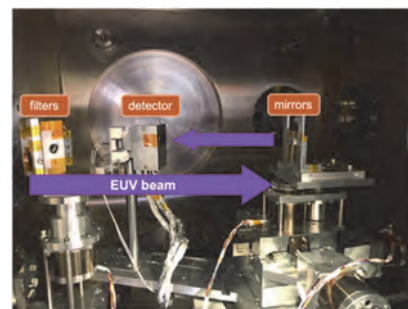


Fig. 1. The setup of the measurements.

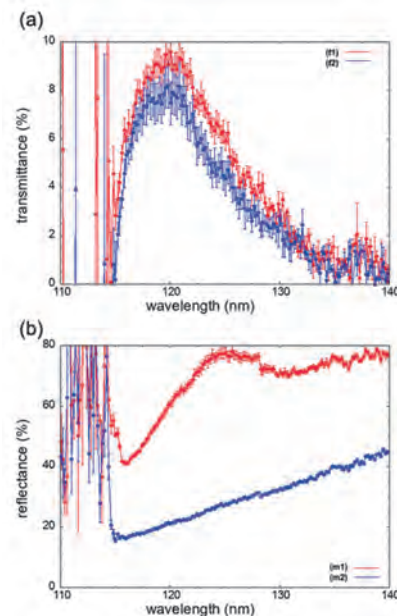


Fig. 2. (a) Transmittance of the filters (b) Reflectance of the mirrors.

BL7B

The Influence of Space Weathering on The Wavelength of The Solar System Organic Matter PAH

J. Yang¹, S. Nishimura^{1,2}, H. Lin¹, K. Yoshioka^{1,2} and I. Yoshikawa^{1,2}

¹Department of Complexity Science and Engineering, Graduate School of Frontier Sciences, The University of Tokyo, Kashiwa 277-8561, Japan

²Department of Earth and Planetary Science, Graduate School of Science, The University of Tokyo, Tokyo 113-0033, Japan

Polycyclic aromatic hydrocarbons (PAH or PAHs), known as polycyclic aromatic compounds or polycyclic aromatic hydrocarbons.

Reflectance spectroscopy can be used to analyze polycyclic aromatic hydrocarbons, because PAH has a very unique ultraviolet absorption spectrum. Each ring structure has a unique UV spectrum (Mansouri 2020), so each isomer has a different UV absorption spectrum. This is particularly useful in PAH identification. Most PAHs are also fluorescent, and when they are excited (when molecules absorb light) they emit light of characteristic wavelengths.

An analysis of the ultraviolet reflectance spectrum of interstellar dust has found an absorption band with a wavelength of 217.5 nanometers.

In order to understand the "extinction bulge" of the 217.5 nm interstellar medium (ISM), the spectral properties of carbon compounds have been extensively studied. The strongest feature in the interstellar extinction curve is the UV "bump" at 217.5 nm (Stecher 1965), also known as the 220 nm feature. The most obvious point of this feature is that the center wavelength is very stable, but the bandwidth varies with the environment of the universe. The ultraviolet spectrum of PAH has this characteristic.

It is known that those PAHs having a particularly large molecular weight have absorption band characteristics in the UV region, and PAH mixtures existing on the earth have an absorption band around a wavelength of 210 nm. Due to the weathering of the universe, PAH may increase the wavelength range of the ultraviolet absorption band in the universe. Therefore, assuming that the absorption band corresponds to the 217.5 nm absorption band appearing in the interstellar darkening curve (the curve depicting the absorption spectrum of interstellar dust), it can correspond to the PAH whose reflection band wavelength is approximately 210 nm on the earth.

This experiment is to observe and analyze the influence of space weathering on the optical properties of PAH. We have prepared PAH samples synthesized in the laboratory and PAH samples exposed on the International Space Station (ISS) (exposed samples) and similarly synthesized and stored in the laboratory (unexposed samples) for comparison experiments. (Both exposed and unexposed samples are made of PAH only, not a mixture.) We compared the reflection characteristics of these samples with the reflection characteristics of non-exposed samples in the 100-300 nm wavelength range (in 1nm step).

The reflection characteristics of the coronene sample show a significant decline near the wavelength of 270 nm, and show a trend in the wavelength region of 210-280 nm, that is, the attenuation of reflected light is more obvious at longer wavelengths (Fig. 2). This trend indicates that due to spatial weathering, the wavelength corresponding to the bottom of the dip may shift to a longer wavelength.



Fig. 1. The main chamber of BL7B.

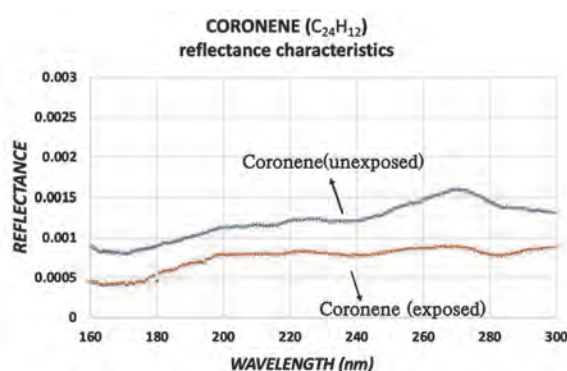
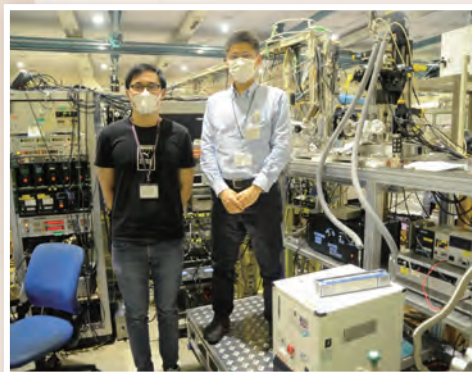
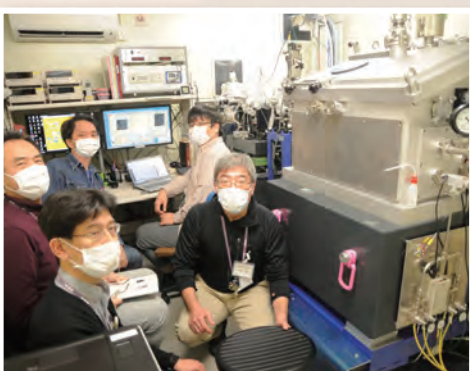
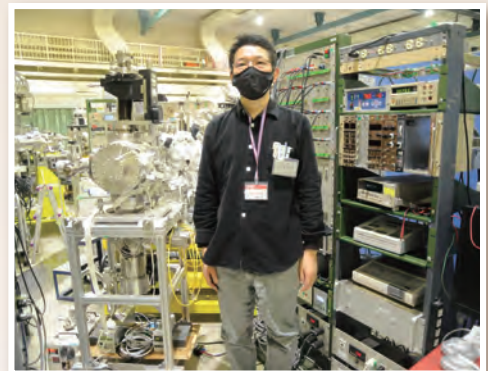
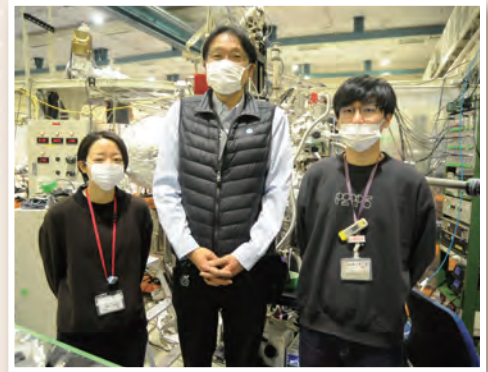


Fig. 2. The reflection characteristics of coronene samples in the wavelength range of 160-300 nm.

- [1] T. P. Stecher, *Astrophys. J.* **142** (1965) 1683.
 [2] E. Mansouri, V. Yousefi, V. Ebrahimi *et al.*, *Sep Sci plus* **3** (2020) 112.

UVSOR User 6



The background is a vibrant red color with a complex geometric design. It features several overlapping circular and linear patterns. A prominent feature is a large, semi-transparent circular graphic on the right side, composed of concentric rings and a dotted border. Diagonal lines and bands of varying shades of red sweep across the page, creating a sense of movement and depth. The overall aesthetic is modern and technical.

IV

List of Publications

List of Publication (2020)

K. Ali, H. Ohgaki, H. Zen, T. Kii, T. Hayakawa, T. Shizuma, H. Toyokawa, Y. Taira, V. Iancu, G. Turturica, C. A. Ur, M. Fujimoto and M. Katoh
“Selective Isotope CT Imaging Based on Nuclear Resonance Fluorescence Transmission Method”,
 IEEE Transactions on Nuclear Science **67** (2020) 1976.

A. Fleurence, C.-C. Lee, R. Friedlein, Y. Fukaya, S. Yoshimoto, K. Mukai, H. Yamane, N. Kosugi, J. Yoshinobu, T. Ozaki and Y. Yamada-Takamura
“Emergence of Nearly Flat Bands Through a Kagome Lattice Embedded in an Epitaxial Two-Dimensional Ge Layer with a Bitriangular Structure”, Phys. Rev. B **102** (2020) 201102(R).

A. Fleurence, Y. Awatani, C. Huet, F. B. Wiggers, S. M. Wallace, T. Yonezawa and Y. Yamada-Takamura
“Band Engineering in an Epitaxial Two-Dimensional Honeycomb $\text{Si}_{6-x}\text{Ge}_x$ Alloy”, Phys. Rev. Materials, **5** (2021) L011001.

K. Fujimori, M. Kitaura, Y. Taira, M. Fujimoto, H. Zen, S. Watanabe, K. Kamada, Y. Okano, M. Katoh, M. Hosaka, J. Yamazaki, T. Hirade, Y. Kobayashi and A. Ohnishi
“Visualizing cation vacancies in $\text{Ce}:\text{Gd}_3\text{Al}_2\text{Ga}_3\text{O}_{12}$ scintillators by gamma-ray-induced positron annihilation lifetime spectroscopy”, Appl. Phys. Express, **13** (2020) 085505.

H. Fukushima, D. Nakauchi, M. Koshimizu, N. Kawaguchi and T. Yanagida
“Synthesis and Scintillation Properties of Ce-doped CaZrO_3 Single Crystals”, Jpn. J. Appl. Phys. **59** (2020) SCCB15.

H. Fukushima, D. Nakauchi, T. Kato, M. Koshimizu, N. Kawaguchi and T. Yanagida
“Photoluminescence and Scintillation Properties of Ce-doped SrLu_2O_4 Single Crystals”, Solid State Sci. **110** (2020) 106471.

L. Guo, H. Yamaguchi, M. Yamamoto, F. Matsui, G. Wang, F. Liu, P. Yang, E. R. Batista, N. A. Moody, Y. Takashima and M. Katoh
“Graphene as Reusable Substrate for Bialkali Photocathodes”, Appl. Phys. Lett., **116** (2020) 251903.

Y. Higaki, K. Kamitani, T. Ohigashi, T. Hayakawa and A. Takahara
“Exploring the Mesoscopic Morphology in Mussel Adhesive Proteins by Soft X-ray Spectromicroscopy”, Biomacromolecules **22** (2021) 1256.

Y. Hikosaka, H. Iwayama and T. Kaneyasu
“Zeeman Quantum Beats of Helium Rydberg States Excited by Synchrotron Radiation”, Journal of Synchrotron Radiation, **27** (2020) 675.

T. Hirahara, M. M. Otrokov, T. T. Sasaki, K. Sumida, Y. Tomohiro, S. Kusaka, Y. Okuyama, S. Ichinokura, M. Kobayashi, Y. Takeda, K. Amemiya, T. Shirasawa, S. Ideta, K. Miyamoto, K. Tanaka, S. Kuroda, T. Okuda, K. Hono, S. V. Eremeev and E. V. Chulkov
“Fabrication of a Novel Magnetic Topological Heterostructure and Temperature Evolution of its Massive Dirac Cone”, Nature Communications, **11** (2020) 4821.

T. Horiai, S. Kurosawa, R. Murakami, Y. Shoji, J. Pejchal, M. Yoshino, A. Yamaji, H. Sato, Y. Ohashi, K. Kamada, Y. Yokota and A. Yoshikawa
“Crystal Growth and Optical Properties of a $\text{Ce}_2\text{Si}_2\text{O}_7$ Single Crystal”, Optical Materials, **109** (2020) 110210.

Motoo Ito, Naotaka Tomioka, Kentaro Uesugi, Masayuki Uesugi, Yu Kodama, Ikuya Sakurai, Ikuo Okada, Takuji Ohigashi, Hayato Yuzawa, Akira Yamaguchi, Naoya Imae, Yuzuru Karouji, Naoki Shirai, Toru Yada and Masanao Abe
“The universal sample holders of microanalytical instruments of FIB, TEM, NanoSIMS, and STXM-NEXAFS for the coordinated analysis of extraterrestrial materials”, *Earth, Planets and Space*, **72** (2020) 133.

K. Iwasawa and Koji K. Okudaira
“Effect of Chemical interaction at Modification Layer/substrate Interface on Molecular Orientation of Dinaphtho[2,3-b:2',3'-f]thieno[3,2-b]thiophene Thin Films”, *Jpn. J. Appl. Phys.*, **59** (2020) 091004.

T. Kaneyasu, Y. Hikosaka, M. Fujimoto, H. Iwayama and M. Katoh
“Polarization control in a crossed undulator without a monochromator”, *New J. Phys.* **22** (2020) 083062.

T. Kaneyasu, Y. Hikosaka, M. Fujimoto, H. Iwayama and M. Katoh
“Electron Wave Packet Interference in Atomic Inner-Shell Excitation”, *Phys. Rev. Lett.* **126** (2021) 113202.

M. Kitaura, K. Kamada, T. Ina, H. Yamane, M. Ishizaki, S. Watanabe, J. Azuma, I. Yamamoto, A. Ohnishi and T. Usuki
“Structural analyses of Gd₃(Al,Ga)₅O₁₂ garnet solid solutions via X-ray and UV absorption spectroscopy experiments for Gd atoms”, *J. Alloys Compd.* **867** (2021) 159055.

M. Kitaura, Y. Taira, M. Fujimoto, M. Katoh and H. Zen
“Visualization of vacancy-type defect complexes in garnet scintillator crystals by ultrashort gamma-ray induced positron annihilation lifetime spectroscopy (in Japanese)”, *Journal of JSSRR*, **34** (2021) 37.

S. Kodama, S. Kurosawa, M. Ohno, A. Yamaji, M. Yoshino, J. Pejchal, R. Král, Y. Ohashi, K. Kamada, Y. Yokota, M. Nikl and Akira Yoshikawa
“Development of a novel red-emitting cesium hafnium iodide scintillator”, *Radiation Measurements*, **124** (2019) 54.

Y. Kurashima, S. Kurosawa, R. Murakami, A. Yamaji, S. Ishikawa, J. Pejchal, K. Kamada, M. Yoshino, S. Toyoda, H. Sato, Y. Yokota, Y. Ohashi and A. Yoshikawa
“Novel Method of Search for Transparent Optical Materials with Extremely High Melting Point”, *Cryst. Growth Des.* **21**(1) (2021) 572–578

T. Mansikkala, M. Patanen, A. Kärkönen, R. Korpinen, A. Pranovich, T. Ohigashi, S. Swaraj, J. Seitsonen, J. Ruokolainen, M. Huttula, P. Saranpää, and R. Piispanen
“Lignans in Knotwood of Norway Spruce: Localisation with Soft X-ray Microscopy and Scanning Transmission Electron Microscopy with Energy Dispersive X-ray Spectroscopy”, *Molecules*, **25** (2020) 2997.

H. Matsuda and F. Matsui
“90°-deflection Imaging Electron Analyzer for Measuring Wide 2D Angular Distribution and Perpendicular Spin Texture”, *J. Electron Spectrosc. Relat. Phenom.* **245** (2020) 147001.

H. Matsushashi, A. Iwamoto, M. Sasaki, K. Yoshida and H. Aritani
“Synthesis of SrO–Al₂O₃ Solid Base Catalysts from Strontium Hydroxide and Aluminum Alkoxide by a Solid-liquid Interface Reaction”, *J. Jpn. Petrol. Inst.*, **64** (2021) 103.

F. Matsui, S. Makita, H. Matsuda, T. Yano, E. Nakamura, K. Tanaka, S. Suga and S. Kera
“Photoelectron Momentum Microscope at BL6U of UVSOR-III Synchrotron”, *Jpn. J. Appl. Phys.*, **59** (2020) 067001.

- G. Michailoudi, J. J. Lin, H. Yuzawa, M. Nagasaka, M. Huttula, N. Kosugi, T. Kurtén, M. Patanen and N. L. Prisle
“Aqueous-Phase Behavior of Glyoxal and Methylglyoxal Observed with Carbon and Oxygen K-edge X-ray Absorption Spectroscopy”, *Atmos. Chem. Phys.*, **21** (2021) 2881.
- M. Nagasaka
“Soft X-ray absorption spectroscopy in the low-energy region explored using an argon gas window”, *J. Synchrotron Rad.*, **27** (2020) 959.
- M. Nagasaka and H. Iwayama
“Photoelectron Based Soft X-ray Detector for Removing High Order X Rays”, *Rev. Sci. Instrum.*, **91** (2020) 083103.
- M. Nagasaka and N. Kosugi
“Soft X-ray Liquid Absorption Spectroscopy in Transmission Mode Realized by Precise Thickness Control”, *Butsuri*, **75**(8) (2020) 496.
- M. Nagasaka and N. Kosugi
“Local Structures of Aqueous Solutions Studied by Soft X-ray Absorption Spectroscopy”, *Journal of the Spectroscopical Society of Japan*, **67**(1) (2018) 2.
- M. Nagasaka
“Operando Observation of Liquid and Liquid-Liquid Interface by Soft X-ray Absorption Spectroscopy”, *Mol. Sci.*, **12** (2018) A0096.
- T. Ogawa, D. Nakauchi, M. Koshimizu, N. Kawaguchi and T. Yanagida
“Scintillation Properties of Pr-doped Ca₂Al₂SiO₇ single crystals”, *Opt. Mater.* **100** (2020) 109565.
- T. Ohigashi, H. Yuzawa and N. Kosugi
“A low-pass filtering Fresnel zone plate for soft x-ray microscopic analysis down to the lithium K-edge region”, *Rev. Sci. Instrum.*, **91** (2020) 103110.
- J. Okabayashi, S. Li, S. Sakai, Y. Kobayashi, T. Mitsui, K. Tanaka, Y. Miura and S. Mitani
“Perpendicular magnetic anisotropy at the Fe/Au(111) interface studied by Mössbauer, x-ray absorption, and photoemission spectroscopies”, *Phys. Rev. B* **103**, (2021) 104435.
- T. Saisopa, K. Klaiphet, P. Songsiriritthigul, W. Pokapanich, S. Tangsukworakhun, C. Songsiriritthigul, C. Saiyasombat, Y. Rattanachai, H. Yuzawa, N. Kosugi and D. Ceolin
“Investigation of solvated calcium dication structure in pure water, methanol, and ethanol solutions by means of K and L_{2,3}-edges X-ray absorption spectroscopy”, *J. Electron Spectrosc. Relat. Phenom.*, **244** (2020) 146984.
- H. Spiridigliozzi, A. Pille, F. Schoenstein, L. Miseur, E. Feldbach, H. Mändar, M. Kitaura and A. Kanaev
“Effects of Ta doping and irradiation with He⁺ ions on photoluminescence of MgAl₂O₄ spinel ceramics”, *J. Euro. Ceram. Soc.*, **40** (2020) 3215.
- T. Tsukamoto, A. Kuzume, M. Nagasaka, T. Kambe and K. Yamamoto
“Quantum Materials Exploration by Sequential Screening Technique of Heteroatomicity”, *J. Am. Chem. Soc.*, **142** (2020) 19078.
- Y. Taira, M. Fujimoto, S. Ri, M. Hosaka and M. Katoh
“Measurement of the phase structure of elliptically polarized undulator radiation”, *New J. Phys.*, **22** (2020) 093061.
- K. Takahashi, M. Arai, M. Koshimizu, Y. Fujimoto, T. Yanagida and K. Asai
“Luminescence Characteristics of Cs₂BaCl₄”, *Jpn. J. Appl. Phys.* **59** (2020) 032003.

- K. Takahashi, M. Arai, M. Koshimizu, Y. Fujimoto, T. Yanagida and K. Asai
“Luminescence and scintillation properties of Cs₂ZnCl₄ and Cs₃ZnCl₅”, Jpn. J. Appl. Phys. **59** (2020) 072002.
- S. Tsunekawa, F. Yamamoto, K. Wang, M. Nagasaka, H. Yuzawa, S. Takakusagi, H. Kondoh, K. Asakura, T. Kawai and M. Yoshida
“Operando Observations of a Manganese Oxide Electrocatalyst for Water Oxidation Using Hard/Tender/Soft X-ray Absorption Spectroscopy”, J. Phys. Chem. C, **124** (2020) 23611.
- H. Wang, M. He, Y. Li, H. Zhang, D. Yang, M. Nagasaka, Z. Lv, Z. Guan, Y. Cao, F. Gong, Z. Zhou, J. Zhu, S. Samanta, A. D. Chowdhury and A. Lei
“Electrochemical Oxidation Enables Regioselective and Scalable α -C(sp³)-H Acyloxylation of Sulfides”, J. Am. Chem. Soc., **143** (2021) 3628.
- O. Yagi, T. Kawai and K. Mizoguchi
“Formation and migration of Vk centers from localized excitons in NaCl:I and NaCl:I, Tl⁺ crystals”, Journal of Luminescence, **226** (2020) 117359.

The background features a large, stylized graphic of concentric circles and radial lines, resembling a sunburst or a target. The circles are composed of dashed lines and small dots, and the radial lines are solid. The overall color palette is a range of warm, earthy tones from light beige to dark brown.

V

Workshops

UVSOR Symposium 2020

Date: October 26 - 27, 2020

Place: Zoom & Remo Conference

October 26th (Mon.)

9:00 – 9:05 Opening Remark **S. Ideta** (UVSOR)

<Session 1, Chair: **H. Iwayama** (UVSOR)>

9:05 – 9:25 Present status and prospects of UVSOR Synchrotron Facility
S. Kera (UVSOR)

9:25 – 9:45 Operando XAS observation of all elements for the active structure induced by carbonate anion for water splitting
M. Yoshida (Yamaguchi Univ.)

9:45 – 10:05 Development of novel scintillation materials with high light-outputs using UVSOR beams
S. Kurosawa (Tohoku Univ.)

10:05 – 10:25 Coffee Break

<Session 2, Chair: **K. Tanaka** (UVSOR)>

10:25 – 11:10 [Invited talk]
Quasi-1D surface electronic states fabricated on III-V semiconductor surfaces
Y. Otubo (Osaka Univ.)

11:10 – 11:30 Coupling between Electron and Charge Density Wave Excitation Mode
Y. K. Kim (KAIST)

14:00 – 17:00 Poster flush for Poster Session (On-demand broadcasting via WEB)*
*Your Poster flush for Poster Session is recorded by using Zoom. Please see the following instruction (“How to Record Your Short Presentation by using Zoom”).

17:00 – 19:00 Poster Presentation

19:00 – Free Discussion

October 27th (Tue.)

<Session 3, Chair: **S. Ideta** (UVSOR)>

9:00 – 9:45 [Invited talk]
Exploring the band structure of black phosphorus with microARPES and nanoARPES
K. S. Kim (Yonsei Univ.)

9:45 – 10:05 Photoelectron momentum microscope 1.0: adding UVSOR specialties to the basic specification
F. Matsui (UVSOR)

10:05 – 10:25 Photoemission spectroscopy of oriented molecular thin film using photoelectron momentum microscope
Y. Hasegawa (IMS)

10:25 – 10:45 Coffee Break

<Session 4, Chir: **T. Ohigashi** (IMS)>

- 10:45 – 11:05 Title: Phase 2 “Team Kochi” for deciphering Hayabusa2 returned sample: in-depth analysis utilizing multi-instruments
M. Ito (JAMSTEC)
- 11:05 – 11:25 Development of key technologies for complete photoelectron measurement
H. Matsuda (UVSOR)
- 11:25 – 12:25 Discussion and Closing Remark
S. Kimura (Osaka Univ.)

Poster Session

- P01 Measurement of femtosecond time delay using frequency- and time-domain interferometry
T. Kaneyasu (SAGA Light Source)
- P02 Electron Wave Packet Interference in Xe 4d Inner-shell Excitation
T. Kaneyasu (SAGA Light Source)
- P03 Lattice Design for a Future Plan of UVSOR
E. Salehi (IMS)
- P04 Measurement of interferogram of undulator radiation at UVSOR-BL1U
S. Kimura (Nagoya Univ.)
- P05 Energy-Dependence of Photoelectron Circular Dichroism of Chiral Molecules
H. Kohguchi (Hiroshima Univ.)
- P06 Analysis of optical vortex UV light irradiation to Zn(II) complex-PMMA films
M. Yoshida (Tokyo Univ. of Science)
- P07 Gamma-induced Positron Annihilation Lifetime Spectroscopy for Cation Vacancies in Long Persistent Phosphors $\text{Sr}_2\text{MgSi}_2\text{O}_7$, Eu, Dy
H. Taniguchi (Yamagata Univ.)
- P08 3-D Isotope-Selective CT Imaging Based on Nuclear Resonance Fluorescence Transmission Method
K. Ali (kyoto Univ.)
- P09 Optical Activity Emergence of Amino Acids by Irradiation with Circularly-Polarized Ultraviolet Light and Spin-Polarized Muon Beams
T. Sakamoto (Yokohama National Univ.)
- P10 Vacancy Defects in $\text{Ce}:\text{Gd}_3\text{Al}_2\text{Ga}_3\text{O}_{12}$ Crystals Revealed by Gamma-ray Induced Positron Annihilation Lifetime Spectroscopy
K. Fujimori (Yamagata Univ.)
- P11 Intrinsic Nature of Photoluminescence Bands in $\beta\text{-Ga}_2\text{O}_3$ Crystals Revealed by Luminescence Spectroscopy
R. Tarukawa (Yamagata Univ.)
- P12 Prospect of Liquid Measurements Using the Soft X-ray Transmission Argon Gas Window
M. Nagasaka (IMS)
- P13 Observation of cobalt-carbonate catalyst for oxygen evolution using operando XAFS
Y. Araki (Yamaguchi Univ.)

- P14 Investigation of the adsorbing anion on the Ni water splitting electrocatalyst by operando XAFS observation
E. Ihara (Yamaguchi Univ.)
- P15 Resonant Soft X-ray Scattering method
H. Iwayama (IMS)
- P16 Glycine betaine-salt complex formation revealed by the liquid-phase inner-shell absorption spectroscopy
S. Ohsawa (Hiroshima Univ.)
- P17 Xe 4s Auger Decay Studied by Multielectron-Ion Coincidence Spectroscopy
Y. Hikosaka (Toyama Univ.)
- P18 Impurity emission of aluminum nitride by visible-soft X-ray excitation
T. Banno (Fukui Univ.)
- P19 Investigation of Photon Energy Drift at BL5B (2)
H. Zen (Kyoto Univ.)
- P20 Evaluation of Polarization Characteristic of Synchrotron Radiation by Observing Zeeman Quantum Beat
Y. Hikosaka (Toyama Univ.)
- P21 Angle-Resolved Photoemission Study of Antiferromagnetic i-MAX phase compound $(\text{Mo}_{2/3}\text{Ho}_{1/3})_2\text{AlC}$
K. Furuta (Nagoya Univ.)
- P22 Angle-resolved Photoemission Study of Graphene on Hex-Au(100) superlattice
K. Matsunaga (Nagoya Univ.)
- P23 The temperature dependence of carrier density and relaxation time for n-type Mg_2Si single crystals investigating by IR spectroscopy
T. Tanimoto (Yamagata Univ.)
- P24 Measurement of the electronic state of $\eta\text{-Mo}_4\text{O}_{11}$ using a momentum microscope
T. Kobayashi (Osaka Univ.)
- P25 Photon-Energy dependence of the photoelectron angular distribution from MoS_2
S. Tanaka (Osaka Univ.)
- P26 Research of deriving complex reflective index by analysis optical interference
M. Horiba (Fukui Univ.)
- P27 Transition from a monolayer to a bilayer in graphene/SiC(0001) by Li-intercalation and occupation of a flat band
M. Hashizume (Tokyo Inst. Tech.)
- P28 Photoemission Study of Solid Electrolytes $\text{Li}_x\text{La}_{(1-x)/3}\text{NbO}_3$ Bulk Single Crystal
R. Yamamoto (Nagoya Univ.)
- P29 Band control by Pd substitution in typeII Dirac material NiTe_2
K. Yoshino (Osaka Univ.)
- P30 The topological electric structure of interface between $\alpha\text{-Sn}$ and InSb
T. Nakaya (Osaka Univ.)

Next Generation Spectro-Microscopy and Micro-Spectroscopy Workshop

Date: October 28 - 29, 2020

Place: ZOOM (online)

October 28th (Wed.)

14:00 – 14:15 Opening Remark

Chair: **T. Ohigashi** (UVSOR)

14:15 – 14:50 Soft-X-ray Photoelectron Momentum Microscopy for Selective Atomic/molecular Orbital Excitation

F. Matsui (UVSOR)

14:50 – 15:25 Operando Electrochemical Scanning X-ray Transmission Microscopy for Lithium-ion Batteries

J. Lim (Seoul National Univ.)

15:25 – 16:00 In Situ Observation of Meta-stable Magnetization State in Fe/W(110) Nanostructures

W-X. Tang (Chongqing Univ.)

16:00 – 16:15 Coffee break

Chair: **F. Matsui** (UVSOR)

16:15 – 16:50 Current Status of the Scanning Transmission X-ray Microscopy Beamline in UVSOR

T. Ohigashi (UVSOR)

16:50 – 17:25 Nano-ARPES Study of Novel Topological Materials

T. Sato (Tohoku Univ.)

17:25 – 18:00 Development of a Laboratory-based In Situ XPS Apparatus for Liquid Samples and Electrochemical Interfaces

T. Masuda (NIMS)

18:00 – 18:30 Discussion and Workshop photo

October 29th (Thu.)

14:00 – 14:05 Second Day Opening

Chair: **S. Kera** (UVSOR)

14:05 – 14:40 STXM at TPS 27A1: Capabilities and Opportunities

H-W. Shiu (NSRRC)

14:40 – 15:15 Photoelectron Related Image and Nanospectroscopy Endstation at TPS 27A2: Capabilities and Opportunities

T-H. Chuang (NSRRC)

15:15 – 15:50 Strain and Permeability of Graphene studied by Cathode Lens Microscopy, Diffraction and Spectroscopy

M. S. Altman (Hong Kong Sci. Tech. Univ.)

15:50 – 16:05 Coffee break

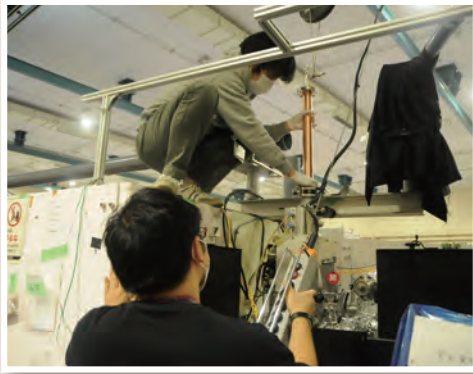
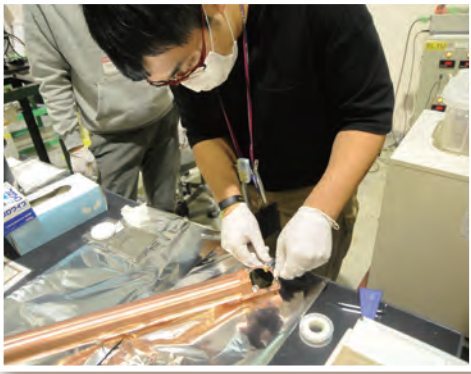
Chair: **K. Tanaka** (UVSOR)

16:05 – 16:40 Visualization of Excitons in 2D Semiconductor by Time-resolved ARPES

M. Man (OIST)

- 16:40 – 17:15 Stability and Inner Structure of Nanobubbles investigated by STXM
L. Zhang (Shanghai Synchrotron Radiation Facility)
- 17:15 – 17:50 Nano-scale Chemical State Visualization using Ptychography-XAFS
N. Ishiguro (Tohoku Univ.)
- 17:50 – 18:30 Discussion and Closing

UVSOR Staff Works







Editorial Board : H. Matsuda M. Fujimoto M. Sakai M. Ishihara

**Institute for Molecular Science
National Institutes of Natural Sciences
Okazaki 444-8585, Japan**

**Tel: +81-564-55-7402
Fax: +81-564-54-7079
<http://www.uvsor.ims.ac.jp>**



ISSN 0911-5730